Doctoral theses at NTNU, 2016:250

Robert Fritzsch

Electromagnetically Enhanced Priming of Ceramic Foam Filters

Doctoral thesis

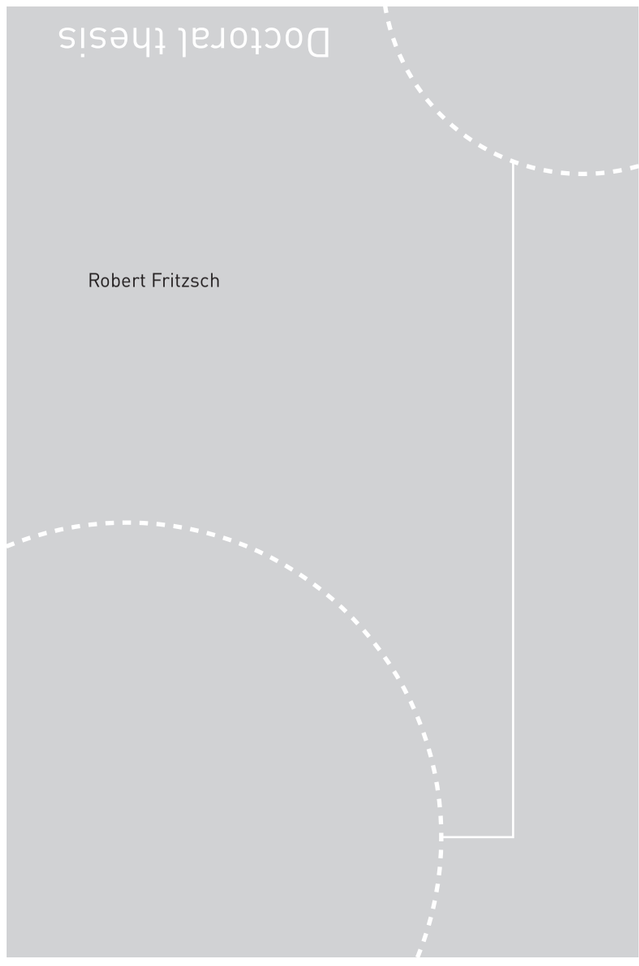

ISBN 978-82-326-1838-5 (printed ver.)
ISBN 978-82-326-1839-2 (electronic ver.)
ISSN 1503-8181

NTNU
Norwegian University of
Science and Technology

Doctoral theses at NTNU, 2016:250

NTNU
Norwegian University of
Science and Technology
Thesis for the Degree of
Philosophiae Doctor
Faculty of Natural Sciences and Technology
Department of Materials Science
and Engineering

NTNU

Robert Fritzsch

Electromagnetically Enhanced Priming of Ceramic Foam Filters

Thesis for the Degree of Philosophiae Doctor

Trondheim, September 2016

Norwegian University of Science and Technology
Faculty of Natural Sciences and Technology
Department of Materials Science and Engineering

NTNU
Norwegian University of
Science and Technology

NTNU
Norwegian University of Science and Technology

Thesis for the Degree of Philosophiae Doctor

Faculty of Natural Sciences and Technology
Department of Materials Science and Engineering

ISBN 978-82-326-1838-5 (printed ver.)
ISBN 978-82-326-1839-2 (electronic ver.)
ISSN 1503-8181

Doctoral theses at NTNU, 2016:250

Printed by NTNU Grafisk senter

Preface

The present work was initiated as the continuation of the research conducted by Dr. M. W. Kennedy in 2010 as part of the "Remelting and Inclusions Refining of Aluminium (RIRA)" project at the Norwegian University of Science and Technology ('Norges Teknisk-Naturvitenskapelige Universitet'), NTNU, in Trondheim, Norway. The core technology of the work is covered by a patent application named "Apparatus and Method for Priming a Molten Metal Filter" [1]. The PhD project was financed by the Department of Materials Science and Engineering (DMSE) at NTNU, and co-funded by industrial partners.

The main aim of the present research work have been to investigate the possibility of scaling the electromagnetic priming system, developed by Dr. M. W. Kennedy, to an industrial scale, and to test the setup together with industrial partners in a pilot facility. The goal was to design a system that would allow the industry to apply higher grade filters using less metal head than today, using no preheating, and increasing the filter thickness by 100 to 200%. The experimental program was carried out both at DMSE-NTNU and at Pyrotek® Electro Magnetic Pumping (EMP®) at the EMP test rig in Burton-upon-Trent, United Kingdom.

Professor Ragnhild E. Aune at DMSE-NTNU was the principal supervisor for the work, and Professor Knut Marthinsen was the co-supervisor. Dr. Shahid Ahktar has given significant contribution to the thesis, as well as Dr. M. W. Kennedy.

Results have been published via conference and journal articles, and have been submitted as the work progressed.

The present thesis consists of two main parts, see Figure I, and the main objects of the research reported include:

1. Establishing the physical properties for different filter grades and for different priming behaviours.
2. Determine the impact of different operating parameters on primability of high grade filters.
3. Determine the impact of operation with and without the use of a magnetic field during filtration.
4. Design an intermediate scale system to validate the applied theory.
5. Establish optimum operation parameters.
6. Design a commercial prototype.
7. Run the prototype in an industrial cast house to determine the effect of both particle removal and efficiency, as well as on casting velocity/rate.

The involved topics during the experiments have been:

- Electromagnetic fields and Induction.
- Magneto Hydro Dynamics and Lorentz Forces.
- Wetting and Priming of tortuous Ceramic Foam Filters (CFFs).
- Fundamental filtration and Inclusions.

- Solidification of aluminium alloys.
- Computerized image processing and acquisition.

Each topic listed above has been investigated through a combination of the following methods:

- Theory described in literature.
- Analytical solution.
- Experimental validation.
- Finite element modelling (FEM).
- Comparison with existing data from literature.

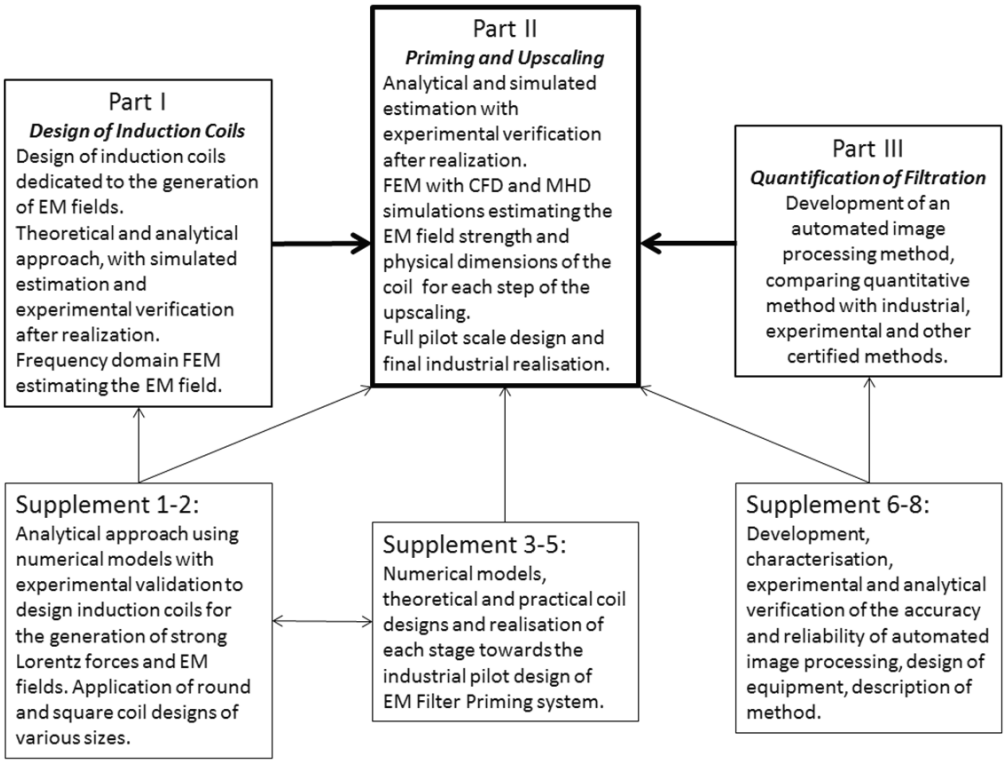

Figure I: Schematic outline of the thesis and the supplements.

Part I *Design of Induction Coils*

Supplement 1 describes the design of coils by using an analytical method based on the applied current, estimating the resulting magnetic field strength by understanding the correlation between voltage drop and empirical/analytical equations deriving the inductance. The inductance equations for multilayer coils was presented by Wheeler in 1928 [2], whereas simple inductance equations for square and round coils was presented in 1982 also by Wheeler [3], but not for multilayer coils. The comparison of different methods to calculate the inductance, as well as how to estimate the voltage drop, was in

the present paper presented for round- and square single/double induction coils of various dimensions. The performance of the designed induction coils are compared to FEM by using COMSOL®4.4 showing excellent agreement.

Supplement 2 gives a more detailed study on the design of special induction coils used for ElectroMagnetic (EM) priming of Ceramic Foam Filters (CFFs) for liquid metal filtration. The induction coils were designed by using a combination of analytical and FEM. Relatively simple empirical equations, published by Wheeler in 1928 and 1982, was used during the design process and found to accurately predict the z-component of the magnetic flux densities of both single- and multi-layer coils as verified both experimentally and by using COMSOL® 5.1 Multiphysics. The present paper discusses the design methodology, showing a simple design path for single and multi-layer round and square solenoidal coils for application to EM Priming.

Part II *Priming and Up scaling*

Supplement 3 describes the investigation of the effect of EM fields on the distribution of particles inside the CFF for a batch filtration setup, and the estimated advantages towards removal of inclusions < 20 µm. The filtration behaviour of 30, 50 and 80 PPI CFF of 10-23 µm large SiC particles were studied by the presence of alternating EM fields in the range of 0.06 to 0.2 T. The EM field was produced by round 4 inch induction coils at a main frequency of 50 Hz. It was discovered that the EM field enhanced the wetting and helped remove the gas from the filter. By comparing the experiments to gravitational trials it was also established that the filters could be primed with less metal head. During the extensive investigation of the particle distribution it was observed that the SiC particles were redistributed within the filter, and as a result the flow pattern inside the CFF was estimated and the essential filtration mechanisms for CFFs studied.

Supplement 4 describes how the 4 inch EM enhanced filtration approach was used to estimate the industrial application of the system. The effect of EM priming was shown with a reduction of the required metal head for 50 and 80 PPI CFF to only 1/3rd of the standard industrial practice. The possibility of priming a stack of 3 filters (150 mm thick filters) was also proven.. The impact of the estimated flow rates induced by the time varying Lorenz forces was presented, and the resulting filter productivity and filtration rates were discussed by comparing EM primed and gravity primed CFF. A model to predict the filtration efficiency as function of velocity and filter thickness was also presented. The replacement of the 30 PPI CFF by the 50 PPI CFF primed by EM fields was emphasised due to higher overall filtration efficiency.

Supplement 5 describes the first stage of the up scaling of the EM priming system by a factor of 2.25 to a 9 inch CFF system. The 9 inch CFF is the smallest industrial applied size filter. The 9 inch induction coil was design to suit industrial cast house standards. Thus, a square shape was chosen for the induction system. The effect that the square coil had on inducing an inhomogeneous EM field was estimated by FEM and later validated by experiments. By using the designed square shaped induction

coil the appearance of a liquid metal meniscus during priming was discussed, and the priming of cold single 50 PPI and cold single 80 PPI CFF proven.

Part III *Quantification of Filtration*

Supplement 6 presents a method to analyse contamination of metal samples by quantification of the particle load. The quantitative particle concentration gives important information about the cleanliness of the investigated metal. The manual quantification of the particle concentration is normally a time-consuming process, where human control can bias and alter the acquired images, the particle count and therefore the perceived cleanliness. The automated image-processing steps for the quantification of SiC-particles, with equivalent diameters from 2 to 25 µm, was investigated and discussed based on rapid solidified spectrographic discs of solidified A356. A total of 700 micrographs were acquired with a standard white light microscope and later analysed. The applied software was Image Pro-Plus 7.0 from MediaCybernetics®, which allowed for design of specific macros, which in turn provides the user with a higher degree of control. The automated results were compared with the results obtained by manually counting the particles in the same micrographs. The impact of the automated results on the estimated filtration efficiency was established to be ~3%.

Supplement 7 is a continuation of the work presented in *Supplement 5*, and describes how an automated stage mounted on a standard light microscope can be used to investigate the presence of inclusions/contaminants in metal samples secured from normal cast and wrought aluminium alloys. The method, which allows for a larger area of sample to be investigated during a short period of time, was used to analyse smaller particles (< 25 µm) with a high degree of reproducibility. The metal cleanliness was evaluated, as well as the filtration efficiency. The limiting factor of the method was identified to be the resolution of the imaging system.

Supplement 8 summarizes the knowledge gained during the present work in regards to acquire and process digital micrographs for metal cleanliness investigations. The most important issues that image processing faces when used for analysing metal samples were in detail discussed, and a comparison made between the proposed method and other more common practices of image processing. The technique used to separate and identify inclusions, particles and pores was successfully tested and applied on samples taken from standard industrial aluminium cast house metal. How the total number of small particles can provide information on metal cleanliness and filtration efficiency was also discussed, together with the methods potential to be a fully automated system.

“Some words might be good, others ideas maybe better. A simple question could tear the construct apart and initiate a new concept, as in re-search.

Understanding or a conclusion is, however, not generated by the written words; understanding first shapes and conclusions later grow within the mind of the men reading them.

Therefore; it is our task to explore and develop our mind in the same way as we need to adapt to progress and failure. Sometimes, we just need to change our perspective.”

Acknowledgements

I would like to thank my supervisor, Prof. Ragnhild E. Aune for offering me the opportunity to challenge myself with this task requiring theoretical and practical skills from the fields of process metallurgy, computer science and electrical engineering. My gratitude goes to her for giving me her trust and her precious time, supporting me on this difficult and long road and giving me the freedom that was required to finally master this challenge.

I am deeply grateful to Dr. Mark W. Kennedy for the intensive technical and theoretical discussions, the mathematical guidance, the long lectures on electrical engineering and the practical help during all my time at NTNU. His detailed reviews of all my publications improved the quality of not only their and my English, but also enhanced the quality of the analytical solutions. He was the person, who could translate my confusing thoughts into brilliant ideas and words.

The practical support of Kurt Sandaunet from SINTEF with foundry equipment and knowledge was of vital importance to initiate the essential intermediate 9 inch scale trials at university. He supplied me with foundry equipment of proper scale and supported me with practical expertise.

The moral and practical support of my good friend Trygve Lindal Schanche, technical engineer at DMSE, is highly appreciated. He helped me with all the 9 inch filter trials at NTNU, and guided my hand to master the metallographic preparations required for the automated image acquisition.

The work and discussions with Shahin Akbarnejad have helped me generate a more general picture and easier understanding of the electrical theory within this thesis. He helped me by conducting the water pressure drop experiments, which is the crosslink between fluid flow and EM field.

The theoretical and moral support of Prof. Knut Marthinsen from DMSE at NTNU during the last stage of the image processing discussion and final publications was essential to completing the final stage realizing the automated image acquisition.

The support by Dr. Shahid Ahktar from Hydro Karmøy, Norway, who supplied the casting material and metal, has been important to conduct this work.

Many more people from the staff at NTNU, as well as SINTEF, have been contributing to this work with their experience, expertise and practical help, and are worth mentioning. At DMSE my thanks go to Prof. Leif Kolbeinson (shrinking core theory, thermodynamics, sustainability and discussions), Dmitry Slizovskiy (casting and many discussions). From SINTEF's department of materials and chemistry; Roar Jensen (electrical engineering, health and safety), Steinar Prytz (technical support, experimental supervision), Stein Rørvik (automated image processing, programming, microscopy) and Martin Syvertsen (image processing) are gratefully acknowledged.

I would like to thank and acknowledge my industrial partners in Norway, England and Sweden. The main support was given as physical resources such as refractory, ceramic foam filters, metal for the priming and filtration, financial support, discussions and technical guidance. My thanks go to Nigel Clear who realized the industrial cooperation, Dr. Neil Keegan who saw the potential of the idea, initiated the cooperation and became a friend during the time of the thesis, Paul Bosworth for his brilliant mechanical engineering skills and beautiful CAD models, Clive Brecknell for ensuring the practicality of the electrical design of the pilot system, Jason Midgley as the strong hand organising the tasks and keeping the moral high, and Hillary Dixon for the summarizing and organizing the work

during the final stage of the project. All these good people are from Pyrotek® EMP Burton-upon-Trent in the United Kingdom. I also want to thank Anders U. Johansson and Robbin Kantarp from SAPA, Finspång in Sweden, for giving me insight in cast house practice and initializing the contact with Pyrotek®. A special thank is going to the R&D from Hydro Karmøy in Norway for the metal used for the casting trials, metallographic samples and metal cleanliness result to validate the automated image processing method in the later stage of the testing.

My deepest gratitude goes to my parents Michael Fritzsch and Katalin Mersitz and to my dear Mara for being by my side and for supporting me during the time of this thesis, my writing process and for strengthening my back when I lost my confidence. I want to thank my daughter Tabea Runa, who was born during the time this thesis has been written, for all the joy, truth, strength she brought to our life, besides the sleepless nights.

I should not forget to thank my fellow PhD and Master students and my friends here in Trondheim and back home in Berlin for all the good discussions about life and work, shared moods, good moments, time consuming side projects, all the good coffee and tea and the unforgettable times. Thanks to Hannes Zedel, David Dominikus Eide Brennhaugen, Paul Wilpert, Anders Fagerbak and Diana Eckert, Stian Wannebo and Gro Hellesnes, Ivar Andre Ødegård, Masoud Hasanabadi, Maren Kirknes Fossum and everyone who I should have mentioned in this section, but now just forgotten.

It was an experience gained only once during a lifetime. I realized how unique my path has been until now, the set of each and every little piece, guiding me, all by your words, laughs, hands and thoughts. Thank you all!

Trondheim, June 2016

Robert Fritzsch

Abstract

Impurities in aluminium can cause detrimental physical and chemical inhomogeneity in the final products, as well as potentially catastrophic failures. Hence, one of the key aspects during production of aluminium and its alloys is to control the amount of inclusions/contaminants remaining within the metal after filtration, *i.e.* controlling the 'Cleanliness' of the produced material. The filtration step is the second stage of inclusion removal (after settling), and the last step of the melt treatment stage prior the casting.

In the filter-boxes used today the metal head is used to prime the filter by gravity, when mounting the filter in the filter-box below the metal level in the launder. If the filter is mounted far below the launder, the priming will be good, but then an extensive amount of metal needs to be drained from the filter-box after each cast (a single filter box typically contains 500-600 kg of sump metal by the end of each cast). In addition, the existing technology also involves significant manual handling of molten metal and hot filters, introducing a human factor, which increases the probability for HES related incidents and adds additional costs.

High Pores Per Inch (PPI) filters have proven to have excellent efficiency for inclusion removal; however, these types of filters, *i.e.* 50-80 PPI, are not commonly applied in industry. One reason that these filters are not used is that they cannot be effectively primed in many commercial cast house installations due to the excessive metal head required.

The electromagnetic (EM) priming technology is a patented innovative concept (US Patent nr. 20150322543), reinventing the fundamental concept of the filter-box by eliminating the need of preheating, extensive metal head and limitations to filter thickness. The main objective of the present work has been to investigate the effect of up scaling of the EM priming technology used for the priming of molten aluminium on Ceramic Foam Filters (CFF). Focus has been on different (i) coil designs (shapes and sizes), (ii) filter grades and thickness, and (iii) aluminium alloy systems. The final goal of the thesis was a 'proof of concept', by realizing the theory, design, construction and validation of the EM priming effect on high grade 23 inch CFFs, *i.e.* on a full industrial scale filter.

EM field modelling, analytical calculations and experimental validations were undertaken to estimate the shape effect of the coil (square versus round) on the shape of the magnetic field, and on the magnitude and direction of the induced Lorentz forces prior to construction of the coils. Lorentz force calculations were performed analytically, and the solutions verified by COMSOL® simulations and later validated by experimental observations. The inductive heating power were evaluated for all inductor sizes, and the Magneto Hydro Dynamics (MHD) induced by the Lorentz forces verified by COMSOL® simulations. Focus was placed on the formation of a meniscus, in order to evaluate the potential benefits of the effectively higher 'gravity head' to achieve priming of the CFFs.

In the present work the EM priming effect was investigated using laboratory scale round 4 inch and intermediate square 9 inch CFFs, as well as industrial pilot scale square 23 inch CFFs. Filters of various grades (30, 50 and 80 PPI) and at different filter thicknesses (50, 100 and 150 mm) was tested using 3 different alloys (A356, A3XXX and A5XXX). Batch reactors were designed for each filter size to mount from 1 to 3 filters in a stack, and used with newly designed and constructed round 4.7, square 12.2 and square 28.9 inch induction coils. These coils were used to investigate the EM priming by application of EM field strengths varying from 0.1 to 0.25 T. A practical approach to designing

induction coils with maximized generation of Lorentz force, and the strongest magnetic fields, beginning with simple inductance calculations, is also presented. The dictum to achieve priming on high-grade cold filters, *i.e.* to use no preheating, was kept throughout the work.

The cleanliness of the metal after filtration of an EM primed CFF was investigated by two methods, *i.e.* (i) a purely theoretical approach using empirical mathematical models to estimate the filtration efficiency, and (ii) a method for quantification of the metal cleanliness by automated image acquisition and processing. The quantification of the melt cleanliness was conducted by a moving stage mounted on a light microscope and self-programmed macros by ImagePro® Plus 7, allowing for a less biased particle and inclusion count. The method has been successfully compared to a manually conducted cleanliness count, revealing a total error below 3%. The results of the automated image processing method have been used to validate the proposed mathematical models.

In the present work the 'proof of concept' has been successfully demonstrated by priming 3 stacked 50 PPI and a stack consisting of one 50 and one 80 PPI 23 inch industrial scale CFFs. A positive effect of the EM field on the priming ability of CFF without preheating was observed, and could be reproduced for every laboratory experiment, as well as for the industrial scale trials. The induced EM priming allowed priming of 150 mm thick high grade CFFs without application of preheating while using normal casting temperatures and less than the standard metal head.

Keywords: Aluminium, Ceramic Foam Filter, CFF, Priming, Filtration, Induction, Coil design, Electromagnetism, Magneto Hydro Dynamics, MHD, CFD, FEM, Metal meniscus, COMSOL, Metal cleanliness, Melt quality, Automated image processing, Particle counting, ImagePro

Supplements

The present thesis includes the following supplements:

Part I	*Design of Induction Coils*
Supplement 1	"Design of Square Induction Coils for the Electromagnetic Priming of Ceramic Foam Filters," **R. Fritzsch**, M. W. Kennedy, and R. E. Aune, Light Metals 2016, DOI: 10.1002/9781119274780.ch132, 777-784.
Supplement2	"Design of circular, square, single and multi- layer Induction Coils for electromagnetic priming Using inductance Estimates," **R. Fritzsch**, M. W. Kennedy, and R. E. Aune, submitted to IEEE.
Part II	*Priming and Upscaling*
Supplement 3	"Electromagnetically Modified Filtration of Liquid Aluminium with a Ceramic Foam Filter," **R. Fritzsch**, M. W. Kennedy, S. Akhtar, J. A. Bakken, and R. E. Aune, *Journal of Iron and Steel Research International (1006-706X, 2012 Issue S1)*, 72-76
Supplement 4	"Electromagnetic Priming of Ceramic Foam Filters (CFF) for Liquid Aluminum Filtration," **R. Fritzsch**, M. W. Kennedy, J. A. Bakken, and R. E. Aune, *Light Metals 2013*, DOI: 10.1002/9781118663189.ch165, 973-979
Supplement 5	"Effect of Electromagnetic Fields on the Priming of High Grade Ceramic Foam Filters (CFF) with Liquid Aluminum," **R. Fritzsch**, M. W. Kennedy, S. Akbarnejad, and R. E. Aune, *Light Metals 2015*, DOI: 10.1002/9781119093435.ch156, 929-935.
Part III	*Quantification of Filtration*
Supplement 6	"Automated Quantification of SiC-Particles in Solidified A356 Aluminium using ImagePro® Plus 7.0," **R. Fritzsch**, B. Mirzaei, M. W. Kennedy, and R. E. Aune, *Characterization of Minerals, Metals, and Materials 2013 (TMS 2013)*, DOI: 10.1002/9781118659045.ch8, 67-77.
Supplement 7	"A novel Method for Automated Quantification of Particles in Solidified Aluminium," **R. Fritzsch**, S. Akbarnejad, and R. E. Aune, *TMS 2014 Supplemental Proceedings*, DOI: 10.1002/9781118889879.ch65, 535-543.
Supplement 8	"Solidified Metal Cleanliness Analysis Using Automated Image Acquisition and Macro Based Digital Image Processing," **R. Fritzsch**, S. Akbarnejad, K. Marthinsen, and R. E. Aune, submitted to IEEE Image Processing.

Presentations

Robert Fritzsch, Mark W. Kennedy, Shahid Akthar and Ragnhild E. Aune, ” Electromagnetically Modified Filtration of Liquid Aluminium with a Ceramic Foam Filter,” EPM 2012, Beijing, China, 22.October to 26. October 2012.

Robert Fritzsch, Mark W. Kennedy, John A. Bakken, and Ragnhild E. Aune , “Electromagnetic Priming of Ceramic Foam Filters (CFF) for Liquid Aluminum Filtration,” *TMS 2013*, San Antonio, USA, 3. March to 7. March 2013.

Robert Fritzsch, Behzad Mirzaei, Mark W. Kennedy, and Ragnhild E. Aune, “Automated Quantification of SiC-Particles in Solidified A356 Aluminium using ImagePro® Plus 7.0” *TMS 2013*, San Antonio, USA, 3. March to 7. March 2013.

Robert Fritzsch, Shahin Akbarnejad, and Ragnhild E. Aune, “A novel Method for Automated Quantification of Particles in Solidified Aluminium,” *TMS 2014*, San Diego, USA, 16. February to 20. February 2014.

Robert Fritzsch, Mark W. Kennedy,Ragnhild E. Aune, “Effect of Electromagnetic Fields on the Priming of High Grade Ceramic Foam Filters (CFF) with Liquid Aluminum,” *TMS 2015*, Orlando, USA, 15. March to 19. March 2015. (Winning the **2015 TMS Light Metals Subject Award - Warren Peterson Cast Shop for Aluminum Production.)**

Robert Fritzsch, Mark W. Kennedy, and Ragnhild E. Aune, “Design of Square Induction Coils for the Electromagnetic Priming of Ceramic Foam Filters,” TMS 2016, Nashville, USA, 15. February to 19. February 2016.

Patents / Papers as Second / Third Author

M. W. Kennedy, **R. Fritzsch**, S. Akhtar, J. A. Bakken, and R. E. Aune, "Apparatus and Method for Priming a Molten Metal Filter," *U.S. Patent Application*, WO2013160754 A1, 2012, 1-26.

M. W. Kennedy, K. Zhang, **R. Fritzsch**, S. Akhtar, J. A. Bakken, R. E. Aune, "Characterization of Ceramic Foam Filters Used for Liquid Metal Filtration," Metallurgical and Materials Transactions B, June 2013, Volume 44, Issue 3, ISSN: 1543-1916, DOI: 10.1007/s11663-013-9799-7, pp 671-690.

Z. Wang, B. Zhang, D. Li, **R. Fritzsch**, X. Zeng, H. J. Roven, W. Ding, "Effect of Heat Treatment on Microstructures and Mechanical Properties of High Vacuum Die Casting Mg–8Gd–3Y–0.4Zr Magnesium Alloy," *Transactions of Nonferrous Metals Society of China*, Volume 24, Issue 12, December 2014, ISSN 1003-6326,

S. Akbarnejad, M. W. Kennedy, **R. Fritzsch**, and R. E. Aune, "An Investigation on Permeability of Ceramic Foam Filters (CFF)," Light Metals 2015, DOI: 10.1002/9781119093435.ch159, 949-954.

Contents

Chapter 1

1. Introduction

The urge of men to enter space and other hostile environments, and to achieve unmatched speeds and efficiencies is driving the demand for materials with exceptional abilities. Simultaneously, the 'technocratic' and 'imperial' age is taking its toll on mankind through environmental changes, resource scarcity, cultural challenges and mass migrations. Combined, these difficulties are demanding a more or less drastic change to maintain our 'golden' age for humankind towards a more sustainable future. Driven by the need for a solution to the environmental and cultural challenges, the market drives the economy and the companies to recognize recycling and reprocessing waste as a cheaper source of metals and minerals for future demands. The reduction in waste generation, the increase in recycling and the general design to reuse of all sorts of energy intensive materials, by not compromising the material abilities, are insidiously.

Filtration is the most applied method to separate phases and inclusions/contaminations from common materials such as aluminium. Inclusions/contaminations may enter the aluminium through various ways, *i.e.* with the ore and other raw materials (recycled metal) used in the extractive metallurgical process, with the refractory materials, from the atmosphere and the environment, and finally through the refining process and/or the melt transfer procedures. Depending on the final application of the metal, any amount of contamination can weaken the metal and increase the possibility of critical failure of the aluminium product /part. This would result in serious economic and reputational consequences to the metal producers and recycling facilities.

A high load of small individual or large inclusions can cause a detrimental effect on the mechanical and chemical abilities of the end products produced from the contaminated metal. A broad variety of methods to remove inclusions from liquid aluminium and improve the metal cleanliness have been developed over a number of years [4-8]. The term metal "cleanliness" was introduced and applied to all kind of molten aluminium processes to find a measure of the melt quality and the estimated physical properties that the final product can deliver. Inclusions have been identified to be the main source of fatigue and failure in regards to products during production and application [9]. This was realized by counting submerged inclusions, and by investigating the effect of the inclusions on the microstructure of the solidified metal. Offline methods, such as Pre-Fill, Podfa, K-mould and many others are available for this purpose, but in-situ methods, such as the LiMCA (Liquid Metal Cleanliness Analyser) [5], AlSCAN [10] or Alspek [11] are favoured by most aluminium cast houses.

The fundamental principles to achieve good cleanliness by a low contamination are settling, flotation, degassing and liquid metal filtration, executed by Deep Bed Filters (DBF) or Particle Deep Bed Filters (PDBF) [12], Ceramic Foam Filters (CFF) [13, 14] and Bonded Particle Filters (BPF) [15]. The CFFs are by any means the most commonly applied filtration technology, and have been used to filter approx. 50% of the world production of aluminium since the 1990's.

The need of the industry to have a filtration system that can be flexibly applied has been answered by the CFF systems. The filtration efficiency of CFFs has a large deviation from acceptable means, especially low-grade filters such as 10-30 Pores Per Inch (PPI). Higher grade filters, *i.e.* 50-60 PPI, have a smaller deviation, higher efficiency, but are difficult to handle. The highest grade CFFs using

80 or more PPI have excellent filtration efficiency, but have a statistically high chance of failing using the standard priming and preheating methods.

The filtration efficiency of CFFs can be easily improved by reducing the filtration velocity [16], but this is in conflict with the high required productivity. The use of tighter filters of a thicker filter media would have the same effect in enhancing the filtration efficiency [17]. Such a setup would, however, require extensive preheating and additional metal head to press the metal into the tight or long tortuous filter sections by gravitational forces. This is clearly unpractical in industrial practice. Known CFF setups using the double filter thickness, such as the "Duplex Filter" [18], are struggling to secure the flow of metal through the thicker filter section and have a high probability of freezing.

Recently the impact of the ElectroMagnetic (EM) field generated by different induction coils was investigated [19-21]. It is well known that EM fields influence the behaviour of conductive liquids. Wherever an EM field penetrates into a liquid conducting fluid, induction occurs and electromotive forces are induced. Those electromotive forces induce characteristic pressure on the fluid, inducing velocity with characteristic flow patterns. A positive effect on the required metal head to successfully "prime" commercial filter was thus discovered, and is today a registered US patent (Nr. 20150322543) [1].

The idea of the patent is to use the EM forces to prime filters and/or filter sections, and thereby introduced a new concept of filtration for liquid metal. The main focus has so far been on utilising this new concept and thereby driving the research towards a system, which allows the application of thicker and finer filters for all sorts of commercial light metal filtration.

The topic of the present work is therefore based on the stepwise up scaling of the patented idea to a full industrial scale filtration system, and the commercialisation of the system with industrial partners to make the technology 'market ready'. The focus was therefore set to be the design of solenoidal and square shaped multilayer induction coils, the understanding of the effect of the EM field on the liquid metal related to the shape and size of the coil, and the effect of the current density and frequency applied to the coils. Besides of Finite Element Modelling (FEM), using Computational Fluid Dynamics (CFD) and Magneto Hydro Dynamics (MHD), experimental validations, by measuring the designed coils and conducting liquid metal experiments. The up scaling of the coil by a factor of more than six, from 4-inch filters (using a 4.7 inch coil) to 23 inch filters (using a 28.9 inch square coil), is shown as a sketch in Figure 1.

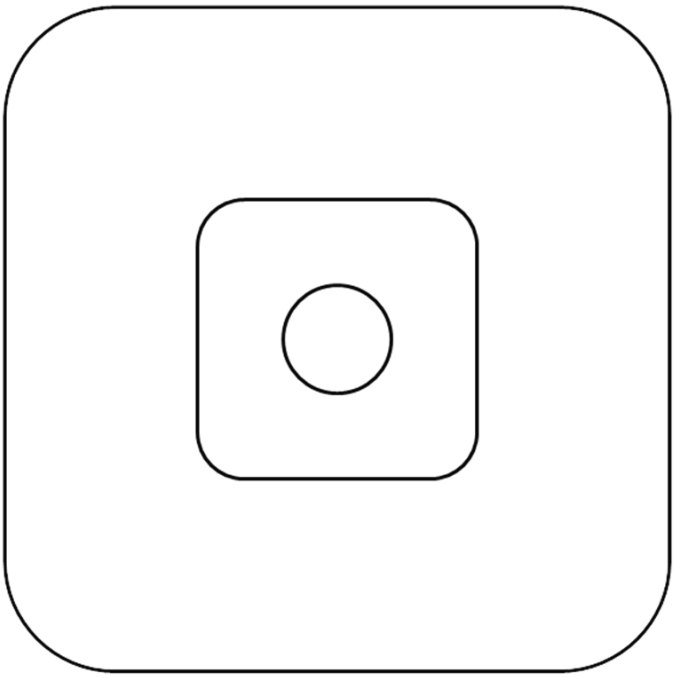

Figure 1: Sketch of the upscaling ration of each coil, starting with the inner circle which represents the 4.7 inch round coil, over the intermediate of 12.2 inch square coil to the final 28.9 inch square coil.

The overall technology used in the present wok will prove to be a small step towards sustainability, as it allows more efficient and less energy intensive recycling of aluminium, which is a common metal that is very energy intensive to produce. The technology presently used is driven by Alternating Currents (AC), inducing electromagnetic forces, and utilizing known fundamental effects such as Lorentz forces. The conductive liquid metals are interacting with the alternating magnetic fields. Using electrical power, the technology is energy efficient compared to traditional natural gas driven preheating and priming units, and it requires less metal head by simultaneously allowing for finer filters to be utilized.

The present work is separated into three logical sections, supported by published or submitted articles:

1. The design of induction coil for ElectroMagnetic (EM) priming.
2. The priming of the Ceramic Foam Filters (CFF), while up scaling the EM system.
3. The filtration efficiency, and automated image acquisition and processing.

Chapter 2

2. Design of Induction Coils

Mankind has known the fundamentals of electromagnetism for more than 100 years, and the principals of metal casting for millennia. Theoretical formulations explaining the fundamental of both electromagnetism and casting are today available, and they are constantly developed to estimate the electrical and physical characteristics of the system of interest. As technology has developed it seems as if some areas have branches, connecting knowledge with the urge to generate interdisciplinary correlation. Some have strong and some have weak collaborations, the collaboration between electrical engineering and the cast house section of material science seems to be a weak.

2.1 Induction Coils for Electromagnetic (EM) Priming

The approach to designing an induction coil for generating the strongest possible Lorentz forces and magnetic flux by application of low frequency, and by ignoring the traditional 'quality factor' for induction coils, is described in detail in Supplement 1 and Supplement 2.

This section gives an overview of the theory, required to understand the principle of EM priming, the effects of coil shape and frequency on the magnetic flux density, and the shape of the magnetic field, which is not given in detail within Supplements 1 and Supplement 2.

2.1.1 Electromagnetic Theory

Electromagnetism is one of the four fundamental interactions that exist in nature. The focus of the electromagnetism is based on the interaction of particles with an electric charge. The well-known physicist J. C. Maxwell contributed to the understanding of this fundamental knowledge by summarizing and completing existing theories from many scientists [22] into his *"A Treatise on Electricity and Magnetism"*, which is a mathematical theory to unify the electric and magnetic phenomena [23]. He derived a set of four equations describing the propagation of electric and magnetic fields, the interaction between them, and how objects influence them. The fundamental equations are summarized in Table 1.

Table 1: Maxwell's equations displayed in differential and integral form.

Differential Form	Integral Form	
$\nabla \cdot \vec{E} = \frac{\rho_e}{\varepsilon_0}$	$\oiint_{\delta\Omega} \vec{E} \cdot dS = \frac{1}{\varepsilon_0} \iiint_{\Omega} \rho_e dV$	Gauss's law
$\nabla \cdot \vec{B} = 0$	$\oiint_{\delta\Omega} \vec{B} \cdot dS = 0$	Gauss's law for magnetism
$\nabla \times \vec{\mathrm{E}} = -\frac{\delta \vec{B}}{\delta t}$	$\oint_{\delta\Sigma} \vec{E} \cdot dl = -\frac{\delta}{\delta t} \iint_{\Sigma} \vec{B} \cdot dS$	Faraday's law of induction
$\nabla \times \vec{B} = \mu_0 \left(\vec{J} + \varepsilon_0 \frac{\delta \vec{E}}{\delta t} \right)$	$\oint_{\delta\Sigma} \vec{B} \cdot dl = \mu_0 \iint_{\Sigma} \vec{J} \cdot dS + \mu_0 \varepsilon_0 \frac{\delta}{\delta t} \iint_{\Sigma} \vec{E} \cdot dS$	Ampere's circuit law

In the equations in Table 1, B is the magnetic flux density [Wb/m^2], E the electric field [V/m], ρ_e the electric charge density [C/m^3], ε_0 the vacuum permittivity [F/m], J the electric current density [A/m^2], t the time [s], l the length [m], $\delta\Sigma$ a boundary curve of any fixed open surface Σ, $\delta\Omega$ a boundary surface of any fixed volume Ω, dS the to Σ normal differential vector element of the surface area S and dV as the differential volume element.

Gauss law states the proportionality of a charge inside a volume and an electric field leaving this volume. The law for magnetism by Gauss shows that over a closed surface the total magnetic flux piercing is zero. In other words, there are no magnetic monopoles. The law of induction by Faraday shows that the voltage accumulated around a closed circuit is proportional to the time rate of change of the magnetic flux enclosed. The final equation, shown by Ampere's circuit law, gives the proportionality of the magnetic flux with the electric currents and changes within the electric field when looking at the defined area they pierce.

Ampère, Biot-Savart and many others, were working on currents generating magnetic fields and deriving equations defining the magnetic field of wires and coupled wires. The third of Maxwell's equations, named Faraday's law is defined as the curl of the electric field to be equal to the rate of change of the magnetic field. Using this, the magnetic field of an infinite long induction coil can be found by the application of Ampère's law [24] for solenoidal coils:

$$\oint_c \vec{B} \cdot \delta\vec{l} = \mu_0 \mu_r I_c \qquad \text{(Eq.1)}$$

$$\text{where } \mu_0 = 4\pi * 10^{-7} \left[\frac{H}{m}\right], and\ \mu_r = 1$$

In Equation 1 (Eq. 1) the magnetic flux density $\vec{B}$ [T] is parallel to a vector of the length $\delta\vec{l}$, which is a tangent to the closed curve C. The permeability is given with μ_0 as the permeability of free space [H/m] and μ_r as the relative magnetic permeability [unitless], and the current I_c [A RMS]. The current can be calculated from the current density normal to the closed curve C. By integrating over a vector area of the surface S, $\delta\vec{s}$ $[m^2]$, normal to $\vec{J}$ and $\vec{I_c}$ the total current can be found to be $\left(\vec{J} * s\right) = I_c$.

Equation 1 (Eq.1) assumes an infinite solenoid and requires the application of a defined integral over a closed path, as shown in Figure 2 (a). The enclosed current has to be the product of N_c turns and the current per turn I_c. The flux density inside the coil is perfectly parallel, assuming the flux of an infinite coil B_{inf}. No r-component of the magnetic flux can be found. Only the z-component exists. Therefore, no flux will be recognised outside the coil. Following the ideal case of the infinite coil with (Eq.1), integrating over a defined path with a length of l_c, assuming only z-components in the magnetic field without having any external flux, we find (Eq.2):

$$B_{inf} = \frac{\mu_0 \mu_r N_c I_c}{l_c} \qquad \text{(Eq.2)}$$

where B_{inf} is the magnetic flux density [T] of the infinite coil looking at a finite length l_c [m], and N_c the number of turns of the coil.

The assumptions from (Eq.2) are not valid for coils with finite length. A theoretical 'current sheet' model of an infinite coil is shown in Figure 2 (a). As can be seen from Figure 2 (a), the induction coil will induce a time varying magnetic flux density B_z [T] field purely in the z-component by application of alternating current. Real coils will always have a not fully homogenized flux distribution and

therefore z- and r-components in the magnetic field. It has to be noted that strong radial components exist in the flux at the ends of the coil, as shown in Figure 2 (b) and (c). Not parallel field lines represent the variation of the z- and r-components in the magnetic field.

The coils are defined by the shape factor χ [unitless], which is defined by the inner diameter of the coil D_c [m] divided by the total length of the coil l_c [m], shown in (Eq.3). With increasing shape factor the magnetic flux density will decrease by similar applied currents, and the more curved the flux lines will appear.

$$\chi = {}^{D_c}/_{l_c} \qquad \text{(Eq.3)}$$

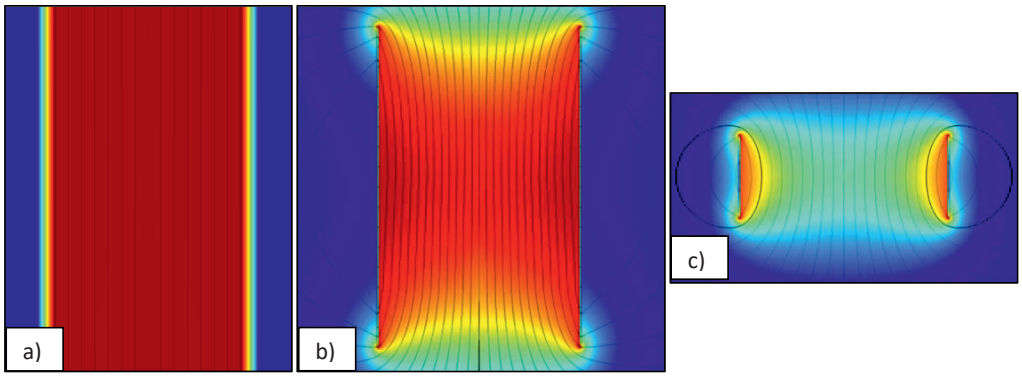

Figure 2: Comparison of the magnetic flux of a representative centre part of an 'infinite' (a), a complete 'normal' (b), and a 'short' induction coil (c). All coils are designed as helical 'current sheet' solenoids, where (a) consists of N=1000 turns with a shape factor (χ=D_c/l_c) χ=0.01, (b) N=16 turns with χ=0.625 and (c) N=4 turns with χ=2.5.

The corrected magnetic field strength for 'real' induction coil can be found by application of a 'short coil correction factor' k_N to the infinite coil assumption. To determine the z-component, of a finite, 'real' coil, the following correlation can be used:

$$B_z = k_N B_{inf} \qquad \text{(Eq.4)}$$

Inserting (Eq.2) into (Eq.4) gives the simple equation:

$$B_z = k_N \frac{\mu_0 \mu_r N_c I_c}{l_c} \qquad \text{(Eq.5)}$$

The inductance correlation of Wheeler was reformulated by Knight [25] in 2010 into an short coil correction factor k_N, originally formulated by Nagaoka in 1909 [26]. The empirical equation, allowing for a direct calculation of the classical 'short coil correction' Nagaoka coefficient, has been presented:

$$k_N = \frac{1}{1+0.4502\left(\frac{D_c+\delta_c}{l_c}\right)} \qquad \text{(Eq.6)}$$

where δ_c is the electromagnetic penetration depth [m] into the coil, which is given by:

$$\delta_c = \sqrt{\frac{\rho}{\pi \mu_0 \mu_r f}} \qquad \text{(Eq.7)}$$

where f is the frequency of the current applied to the coil [27], and ρ represents the electrical conductivity. The correlation of the penetration depth and the frequency from (Eq.7) is shown in Figure 3. The correlation of the resistivity as the inverse of the conductivity is given with:

$$\rho = \frac{1}{\sigma} \qquad \text{(Eq.8)}$$

where σ is the electrical conductivity [S/m].

The electromagnetic penetration depth, from (Eq.7) can be used to calculate the penetration depth into a conductive material, such as liquid metal or a work piece. It is dependent on the conductivity and the frequency, whereas it is known that the conductivity is dependent on the temperature and on the physical state of the material. Brandt and Neuer [28] have given a good set of reliable data for the resistivity, which is correlated to the conductivity by (Eq.8) and as a function of temperature for liquid and solid aluminium alloys.

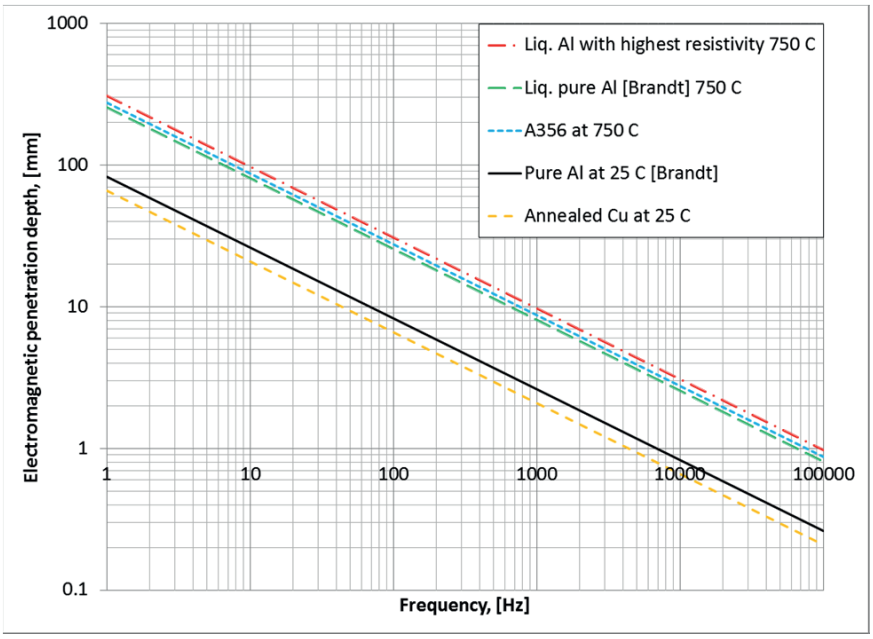

Figure 3: Double logarithmic graph of electromagnetic penetration depth over the frequency of the applied current for different metals and physical states. The two lower lines represent the solid fraction, 100%IACS annealed copper standard and pure aluminium at 25 C. The other three samples are at 750 C, which is a common casting temperature for industrial standards. They represent the range of the electromagnetic penetration depth of most alloys used in the industry. The highest resistivity alloy found is a $Al_{12}Si_3Mg$ alloy, and the lowest resistivity is a pure 99.9%Al [28]. A356 represents a standard casting alloy, which is in between both lines.

Eq.5 is valid for coils with a non-conductive material inside, e.g. pure air coils as shown in Figure 4 (a). A piece of conductive matter inserted into the coil will induce a field opposing current into the work piece. It is known, based on Lenz's law and the conservation of energy, that an induced electromotive force (here the induced current inside the work piece) opposes the original magnetic

flux that produced it. The result is a reduction of magnetic flux and field intensity into the work piece, and a concentration of flux in the gap between coil and work piece. The magnetic flux changes, as shown for different frequencies in Figure 4 (b) applying 50 Hz, (c) applying 500 Hz and (d) applying 10 kHz.

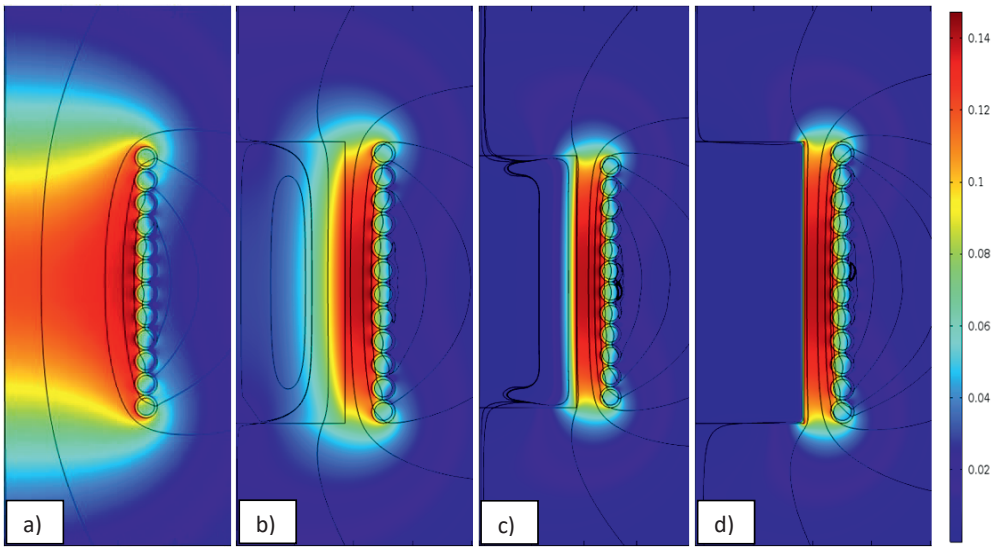

Figure 4: Using a simple COMSOL® model of a 12 turn induction coil with 96mm inner diameter by 96mm high (χ=1) shows the magnetic flux density [T] and it's distribution while 1000 A RMS have been applied. The work piece shown in figure (b), (c) and (d) consists of solid pure aluminium (37.7 MS/m). The frequency of the applied current is 50 Hz for figure (b), 500 Hz for figure (c) and 10 kHz for image (d). Comparing figure (a) to figure (b), (c) and (d) shows the variation in the flux density with and without a work piece by the flux being concentrated in the area of non-conductive matter. The electromagnetic penetration depth into the work piece changes significantly with increase of the frequency up to no actual penetration with high frequency (skin effect) shown in figure (d).

As a part of the Technical Licentiate thesis [29] and later PhD thesis [30] of M. W. Kennedy an improved version of the short coil correction factor was postulated and proven to be more accurate than the nearly unknown method Vaughan and Williamson proposed in 1945 [31]. Kennedy introduced the electromagnetic penetration depth, as shown in Eq. (6), into the calculation of the short coil correction factor of Vaughan and Williamson for induction coils with a work piece. This was possible due to the nature of coils producing a fixed number of flux lines at any given current. If a conductive work piece reduces the area inside the coil where the flux is supposed to be, it concentrates in the air gap between the work piece and the coil. Additionally, the length the magnetic flux that penetrates into the work piece is dependent on the frequency of the applied current, and as a result the real impact of the work piece is dependent on the electromagnetic penetration depth, which can be expressed as follows:

$$k_N^* = k_N \left(1 - \left(\frac{D_w - \delta_w}{D_c + \delta_c}\right)^2\right) + \left(\frac{D_w - \delta_w}{D_c + \delta_c}\right)^2 \qquad \text{(Eq.9)}$$

where k_N^* is the modified short coil correction factor, or modified Nagaoka coefficient [unitless], D_w the diameter of the work piece [m], D_c the inner diameter of the coil [m], δ_w the electromagnetic penetration depth [m] into the work piece, and δ_c the electromagnetic penetration depth [m] back into the coil.

2.1.2 Lorentz Forces, the Reactive Force

To derive the Lorentz force, a well-known simplified version of Eq.10 was applied by M. W. Kennedy [30], using only the real part of the cross product of the complex conjugate of the current density and the magnetic flux density to resolve the force for each radial position in the work piece. The assumption is based on the domination of the z-component of the magnetic flux density, inducing only a negligible amount of Lorentz forces in the z-direction. This gives a simplified model that can be used to calculate the challenging solution of the Lorentz forces as a result of the changing phase shift of the phasors, which in turn is the result of the penetration into the work piece.

$$\left|\vec{\mathrm{F}}_{\mathrm{L}}\right| = \mathrm{Re}\left\{\vec{\mathrm{J}}^{*} \times \vec{\mathrm{B}}\right\} \qquad \text{(Eq.10)}$$

where $\vec{\mathrm{F}}_{\mathrm{L}}$ is the time averaged Lorentz force acting on the fluid [N/m^3], $\vec{\mathrm{J}}^{*}$ the complex conjugate of the RMS value of the induced current density [A/m^2], and $\vec{\mathrm{B}}$ the complex RMS value of the magnetic flux density [T]. It is assumed that the gradient of the Lorentz force is zero, *i.e.*:

$$\nabla \times \vec{F}_{L} = 0 \qquad \text{(Eq.11)}$$

The Lorentz force $\vec{F}_{L}$ is acting on the fluid as a reactive force, inducing a velocity. This is the force that is driving the principle of electromagnetic motion, such as electromagnetic pumping and priming. It is pushing the conductive liquid metal inducing a velocity head above the filter, which in turn enables the EM field to prime the filter/filter section. In a simplified way, it obeys the right hand rule shown in Figure 5.

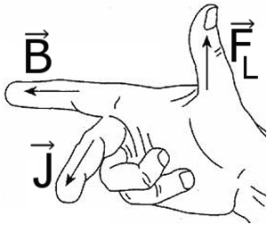

Figure 5: Right hand rule, showing the Lorenz force $\vec{\boldsymbol{F}}_{\boldsymbol{L}}$ as the cross product of the magnetic flux $\vec{\boldsymbol{B}}$ and the current density $\vec{\boldsymbol{J}}$.

The modified Nagaoka coefficient corrects for the radial component of the magnetic field in a non-infinite coil. Therefore, it can be assumed, similar to (Eq.4) and as presented in Figure 2, that the remaining magnetic flux density, same as the field intensity is the z-component.

$$H_z = k_N^{*} \frac{N_c I_c}{l_c} \qquad \text{(Eq.12)}$$

An expression for the solution of the local magnetic field intensity $\vec{\mathrm{H}}$ as a function of depth r is necessary to evaluate the effect of the magnetic field on the work piece. Such an expression can be found by applying the solution to a zero order Kelvin-Bessel function [32]:

$$H_z(r) = \frac{ber\xi_r + jbei\xi_r}{ber\xi_R + jbei\xi_R} H_z \qquad \text{(Eq.13)}$$

$$\xi_r = \frac{r\sqrt{2}}{\delta_w} \qquad \text{and} \qquad \xi_R = \frac{R\sqrt{2}}{\delta_w}$$

where R is the outer radius of the work piece [m] and r is the radius of interest [m].

The derivation of Eq.13 is a complex differential equation requiring the solution of Faraday and Ampere's laws. Solutions of the Bessel functions can be found in the literature [33, 34], or are free available on the web by, for example, Keisan Casio [35].

The induced current in phi-direction at depth r ($J_\phi(r)$) and the z-component magnetic flux density at depth r ($B_z(r)$) can be found by:

$$J_\phi(r) = -\frac{\sqrt{2}}{\delta_w}\frac{ber'\xi_r + jbei'\xi_r}{ber\xi_R + jbei\xi_R} H_z \qquad \text{(Eq.14)}$$

$$B_z(r) = \mu_0\mu_r \frac{ber\xi_r + jbei\xi_r}{ber\xi_R + jbei\xi_R} H_z \qquad \text{(Eq.15)}$$

where the ber' and bei' are the derivatives of the real and imaginary zero order Kelvin Bessel function [34].

Giving the solution to the Lorentz forces by combining Eq.14 and Eq.15 into Eq.10, the following can be expressed:

$$\left|\vec{F}_L\right| = Re\{\vec{J}^* \times \vec{B}\} = -\mu_0\mu_r \frac{\sqrt{2}}{\delta_w}\left(\frac{ber'\xi_r + jbei'\xi_r}{ber\xi_R + jbei\xi_R}\right)\left(\frac{ber\xi_r + jbei\xi_r}{ber\xi_R + jbei\xi_R}\right) {H_z}^2 \qquad \text{(Eq.16)}$$

Reducing the equation to the real part only gives:

$$\vec{F}_L = -\mu_0\mu_r \frac{\sqrt{2}}{\delta_w}\frac{ber\xi_r ber'\xi_r + bei\xi_r bei'\xi_r}{ber\xi_R + bei\xi_R} {H_z}^2 \qquad \text{(Eq.17)}$$

Simplified to an applicable and practical equation to estimate the resulting Lorenz forces for a given coil dimension gives further:

$$F_L = -\frac{\mu_0\mu_r}{\delta_w}\left(\frac{N_c I_c k_N^*}{l_c}\right)^2 \varphi(R,r) \qquad \text{(Eq.18)}$$

With $$\varphi(R,r) = \frac{\sqrt{2}\,(ber\xi_r ber'\xi_r + bei\xi_r bei'\xi_r)}{ber\xi_R + bei\xi_R} \qquad \text{(Eq.19)}$$

The full derivation of the equation is shown in [29, 36].

Effective conductivity of Ceramic Foam Filters

In order to validate the model of the Lorentz force and the finite element flow field model, the measurement of the effective conductivity of the CFF has been repeated by S. Akbarnejad [37] using the same method as described by M. W. Kennedy [30]. The existence of the non-conductive ceramic material influences the conductivity of the liquid aluminium. The penetration depth, the effect of the magnetic field, the resulting Lorentz force and the flow field have a drastic change within, before and after the filter.

A continuation of experiments to verify previous results by Kennedy *et.al* [38], were conducted on 50 and 80 PPI CFF filter elements, testing the effect of a variation of the thicknesses of the filters.

The metal conductivity can be calculated as:

$$\sigma_m(T) = \frac{\sigma_p^*}{24.77*10^{-8}\left(1+0.000571\left[T_{exp}-933.2\right]\right)*65} \qquad \text{(Eq.20)}$$

where σ_p^* is the conductivity at room temperature of the solidified metal [% IACS] and T_{exp} the temperature measured during the experiment [K].

Brandt and Neuer [28] presented the conductivity data for pure aluminium, and corrected the actual measured data by considering the different solid alloys at ambient temperature.

The tortuosity τ is defined as the longer path that the liquid metal takes through the filter. The path is further changed by the area of non-conducting material inside the filter, which is equal to the porosity allowing for the estimation of the ratios of conductivity, tortuosity and resistivity of filter material sections, *i.e.*:

$$\frac{\sigma_m}{\sigma_f} = \frac{\tau}{\varepsilon} = \frac{R_f}{R_m} \qquad \text{(Eq.21)}$$

where σ_f the electrical conductivity of the filter element [S/m], R_f the resistivity of the filter [Ωm], and R_m the resistivity of the metal [Ωm].

The data of porosity and tortuosity with the ration of the resistances used for the modelling section of the present work is summarized in Table 2.

Table 2: Summary of used tortuosity and porosity data for finite element modelling. [30, 37]

CFF [PPI]	Porosity [ε]	Tortuosity [τ]	Effective resistivity [R_{filter}/R_{metal}]
30	0.892	1.3	1.5
50	0.863	2.2	2.5
80	0.865	3.2	3.7

2.1.3 Coil Design

The flow sheet of the induction coil design is shown in Figure 6. The coil design approach is based on the experimental results from the 4.7 inch diameter round double coils used previously by M.W. Kennedy [30]. It should be pointed out that the chosen approach is fully based on current, and voltage is not used to determine the coil characteristics. This allows for accurate Lorentz force, magnetic field and generally better coil design criteria. Using the inductance and reactive power, the required voltage can be calculated. This method allows a precise first estimate of the physical characteristics of the designed coils.

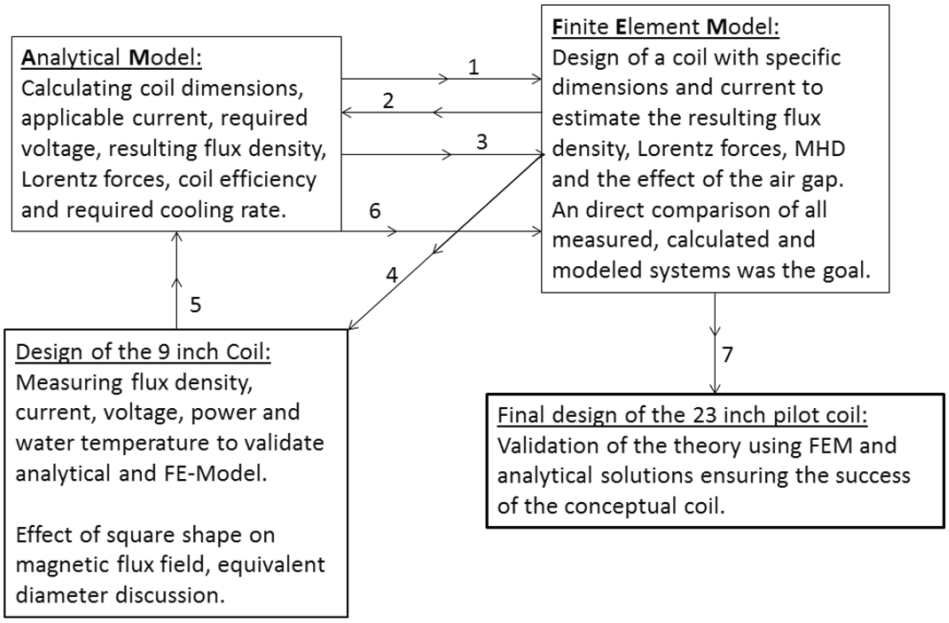

Figure 6: Schematic approach of the up scaling process of the induction priming coil during the present work.

Each step is described in detail as follows:

1. Analytical calculation of possible coil dimension for application of 9 inch square CFF. Design for current to achieve magnetic field B_z and Lorentz forces F_L.
2. FEM of a 9 inch filter system, discussing the resulting field strength, coil impedance and power. The discussion was aiming at finding an air gap size that would fit as much insulation around the filter as possible by losing as little field strength as possible. The increase of impedance by the effective area was a critical design criterion.
3. Redone analytical and FEM for a suitable tube size, wall strength and available coil current; determine the final dimensions of the square coil.
4. Construction of the 12.2 inch square coil by applying double silica glass sleeve insulation, and connecting high pressure screw valves for the cooling water supply. The coil characteristics was validated by measurements of inductance and power by ‘air coil’ trials, and later optimized in regards to suppression of vibrations, allowing for more current to be applied.

5. Using the scale ratios of the existing 12.2 inch square coil the up scaling to the 28.9 inch industrial size was undertaken. The final coil was designed to suit both cases, *i.e.* a low frequency of 25 Hz and below, and the mains frequency of 50 Hz within the experimental test-rig of the industrial partners.
6. A full scale FEM was utilized in 2D using axial-symmetry and equivalent diameter ratios, and in 3D using a full industrial CAD model, validating the analytical calculations by modelling. The construction of the pilot priming coil was initialized.
7. The finished coil was shielded by a RFM® board surrounding the 23 inch filter ensuring that a sufficient air gap existed between the coil and the filter setup. The estimations of the analytical and FEM was validated by measurements, and the coil was accepted for industrial testing.

The methodology applied for the design of the priming coils is based on the current, and starts with the required or aimed magnetic flux that the coil is supposed to generate. The time averaged Lorentz forces introduced by Eq.10, and further described by Eq.11 to Eq.19 can be used to estimate the magnetic flux density B_z introduced in Eq.5. The method requires the use of a short coil correction factor to be able to estimate the magnetic field and the magnetic flux density.

The inductance L is a useful parameter when correlating the required parameters when designing an induction coil. The general definition of the inductance is the flux linkages per unit current. The flux can be correlated to the magnetic flux density B_z and the effective area of the coil A. Furthermore, the inductance is correlated with the applied current I and the total reactive power Q. The correlations can be shown as:

$$L = \frac{N\Phi}{I_c} = \frac{B_z NA}{I_c} = \frac{Q}{I_c^2 2\pi f} \qquad \text{(Eq.22)}$$

where L is the inductance [H], Φ the total flux [Wb], A the total area of the cross section of the induction coil [m^2], B_z the magnetic flux density in the z-direction [T] (as presented with Eq.5), and Q the total reactive power [VAr]. The computation of area A varies with geometry, *e.g.* round vs. square coil, single vs. double coil and/or with the applied frequency, which has a directly proportional effect on the inductance. The frequency dependent effective area occupied by the coil and the 'air-gap' of a real*, i.e.* non-current sheet coil, as shown in Figure 7 is given by Eq.23, and is valid only for cases where $\delta_c < d_c$:

$$A = \frac{\pi(D_c+\delta_c)^2}{4} \qquad \text{(Eq.23)}$$

The dimensions and ratios of square and round coils are shown in Figure 7.

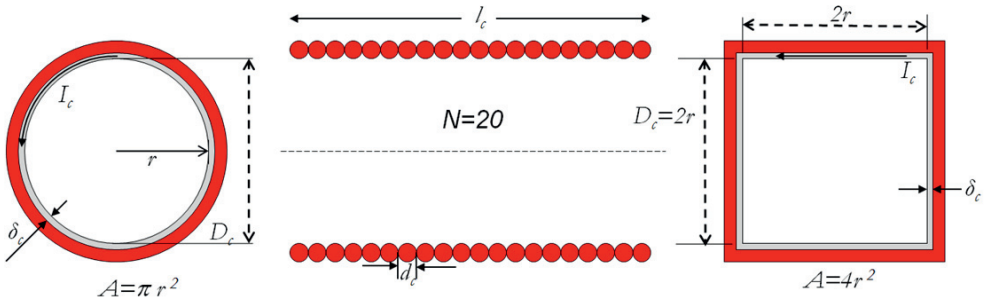

Figure 7: A sketch, similar to the sketch of Baker in 1957 [39], of a 20 turn single layer induction coil with a round and a square cross section. D_c = inner coil diameter [m]; r = coil radius [m]; A = coil area [m^2]; N = number of turns [unitless]; l_c = axial coil length [m]; I_c = applied coil current [A]; δc = electromagnetic penetration depth in the coil [m], and dc = width of the coil [m]. The pitch is shown at the minimum, *i.e.* equal to the diameter of the coil wires.

For multi-layer coils the value of B_z can be established based on first measuring L on existing coils and then applying Eq.22. The empirical, but accurate, equation of Wheeler from 1928 [2] for the inductance of a multi-layer coil can be used to estimate L prior to constructing a coil, and has been transformed from imperial to SI units with dimensions in [m] as follows:

$$L = \frac{31.496\, r^2 N^2}{6r+9l_c+10c} \qquad \text{(Eq.24)}$$

where L is the inductance of a multi-layer coil [μH], N the number of turns, r the average radius [m], l_c the length measured top to bottom of the coil, and c the thickness of the coil [m] as shown in Figure 8. Wheeler's Eq.24 allows a simple and primitive first approximation of the inductance of the coil, and has been identified to be most accurate.

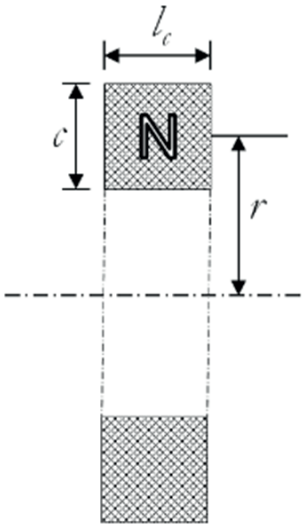

Figure 8: Simple model of a multi-layer induction coil with N turns, radius r, length $\boldsymbol{l_c}$, and thickness c. [30]

After determining the inductance, the required RMS value of the voltage can be calculated. For any given coil, single or multi-layer, the applied current is directly proportional to the strength of the magnetic field, as shown in Eq.22. The coil impedance is linking the RMS value of the current with

the RMS value of the voltage as shown in Eq.25. The impedance is directly related to the total reactance and alternating coil resistance (Eq.26), where the total reactance of the coil is defined by the impedance and the applied frequency (Eq.27) [39]:

$$V = I_c Z \quad \text{(Eq.25)}$$

$$Z = \sqrt{R^2 + X^2} \quad \text{(Eq.26)}$$

$$X_{total} = \omega L = 2\pi f L \quad \text{(Eq.27)}$$

where Z is the coil impedance, [Ω], R is the coil resistance [Ω], and X_{total} is the total reactance [Ω].

Baker approximated the coil reactance X_{total} as being equal to his empirically estimated resistance using a formula which was only accurate at high frequencies [39]. What constitutes a high frequency can be practically defined by a coil with the ratio $d_c > \sim 2\delta_c$. At high frequencies the resistance and the reactance of the coil becomes equal to a fixed ratio. Baker's resistance formula (and therefore reactance) cannot be accurately applied at low frequencies, and if applied result in a serious error for cases where $\delta_c > d_c$.

The alternating current resistance R of the coil used in Eq.26 can be estimated for both low and high frequencies [40] by:

$$R = \pi \frac{N^2 \rho (D_C + \delta_C)}{(\delta_C l_c k_r)} \quad \text{(Eq.28)}$$

where k_r is the coil space factor [unitless], *i.e.* defined as the fraction of the coil occupied by copper. The coil space factor is defined as follows:

$$k_r = \frac{d_C N}{l_C} \quad \text{(Eq.29)}$$

With the inductance L, the total reactance X_{total}, the alternating coil resistance R, and the RMS values the voltage V can be determined.

Conceptually, the total flux Φ, inductance L and reactive power Q can be imagined as the sum of three 'parts', *i.e.* originating in the volume occupied by (i) the air gap, (ii) the coil conductors, and (iii) the work piece (if there is one) [31, 39], as indicated in Figure 9. The total reactive power shown in Eq.22 can then be calculated by the sum of these three parts.

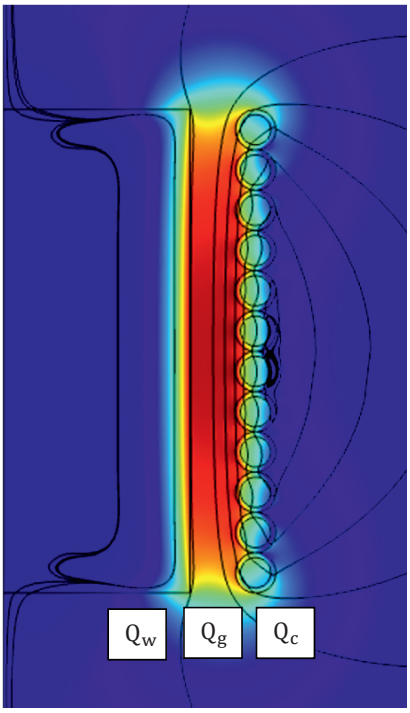

Figure 9: Display of the three 'parts' of the reactive power within a coil, work piece and 'air' gap. As we can see, there is flux in the coil, in the air gap and in the work piece.

$$Q = Q_g + Q_c + Q_w = I_c^2 L 2\pi f = I_c^2 X_{total} \quad \text{(Eq.30)}$$

where Q_g is the reactive power produced inside the air gap, Q_c the reactive power produced by the flux inside the coil, and Q_w the reactive power produced by the flux linking the work piece with the coil (if a work piece is present [29, 36]).

In order to specify the required power supply to run the coil in a real application, it is necessary to also define the required apparent and real power:

$$P_{apparent} = IV \quad \text{(Eq.31)}$$

$$P_{real} = IVcos(\varphi) \quad \text{(Eq.32)}$$

$$P_{reactive} = IVsin(\varphi) \quad \text{(Eq.33)}$$

where φ is the phase angle between the current and the voltage, and $cos(\varphi)$ is traditionally referred to as the power factor, which can be calculated by:

$$cos(\varphi) = \frac{R}{\sqrt{R^2+X^2}} \quad \text{(Eq.34)}$$

During the present work, the apparent, real and reactive powers, as well as the power factor, have been measured and monitored for all experimental trials for all coils. The monitoring of the power was used as a safety measure, as an increase in power indicates a change in resistance and may require an immediate stop of the experiment.

The quality design factor is critically discussed in *Supplement 2.*
The coil design is described in detail in *Supplements 1* and *2*.

Chapter 3

3. Priming Theory

How to design a coil generating a strong magnetic field was described and discussed in Chapter 2. It was also discussed how to determine the resulting Lorentz force, the effective conductivity and the tortuosity of the used filters. The next step is the initiation of the liquid metal filtration stage. The stages of a successful priming operation with the required priming height and pressure are presented in the following section. The effect of the EM field on the priming of the filter in comparison to pure gravity priming and EM priming theory, as a result of the undertaken trials, will also be described. The EM priming was introduced and presented in *Supplement 3* and *4*, and the first stage of industrial upscaling is shown in *Supplement 5*.

Ceramic Foam Filters (CFFs), presented in Figure 10, are characterized by the open structure with very high porosities and surface area. The open and web-like structure, shown in Figure 10 (a) to (c) offers a low resistance to fluid flow, and a high filtration efficiency for particles over 10 to 20 µm [41]. The structure of tortuous paths allows sufficient physical stability, and simultaneous capture of inclusions, creating a clean, smooth flowing metal exiting the CFF [42].

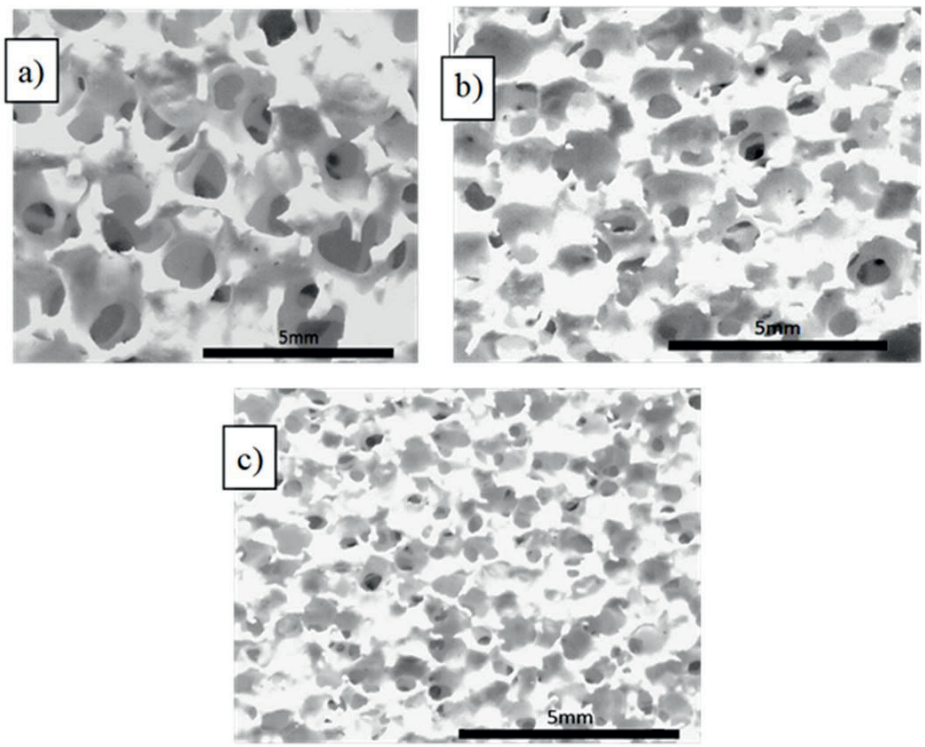

Figure 10: Morphology of low to high grade CFF. The different grades are grouped into (a) 30 PPI, (b) 50 PPI and (c) 80 PPI [43].

The application of CFFs started in the late 1970 and are now, as previously mentioned, the most commonly applied filtration process, used for >50% of the global production of aluminium since the

1990's [44]. The filters are installed in the filtration unit, which contains the filter bowl, the sump with outlet, the pre-heating system and a lid, as shown in Figure 11 (a). The work principle of the in-line horizontal mounted CFF is shown in Figure 11 (b).

In the filter boxes applied today a metal head is used to generate sufficient pressure, initiating the priming of the filter, as shown in Figure 12 and Figure 13. The pressure is traditionally generated by mounting the filter in the filter box below the metal level in the launder. If the filter is mounted far below the launder, the metal head will be large, inducing a high gravitational force. In numbers, the priming height has a range from 100 to 400 mm metal head above the filter, depending on the filter grade [38, 45, 46]. The downside of the present setup is the extensive amount of metal which needs to be drained from the low filter-box after each cast (around 500-600 kg, depending on the filter box size).

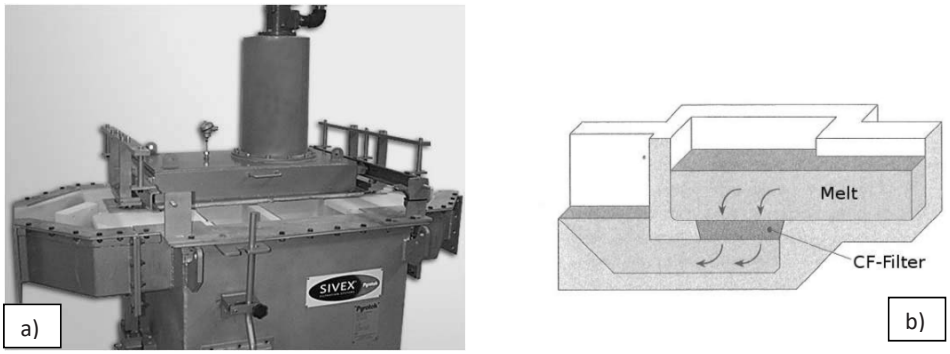

Figure 11: In (a) a commercial "Turnkey Sivex® Filter Box" in-line filter box with pre-heating burner mounted within the lid is shown (constructed and supplied by Pyrotek™ Sivex®). In (b) a sketch showing the work principle of the in-line horizontal CFF box is presented. [47]

High PPI filters have excellent efficiency for inclusion removal. These filters, *e.g.* 50-80 PPI, are not commonly applied in industry. Mainly because they cannot be effectively primed in many commercial cast house installations due to the excessive metal head required.

In modern cast house practices it is unthinkable not to preheat the filters prior to a cast. The preheating technique requires between 0.5-2 hours, depending on the filter grade [17]. Uneven or insufficient preheating is one of the main reasons for unsuccessful initiation of a cast. This may result in dramatic financial consequences for the cast house; the metal within the launder is lost, the metal within the filter box has to be melted by gas torches and a new preheating sequence has to be initiated, while the furnace has to be kept on temperature. This can lead to extensive material, capital and time loss.

3.1 Priming of the Filters

The traditional metal head [38, 45, 46, 48] required for the priming of preheated filters of different PPI is presented in Figure 12. The resulting static pressure and the resulting weight on the filter depending on the applied metal head are shown in Figure 13.

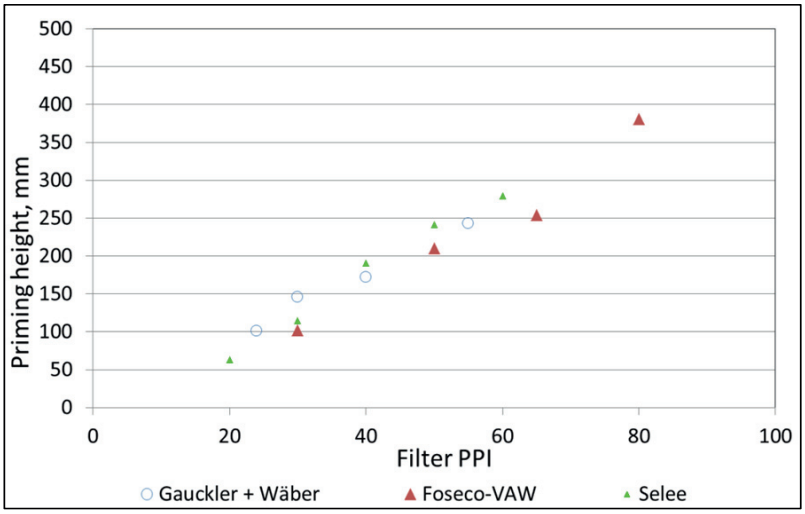

Figure 12: Priming height versus filter PPI from different producers [38, 45, 46]. This illustrates the required amount of metal head above the filter for the different filter grades / PPI.

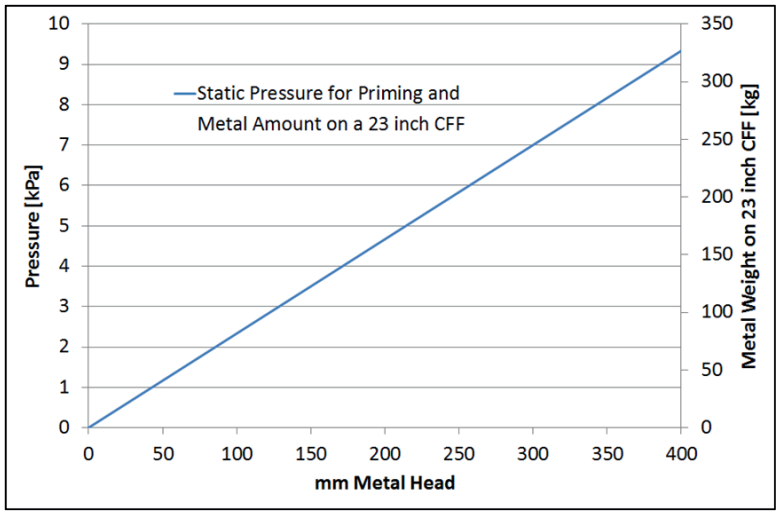

Figure 13: Static metal head required for different filters using the average data shown in Figure 12 [38, 45, 46], plotted with the metal weight on a standard 23 inch CFF. The density of pure aluminium with 2380 kg/m^3 was used.

The total pressure acting on the filters can be described as follows:

$$P = P_D + P_S \quad \text{(Eq.35)}$$

$$where: \; P_D = \tfrac{1}{2}\rho v^2, \quad \text{(Eq.36)}$$

$$and \quad P_S = \rho g h \quad \text{(Eq.37)}$$

where P is the total pressure at the interface of the filter [Pa], P_S the static pressure [Pa], P_D the dynamic pressure [Pa], ρ the density of the fluid, here liquid aluminium [kg/m^3], v the superficial

velocity [m/s], g the gravitational acceleration [m/s^2], and h the fluid head above the interface to determine the pressure [m].

During initiation of traditional priming, the dynamic pressure can be assumed to be $P_D = \frac{1}{2}\rho v^2 = 0$ as no external forces are applied, and no velocity gradients exist. Besides the inlet velocity during the filling of the filter bowl, and the thermal convection within the metal, no forced convection within the metal head prior to the priming can be found. The total pressure required to traditionally prime the filters is generated by the metal head, here defined as the static head.

The pressure is based on the physical abilities, such as density, viscosity and surface characteristics of the used liquid metal and the applied filter material. Surface characteristics, such as surface tension, contact angle and wettability are believed to be of significant importance, and are still topics of scientific investigations [49-51].

The understanding of the wetting behaviour of molten aluminium on alumina, which is the common filter material, is essential to comprehend the physics of priming and filtration. The contact angle is used to characterize the wetting behaviour. The contact angles of Al on Al_2O_3 has been reported to be between 88 to 167° at temperatures between 700 and 1200°C in different environments as shown in Figure 14 [50]. It is also believed, that the filtration efficiency depends on the physical abilities of the filters, the material, the wetting angle, the chemical stability, etc., as well as the used metal alloy [52, 53].

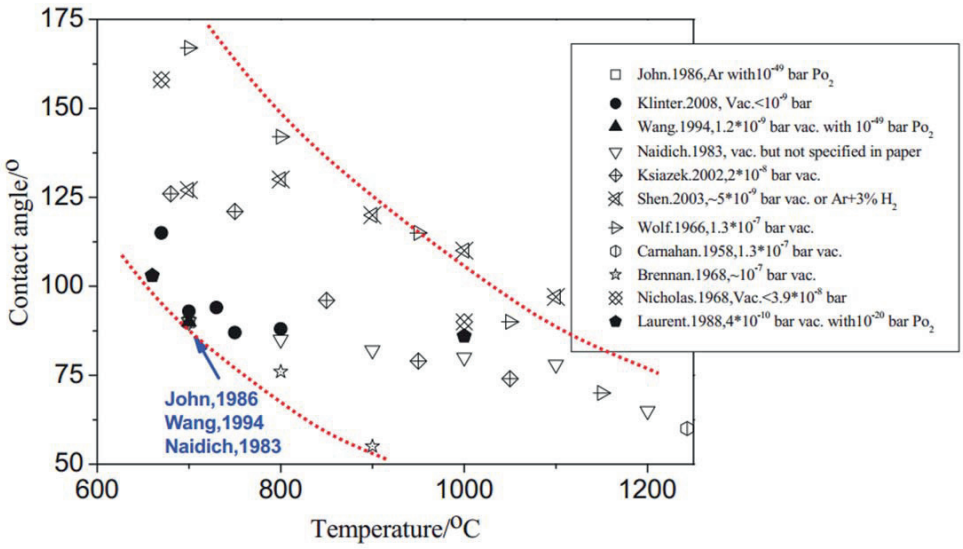

Figure 14: Literature review of the existing contact angles over temperature studies executed since 1958, conducted by Bao in 2011 [50]. The broad deviation between the investigations indicates the effect of atmosphere, pressure and oxidation level. Effects of vibrations are not included in this review.

A linear correlation of static to dynamic pressure is therefore not applicable.

3.2 Effects of the EM field on Priming

In industry today, EM fields are commonly used for casting and microstructural control, such as the ElectroMagnetic Cast (EMC) [54, 55], for meniscus control in continuous casting [56], and other applications [57]. The micro- and macrostructure is modified by induced vibrations and MHD by the low frequency EM field applied during or prior to the solidification process of various alloys [58, 59]. The effect of electromagnetic separation using an induced-current separator was first presented by El-Kaddah *et al*. [60-62], and the positive effect of the EM field on wettability and priming of filters was coincidentally discovered and is now a novel technique [1].

The priming height required for the EM priming is correlated to the static and induced dynamic metal head, the frequency, inducing surface vibrations, Lorentz forces, and the resulting EM field strength.

Two different stages of the priming process have been identified. The first stage was the formation of a meniscus, and the second stage was the penetration into the filter.

3.2.1 Meniscus

When a liquid metal is placed in the effective range of an AC magnetic field, eddy currents are induced in the metal. These currents counteract the initial current flow and give rise to resistive heating of the metal. The induced eddy currents also interact with the magnetic field to produce Lorentz forces in the bulk of the metal, depending on the penetration depth. These forces induce velocity gradients within the liquid metal, and it also introduces a meniscus shape if the metal surface is close to the coil position. The aluminium industry have been trying to control the meniscus shape since the early 90's [63].

It is a well-known fact that low frequency, below kHz range, induces violent stirring, as the penetration depth is larger and the induced Lorentz forces will generate strong velocity gradients deep within the metal. By application of strong currents these strong MHD effects are expected to introduce massive gradients. This is a phenomena commercially used for EM pumping systems [64] and EM flow control systems [65].

An experimentally validated FEM for a meniscus can be seen in Figure 15 [66]. This model shows a meniscus with a solid plate at the bottom. The induced current generates strong MHD mixing, and the flow field results in a stable meniscus. The FEM indicates that the metal has a strong velocity gradient, homogenizing the melt temperature. The gradient pushes the metal away from the wall, towards the centre, which introduces two counteracting metal loops, lifting the meniscus to a maximum height in the centre.

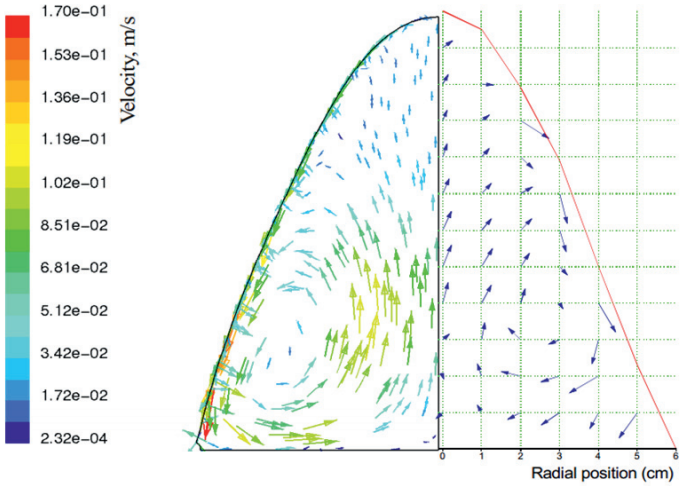

Figure 15: Visualization of a k-ε turbulence FEM showing a sodium meniscus. At the left side is the model predictions presented, and at the right side the measured velocity [66].

3.2.2 Inductive Heat

The EM fields will also introduce thermal heat within the metal by induction of eddy currents. Inductive heat has since the beginning of the last century been applied as a standard heating method [67], and by further developing the method [68] it is today being used to heat billets, melt metal and stabilize temperature. The energy dissipation occurring within the priming system can be evaluated, and can account for the thermal loss during the priming stage and the draining stage. The dissipated power is dependent on the amount of current induced within the workpiece depending on the strength of the magnetic flux, penetration depth and the applied frequency:

$$P_{diss} = I^2 R_{AC} = A \frac{\rho}{2\delta} \left(\frac{B_Z}{\mu_0} \right)^2 \qquad \text{(Eq.38)}$$

where P_{diss} is the power dissipated into the metal [W]. The effective area A, magnetic field B_Z, electrical conductivity ρ and penetration depth δ have been discussed in Chapter 2.

The current is mostly concentrated at the surface and within the first penetration depth, and the density reduces approx. exponentially with the distance r from the surface of the work piece, *i.e.*

$$I = I_0 e^{\left(\frac{1}{\delta} dr\right)} \qquad \text{(Eq.39)}$$

When discussing the penetration depth and dissipation of power into a liquid it has to be considered that the liquid experiences a physical force, introducing motion at the same time. This enhances the homogenization of the induced power by inductive effects over the full volume of the work piece, and may change the physical appearance of the work piece, *i.e.* the meniscus shape.

3.2.3 Vibrations

The frequency defines the penetration depth, as discussed in Chapter 2 and shown in Eq.7 for induction coils, and the rate of the change of the alternating induced current within the work piece. The change of the current direction introduces a change in the direction of the Lorentz forces. This

induces, following the theory previously presented, physical motion that is measureable as vibrations at a rate of twice the frequency.

The Lorentz forces define the amount of force within a conductive volume, experienced by every alternating cycle. The exact amount of energy required to fracture the aluminium oxide layer, by electro-motive forces are yet unknown, similar to the effect of the EM field on the wettability of aluminium on alumina.

Chapter 4

4. Quantification of Filtration

4.1 Filtration and Filtration Efficiency

The theory of the filtration efficiency, correlated by fluid flow and pressure drop, is presented in the present chapter. Pressure drop calculations are being used to estimate the superficial and interstitial velocities inside the filters to be able to estimate the filtration efficiency. The work on the pressure drop has been conducted by Kennedy *et al.* [38, 43], and was continued by Akbarnejad *et al.* [37].

During the present work, no experimental trials evaluating the filtration efficiency of EM primed filter has been conducted. Nevertheless; a technique has been developed, where particles automatically acquired from micrographs were used to estimate the filtration efficiency of any filter. This method of particle quantification was applied to industrial projects even during the duration of the present work.

The theory of automated image processing and particle quantification has been introduced in *Supplement 6* where the main focus was on counting artificially added SiC particles within an A356 aluminium alloy filtered in a lab scale EM primer system [30]. *Supplements 7* and *8* focuses on the application of a similar method to identify inclusions and quantify cleanliness from industrial cast house samples.

4.1.1 Filtration Fundamentals

Material Constants and Equations

To evaluate the following theoretical equations and models it is essential to know the correct condition and properties of the material during the stage of filtration. The density of pure aluminium can be calculated using the following correlation:

$$\rho_{Al} = 2377.23 - 0.311\,(T - T_r) \qquad \text{(Eq.40)}$$

where ρ_{Al} is the density of pure aluminium [kg/m^3], T_r the reference temperature, and T the temperature [K or °C]. A typical temperature for casting pure aluminium has been reported to be between 973 K and 1023 K. The density of pure aluminium ranges, within this temperature interval, from 2349 to 2365 kg/m^3 [69].

The viscosity of pure aluminium can be found by using:

$$u_{Al} = u_0 \cdot 10^{\left(-0.7324 + \frac{803.94}{T}\right)} \qquad \text{(Eq.41)}$$

where u_{Al} is the viscosity of pure aluminium [Pa·s], and u_0 is defined as 10^{-3} [Pa·s]. In the temperature interval from 973 K and 1023 K the viscosity of pure aluminium is between $1.13 \cdot 10^{-3}$ and $1.24 \cdot 10^{-3}$ [Pa·s] [69].

Looking at a filter as a liquid-solid system, where the two phases will interact with each other, the effective viscosity has to be applied. The correlation can be found by the Einstein-Roscoe equation for smooth rigid spheres suspended in a liquid: [70]

$$u_{eff} = u_{Al}(1 - \alpha f)^n \quad \text{(Eq.42)}$$

where u_{eff} is the effective viscosity of the liquid with submerged solids, α and n are constants (recommended value of 1.35 and 2.5), and f [unitless] the volume fraction of solids in the liquid [70].

CFFs are specified to be a high tortuosity foam system. This means that the CFFs have a complex structure with double or more real path lengths inside the filter compared to parallel tubes. As a result, the superficial velocity cannot be assumed to be equal to the interstitial velocity inside the filter media. Only the inlet and the outlet velocity can be measured. To calculate the filtration efficiency the interstitial velocity is required to be estimated. To assume the correct physics the interstitial velocity has been defined as:

$$w_i = \frac{w_s \tau v_f}{\varepsilon(v_f - v_d)} \quad \text{(Eq.43)}$$

where w_s is the superficial velocity [m/s], τ the tortuosity [unitless], v_f the filter total volume [m^3], ε the total porosity [unit less], and v_d the filter dead volume [m^3].

The dead volume v_d is defined as the difference between the total porosity and the porosity of the filter that is available for flow. In the literature it has been reported that the dead volume is in the range of 30–40% of the total volume for 30 to 80 PPI CFFs [71]. To simplify, the dead volume v_d used in the present work, is defined to be approx. 30% for all CFFs.

The total porosity of each filter is detrimental to the ability to calculate the pressure drop, and to generate proper FEM in the long run. The total porosity ε can be determined by:

$$\varepsilon = 1 - \frac{m_f}{V_f \rho_f} \quad \text{(Eq.44)}$$

where ρ_f is the true particle density [kg/m^3], m_f the measured dry mass of the filter [kg], and V_f the volume [m^3].

The tortuosity of a filter, in terms of fluid flow, can be defined as the ratio of the real path length through the filter divided by the shortest possible length:

$$\tau = \frac{l_r}{l_0} \quad \text{(Eq.45)}$$

where l_r is the real length [m], and l_0 the height of the filter or the shortest possible length [m]. It should be mentioned that it is not possible to calculate the tortuosity by applying Eq.45. This is due to the complexity of the CFF structures making it impossible to measure the real length of the fluid inside the foam like structure. Another theory on how to determine the tortuosity can be found in the literature using the pressure drop of the filter to estimate the tortuosity [38].

The physical morphology of Deep Bed Filters (DBF) and Bonded Particle Filters (BPF) can be pictured as an inverted CFF.

To calculate and model the flow field of the liquid metal inside a tortuous filter, a proper understanding of the physical properties of each filter type is required. For CFFs the transition of the

pressure drop from first order behaviour to the second order is occurring in the velocity range above 0.01 m/s for 80 PPI CFF and slightly higher for lower grade CFFs [72]. The first order term (Darcian) and the second order term (Non-Darcian) of the Forchheimer equation [73] is known to be:

$$\Delta P = L\left(\frac{\mu}{k_1} w_s + \frac{\rho}{k_2} w_s^2\right) \quad \text{(Eq.46)}$$

where ΔP is the pressure drop [Pa], L is the total length, in this case the thickness of the filter [m], w_s the superficial fluid velocity [m/s], μ the dynamic viscosity of the liquid [Pa·s], ρ the fluid density [kg/m^3], and k_1 [m^2] and k_2 [m] the Darcian and non-Darcian permeability constants. The Darcian (first) term represents the viscous energy losses, and the non-Darcian (second) term the kinetic [38].

The empirical Ergun equation can be applied to estimate an analytical solution of the pressure drop of bed or soil filters [74] and is known to be:

$$\Delta P = L\left(\frac{150\mu}{D_p^2}\frac{(1-\varepsilon)^2}{\varepsilon^3} w_s + \frac{1.75\,\rho}{D_p}\frac{(1-\varepsilon)}{\varepsilon^3} w_s^2\right) \quad \text{(Eq.47)}$$

where D_p is the spherical equivalent diameter of the areas available for flow [m], and ε is the void fraction, *i.e.* the porosity of the bed, or "open" porosity for fluid flow [unitless]. It has been reported in literature that the Ergun equation has difficulties in assuming the correct pressure drop for non-spherical particles [52, 75].

In Table 3 the parameters presently used for the Forchheimer (Eq.46) and the Ergun (Eq.47) equations are summarized. The theoretical values for the pressure drop are based on this calculated, and the outcome presented in Figure 16 demonstrating an equal pressure drop for high-grade CFFs and highly efficient small grain deep bed filters.

Table 3: Parameters of three standard CFFs [38], and two theoretical deep bed filters.

Forchheimer Equation (Eq.46)								
CFF PPI	Total Porosity (Eq.44) ε	Tortuosity (Eq.45) τ	Effective Resistivity R_{filter}/R_{metal}	Window Diameter d_w , μm	Cell Diameter d_c , μm	Strut Diameter d_s , μm	Darcian Term k_1 , m^2	Non-Darcian Term k_2 , m
30	0.892	1.3	1.5	961	1668	185	5.08E-8	5.46E-4
50	0.863	2.2	2.5	623	1132	190	1.57E-8	1.66E-4
80	0.865	3.2	3.7	383	683	119	6.52E-9	1.15E-4

Ergun Equation (Eq.47)			
Deep Bed Filter DBF	Total Porosity [17] ε	Eq. Spherical Particle / Media Cell Size D_p , [m]	Bulk Density of Media ρ , [kg/m^3]
1 (grain size 1 mm)	0.47 – 0.53	0.001	2.3
2 (grain size 3 mm)	0.47 – 0.53	0.003	2.3

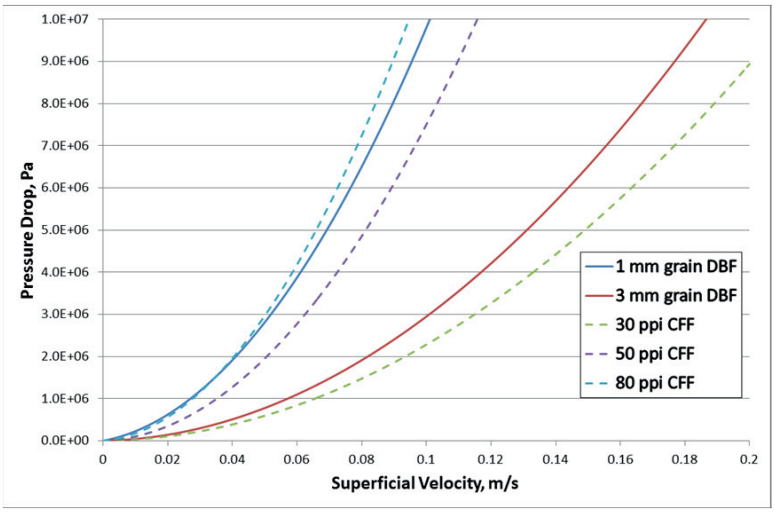

Figure 16: The pressure drop as a function of the superficial velocity for 2 Deep Bed Filters (DBF) (calculated by using the Ergun Equation (Eq.47) with a 50 mm thick filter bed), and for a stack of 3 CFFs (calculated using the Darcy-Forchheimer Equation (Eq.46)). All calculations are based on the data presented in Table 3, showing the correlation of the pressure drop and superficial velocity of CFFs in comparison with DBFs.

Physical Filtration Mechanisms

Physical filtration or surface filtration describes the removal of submerged inclusions and particles by sedimentation, settling, inertial impaction, Brownian motion, interception, sieving and/or cake filtration by an inert filter media. The filters are usually constructed from process suiting refractory material, as shown for phosphate-bonded alumina in Table 4.

Table 4: Chemical composition of a standard phosphate bonded alumina CFF.

Al_2O_3	SiO_2	Other Oxides
80-82%	5-6%	12-15%

The fundamental mechanisms for filtration are listed below:

Inertial Impaction

Impaction is based on the mass and therefore the inertia of a particle. Particles with a density higher than liquid aluminium, with a sufficient size, have enough momentum to impact upon the surface, as shown in Figure 17 (a). Particles with lower density cannot reach the surface of the filter due to the high resistance of the fluid and the drag forces, as well as insufficient momentum [76].

Interception

Interception is based on the collection of particles larger than the streamline they are following towards the filter grid, as shown in Figure 17 (b). If the velocity is very high, the inclusions and particles with sufficient density are collected through interception. The inclusions/particles will, however, immediately be re-entrained due to the drag forces, as

well as to the fluid flow boundary layer. The velocity has to be moderate to allow for interception to occur. If inclusions/particles are collected as a result of interception, there is a high probability that extensive bridging occur and finally clogging of the filter [76].

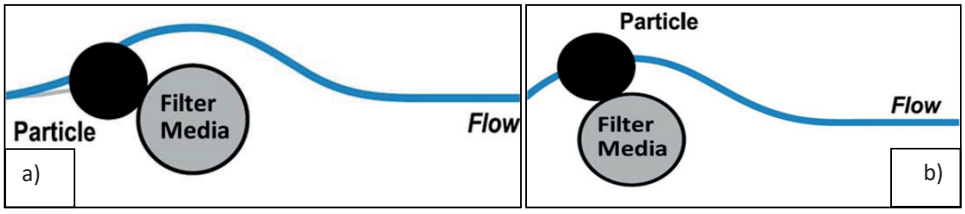

Figure 17: Schematic illustration of the principle behind inclusion/particle collection via (a) inertia and (b) interception. [47]

Brownian motion

Brownian motion is a vital mechanism for the collection of particles with a diameter ≤0.3 µm. It is most significant for particles with an average size in the range of 0.01 to 0.1 µm. The particles in this size range have an erratic and constant movement while suspended in the liquid, and can be trapped when they hit an obstacle, see Figure 18 (a) [77]. Due to the high surface energy there is, with time, a tendency, for the smaller particles to agglomerate and form larger inclusions.

Sedimentation and Gravity Deposit

Particles within a resting fluid have two forces acting on them, *i.e.* the gravitational force accelerating the particle towards the earth, and the fluid resistance/drag force upwards. If one of these forces is dominating, the particles will float or settle with time, as shown schematically in Figure 18 (b) for settling. If both forces are equal, the particles will be stable in their position. The settling velocity can be very slow for small particles [78], while settled particles can easily be re-entrained into the melt due to turbulence or any kind of disturbance [79].

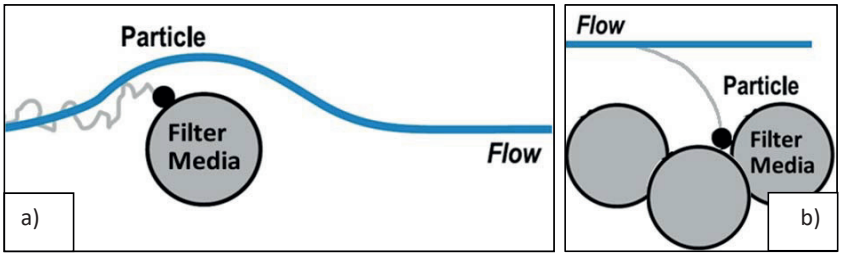

Figure 18: Schematic illustration of the principle behind inclusion/particle collection via (a) Brownian motion and (b) sedimentation or gravity deposition [47].

Sieving

Sieving is based on the collection of particles larger than the filtration grid or the window size of the filter, as shown in Figure 19 (a). This filtration mechanism is only applicable to particles that are in the size range of the filter orifice, or as a result of the formation of

agglomerates with a size exceeding the window size of the filter. In combination with the generation of brides and filter cake, sieving remains essential.

Cake filtration

Cake filtration generates a fine mesh of agglomerated particles, which by itself sieve new particles, extending the cake until the pressure drop rises so high that the filter cake clogs. A clogged filter will stop the metal flow, disabling the filter unit. A clogged filter is shown in Figure 19 (b).

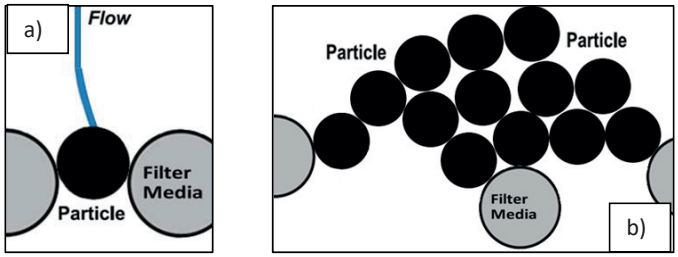

Figure 19: Schematic illustration of the principle behind inclusion/particle collection via (a) sieving and (b) cake filtration showing a clogged filter.

4.1.2 Estimation of Filtration Efficiency

Reducing the volume available for fluid flow by using higher PPI filters will result in a higher interstitial velocity inside the filter, while the superficial velocity above and below the filter remains constant. The resulting filtration efficiency will be reduced with an increasing interstitial velocity.

Apelian and Mutharasan [80] has presented a model using the superficial velocity to estimate the filtration efficiency. The model has not only been applied by them, but also by many other researchers, *i.e.* Frisvold [52] and Ray *et al.* [17]. By using Apelian and Mutharasan's model, the filtration efficiency for each size group of particles can be estimated using the following equation:

$$E_0 = 1 - exp^{-\frac{K_0 L}{w_s}} \qquad \text{(Eq.48)}$$

where E_0 is the initial filtration efficiency [%], w_s is the superficial velocity [m/s], L is the thickness of the filter [m], and K_0 is the 'kinetic' parameter [s^{-1}].

The interstitial velocity is dependent on the tortuosity, porosity, wetting, turbulence, etc., and it is therefore difficult to measure and/or monitor the interstitial velocity during a cast. For reasons of practicality, the model by Apelian and Mutharasan's is explicitly described by application of the superficial velocity w_s. The superficial velocity is usually readily known and unambiguous. By using the 'kinetic' parameter K_0 Apelian and Mutharasan's accounts for the interstitial velocity, as well as the type of filter media applied during the cast. This number is determined by empirical investigations.

Using the theory proposed by Kennedy [30], the filtration efficiency is dependent on the number of cells that the individual fluid element must traverse in the passage from the inlet to the outlet of the

filter, see Eq.49. This model assumes that the filter is a pore-like structure, and that every cell has only one inlet and one outlet:

$$N_c = \frac{\tau L}{(d_c + d_s)} \quad \text{(Eq.49)}$$

where N_c is the number of cells that the fluid has to pass, d_c the cell or pore diameter [m], and d_s the strut diameter [m]. For a standard CFF with 50 mm thickness, and with the tortuosity and geometry data presented in Table 3, the statistical chance of collecting inclusions in the case of 80 PPI filter is with approx. 200 events nearly 6 times larger than the approx. 35 events within a 30 PPI filter. The 50 PPI filter has on average of 83 events.

With the number of possible interactions N_c between filter and inclusions/particle, the estimated collection probability per 'event' or cell can be formulated as follows:

$$E = 1 - exp^{-\eta N_c} \quad \text{(Eq.50)}$$

where η is the collection probability of each cell of the filter (assumed to be very small). The similarity between Eq.48 and Eq.50 is obvious, and it shows that the 'kinetic' parameter multiplied with the thickness of the filter divided by the superficial velocity, $\frac{K_0 L}{w_s}$, is equal to the probability η, multiplied by the number of events N_c. It can be assumed that the efficiency proposed by Apelian and Mutharasan [80] behaves proportionally the probability of individual events throughout the filter [30]:

$$\frac{K_0 L}{w_s} \sim \eta N_c \quad \text{(Eq.51)}$$

4.2 Quantification of Filtration Results

As previously mentioned, gaining the knowledge of the melt cleanliness is a key parameter for the industry as it affects *e.g.* the mechanical and chemical properties, as well as the quality, of the end product. This in turn directly influences the market price of the metal, leading to financial consequences for the cast houses that do not know the metal cleanliness of every single batch of metal they produce. As a result it is therefore essential to identify the presence of both single large inclusions, as well as a high number of small inclusions.

The Liquid Metal Cleanliness Analyser (LiMCA), presented in 2001 by R. Guthrie and M. Li [5], counts particles down to 20-25 µm in spherical diameter in-situ during the casting process. LiMCA is today considered to be the state-of-the-art in non-metallic particle monitoring during casting of aluminium. The technology has the advantage of delivering the measured/detected metal cleanliness in-situ over the full time of a cast. This technology can, however, not distinguish between gaseous, liquid and solid inclusions. Moreover it lacks the ability to distinguish between spherical particles, agglomerates, folded bi-films and/or clusters. This again affects the accuracy of the results, *i.e.* it affects the particle count in view of particle size and size distribution during cleanliness characterization.

As a result, it has been essential to develop an inexpensive and stable analytical method capable of determining the accurate cleanliness of the metal with a high degree of accuracy, whilst being faster in use than the presently known methods. The new method should also be less susceptible to human bias than manual counting.

The main objective of the "quantification of filtration efficiency" work was therefore to find an accurate method that with a clear time saving could generate a quantitative particle count by distinguishing between inclusions, pores and phases in solidified aluminium samples. As a result, a computer based method to auto acquire micrographs over a large surface area at various magnifications was presented, together with computerized macros that simultaneously could process the micrographs. The proposed method proved not only to be very useful for analytical modelling of the particle count, but also for the estimation of the filtration efficiency of different CFFs, as well as for the metal flow rates.

Based on the obtained results shown in *Supplements 6* to *8*, the particle size and distribution, as well as the degree of porosity of the given samples could be evaluated. The advantages and disadvantages of the image processing steps, as well as the strong and weak points of the method are described and discussed. The reproducibility and accuracy of the obtained data is also given attention.

4.2.1 Automated Image Acquisition and Particle Counting Method

During the development of the automated image acquisition and particle counting method used for analysing the particle load of solid aluminium samples, two different methods were used to acquire the micrographs. Both methods were based on the use of Rapidly Solidified Spectrographic Discs (RSSD) samples, prepared by metallographic methods following the Struers® Catalogue and Struers® "e-Metalog" to a mirror like finish, as well as the use of the Image Pro Plus® 7.0 software from MediaCybernetics® to program the applied macros.

Initially, images (micrographs) were acquired manually using a Leica MeF4M light microscope equipped with a Jenoptic® ProgRes-C10 Plus 10 MP CCD camera. The program used to capture the images was the ProgRes Image Capture Software supplied by Jenoptic®. The developed method was based on the comparison between a manual particle count of 700 images and the automated particle count of the same images. The benchmarking of the method is in detail discussed in *Supplement 7*.

The next step in the development of the method was the automation of the image acquisition. A microscope, type Reichert MeF3 A, was modified by installing a Sony DXC 950P 1.2 MP camera and a moving stage based on micro step motors. The automated microscope allowed for acquisition of a grid of high magnification micrographs over the whole area of every sample. As a result, approx. 6.25% of the total sample area was digitalized with a 500 times magnification. The method of acquiring the images is presented in Figure 20 (a) to (d) and discussed in detail in *Supplement 7* and *8*.

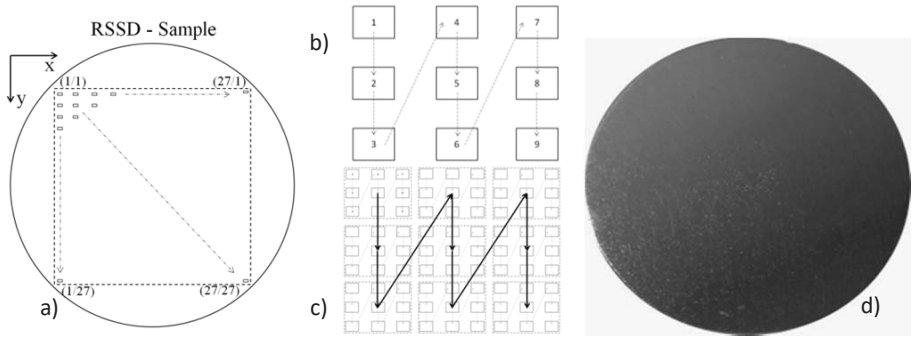

Figure 20: (a), (b) and (c) are sketches of the pattern of images that were acquired by the use of the automated stage for each of the samples investigated (a factor of 3 was used in both *x* and *y* direction), and (d) a surface image of a real polished metal sample.

The method to acquire the particle count has during the different stages of the development changed slightly. The initial method, as presented in *Supplement 6* is based on the following 5 steps:

1. Adjusting the image intensity.
2. Correction of the contrast.
3. Using a sharpen filter function.
4. Flattening the image.
5. Counting the separated particles.

The designed macro was applied on metal samples from an aluminium rod cast house, and the cleanliness of the unfiltered- and filtered metal samples was identified to be high with very few inclusions larger than 10 µm. The inclusions identified were mainly TiB_2 particles originating from the addition of a grain refiner. The particles proved to have a size distribution of 2 to 4 µm in spherical diameter. A higher magnification, *i.e.* 500 times, was applied allowing smaller particles to be identified. The overall outcome was that a larger area then usual had been evaluated by the use of the automated moving stage, granting a higher statistical reliability of the results. The human bias was also eliminated.

The method is further discussed in *Supplement 7*, and the optimizations of the results are summarized in *Supplement 8*. The optimized method is based on the following 8 steps:

1. Applying a filter to flatten the image.
2. Subtracting the background noise image.
3. Applying a high pass Gauss filter.
4. Using a sharpen function.
5. Processing the image with a morphological filter function.
6. Additional sharpen function.
7. Adjustment of the value of gamma, contrast and brightness.
8. Count all objects of a certain size and of spherical shape.

Chapter 5

5. Discussion and Results

During the present work a broad variety of topics have been included and discussed, and a widespread diversity of results produced. The scientific development and the interconnection of the fluid flow and the EM theory used for the round 4 inch laboratory scale priming and filtration system is presented in Figure 21. It is in this regard essential to point out the importance of every single segment of the experimental validation of the fluid flow and the electromagnetics in regards to the priming and filtration of liquid aluminium.

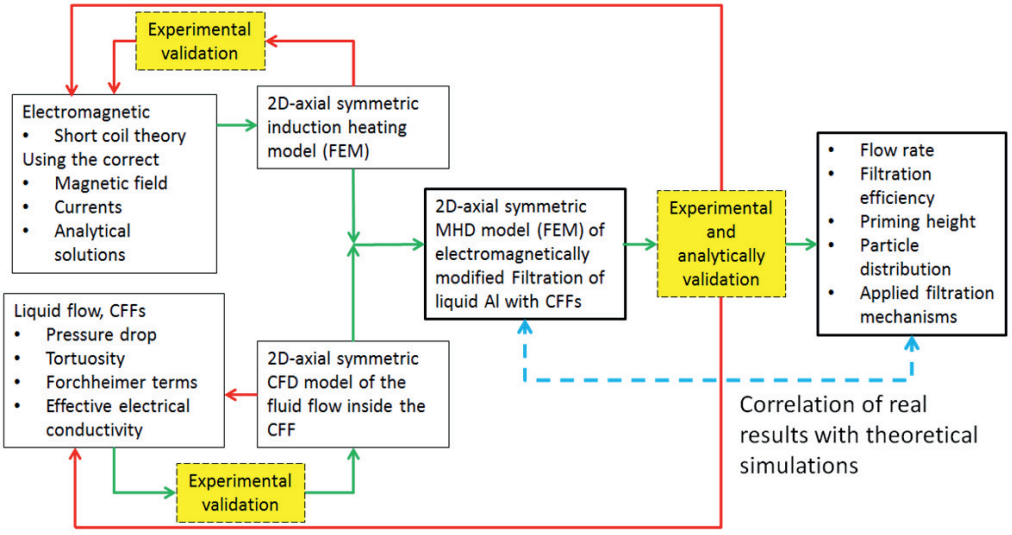

Figure 21: Flow sheet of the development of the theory behind the EM priming, CFD and MHD modelling work using the round 4 inch laboratory scale setup. The sketch shows the interconnection of the fluid flow and the EM theory being addressed separately and combined with the MHD model, which allowed for the further development of the EM priming system.

With the theoretical tools developed during the first part of the work, the design of a larger EM priming unit could be initiated. For the second part of the work the main focus was on the design of an industrial pilot size EM priming system. In this regards the validation of a square induction system was required prior to reaching the final stage of the up scaling. The different intermediate steps of the process are presented in Figure 22. The focus at this point was on the understanding of the effect that the shape and size of the coil had on the EM priming principle.

During the duration of the present work, an industrial pilot size EM priming system was designed and put into operation. The setup was later used for verification of the EM priming principles introduced.

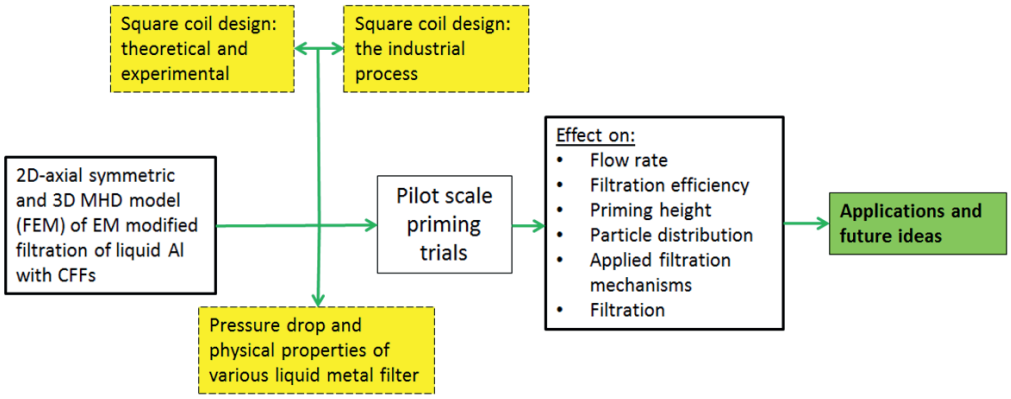

Figure 22: Flow sheet of the different intermediate steps of the up scaling of the EM priming system.

The results of the present work and the observations made during the up scaling process are presented and discussed in the following subsections.

5.1 Coil Design

Mankind have known the fundamental principle of induction coil design for a century, however, it cannot be used directly to describe the proposed EM priming system. Thus, the essential parameters for the design of the coils have been identified and the theoretical approach validated by experiments and FEM. The proposed design method is based on either considering the limits of an already available power transformer, or to find the specification of a new transformer generating a target average flux density. It should be one more time noted that the presently proposed approach has been based on current.

Simple inductance and magnetic flux correlations were used to derive the theoretical design equations for induction coils of various shapes, as shown in *Supplement 2*. Wheeler's single and multi-layer approach was found to be accurate in determining the inductance for the 50 to 60 Hz cases, but less accurate at high frequency when $\delta_c < d_c$.

The application of an equivalent round diameter to the theoretical calculations of square coil magnetic flux densities has been found by experimental, analytical and FEM means to be sufficiently accurate (< 1% error) for design purposes.

The application of modern finite element software, such as COMSOL® allows the solution of simple, fast and accurate 2D-axisymmetric models. By using the equivalent diameter it can be used as an approximate solution for square coils. The 3D models give a spatial resolution of the results, but are much more resource-demanding and slower to execute. If 3D models are applied at high frequency the ability to mesh at a spacing of $< \delta_c$ becomes doubtful. The violation of this criteria has already been reported in literature to lead to extreme errors [81]. When comparing the 3D FEM with analytical solutions, the analytical solutions will give the smallest error. However; the FE-Models allows for a 3D visualization of the shape of the resulting fields. In other words, through FEM it is possible to combine the EM results with fluid dynamics and Joule heating simulations to design more advanced aspects of the systems.

The inhomogeneity in the corners of the square coil has been observed to be advantageous for the EM priming, and is therefore not corrected for. The use of corner screens made of ferromagnetic material can be used to smoothen the non-uniformity of the magnetic field in the corners [54, 56, 82].

5.2 Priming

It has been observed that there is a controversial principle of understanding how filtration of aluminium alloys occurs in detail. A common understanding is that filters do filtration of all kind/sort of inclusions. Its filtration efficiency depends and on the overall surface energy, wetting angle, density, size, superficial velocity, etc. The priming of the filter, however, has been understood as the initial filling of the filter with metal. It is in this regard that two different ways of understanding how metal penetrates the filters and how particles are collected within the filters exists.

It is believed by most people, and therefore most commonly assumed, that priming means that 100% wetting of the filter material by the metal is achieved. A “good” priming would therefore be seen as a fully wetted and primed filter that, through various filter mechanisms, would allow for particles to be collected. The interaction surface is, in this regard, dependant on the different characteristics of the filter material towards the metal alloy used. The filtration efficiency, on the other hand, is dependent on the available filtration area and the physics of the applied filter.

Others believe that particle removal occurs at the interface of the metal inherent oxide layer, and that the priming occurs as the folding of a thin oxide film over the filter surface. The priming is, in this case, driven by the static pressure and the partial pressure of oxygen forming oxide films as penetrating into the filter. In other words, the metal does not get in direct contact with the filter material. Particles would be removed by the similar filtration mechanisms, but the resulting surface morphology and chemistry would be different due to the presence of the oxide film. The filtration efficiency would, however, still be dependent on the available filtration area, but it would be less dependent on the filter material.

As the focus of the present work is on priming of filters, no further discussions on how metal penetrates the filters or how particles are collected within the filters will be included in the present work. It should, however, be mentioned that the author, based on personal experience, supports the theory that a primed filter is a material wetted by the filtered metal or metal alloy.

It is important to point out that the key factor to utilizing any type of filter is to properly prime it with the media supposed to be filtered. The effect of the EM field on the priming of various CFF has, in the present work been identified, and the positioning of the coil position towards the filter identified as a critical parameter.

A summary of the most important experimental trials performed, together with the applied metal height in each case, is shown in Table 5. By application of EM fields from 0.12 to 0.2 T, using the three different induction coils designed, the following was validated in each case:

- All filter system sizes were successfully tested (round 4-, square 9-, and square 23-inch filters).
- All filter grades from 30 to 80 PPI CFF were primed without preheating.
- Multiple CFF (stack of 3 filters) of 30, 50 and 80 PPI were primed at room temperature using all filter system sizes (round 4-, square 9-, and square 23-inch filters).

- Priming of every filter grade was achieved with equal or less metal head as in traditional industrial methods.

Table 5: Summary of successful experimental results showing the small 4-inch coil trials conducted by Kennedy [30] together with the 9- and 23-inch trials presently conducted.

Filter size [inch]	Filter Grade [PPI]	Filter Thickness [mm]	EM field [T]	Metal head [mm]
4 round	50	50	0.2	100
4 round	80	50	0.2	100
4 round	50	150	0.2	150
4 round	80	150	0.2	150
9 square	50	50	0.12	50
9 square	50	150	0.12	150
23 square	50	50	0.15	200
23 square	50	150	0.15	200
23 square	50 + 80	100	0.15	250

The EM priming of standard industrial CFF was shown to be successful for round 4-inch, square 9-inch and square 23-inch filters using standard grade filters of 30, 50 and 80 PPI. The application of several standard filters stacked above each other and sealed at the edges was successful for double and triple filters of 50 and 80 PPI for all filter sizes.

Electromagnetic priming could be accomplished with minimal liquid metal over the upper surface of the filter. A liquid height of 50-200 mm over the top turn of the induction coil was sufficient to prime the cold filters [1]. The induced static pressure reached from 1.1 to 2.4 kPa, which proved not to be sufficient for gravitational priming but sufficient to achieve adequate priming of all grades of CFFs when an EM field was used.

The required priming height for sufficiently preheated single layer CFF, using industrial standard preheating procedures [38, 45, 46], is shown in Figure 23 together with the results of the lab-scale and the full industrial scaled single and multiple filter priming trials. First presented in *Supplement 3,* the graph was improved by the addition of results from new experimental trials. The fine dotted line shows the results of the lab scale filters using the 4- and 9 inch coils, as presented in *Supplement 4* and *5*. The large red crosses markers are the conducted industrial pilot scale test performed in the 23 inch Electro Magnetic Primed Filter (EMPF) system using regular industrial 23 inch CFF from Sivex® without any preheating (all EM trials were conducted using the filters at room temperature). The EMPF trials were also performed using thicker filters, *i.e.* a stack of triple 50 PPI CFF filter and a stack of 50 plus 80 PPI CFF. This would by means of traditional priming be unthinkable even with preheating of the filters.

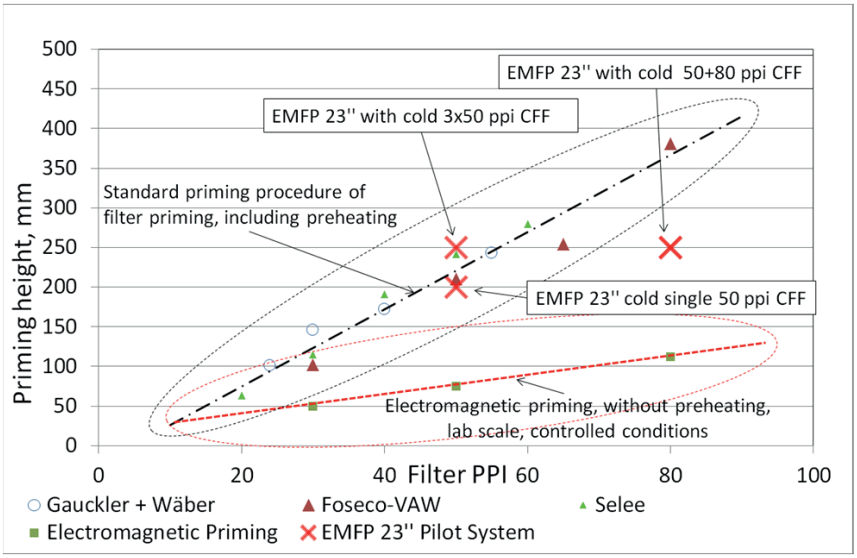

Figure 23: Priming height versus filter PPI from different producers [38, 45, 46]. A comparison is made with the results obtained from earlier electromagnetic priming trials using different size of filters and field strengths, and the results from the 23 inch pilot scale sized filtration trials.

5.2.1 Stage 1: The Formation of a Meniscus

During the initial stage of priming by EM fields all the designed coils generated a meniscus with different characteristic shapes for the round and the square coils. Even the behaviour of the meniscus on the filter surface was different allowing only some metal at a time to flow into the filter. As discussed in the patent application [1] the coil has to extend above the upper surface of the top filter by one coil turn, or at least 5% and preferably 10% of the coil radius, to be sufficient in priming the filter and to avoid a meniscus formation. The formed meniscus itself was identified to help the priming of the filters, as it introduced an artificial static head above the filter. A height of 10% was proved to supresses the generation of an uncontrolled meniscus and metal spill could be excluded. A complete suppression of the meniscus would require additional metal.

The meniscus is generated by the induced Lorentz forces. Based on the position of the induction coil towards the conducting metal and the variation of conductivity within the filter, the coil position has detrimental effect on the behaviour of the metal. A curl in the magnetic field is induced as the conductivity varies within the filter material, or during the priming stage, resulting in large gradients in the Lorentz forces. This in turn introduces a velocity gradient which pushes the metal inwards, in a curl like shape, forcing the metal to form a column in the centre of the crucible above the filter. The meniscus is the result of the curl in the EM field, as indicated in Figure 2 and Figure 24.

The priming of a tortuous filter is still a poorly understood topic. It has to date been impossible to look into a filter during priming with liquid metal, and sectioning after the trial reveals only a frozen image of the dynamic process of priming with a liquid. Many investigations have, due to this, been conducted to

try to spread some light on the physics of the filters. Examples of such work are the tortuosity and permeability studies using water as a liquid media, due to its similar viscosity as aluminium [37, 38, 83-86]. The tortuosity and permeability allows a person skilled in the art to model and calculate the pressure drop over the filter, and to simulate the final metal flow within a CFF after successful priming when full wetting is obtained. Nevertheless; the high surface tension of liquid metal, the wetting behaviour towards common filter materials, and the non-wetting oxide film covering aluminium within an oxygen containing atmosphere complicate the process of priming [50]. The full sets of physics occurring during the initiation of priming are yet to be discovered. The effects of the EM field are discussed to neglect and remove some of the resistances during the priming stage, but the accurate theoretical description has not yet been discovered.

It has been assumed by the present author that during the initial stage of priming, the molten aluminium starts to solidify as it flows into the thin tortuous cold filter sections. In conventional priming trials the filter would freeze, and the cast would have to be stopped. However, by using the EM field the solidified metal would be melted again due to a combination of effects, *i.e.* due to the MHD within the system that will homogenizes the temperature within the filter bowl and secure that the metal remains liquid. As a final consequence of the combination of EM effects, the installed filter will be primed. The following list of mechanisms has been observed:

- Electromagnetic induction induces joule heat inside the frozen metal blocking the tortuous filter. The conductivity increases during the solidification of aluminium, encouraging larger amounts of heat being generated within the solidified metal tips while slightly reducing the EM penetration.
- Electromagnetic pressure and Lorentz forces drive the metal further into the filter. If the coil has more than 1/3 of its total length above the surface of the highest filter the resulting flow field will push the metal inwards the filter.
- Alternating electromagnetic fields induce strong 100 Hz vibrations when using 50 Hz main frequency. It is assumed that the surface tension of the liquid Al towards Al_2O_3 is dramatically reduced by the vibrations. This enhances the wetting and reduces the required metallostatic pressure. Additionally, the protective oxide film of the aluminium becomes fractured with every vibration cycle, helping to avoid the formation of thick/old oxide films.
- MHD above the filter generates a mixing of the metal reservoir above the filter which homogenizes the temperature. Heat can be continuously conducted to the interface of the metal and the cold filter. The heat then preheats the filter sufficiently. This further explains why a certain time is required to prime the filters, while simultaneously avoiding freezing of the metal inside the filter. The MHD additionally generates the meniscus.
- The generation of a meniscus supplies the process of priming by an artificially generated metal head, forcing the metal by additional gravitational pressure into the filter, supported by the dynamic pressure.

In Figure 24 (a) and (b) a MHD model of the 9 inch experimental setup was calculated using COMSOL®, showing the liquid metal meniscus and the velocity field at two different stages of the priming. The model, based on the application of a current of 1250 A, generated a magnetic field of 0.12 T. This resulted in the metal circulating with a calculated maximal velocity of 0.68 m/s. It was the two opposing curls that generated the meniscus, as shown in Figure 24 (a). After reaching a certain temperature within the filter, which was assumed to be in the range of the melting temperature of the used alloy, the metal

penetrated the filter by the dynamic pressure induced by the EM field, the Lorenz forces and the static pressure. The process of priming was improved by the electromagnetic field, as shown in Figure 24 (b), where the resulting dynamic velocity flow field forced the metal into the filter.

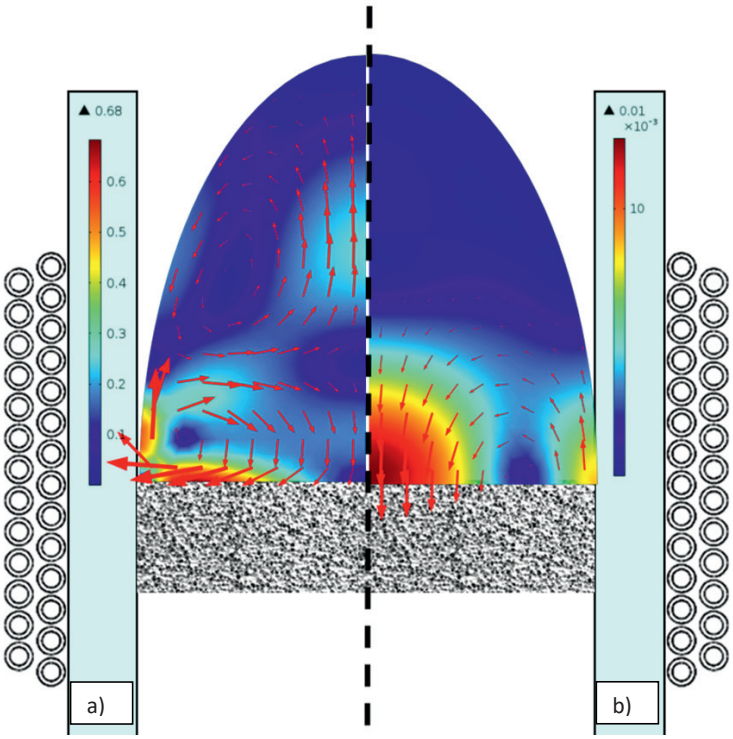

Figure 24: Steady state FEM generated with COMSOL® using the 9 inch coil system shows; (a) the induced flow field during the priming stage inside the meniscus, and (b) the flow direction as the filter has reached a sufficient temperature and the metal can penetrate the filter. The bottom line represents the rough filter surface and is modelled as (a) wall function with roughness, and (b) with an open border boundary condition (initiation of priming). The resulting force driving the metal into the filter is highest in the centre of the filter.

A formation of a metal meniscus during the EM priming process, as shown in Figure 24, was identified to be beneficial for the priming itself. The meniscus guarantees a homogeneous metal temperature during priming as it is generated by strong velocity gradients, which in turn generate good mixing. Not to forget, it also enhances the static pressure by the meniscus height as an 'artificial' gravitational metal head. The surface remains without turbulence, and no additional entrainment of oxide and/or bi-films could be observed by investigations of the metallographic samples collected. The EM field induces, together with the meniscus shape, a flow field with a maximal dynamic velocity field directed into the surface of the centre of the filter, as shown in Figure 24 (b). The experimental results obtained show a stable meniscus for the round 4.7 inch long coil, as shown in Figure 25 (a), presented and initially discussed in *Supplement 3*. The 9 inch system used a square coil with a 12.2 inch diameter, as shown in Figure 25 (b). The change of the magnetic field, and a change in behaviour of the metal within the field due to the different coil shapes, can be seen. The movement of the metal surface was less stable and the meniscus

oscillated shaping a less meniscus-like column. The oxide layer remained semi-stable. No significant change of oxide concentration within the metal was observed even if it was expected. In Figure 25 (c) the semi stable meniscus and strong eddy currents inside the corners of the crucible can be seen. The lower part consisted of a metal column, where the metal elevated into a more elliptic shaped meniscus, while the magnetic field remained strong enough to lift the metal above the normal metal meniscus level towards the centre of the crucible. This generated an additional metal head as it elevated the metal, enhancing the potential energy of the metal, and inducing a strong dynamic velocity towards the filter surface. This has been discussed in detail in *Supplement 5*.

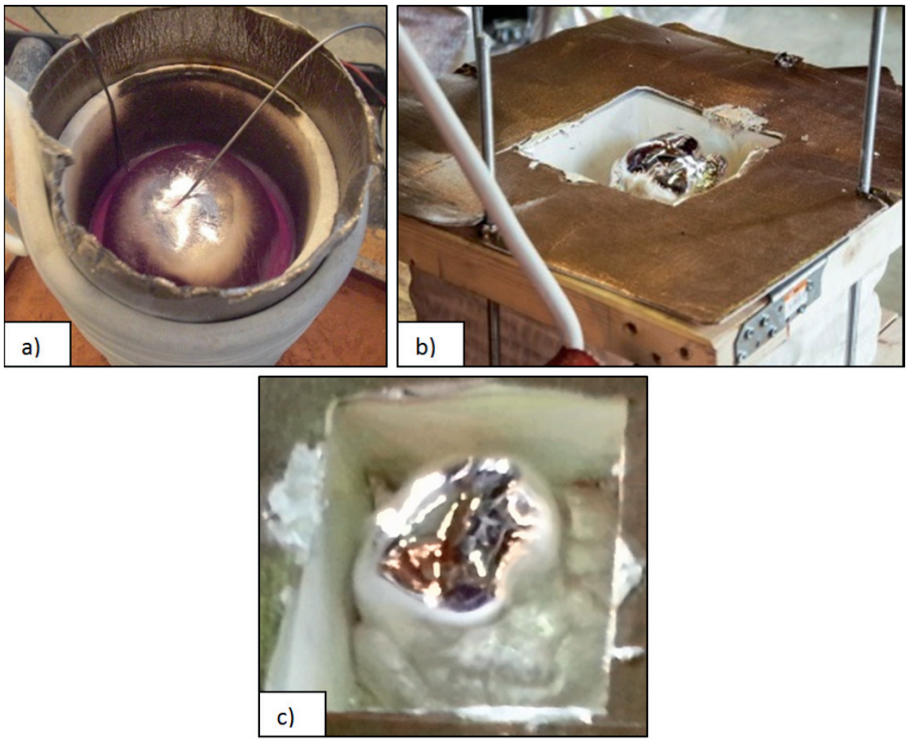

Figure 25: Formation of stable menisci for the 4- and the 9 inch experimental trials. The round 4.7 inch coil generated a stable almost static meniscus, while the square 12.2 inch coil had a stable but slightly oscillating meniscus. The meniscus height was approx. 100 mm for the 4.7 inch coil using 0.22 T and approx. 160 mm for the 12.2 inch coil using 0.12 T.

The EM priming industrial scale 23 inch filter box was implemented by the use of a 28.9 inch square coil. Investigating the 'air'-coil, the application of a current of 580 A RMS induced an EM field of ~0.135 T. In the case of metal filtration, the effective area and consequently the AC resistance of the coil was significantly reduced. The voltage drop required to drive the current was established to be 430 V when the system was filled with metal, resulting in a current of 650 A RMS.

The rotating nature of the field was shown experimentally by using only 50 mm of metal head, see Figure 26 (a) and (b). The initial formation of the meniscus, seen in Figure 26 (a), proved to be driven by the

strong Lorentz forces pushing the metal out of the corners into the centre of the filter box as indicated by the red arrows in Figure 27. The meniscus later collapsed due to the gravitational weight of the metal as shown in Figure 26 (b). Due to the magnetic flux surrounding the metal, the Lorentz forces chaotically pushed the metal around. The presence of a meniscus continued during a short period of time, but it was observed that it was rotated by approximately 90 degrees with the direction of the current. The movement of the wobbling metal dissipated the effect of the EM force, as well as the gravitational force in all directions. The thickness of the metal layer after solidification, approx. 45mm, can be seen in Figure 26 (c).

The behaviour of the meniscus was firstly established to be influenced by a combination of the EM penetration depth of the used frequency (50 Hz), and the conductivity of the alloy, see Figure 3, and secondly by the total metal head. The EM flux lines penetrated with the first or second penetration depth, *i.e.* through the metal layer, bending the flux lines only slightly while inducing current.

The use of too little metal, described by the patent application [1] for a case where the coil continues above the surface of the metal head, proved to result in an unevenly distribution of the Lorenz forces. The induced flux density above and below the metal reservoir was much higher than inside the metal. The resulting induced Lorentz force from above and below the metal, as shown in Figure 27, was identified to generate strong MHD. The square shape of the coil further enhanced the corner effects, as the field in the corners was less homogeneous and stronger (discussed and presented in *Supplement 5*). The rotating nature of the EM field induced a vortex-like rotating flow field, counteracting the priming of the filter. The induced MHDs were directed and dissipated the induced forces.

Figure 26: The generation of an unstable meniscus while applying ~45 mm metal head onto the filter surface is shown in (a) and (b). In (a) the meniscus is in the process of being formed, but collapses and rotates/wobbles as seen in figure (b). In (c) the solidified metal after the trial is shown. The thickness of the layer was measured to be 45 mm which represents a penetration depth of ~4/3 (not sufficient for EM priming, see Figure 3).

The FEM for the EM field shown in Figure 27, clearly indicates the existence of strong Lorentz forces induced from below and above the metal reservoir. The insufficient thickness, which is directly connected to the penetration depth, can be seen as the magnetic flux lines penetrate through the metal layer.

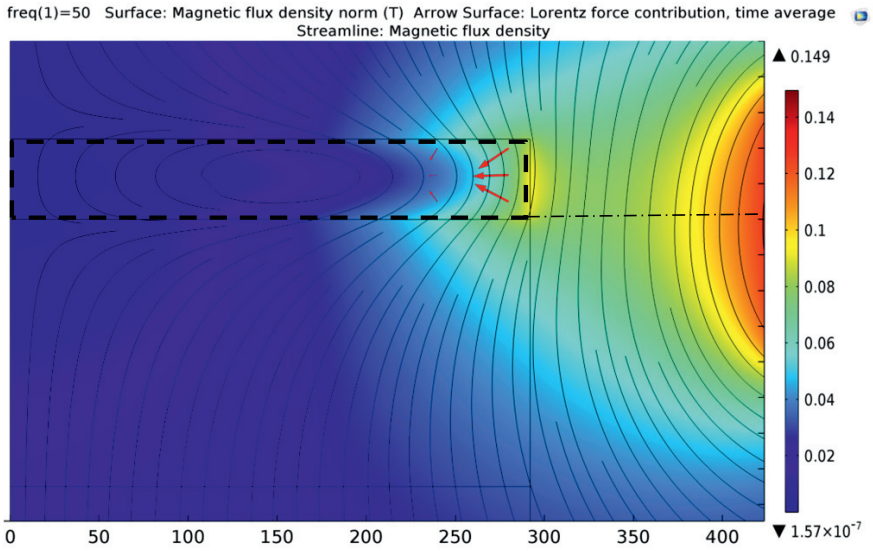

Figure 27: A COMSOL® model showing the EM flux field when applying only 45 mm metal head, indicated as the black dotted box. It can be observed, that the flux lines go through the metal, while only bending partially. The flux surrounds the metal, indicated by the blue-yellowish colour around the corners, inducing Lorentz forces from above and below the metal. This in turn will introduce velocity fields pushing the metal in all directions.

It was also establish to suppress the wobbling and chaotic mixing by using a metal head of minimum 3 times the penetration depth of the applied frequency in z-direction, as well as filling the coil to at least 50 % of the coil length above the final coil turn. As can be seen in Figure 28, the EM field can develop partly below and partly within the metal inducing the Lorentz forces in a single direction. This in turn allows the MHD to successfully prime the filter, or a stack of filters. A model and a picture of a good priming situation are shown in Figure 28 and Figure 29 respectively.

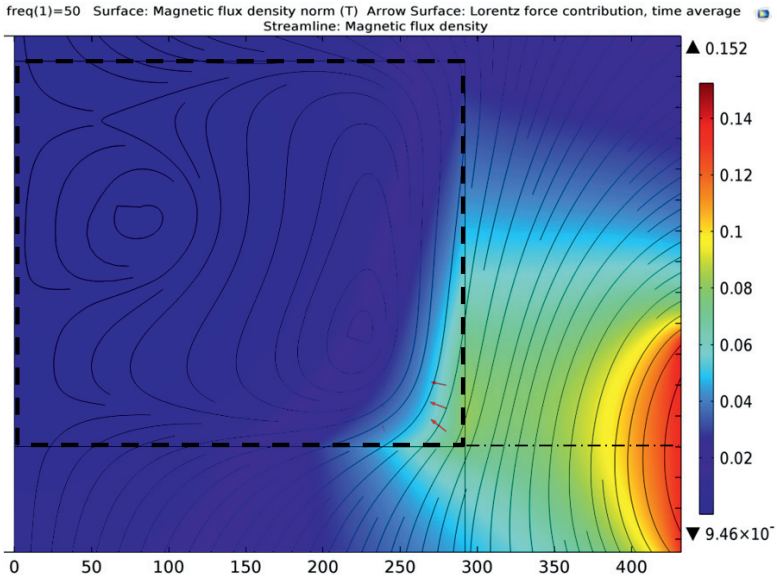

Figure 28: A COMSOL® model showing the resulting EM flux lines when applying a very high metal head (250 mm). The obtained Lorentz force initiates a stable MHD flow field, as well as the existence of a fluid flow within the metal. Together this allows for the initiation of the priming sequence.

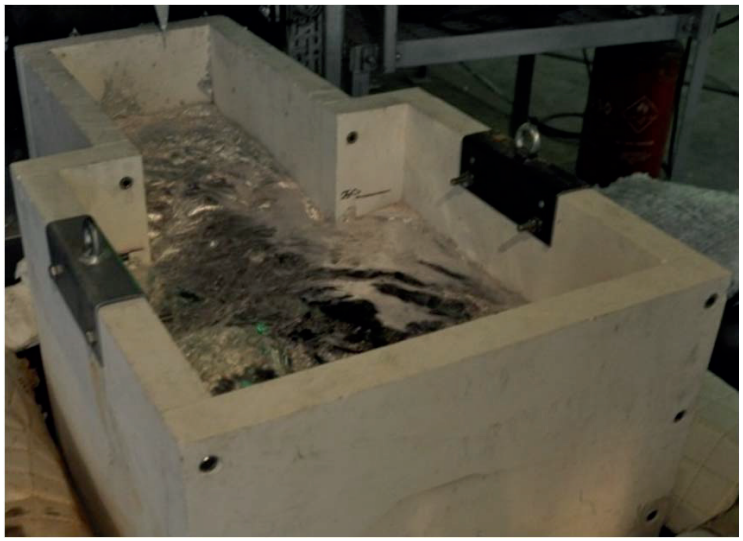

Figure 29: The 23 inch filter box filled with 200 mm static metal head above a stacked 150 mm thick 50 PPI CFF. The induction coil is electrified with 660 A inducing a magnetic field of approx. 0.15 T. The effect of the EM field was observed by the strong, well-like flow of the metal pool from the centre towards the side.

5.2.2 Stage 2: Metal Penetration of the Filter

As discussed earlier, it is impossible to observe the priming process of liquid metal on the filter in-situ, and post testing cannot deliver all required information. However, the observations made are discussed in the present section, and it is hoped to spread some light on the topic of metal penetration and priming

In regards to traditional priming it is believed that the moment molten aluminium initiates priming and starts to penetrate into the structure of a CFF, the metal has overcome the surface tension and the wetting issues existing between aluminium on alumina. At the very same time, the metal loses temperature, the thickness of the oxide layer increases, and the viscosity of the molten metal changes. If the filter temperature is too low compared to the melt temperature and far below the melting point of the used alloy, the obtained temperature gradient would freeze the top layer of the filter and priming cannot occur. It is important to remember that the gravity head only supplies the metal with an initial pressure/force used to overcome the resistance of the filter. The moment the molten metal finds its way through the CFF the hot metal flow will supply heat to the filter, as well as to the frozen sections which will melt again, utilizing the full filter volume for filtration over time. The process of traditional priming depends on the following parameters:

- Sufficient preheating of the filter and the filter box.
- The casting temperature.
- The metal alloy used, *i.e.* wettability and melting point/eutectic.
- The characteristics of the used filter, *i.e.* PPI of the CFF.
- Allowance of static metal head of the filter box installed.
- Quick passage between heating and the first metal entering the filter.
- The particle load.

In comparison the EM priming casts the metal directly on cold filter surfaces. The melt has, however, to be kept in motion to avoid freezing. Additional Joule heat is supplied by the EM field and used to overcome the large temperature loses. The thermal energy of the metal is used to preheat the filter. When reaching the required temperature, metal penetrates into the filter driven by the static and dynamic pressure induced by the EM field and the MHD. The resulting EM vibrations reduces the surface tension, as well as the wetting angle, and allows for an even and fast priming of the whole filter volume. The metal remains in motion as the velocity fields recirculate the melt above, below and within the filter. At the same time, the remaining gases within the filter are successfully removed utilizing the full vertical and horizontal volume for filtration. The total time needed for EM priming varies and depends on the following:

- The casting temperature.
- The initial temperature of the filter and the filter box.
- The characteristics of the used filters, *i.e.* thickness and PPI of the used CFF.
- The metal alloy used, *i.e.* conductivity, wettability, and melting point/eutectic.
- The coil parameters, *i.e.* current and frequency applied.
- The metal head above the filter.
- The particle load.

The priming is also dependent on the size of the filter, the field strength coupled by the penetration depth of the applied frequency, and the shape of the coil. Nevertheless; all the different grade filters, as well as size of induction coils, used in the present work have shown a similar formation of a cone like shape of metal through the filter as the alumina filter material is wetted by the metal. The cone like shape is a result of the filter being starved of metal directly after the first initiation of priming occurs. Samples of the cone like shape are shown in Figure 30 (a) for the 9 inch 50 PPI CFF, and Figure 30 (b) for the 23 inch 50 PPI CFF. As can be seen from the figure, the metal primes the filter from the centre; it exits the filter in the centre, and continuously enlarging the available volume for flow by priming towards the sidewalls. As these filters were starved directly after initial priming, they could not achieve full priming of the full filter volume due to lack of metal and draining.

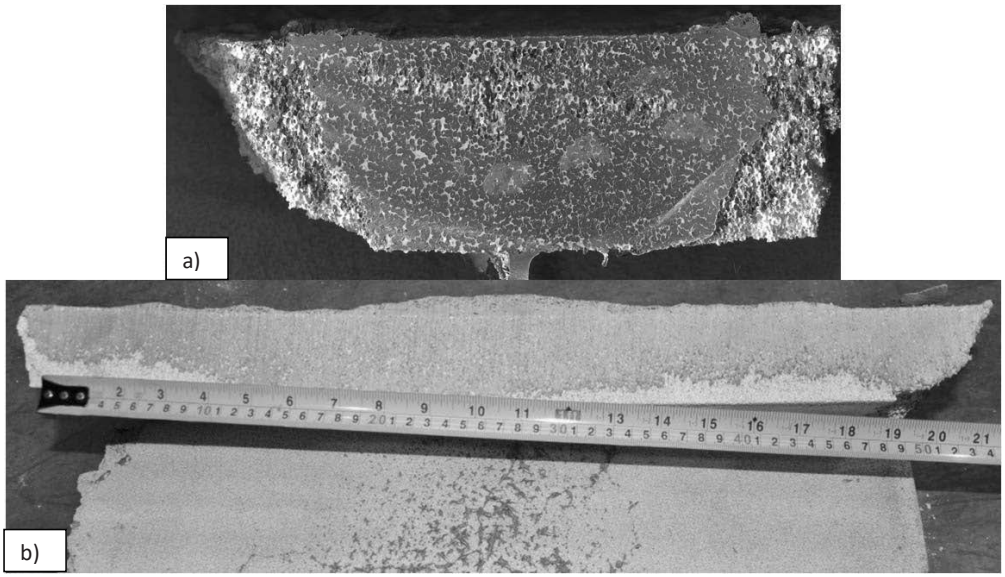

Figure 30: Starved and drained filters after EM priming using only enough metal to initiate the priming. A cone like shape where metal exits the filter in the centre can be observed. It is usually possible to identify a starved filter by the white bottom of the CFF filter after the trial. The filters were both in contact with the metal for only 10 to 20 seconds.

For the designed EMFP 23 inch priming system a frequency of 50 Hz was used, resulting in a star like shaped priming area as shown in Figure 31 (a) and (b). The filter shown is a single 80 PPI CFF primed with 250 mm metal head and starved after initial priming. The trial took approx. 2 minutes until initial priming. The filter was chiselled after the trial to remove all un-wetted areas. During evaluation of the filter after casting it was established that the filter was primed 25 mm (50 %) over the whole area of the filter, and that metal had wetted the remaining 25 mm in a star like shape, indicated in red in Figure 31 (a).

The obtained star like shape of the priming zone can be explained by looking at the MHDs generated within the system, as well as the EM penetration depth. As a result of the MHDs a strong dynamic velocity field with the highest pressure at the centre of the filter was induced, and the EM penetration

depth generated the strongest vibrations and the highest induced Joule heat within the corners of the coil. A star like shape on the initial priming zone was the result. The major contribution has been assumed to be from the MHD effect, as the EM penetration depth diminishes towards the centre of the filter.

Looking at industrial standards, it is already a challenging task to prime a high tortuosity 80 PPI CFF even after extensive preheating. During traditional priming approx. 350 to 400 mm metal head are needed to induce sufficient static pressure to get the 80 PPI CFF utilized.

Priming a cold 80 PPI CFFs by application of only 250 mm metal head using only EM fields to prime the filter, has in the present work been identified as a not easily overcome challenge. The metal is required to penetrate into the fine channels of the filter, and to form an oxide layer surface while in contact with the filter media. At the same time, it is required that a flow of metal is maintained into the cold filter at all time. The metal will supply the heat to re-melt the frozen metal tip by convection, which will be supported by Joule heat and strong EM vibrations. In Figure 32 a piece of a primed 80 PPI CFF metal sample is presented, reviling a fine anthill like structure. As can be seen from the figure, the filter appears to have been more like a capillary like structure, and during priming of the cold filter only small amounts of metal have supplied the heat needed to melt the solidified tip. Overall, this makes the initial priming of the 80 PPI CFF more time consuming by approx. 2 minutes.

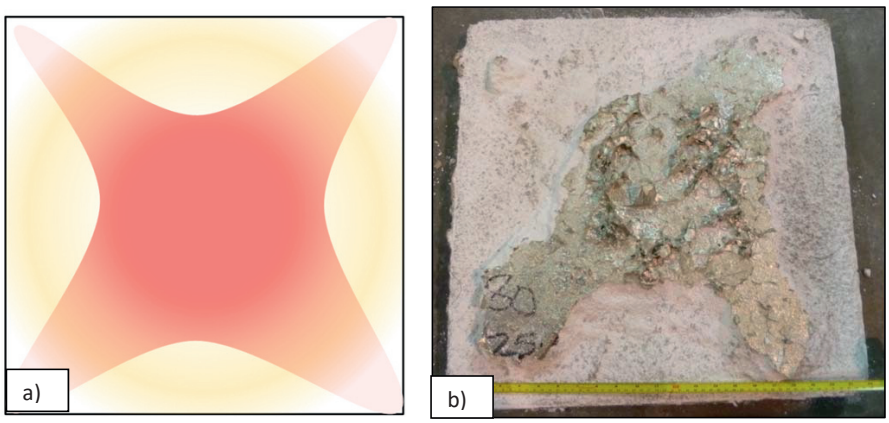

Figure 31: (a) The EMFP estimated 23 inch 80 PPI CFF initial priming zones in red and the growth zones in yellow. The test was performed applying a current with 50 Hz and a magnetic flux of 0.15 T. In (b) similar observations are made for the experimental trial of a single 80 PPI CFF starved after initial priming and after chiselling the unwetted filter sections.

It was, however, observed that the 50 PPI CFF primes significantly faster than an 80 PPI CFF using the electromagnetic field on cold filters. The difference is assumed to be due to the significant difference in tortuosity of the filters, as presented in Table 2 . It is also assumed that this indicates a change in the fundamental filtration modes applied to the highest-grade filters. When investigating the structure of the CFF more in detail, it appears that the 80 PPI CFF has a more cell like structure than the 50 PPI CFF which seems to have a more open web like porosity.

Figure 32: A piece of a primed 80 PPI CFF metal sample showing the fine anthill like structure. To secure the sample the CFF was chiselled out of the metal matrix.

In the present work it was observed that the bottom of filters not submerged in metal for some time gave an impression of being white*, i.e.* an impression of not being primed. Even if the weight of the filter after a trial suggested that it was 96 to 99 % primed with metal, a not wetted filter bottom was observed. It is believed that solidified droplets of metal drain out of the filter over the whole area of the filter at the end of the trial. The droplets can be seen as needle like structures, shown in Figure 33. This phenomenon was observed when starving the filters, as shown earlier in Figure 30 and Figure 31, and when there was insufficient metal available during priming to fill the sump with metal below the filter. The metal appears not to wet the bottom of the filters by itself, and simply drains out of the filter after the trial.

Figure 33: Solidified aluminium “needles” sticking out of the filters after a successful priming trial when starving the filter of metal and not submerging the filter in a metal bath. The present filter is a single 50 PPI CFF primed with 200 mm metal head. The metal was allowed to exit the filter box directly after the first metal penetrated through the filter. The weight of the filter after the trial suggests 96 % priming.

5.2.3 The Effect of the Square Shape of the Coil on the Priming of the Filter

To be able to estimate the magnetic flux density in the corners of a square induction system, a 3D FEM, as shown in Figure 34, was required.

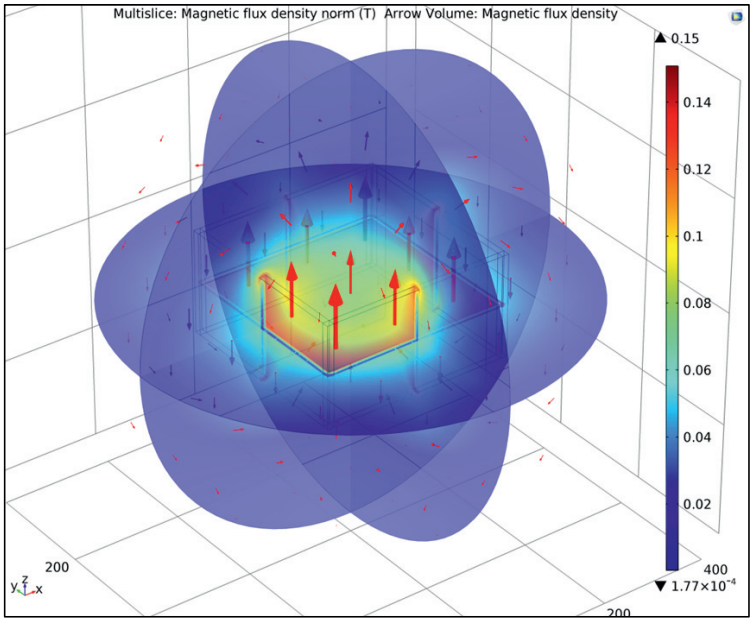

Figure 34: Multiple sliced image of the 3D FEM of the 9 inch square induction coil without metal, calculated by using the software COMSOL® 5.1. The current applied with the coil was 1250 A.

However, the application of a 3D FEM needs significantly more calculation time and power compared to the 2D axisymmetric models used for the design and validation of the round induction coils. Nevertheless; the 3D model can give a three-dimensional resolution of the resulting magnetic flux.

By application of computerized models the variation of frequencies can be investigated as it changes the penetration depth into the metal, and thereby the physics at the coil and workpiece. To achieve accurate results the mesh of the applied model was in the present work required to be $< \delta_c$ between each meshing node. Violating that would lead to significant errors [81]. Knowing that the penetration depth of 50 Hz was in the range of 35 to 45 mm, see Figure 3 , a mesh within that range was generated to allow for accurate solutions. It should be mentioned that if a high frequency model should be developed in 3D instead, the criterion $< \delta_c$ would have becomes difficult to satisfy.

It has been proven in the present work, which for the square induction coil the strongest EM field is obtained in the regions of corners of the coil. The calculated and modelled EM flux distributions for a 9 inch square coil over the diagonal and the centre line are shown in Figure 35 (a) and (c). The FEM estimation, shown in Figure 35 (b), indicates with a black dotted line and a red solid line where the measurements were acquired. The components of the magnetic flux density B_z in Figure 35 (c) was analytically estimated using Matlab®. The estimate in Figure 35 (a) was assumed by using Eq.5. Measurements were conducted in 10 mm steps on the diagonal and the centreline. The results have been discussed in detail in *Supplement 1, 2* and *5*.

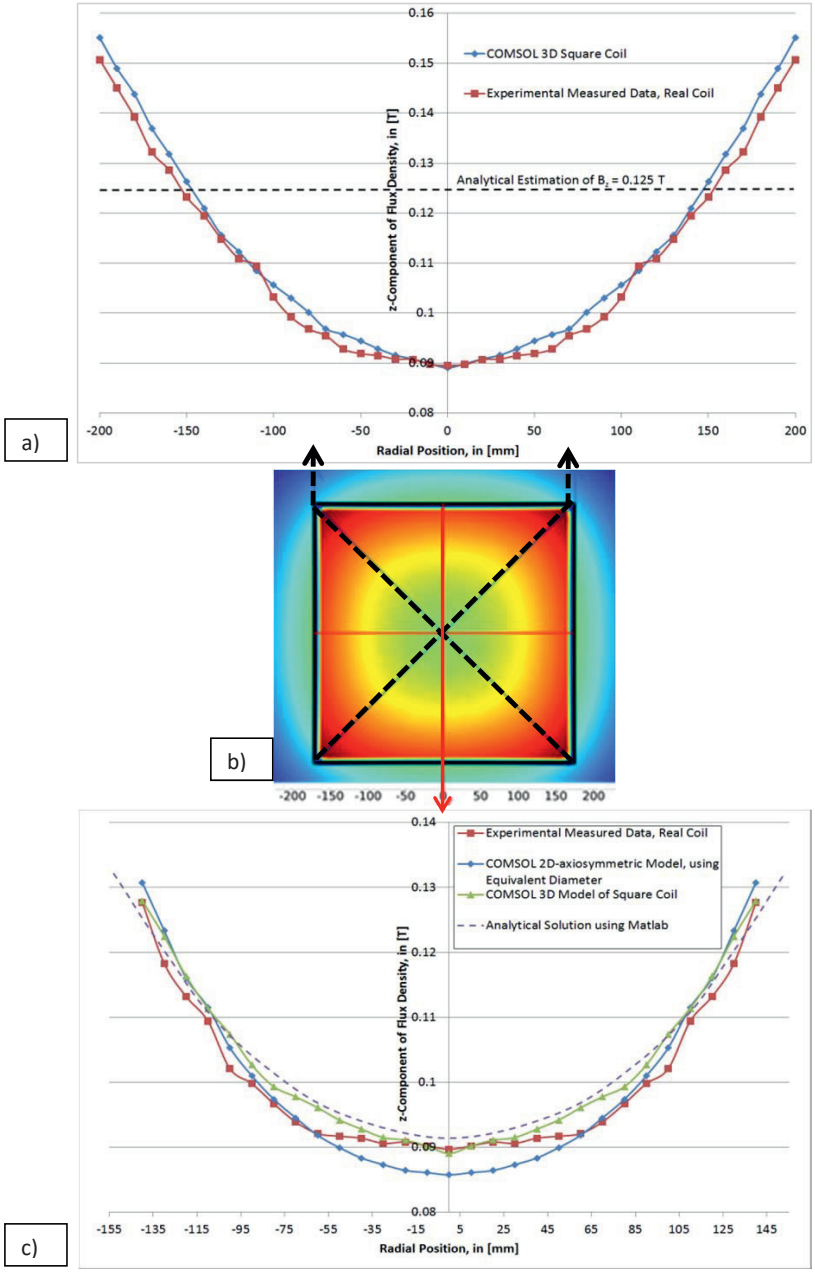

Figure 35: : Diagonal (a) and centre line (c) measurements of the axial flux density, B_z, for the 9 inch square coil measured in 10 mm steps at the centre of the coil. The obtained results are compared with 2D-axisymmetric models using the equivalent diameter, see (a) and (c), and a 3D model, see (b), solved by the use of COMSOL® 5.1. The analytical estimate of the average flux density using the inductance formula of Wheeler (Eq.24), shown as the black dotted line in (a) and (c), was calculated using

Matlab®. The magnetic field was generated by application of 1250 A RMS, and measured from r_c= 0 to 140 mm. The data is mirrored at the centreline r_c= 0 mm to generate a complete picture of the flux.

The variation of the total field strength over the area of the coil, by comparing measurements and modelled results of the diagonal to the centre, has given a strong indication of the variation of the time required to prime different regions of the filter when using only EM fields and insufficient static pressure. It was in the present work established that the regions with the strongest fields primed faster. It further appeared, that the pure EM priming effect was insignificant compared to the effect of the induced dynamic velocity. This was observed in several trials, *e.g.* in the 80 PPI CFF trial shown in Figure 31 (b).

During the evaluation of the EM penetration depth of the industrial EM priming system, the field strength proved to diminish to zero towards the centre of the filter when metal was introduced into the system. The penetration depth was established to be in the range of 10's of millimetres, *i.e.* 35 to 45 mm, and a rule of thumb tells that after the third penetration depth into the metal the resulting Lorentz forces and the induced current approaches zero.

A 2D axisymmetric model of the 80 PPI CFF is shown in Figure 36, visualizing the exponential decrease of the EM flux within the metal during the priming stage when using 50 Hz. The violet section represents the area of significant EM effect on the CFF. The colourless hole in the middle represents the region with only minor EM effect during the priming stage. Comparing Figure 36 with the shape of the initially primed sections of the 80 PPI CFF in Figure 31 (b), it is assumed that the direct contribution of the EM field on the priming of the filter was not a major contribution. It does, however, add towards priming within the corner regions of the filter. The effect of the EM field introducing the MHDs appeared to be of major importance. The EM field further supported the dynamic velocity by inductive heat and electromotive vibrations.

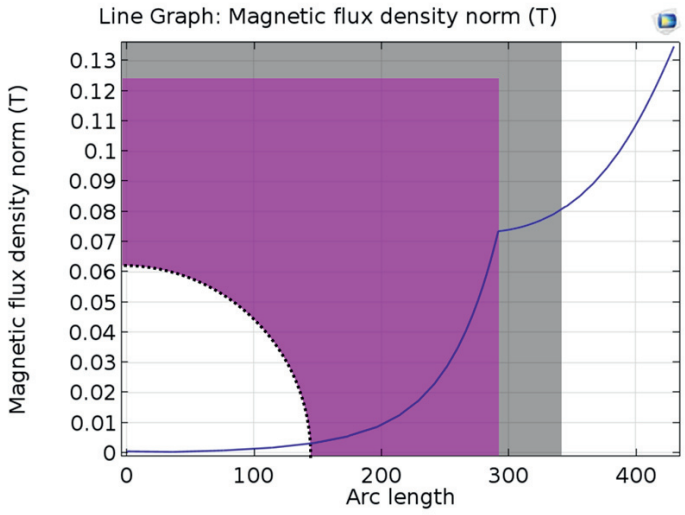

Figure 36: A quarter of the 23 inch CFF box showing the estimated magnetic flux at the filter interface centreline as filled with metal. The violet section represents the area within the third penetration depth, where a direct impact of the EM field can be expected. The white round section in the centre is the area were only minor EM effects can be expected. The grey area represents the schematic insulation, here as a non-conductive media.

5.2.4 Priming of Stacked Filters

One of the goals of the present work has been to show that the EM priming system could be utilized for all scales, and even on thicker filter sections.

The priming of a stack of filters was proven to be successful for all coil dimensions designed, and a discussion on the usability of thick filters presented, see *Supplement 3, 4 and 5*. The priming procedure was similar to the procedure developed for single filters, *i.e.* using CFFs at room temperature, pouring metal at a temperature of ~720°C onto the filters while simultaneously electrifying the coil. Fully wetted filters were obtained for the 4-, 9- and 23 inch filter tests with stack of filters, as shown in Figure 37 and Figure 38. The large filters were, however, partially drained due to the impracticality of filling the filter bowl and sump with ~500 kg of liquid metal, which would have been necessary to fully submerge the filters in metal after priming. Due to the insufficient amount of metal in the metal sump, air remained below the filter, and even after priming the metal did not wet the bottom side of the filter.

It should be mentioned that the different appearance of the surface of the filters is believed to be due to the different cutting operations used, the shrinking within the 4 inch filter, and the draining of the 23 inch filter. The cutting of the filters after the hot metal experiments were conducted by using a band saw and a water jet system. The band saw generated a clean cut and a shiny surface, but the band saw blade was destroyed during the process of cutting thicker filter metal samples. The water jet system was therefore used for cutting the 23 inch filters, which ended up with a rough and dull surface.

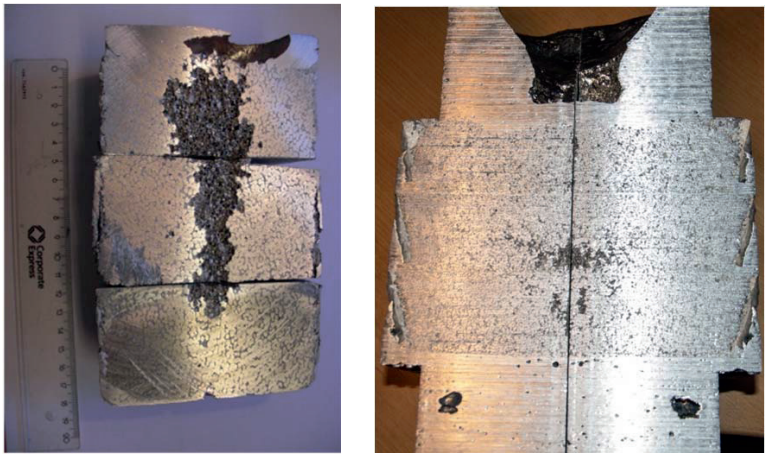

Figure 37: Fully primed triple 50 PPI filter, *i.e.* stack of 3 50 PPI filters, using the 4- and 9 inch priming coil filter systems on cold filters. The alloy used was A356 for the 4 inch trial, and a 3XXX series alloy, supplied by Hydro Aluminium Karmøy, Norway, for the 9 inch trials. As the experimental setup did not allow for the systems to be drained after ending the trail, the full filter box was solidified and cut by a band saw giving the shiny appearance.

Figure 38: Fully Primed triple 50 PPI filter using the 23 inch filter system using pure aluminium with 1% Mg similar to a 3XXX series alloy. The filter has been starved with metal and therefore initiated draining prior the metal could fill the sump of the filter box. The filters have therefore not been submerged in metal. The samples have been cut by a waterjet cutting system, which makes the surface appear to be dull.

5.3 Filtration Efficiency

5.3.1 General Discussion

The fundamental correlation of inclusion and particle removal has been presented in Chapter 4. By the use of filters the melt quality can be improved either by using high-grade filters, lower velocities, or thicker filter sections. The industrial practice applied by most aluminium producers today do, however, not allow for the use of high-grade filters (50-80 PPI) or even ticker filter sections. The EM priming principal has proven to offer new ways of increasing the quality of the final product.

In the present work a theory to estimate and calculate the filtration efficiency has been presented, and the increase of filter thickness has been identified as a promising factor for improvement towards higher filtration efficiency. The analytical model recommended to estimate the filtration efficiency has been presented by Apelian et al. [80], see Eq.48. From the equation, the relation of the thickness L of the used filters towards the filtration efficiency increases by the factor of e^{-L}. The estimated increase in filtration efficiency by the possibility of application of thicker, highly efficient CFF could therefore revolutionize the filtration technology for the aluminium cast houses.

Until today, when looking at the traditional priming technology, the maximum allowable metal height in filter boxes dictates the type of filters that can be applied. Based on the analysis of the filter permeability, it is in this regard the pressure drop during casting and not the initial priming height that typically should limit the type of filter and flow rate of metal applied.

The efficient removal of gas from the CFFs, the improved wetting and the utilization of the whole filter volume for metal flow by application of EM priming should allow for lower metal height during filtration for a given throughput, or a higher throughput for a given metal height while maintaining constant and reproducible filtration efficiency. This may also make it practical to use for example 50 PPI CFFs, which offers a more consistent filtration performance, instead of 30 PPI CFF, or any lower grade filter used in industrial practices today, with an overall improvement of the general metal quality as a result.

The improved gas removal, previously discussed, allows for a filter box design with a plane filter. Traditional filter systems have a 3° angle to allow the gas to exit the filter at the higher end. The fully horizontal (plane) design will be easier to maintain and it will be more robust during the application. Even the handling, mounting and removal of CFFs will be greatly improved.

The application of EM fields to prime foam filters, or any other filter type, can also lead to the development of new filter designs, new filter medias and/or filtration methods. New design ideas such as chemical active filtration are currently being investigated, as well as combined filtration media. All could be made possible as the EM priming can occur on any non-conductive material at any shape or form as long at it can be fitted in a filter-containing box. It is believed that the EM priming has the potential to revolutionize the filter box design and filtration technology.

5.3.2 Filtration Efficiency Estimate

The alloy, the inclusion type and the pore size of the filter [17] are essential to determine the 'kinetic' parameter K_0. A collection of K_0-values are presented in Table 6 and Table 7. The data presented by Kennedy *et al.* [87] shows results for small particles based on a few small scale experimental results, whereas Ray *et al.* [17] present data for a large variety of inclusion sizes. It should, however, be mentioned that Ray *et al.* [17] do not give information in regards to the applied velocities.

Table 6: The 'kinetic' parameters K_0 [1/s] to be used in Eq.48. The pseudo interstitial velocity presented on the left side [17], and a corrected K_0 [88] for use of a superficial velocity on the right side, shown for application of two type CFF filters and a 1XXX alloy

Size Group	**30 PPI CFF**	**50 PPI CFF**	**30 PPI CFF**	**50 PPI CFF**
	K_0 from literature [17]		Superficial corrected K_0 [88]	
15-20 µm	0.205	0.301	0.164	0.241
20-25 µm	0.250	0.360	0.200	0.288
25-30 µm	0.283	0.429	0.226	0.343
30-35 µm	0.323	0.478	0.258	0.382
35-40 µm	0.375	0.547	0.300	0.438
40-45 µm	0.409	0.627	0.327	0.502
45-50 µm	0.452	0.783	0.362	0.626
50-55 µm	0.509	0.940	0.407	0.752
55-60 µm	0.596	1.100	0.477	0.880
60+ µm	0.725	1.350	0.580	1.080

Kennedy [30] has evaluated K_0- values during lab scale filtration experiments for particles and inclusions in a size range from 2 to 25 µm, as presented in Table 7 which is used to compare the estimated filtration efficiencies.

Table 7: The 'kinetic' parameters K_0 [1/s] to be used in Eq.48,together with the overall filtration efficiency. The parameters have been determined by gravity filtration experiments using the A356 alloy and for particles in the size range 2-25 µm.

Ceramic Foam Filter		K_0					
	PPI	**2-5 µm**	**5-10 µm**	**10-15 µm**	**15-20 µm**	**20-25 µm**	**Total removal**
Kennedy [30]	**30**	0.046	0.045	0.049	0.060	0.058	0.049
	50	0.087	0.087	0.062	0.071	0.066	0.085
	80	0.038	0.053	0.055	0.065	0.055	0.054

Based on the work conducted by Kennedy [30] the present author concluded that the K_0-values presented together with filtration efficiency data in the work reported by Ray *et al.* and Keegan and Ray [17, 89], do not define the velocity used to calculate the filtration efficiency. The K_0-values do, however, appear to be too large to achieve the measured filtration efficiency for the applied CFFs. In Figure 39 (a) the filtration efficiency as a function of the efficiency distribution over the pore size of the filters, reproduced from the work by Keegan and Ray [89], is presented. The calculated filtration efficiency over the superficial velocity using the given K_0-values is presented with the same scale of efficiency in Figure 39 (b). The filtration efficiency was calculated by using the industrial casting velocity data from Table 8 and the unmodified K_0-values from Table 6 for a 50 PPI and a 30 PPI CFF.

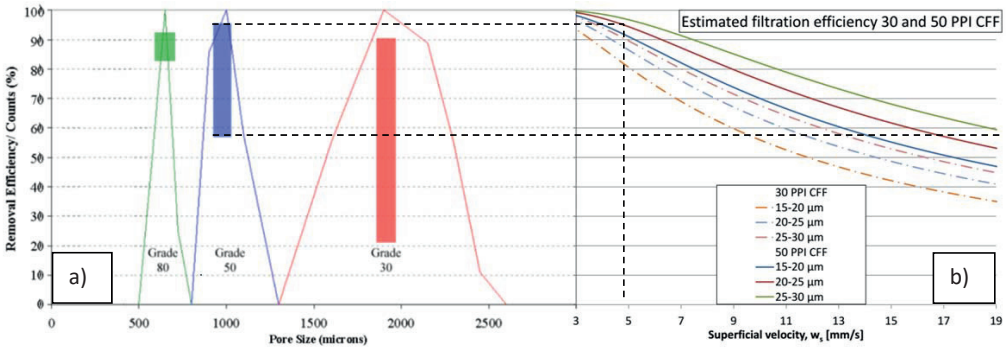

Figure 39: (a) The pore size of different grades of PPI CFF showing the range of the distribution of the measured filtration efficiency for Sivex filters [89], not stating the applied filtration velocities for these trials, maybe due to secrecy, and (b) the theoretical calculated filtration efficiency vs the superficial velocity calculated using the data from Table 8 and the unmodified K_0 values from Table 6. Both plots are using the same y-axis showing the removal efficiency of inclusions in comparison to pore size and superficial velocity.

The filtration efficiency presented in Figure 39 (a) clearly shows a wide distribution of the filtration efficiency for a 30 PPI CFF, displaying that the efficiency measurements varies between ~22 to 90 %. For a 50 PPI CFF the efficiency is in the range from ~58 to 95%, and for an 80 PPI CFF from ~83 to 92%. From Figure 39 (b) the effect of the superficial velocity on the filtration efficiency can be seen. As both graphs in Figure 39 (a) and (b) are using the same y-axis a correlation between pore size and superficial velocity can be made. For inclusions/particles with 15 µm spherical diameter, which are the smallest inclusions evaluated by Ray *et al.* [17], the lowest statistical removal efficiency is reported. The estimated filtration efficiency for a 30 PPI CFF using the highest given and recommended casting velocity of 19

mm/s, as summarized in Table 8 is approx. 41%, which stays in large contrast to the distribution showed in Figure 39 (a) with approx. 21 %.

Table 8: Compilation of metal velocity and flow rate data for some selected industrial casting applications. [17]

Process	Standard velocity [mm/s]	Metal flow [kg/(m^{2}s)]	Typical CFF in application
Billet casting	10 – 19	19 – 36	30 to 40 PPI
Slab casting	6 – 15	17 – 29	40 to 65 PPI
Continuous casting	3 - 10	6 - 19	20 to 50 PPI

Looking at the results presented in Figure 39 (b) the K_0-values presented in Table 6 seemed to be too large in regards to real filtration efficiency. This can be caused by the use of a pseudo interstitial velocity instead of the superficial velocities when estimating the K_0-values. The values by Ray *et al.* [17], presented in Table 6 have been adjusted by regression. The regressed values were then used to calculate the filtration efficiency in regard to the superficial velocity, shown in Figure 40 and Figure 41.

Another interesting approach was taken by Frisvold [52]. In his theory the filtration efficiency by the removal of inclusions/particles is proportional to the concentration and the surface area of the filter. The theory is supporting the formation of bridges and filter cake, generating a mesh of fine particles above and within the first mm of the filter, sieving and filtering inclusions with the inclusions of similar size. The same assumption was later made by other researchers [90-92]. The concentration of particles has been found to exponentially decay within the depth of the filter. The function of particle concentration over the filter is dependent on the filter grade or PPI and its depth or filter length. This theory supports the EM priming technology, as it allows for finer CFF filters to be used with similar or better filtration results. Thicker filter sections might become interesting when allowing for several ‘stages’ of filtration, bridge formation within every ‘stage’ filter, and/or recapturing entrained inclusions within the very same filter.

5.3.3 Calculated Filtration Efficiency

Using the modified ‘kinetic’ parameters presented in Table 6 and the experimental values of the ‘kinetic’ parameter presented in Table 7, with the velocity data from Table 8, the calculated filtration efficiencies over superficial velocities for standard filter applications can be estimated. In Figure 40 and Figure 41 the filtration efficiency for single filters are presented. The multi filter filtration efficiencies over velocity are presented in *Supplement 4* and in Figure 42 for comparison to the single estimated filtration efficiencies.

As can be seen from Figure 40, a 30 PPI CFF can be efficient toward the removal of coarse inclusions and particles, *e.g.* agglomerates of small inclusions, bi-films or single large inclusions. The open structure, or web like structure, of the 30 PPI filter permits larger inclusions to be collected without reducing the area available for flow, hence avoiding blockage or clogging of the filter. The filtration path is only slightly tortuous (1.3, or 30% longer path length compared to a straight tube), and small inclusions have a high probability of not being collected. The filtration efficiency is, however, assumed to be more stable towards higher filtration velocities. If a 30 PPI CFF builds up a filter cake the throughput and the pressure drop of the filter will be dependent on the generated filter cake. Likewise, the filtration efficiency may

reach very high numbers prior to an inclusion entrainment, which can have detrimental effects on the quality of the cast product and should therefore be avoided under all circumstances.

A filter cake can be avoided when using sufficient filter area, where large amounts of huge inclusions are collected within the filter instead of agglomerating to a filter cake. To avoid clogging short settling time, degassing and slag removal prior to filtration should be considered to further remove the large inclusions. The pressure drop of the filter would, as a result, not increase dramatically, the interstitial velocity would remain moderate, and entrainment of inclusions could be avoided. A reduction and variation of the filtration efficiency over time of the casting process would also be avoided. The probability that smaller/finer particles are collected in the 30 PPI CFF are limited, as these particles easily can pass through the coarse filter web.

The difference between the estimated filtration efficiencies from both studies presently mentioned exceeds a critical limit. Nevertheless; the real filtration efficiency was estimated to be in the range of the deviation when comparing the results with the efficiencies presented in Figure 39 (a).

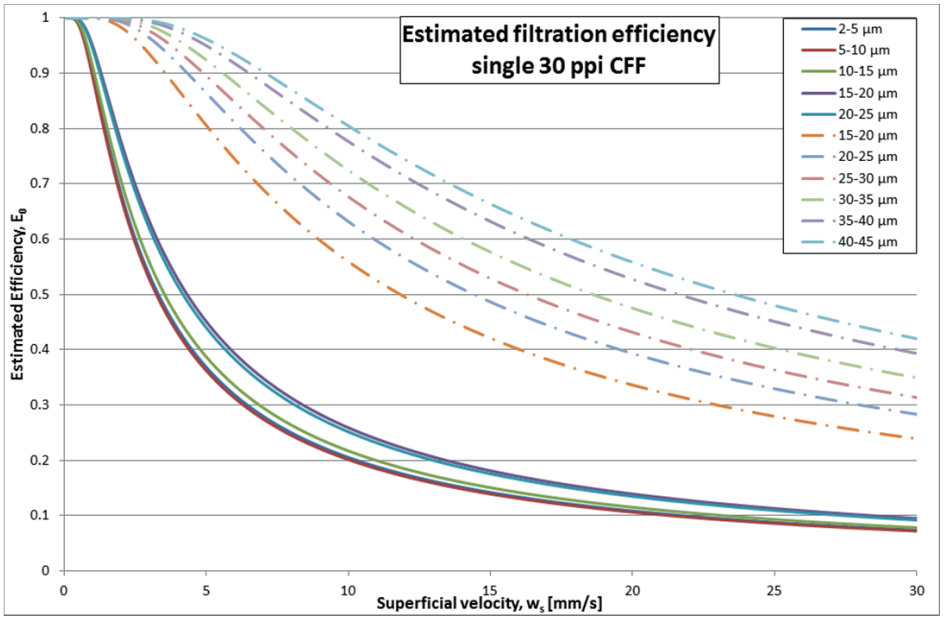

Figure 40: Estimated filtration efficiency of a single 30 PPI CFF for particles in the size range of 2 to 25 µm (based on the data from Kennedy *et al.* [38], see full lines), and the superficial corrected 15 to 45 µm data (by Ray *et al.* [17] presented in Table 6 see dotted lines), versus common industrial superficial velocity [mm/s] data (presented in Table 8). The dependency of the efficiency and the velocity is clearly visible.

The filtration efficiency of a single 50 PPI CFF is presented in Figure 41, and shows a higher probability of collecting finer inclusions and particles (as expected). It should, however, be mentioned that the K_0-values derived by Kennedy *et al.* [38] are not recommended for the 50 PPI CFF due to the small number

of samples investigated. The real filtration efficiency was, as a result, assumed to be somewhere in the range of both the methods discussed.

It was therefore concluded that a single 50 PPI filter suits the final filtration stage by application of low enough superficial velocities. A high efficiency in collecting the coarse inclusions, which might have re-entrained into the metal during a previous stage, is believed to allow for a high cleanliness to be reached in the final product.

A downside to using finer filters, *e.g.* 50 PPI, was identified to be the collection of high quantities of large inclusions, which would generate bridges or even in some cases a filter cake. The generation of artificial obstacles would reduce the area available for flow, which in turn would increase the pressure drop and the interstitial velocity. The average path length within a 50 PPI CFF is ~120% (tortuosity of 2.2) longer than in a straight tube. As a result the interstitial velocity within a 50 PPI filter is already much higher than in a 30 PPI (tortuosity of 1.3). A further increase of the interstitial velocity would reduce the filtration efficiency. Already collected inclusions would then be "washed out"/re-entrain if sufficient metallostatic pressure was supplied, forcing the metal into the filter. It is important to remember that if the pressure drop reaches a critical value the inclusions cannot be flushed out of the filter, and the filter would clog and freeze.

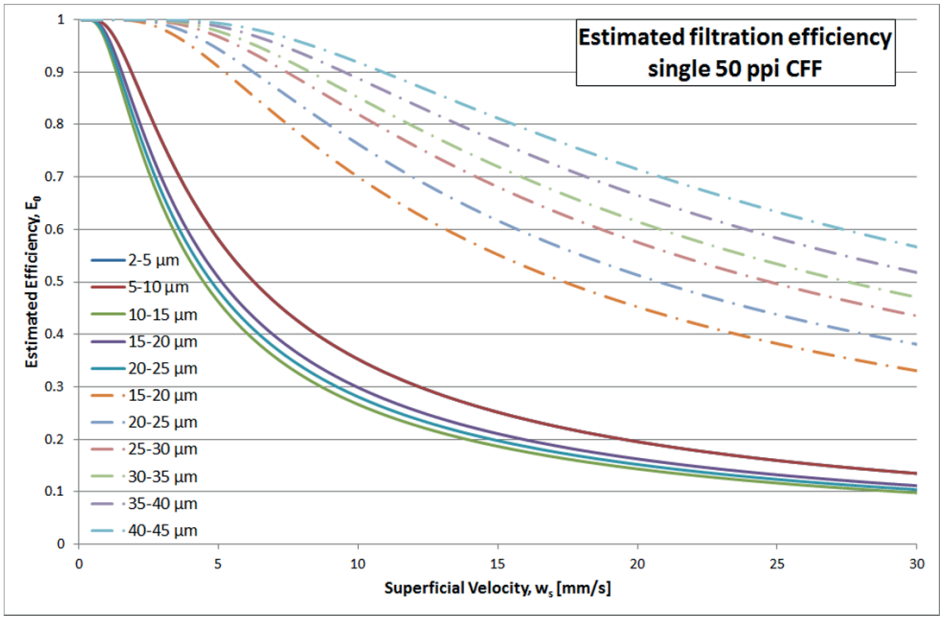

Figure 41: Estimated filtration efficiency of a single 50 PPI CFF for particles in the size range of 2 to 25 µm (based on the data from Kennedy *et al.* [38], see full lines), and the superficial corrected 15 to 45 µm data (by Ray *et al.* [17] presented in Table 6 see dotted lines), versus common industrial superficial velocity [mm/s] data (presented in Table 8). In comparison to the result of the 30 PPI CFF, higher filtration efficiency in regards to inclusions of all sizes is at average seen to exist.

A theoretical calculation of the filtration efficiency of thicker filters is explored in Figure 42(based on the work presented in *Supplement 4*). The impact of alternate thicknesses on filter performance for 30 PPI filters, using the base case superficial filtration velocity of 7.3 mm/s, reveals a remarkable increase in the filtration efficiency when applying the filtration estimation by Apelian *et al.* [80] presented in Eq.48. As can be seen from the figure, approximately 90% filtration efficiency can be reached at the default 7.3 mm/s filtration velocity using 100 mm or thicker 30 PPI filters. This represents an improvement of more than 20% in regards to the total filtration efficiency.

A comparison between Figure 23 and Figure 43 indicates that a much higher metal head is required to prime than to sustain flow after priming. This is also the case when assuming much thicker, *e.g.* 150 mm, filter sections. In the present work it was proved that by applying EM priming to stacks of filters placed in existing filter box installations, a significant higher filtration efficiency compared to what could be reached traditionally by a standard thicknesses of 50 mm filters, see Figure 42.

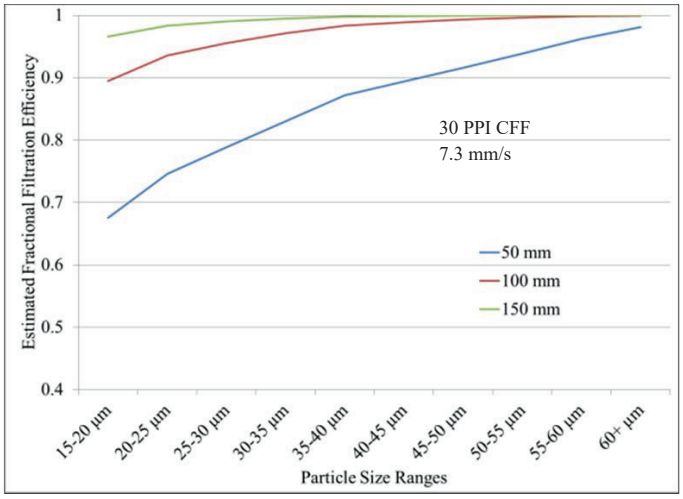

Figure 42: Estimated fractional filtration efficiency vs. particle size from 15 to >60 µm for three different filter thicknesses from 50-150 mm using 30 PPI CFFs.

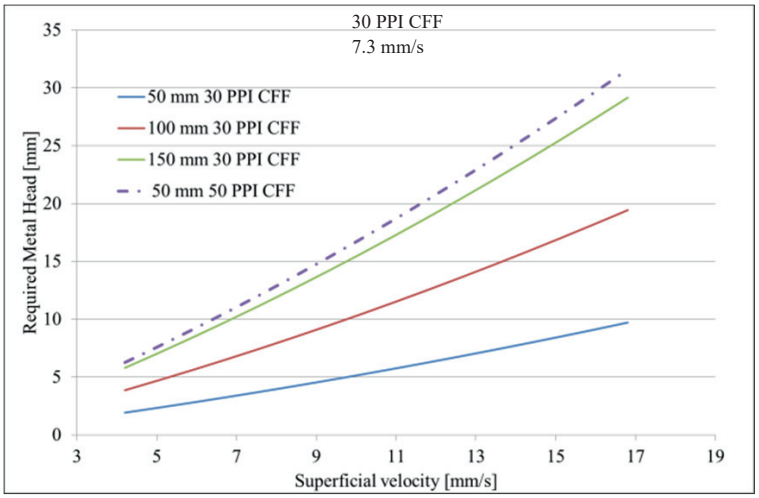

Figure 43: Metal head required to sustain flow as a function of the superficial velocity in [mm/s] and the filter thickness L in [mm]. The correlation can be found using the Forchheimer equation presented in Eq.46 for 30 and 50 PPI CFF.

5.4 Automated Quantification of Inclusions

As part of the present work it became obvious that it was required to develop a method to quantify the cleanliness of metal samples by simple means of light microscopy and metallographic preparation. The developed method has been proven its usefulness in various investigations; see *Supplement 6, 7* and *8*. Further developments to make the method comparable to industrial standards have been undertaken, and are currently in the stage of implementation at NTNU.

Being a semi-automated method the skill required by the operator has been identified to be one of the key issues when implementing this technique in the field. The stage control, data communication and quality of equipment used have proven to have a crucial effect on the quality of the received results. Complications and key issues with the automated quantification of inclusions are discussed in the following section.

The single particles observed in the initial study, *i.e. Supplement 6,* was approx. 15-25 µm in spherical diameter. In the second study, *i.e. Supplement 7* and *8*, the particles had an average spherical diameter of 1-8 µm. The observed bi-films in both cases showed a minimum diameter of 0.1 µm [93]. It was proved that all particles with a minimum size of 0.2 µm on any length of the diameter (ferret diameter) was in the range of the resolution of visible light of the experimental setup used, and could therefore theoretically be identified.

The identification of particles in the size range < 2 µm was found to be challenging, or impossible, due to the noise obtained with the images retrieved from the imaging system, by the restrictions to the resolution of the camera, as well as the aperture and finesse of the lenses used. In other words, the acquired resolution of inclusions in that size range was too low when using standard light microscopes. In the image-processing setup used in the present work the limiting factor of the resolution was the detector of the camera and the optical system of the applied microscope. To be able to resolve the grey level

gradients distinguishable for each individual particle by the amount of light being allowed to interact with the sensor within a certain time became a main area of focus for this part of the work.

Two digitally enlarged 3 µm large particles, captured by the ProgRes C10 10 MP camera and the SonyDXC 950P 1.2 MP camera, *i.e.* two cameras with different resolutions, are presented in Figure 44 (a) and (b). The ProgRes C10 10 MP camera (a) had a resolution of 2080x1542 pixels (3.2MP) with 1071.2 x794.1 µm, and the SonyDXC 950P 1.2 MP camera (b) a resolution of 764 x 580 pixels (1.2 MP) with 191 x 143 µm. The magnifications used were 200 (a) and 500 times (b). The particle with the blurred edge, shown in Figure 44 (a), would give a less accurate particle size and therefore a partially 'wrong' area count, and was later identified to bias the total particle/inclusion concentration. The particle shown in Figure 44 (b) would allow for a 'more' accurate count. It is important to remember that the total difference in inclusion count does not only shift the counted inclusions of each size group, but it also alters the estimated filtration efficiency.

To remove the blur and sharpen the contour of the particles, different mathematical filters and methods can be applied [94, 95].

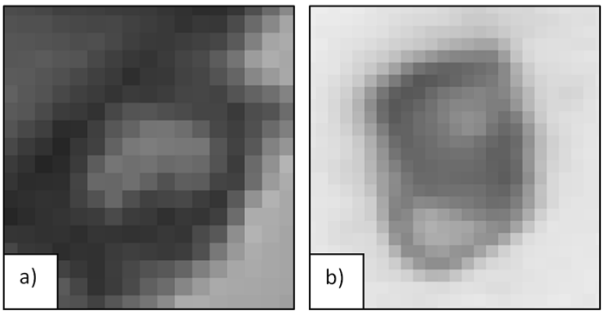

Figure 44: Comparison between the resolutions of two ~3 µm particles that were digitally enlarged. Image (a) has a resolution of 0.2656 μm^2/pixel using 200 times magnification, and (b) 0.0625 μm^2/pixel using 500 times magnification.

The 1.2 MP CCD camera implemented with the automated moving stage for the industrial trial samples, see *Supplement 7* and *8*, was used to take the picture shown in Figure 44 (b).

The resolution was identified to be a key element in regards to the automated image-processing method, and to its ability to retrieve the information from the images. Every single pixel resolved an area of 0.0625 μm^2. Four pixels have been defined to be enough to resolve an edge of an obstacle. To be on the safe side, twelve pixels in one direction were set as the logical limit to be able to identify a particle. This criterion gave a corrected spherical diameter of 3 µm as the smallest diameter that could be identified in regards to obstacles/pores/phases etc., and 6 µm in regards to the corrected spherical diameter in regards to particles/inclusions. The method was applied and results retrieved with an acceptable error. It should, however, be noted that all identified particles below 6 µm were excluded. Nevertheless; particles/inclusions/obstacles/pores/phases with a corrected spherical diameter down to 1.5 µm were identified.

In regards to work on aluminium and its alloys, the present author has not found filtration efficiency data reported in literature for particles < 15 µm in diameter. This is believed to be due to LiMCAs inability to

analyse inclusions below the limit of 20 µm in size. Furthermore, LiMCA cannot distinguish between different types of inclusion, agglomerates, gas bubbles, bi-films or 3D resolution of inclusion shapes. When comparing the trends of the particle load to the particle count in steel samples, similarities can be seen [96].

To identify inclusions and distinguish between agglomerates and larger inclusions, sufficient resolution is, as previously mentioned, an absolute necessity. In Figure 45**Figure 45**, an enlarged agglomerate of three 2 to 4 µm large inclusions is shown, giving an insight into the difficulties of fully automating the particle acquisition.

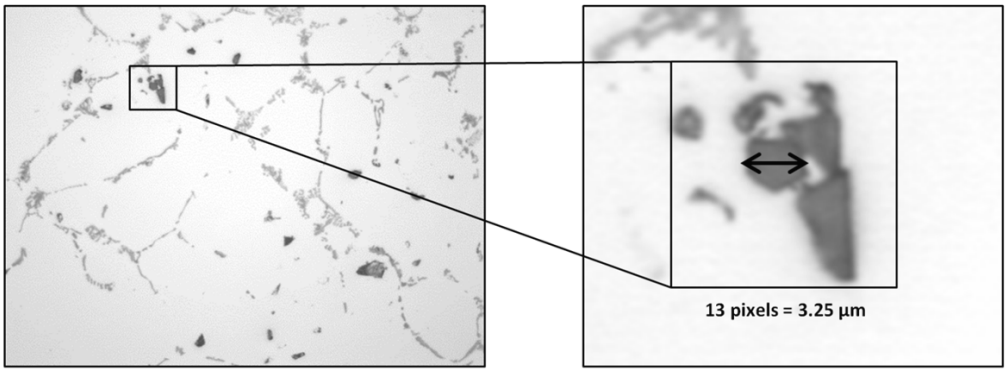

Figure 45: An original, unmodified image of metal before filtration. The surface was acquired with a 50 x optical magnification, a 10 x eyepiece and an aperture of 1, giving a 500 x magnification. The metal phase seen as white in the image, the eutectic phase as brighter grey, and the particles as brighter grey to dark grey, can at this stage only be identified by a very skilled person. The image on the right side shows an enlarged section of the main image on the left, reviling the existence of a cluster of particles that have agglomerated during the casting. The size of the particles was estimated by defining the length of one pixel to be 0.25 µm x 0.25 µm without any spherical correction.

It was in the present work also established that the image-processing method presented with *Supplement 7* and *8* (2. Macro) was less accurate when comparing the statistics than the image processing method presented with *Supplement 6* (1. Macro).

The first macro (1. Macro), from *Supplement 6*, was applied to a controlled environment of particles, and less images with higher resolution was used for the particle count. The second macro (2. Macro), presented in *Supplement 7 and 8*, was nevertheless more powerful. The environment was not controlled, and real industrial metal cleanliness samples were applied. The images were acquired on an automated moving stage with a camera using lower resolution (clearly more economic than manually enquiring of the images) smaller inclusions, *i.e.* inclusions down to 6 µm, were still successfully identified.

The method proposed allows for the identification of smaller inclusions/particles, pores etc., a new range of quantitative particle counting methods can be developed. The path of acquiring more images and therefore analysing larger areas per sample in less time was presently applied to grant statistical reliability, and to produce results that could be compared with currently applied industrial methods.

The further developed macro was more precise and could not only distinguish between phases and particles, but also between different particles by their individual shape. The results of both methods discussed in the present work are presented in Figure 46 from (a) to (d) showing the power of automated image processing and the development of the overall method over time. The results reported in the present work proves that the method of automated image acquisition and particle quantification is an analytical process that is efficient, gives reproducible results, and it is non-destructive in regards to collected samples.

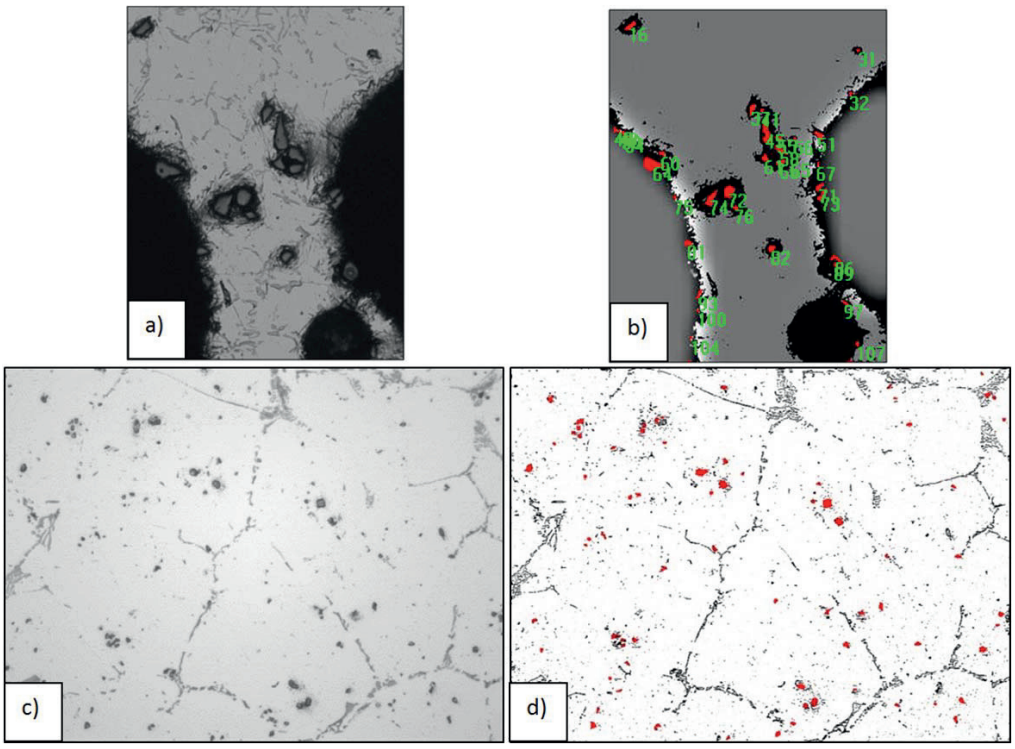

Figure 46: The different stages of the development of the macro. Image (a) and (b) shows the artificially added SiC particles with a size of 15-25 µm in spherical diameter. The image as acquired is shown in (a), and in (b) the particles identified by the macro is seen. Image (c) and (d) shows a natural contamination of small inclusions in the size range 1-8 µm of a regular industrial sample. The image as acquired is shown in (c) and after application of the macro in (d). As there were too many inclusions identified in (d), the numbers have been removed to avoiding confusion.

It should be mentioned that the resolution is not the only parameter to consider when working with image processing. Larger resolution alone would allow for mathematical methods and filters to distinguish between different levels of contrast, which require a uniform illumination and a non-reflective sample surface. The illumination, the wavelength of the used light, the surface reflections, vibrations, artefacts, and many other parameters can alter the efficiency of the image-processing steps. The metallographic preparation, surface lubrication, chemical reactions with lubrications and/or air, as well as the polishing time, can also alter the inclusion appearance and might remove inclusions prior the imaging step. Furthermore, the programming and automatic adjustment of the macros towards the different variables of

each set of images was also identified to be a challenging topic. The method applied for the imaging samples within this thesis had a minor number of variables that required adjustments prior processing of a set of images.

Due to the high potential of future applications being fully automated, the proposed image-processing method could be used in parallel to, and as fast as, the spark analysis equipment used for quality control in the aluminium industry today. The method could, in other words be an additional quick and cheap quality control method, requiring very limited investment. A modified version of the method could also be applied in other metal producing industries that has crucial cleanliness requirements.

Chapter 6

6. Overall Conclusions

The main goal of the present work was to achieve a 'proof of concept' in regards to realizing the theory, design, construction and validation of the EM priming technology on a full industrial scale filter. Its effect on high grade 23 inch CFFs was also to be evaluated while keeping the dictum to achieve priming on high-grade cold filters and on cold stacked filters without preheating. The method was successfully demonstrated by priming 3 cold stacked 50 PPI 23 inch industrial scale CFFs without preheating, as well as a stack of one 50 PPI and one 80 PPI 23 inch CFF .

6.1 Coil

Theoretical design equations for simple induction coils of various shapes have been developed and validated based on simple inductance and magnetic flux equations. A straight forward method has been designed for round, square, single or multi-layer induction coils, which is capable of generating a target magnetic flux density beginning with only the coil geometry.

When designing induction coils, it has been shown that the application of an equivalent round diameter to the theoretical calculations of square coil magnetic flux densities has been sufficiently accurate. Further, a method to design an induction coil to an existing/available power transformer, or to find the specifications of a new transformer that could generate a target average flux density for a given coil dimension relating the magnitude of B_z to the value of the inductance.

6.2 Priming

The regular industrial priming procedure for CFFs has traditionally only been supported by the effect of potential energy (the metal head), which induces a static pressure at the metal filter interface to overcome the surface tension of aluminium, and thus allows the filter to be primed. These priming systems require extensive preheating of the filters to avoid freezing of metal at the interface, and massive amounts of metal to prime the filters. After initial priming, it is known to be difficult to utilize unprimed filter sections during the whole cast, as the static head is reduces after priming and the pressure drop of the filter drops significantly in the regions were the filter is primed. The metal flow will than follow the path of the least resistance, *i.e.* lowest pressure drop, inducing higher interstitial velocity as less area is available. Overall this results in a decrease in filtration efficiency. This can explain the large variation of estimated filtration efficiencies for commercial CFF presented in Figure 39 by N. Keegan *et al.* [89].

The electromagnetic priming of CFF is, as previously mentioned, a novel method which uses a combination of forces:

- Static pressure,
- Dynamic velocity (dynamic pressure),
- Inductive heat (Joule heat),
- Electromotive forces (vibrations) and
- Lorentz forces (MHD).

The combination of these effects generates a robust system, allowing the EM priming system to prime:

- Commercial cold CFF,
- Stacked CFF (150 mm thick) up to 80 PPI grade, without preheating,
- High grade CFF, while reducing the traditionally required metal head,
- Round or square design of filters.

The system is assumed to work on DBF or BPF in the very same way as it does for the CFF.

6.3 Filtration

Increasing the available area for filtration by improved priming, exploiting larger filtration volumes by greater removal of gas from the inside of the filters, as well as improving filter wetting resulted in higher throughput and casting velocities without altering the filtration efficiency of the applied filter grade. This proved to allow for an optimized (similar) metal head for both priming and casting, implying the use of thicker filters.

To further increase the melt quality in regards to removing solid inclusions by filtration, the following possibilities have in detail been discussed:

- Application of finer, higher grade filters (filter grade).
- Using thicker filter sections (increased filtration length).
- Reducing filtration speed (interstitial velocity).

With the EM priming technology both higher grade filters and thicker filter sections have successfully been efficiently primed with the use of a low metal head. Higher filtration efficiencies for a given filter box installation was obtained. A theory to estimate the filtration efficiency has also been presented.

6.4 Automated Quantification

A powerful tool to analyze highly contaminated samples using minimal time and effort was developed. The method proved to be capable of:

- Non-destructive quantitative inclusion count.
- Distinguish between particles, pores and phases.
- Provides information on metal cleanliness and filtration efficiencies.

Chapter 7

7. Future Work

The collaboration with Pyrotek™ EMP®, Burton-on-Trent, UK, as the industrial partner during the upscaling and priming part of the present project, *i.e.* during the design, construction and testing of the 23" filter priming system using a 28.9'' square coil, secured the overall success of the project. The theory used to design the coil, as well as the outcome of the pilot tests performed on single to triple 23" CFFs, *i.e.* on typical industrial sized filters, has in detail been reported during the sequence of the project,. The 23'' filter priming system, named EMFP or EM Primer, is now in the last stages of commercialization.

The goal of the present project team is to continue the collaboration through upcoming PhD research projects focusing on further developing and initiating novel technology using the EM priming system as the fundamental basis. The following is in this regard of interest:

- The effect of EM fields on the contact and wetting angles of different alloys and surface materials using various frequencies and field strengths.
- Permeability testing to further validate and investigate the flow and priming characteristics of CFF systems.
- The use of FEM and CFD to estimate the MHD, as well as the fluid flow during priming and filtration, using COMSOL® Multiphysics.
- The use of FEM for design of complex 3D structures, such as induction coils of various shapes, will be generated and compared to observations made during use of the existing systems.
- Applications of the EM priming technology for traditional filtration systems such as the Bonded Particle Filter (BPF) or the Deep Bed Filter (DBF).

A stable and honest collaboration between different departments at NTNU, and the industrial partners from Pyrotek™ has been established. With this collaboration the development of novel filter priming systems, filter boxes and filter designs is planned. The continuation of the filtration system development, and the implementation of academic knowledge paired with industrial experience is the main goal of the existing and future collaboration.

It should be noted that the EM separation technology was first mentioned in regards to handling of gold and silver by E. Gates [97] in the 19th century. The theory was later applied by El. Kaddah [61] on liquid aluminium to separate non-conductive particles, and it was further developed by him [60]. El. Kaddah was honoured for his work by a separate Symposium at the 2015 TMS Conference in Nashville, US. The priming coil, discussed in the present work, could be modified for applications of EM separation within the CFF during the filtration stage. This is also a topic for an upcoming PhD student at NTNU.

The continuation of the metal imaging and image processing work presented are presently in the process of being fully implemented at the DMSE-NTNU, with support from Hydro Karmøy, Norway, and the following is in this regard of interest for further investigation:

- The programming and automatic adjustment of the macros towards the different variables of each set of images, as well as automation and automated variable adjustment for certain parameters.
- Automated image acquisition and stage control, as well as automated sample preparation.
- The effect of different surface preparation techniques and atmospheres on the reliability of the method.
- Application of *e.g.* frequency adjustable light sources to change the contrast ratios of the image sets to enhance the statistical reliability of the method.
- Implementation of modern programing software and algorithms to enhance the reliability of the method generating an independent and highly efficient imaging processing system using adjustable codes to process the acquired images.

It should be pointed out that to reach the above goals a multi disiplanery project should be enitiated with experts from different fields actively contributing to the outcome.

Chapter 8

A list of the references referred to in the present work.

8. References

[1] M. W. Kennedy, R. Fritzsch, S. Akhtar, J. A. Bakken, and R. E. Aune, "Apparatus and Method for Priming a Molten Metal Filter," U.S. Patent, WO 2013160754 A1, 2012.

[2] H. A. Wheeler, "Simple Inductance Formulas for Radio Coils," *Proceedings of the IRE,* vol. 16, pp. 1398-1400, 1928.

[3] H. A. Wheeler, "Inductance Formulas for Circular and Square Coils," *Proceedings of the IEEE,* vol. 70, pp. 1449-1450, 1982.

[4] K. Brondyke and P. Hess, "Filtering and Fluxing Processes for Aluminium Alloys," in *JOM-Journal of Metals*, pp. 119, 1964.

[5] R. Guthrie and M. Li, "In Situ detection of inclusions in liquid metals: Part II. Metallurgical applications of LiMCA systems," *Metallurgical and Materials Transactions B,* vol. 32, pp. 1081-1093, 2001.

[6] K. Turner, *Solid-Liquid Filtration and Separation Technology*. VCH: Weinheim, Germany: By A. Rushton, AS Ward, and RG Holdich, 1997.

[7] P. Netter and C. Conti, "Efficiency of Industrial Filters for Molten Metal Treatment: Evaluation of a Filtration Process Model," *Essential Readings in Light Metals: Cast Shop for Aluminum Production, Volume 3,* pp. 271-284, 1986.

[8] M. E. Schlesinger, *Aluminum recycling*: CRC Press, 2013.

[9] D. E. Groteke, "The Reduction of Inclusions in Aluminum by Filtration," *Modern Casting,* vol. 73, pp. 25-27, 1983.

[10] J. Martin, F. Tremblay, and G. Dube, "Alscan: A New and Simple Technique for In-line Analysis of Hydrogen in Aluminum Alloys," *Light Metals,* pp. 903-912, 1989.

[11] A. Pascual, "Emerging melt quality control solution technologies for aluminium melt," *China Foundry,* vol. 6, pp. 358-365, 2009.

[12] G. Le Roy, J. M. Chateau, and P. Charlier, "PDBF: Proven Filtration for High-End Applications," *Light Metals,* pp. 651-655, 2007.

[13] N. Keegan and S. Ray, "An evaluation of Industrial Filtration Systems," ed: Alcastek, 2002.

[14] L. Gauckler, M. Waeber, C. Conti, and M. Jacob-Duliere, "Ceramic foam for molten metal filtration," *JOM,* vol. 37, pp. 47-50, 1985.

[15] D. Neff and E. Stankiewicz, "The Mulicast Filtration System," *Light Metals,* pp. 821-828, 1986.

[16] R. Mutharasan, D. Apelian, and C. Romanowski, "A Laboratory Investigation of Aluminum Filtration Through Deep Bed and Ceramic Open-Pore Filters," *J. Metals,* vol. 33, pp. 12-17, 1981.

[17] S. Ray, B. Milligan, and N. Keegan, "Measurement of Filtration Performance, Filtration Theory and Practical Applications of Ceramic Foam Filters," 2005, pp. 1-12.

[18] L. S. Aubrey, C. L. Oliver, and B. T. MacPhail, "Dual stage ceramic foam filtration system and method," ed: Google Patents, 1997.

[19] R. Fritzsch, M. W. Kennedy, S. Akhtar, J. A. Bakken, and R. E. Aune, "Electromagnetically Modified Filtration of Liquid Aluminium with a Ceramic Foam Filter," *Journal of Iron and Steel Research, International,* pp. 72-76, 2012.

[20] M. W. Kennedy, S. Akhtar, J. A. Bakken, and R. E. Aune, "Effect of Electromagnetic Force on the Removal of Inclusions from Liquid Aluminum by a Ceramic Foam Filter in Continuous Filtration Tests," *Submitted to Metallurgical Transactions B,* 2011.

[21] R. Fritzsch, M. W. Kennedy, S. Akbarnejad, and R. E. Aune, "Effect of Electromagnetic Fields on the Priming of High Grade Ceramic Foam Filters (CFF) with Liquid Aluminum," *Light Metals,* pp. 929-935, 2015.
[22] E. Agastra and S. Selleri, "The Pavers of Maxwell's Pathway to His Equations [Historical Corner]," *Antennas and Propagation Magazine, IEEE,* vol. 56, pp. 308-316, 2014.
[23] J. C. Maxwell, *A treatise on electricity and magnetism* vol. 1: Clarendon press, 1881.
[24] A.-M. Ampère, *Mémoires sur l'électromagnétisme et l'électrodynamique*: Gauther-Villars et cie, 1921.
[25] D. Knight. (2010, August 25). *3.1. Solenoids: Part 1.*
[26] H. Nagaoka, "The Inductance Coefficients of Solenoids," *Journal of the College of Science,* vol. 27, pp. 18-33, 1909.
[27] R. Fritzsch, B. Mirzaei, M. W. Kennedy, and R. E. Aune, "Automated Quantification of SiC - Particles in Solidified A356 Aluminum Using Imagepro® Plus 7.0," *Characterization of Minerals, Metals, and Materials 2013,* pp. 67-77, 2013.
[28] R. Brandt and G. Neuer, "Electrical resistivity and thermal conductivity of pure aluminum and aluminum alloys up to and above the melting temperature," *International Journal of Thermophysics,* vol. 28, pp. 1429-1446, 2007.
[29] M. W. Kennedy, "Magnetic Fields and Induced Power in the Induction Heating of Aluminium Billets," Licentiate, Materials Science and Engineering, KTH, Stockholm, Sweden, 2012.
[30] M. W. Kennedy, "Removal of Inclusions from Liquid Aluminium using Electromagnetically Modified Filtration," PhD, Department ofMaterials Science and Engineering, NTNU, Trondheim, 2013.
[31] J. Vaughan and J. Williamson, "Design of Induction-Heating Coils for Cylindrical Nonmagnetic Loads," *American Institute of Electrical Engineers, Transactions of the,* vol. 64, pp. 587-592, 1945.
[32] H. Dwight and M. Bagai, "Calculations for coreless induction furnaces," *American Institute of Electrical Engineers, Transactions of the,* vol. 54, pp. 312-315, 1935.
[33] R. S. M. T. Committee and F. W. Olver, *Bessel functions*: Camb. UP, 1960.
[34] N. McLachlan, "Bessel Functions for Engineers. 1955," ed: Clarendon Press, Gloucestershire.
[35] K. Casio. (2016, 27.01.2016). *Bessel function calculator*.
[36] M. W. Kennedy, S. Akhtar, J. A. Bakken, and R. E. Aune, "Empirical Verification of a Short-Coil Correction Factor," *Industrial Electronics, IEEE Transactions on,* vol. 61, pp. 2573-2583, 2014.
[37] S. Akbarnejad, R. Fritzsch, M. W. Kennedy, and R. E. Aune, "An Investigation on Permeability of Ceramic Foam Filters (CFF)," presented at the Accepted to 2015 TMS Annual Meeting & Exhibition, 2015.
[38] M. W. Kennedy, K. Zhang, R. Fritzsch, S. Akhtar, J. A. Bakken, and R. E. Aune, "Characterization of Ceramic Foam Filters used for Liquid Metal Filtration," *Metallurgical and Materials Transactions B,* vol. 44, pp. 671-690, 2013.
[39] R. Baker, "Design and Calculation of Induction Heating Coils'," *AIEE Trans,* vol. 57, pp. 31-40, 1957.
[40] M. W. Kennedy, S. Akhtar, J. A. Bakken, and R. E. Aune, "Review of Classical Design Methods as Applied to Aluminum Billet Heating with Induction Coils," *TMS 2011, EPD Congress,* pp. 707-722, 2011.
[41] F. Acosta G, A. Castillejos E, J. Almanza R, and A. Flores V, "Analysis of liquid flow through ceramic porous media used for molten metal filtration," *Metallurgical and Materials Transactions B,* vol. 26, pp. 159-171, 1995.
[42] P. Sandford and S. Sibley, "Optimization of Al Casting Productivity Using Foam Filter Technology and Application (96-157)," *Transactions of the American Foundrymen's Society,* vol. 104, pp. 1063-1068, 1996.

[43] K. Zhang, "Liquid Permeability of Ceramic Foam Filters," Master of Science, Department of Materials Science and Engineering Norwegian University of Science and Technology, Trondheim, Norway, 2012.
[44] K. Butcher and D. Rogers, "Update on the Filtration of Aluminum Alloys with Fine Pore Ceramic Foam," pp. 797-803, 1990.
[45] J. E. Dore and C. Bickert, "A Practical Guide on How to Optimize Ceramic Foam Filter Performance," *Light Metals,* pp. 791-796, 1990.
[46] N. Keegan, W. Schneider, and H. Krug, "Evaluation of the Efficiency of Fine Pore Ceramic Foam Filters," *Light Metals,* pp. 1031-1041, 1999.
[47] R. Fritzsch, "Filtration of Aluminium Melts using Ceramic Foam Filters (CCF) and Electromagnetic Field," Masters, Department of Materials Science and Engineering, NTNU, Trondheim, 2011.
[48] Pyrotek, "840 - Filtration Solutions."
[49] J. Champion, B. Keene, and J. Sillwood, "Wetting of Aluminium Oxide by Molten Aluminium and other Metals," *Journal of Materials Science,* vol. 4, pp. 39-49, 1969.
[50] S. Bao, "Filtration of Aluminium - Experiments, Wetting, and Modelling," PhD., Materials Science and Engineering, NTNU, 2011.
[51] S. Ip, M. Kucharski, and J. Toguri, "Wetting Behaviour of Aluminium and Aluminium Alloys on Al2O3 and CaO," *Journal of Materials Science Letters,* vol. 12, pp. 1699-1702, 1993.
[52] F. Frisvold, "Filtration of aluminium: theory, mechanisms, and experiments," Norwegian University of Science and Technology, 1990.
[53] H. Görner, "Removal of dissolved elementsin aluminium by filtration," Norwegian University of Science and Technology, 2009.
[54] C. Vives, "Electromagnetic refining of aluminum alloys by the CREM process: Part II. Specific practical problems and their solutions," *Metallurgical Transactions B,* vol. 20, pp. 631-643, 1989.
[55] C. Vives, "Electromagnetic Refining of Aluminum Alloys by the CREM Process: Part I. Working Principle and Metallurgical Results," *Metallurgical Transactions B,* vol. 20, pp. 623-629, 1989.
[56] K. E. Blazek, W. F. Praeg, J. G. Rachford, and Y. H. Wang, "Electromagnetic Meniscus Control in Continuous Casting," ed: Google Patents, 1999.
[57] M. Garnier, "Electromagnetic Processing of Liquid Materials in Europe," *ISIJ International,* vol. 30, pp. 1-7, 1990.
[58] J. Dong, Z. Zhao, J. Cui, F. Yu, and C. Ban, "Effect of Low-Frequency Electromagnetic Casting on the Castability, Microstructure, and Tensile Properties of Direct-Chill Cast Al-Zn-Mg-Cu Alloy," *Metallurgical and Materials Transactions A,* vol. 35, pp. 2487-2494, 2004.
[59] C. Vives, "Effects of Electromagnetic Vibrations on the Microstructure of Continuously Cast Aluminium Alloys," *Materials Science and Engineering: A,* vol. 173, pp. 169-172, 1993.
[60] N. El-Kaddah, A. Patel, and T. Natarajan, "The Electromagnetic Filtration of Molten Aluminum using an Induced-Current Separator," *JOM,* vol. 47, pp. 46-46, 1995.
[61] N. El-Kaddah, "Apparatus and a method for improved filtration of inclusions from molten metal," ed: Google Patents, 1990.
[62] T. Natarajan and N. El-Kaddah, "A new method for three-dimensional numerical simulation of electromagnetic and fluid-flow phenomena in electromagnetic separation of inclusions from liquid metal," *Metallurgical and Materials Transactions B,* vol. 33, pp. 775-785, 2002.
[63] B. Q. Li and J. W. Evans, "Computation of Shapes of Electromagnetically Supported Menisci in Electromagnetic Casters. I. Calculations in Two Dimensions," *Magnetics, IEEE Transactions on,* vol. 25, pp. 4443-4448, 1989.
[64] M. Carter and T. Steinke, "Process and System for Pumping Molten Metal," ed: Google Patents, 1973.
[65] R. M. Del Vecchio and R. M. Slepian, "Liquid Metal Electromagnetic Flow Control Device Incorporating a Pumping Action," ed: Google Patents, 1989.

[66] E. Baake, A. Umbrashko, B. Nacke, A. Jakovics, and A. Bojarevics, "Experimental investigations and LES modelling of the turbulent melt flow and temperature distribution in the cold crucible induction furnace," 2003, pp. 214–219.
[67] E. F. Northrup, "Method and Apparatus for Electric Heating by High-Frequency Currents," ed: Google Patents, 1918.
[68] O. Lucia, P. Maussion, E. J. Dede, and J. M. Burdio, "Induction Heating Technology and its Applications: Past Developments, Current Technology, and Future Challenges," *Industrial Electronics, IEEE Transactions on,* vol. 61, pp. 2509-2520, 2014.
[69] M. J. Assael, K. Kakosimos, R. M. Banish, J. Brillo, I. Egry, R. Brooks*, et al.*, "Reference data for the density and viscosity of liquid aluminum and liquid iron," *Journal of physical and chemical reference data,* vol. 35, p. 285, 2006.
[70] R. Roscoe, "The viscosity of suspensions of rigid spheres," *British Journal of Applied Physics,* vol. 3, p. 267, 1952.
[71] E. Moreira, M. Innocentini, and J. Coury, "Permeability of ceramic foams to compressible and incompressible flow," *Journal of the European Ceramic Society,* vol. 24, pp. 3209-3218, 2004.
[72] B. Hübschen, J. Krüger, J. Keegan, and W. Schneider, "A new approach for the investigation of the fluid flow in ceramic foam filters," *Light Metals,* pp. 809–815, 2000.
[73] P. Forchheimer, "Wasserbewegung durch boden," *Z. Ver. Deutsch. Ing,* vol. 45, p. 1788, 1901.
[74] S. Ergun and A. A. Orning, "Fluid flow through randomly packed columns and fluidized beds," *Industrial & Engineering Chemistry,* vol. 41, pp. 1179-1184, 1949.
[75] I. Macdonald, M. El-Sayed, K. Mow, and F. Dullien, "Flow through porous media-the Ergun equation revisited," *Industrial & Engineering Chemistry Fundamentals,* vol. 18, pp. 199-208, 1979.
[76] K. E. Noll and M. J. Pilat, "Inertial Impaction of Particles upon Rectangular Bodies," *Journal of Colloid and Interface Science,* vol. 33, pp. 197-207, 1970.
[77] L. Damoah and L. Zhang, "Removal of Inclusions from Aluminum Through Filtration," *Metallurgical and Materials Transactions B,* pp. 1-22, 2010.
[78] B. Friedrich, C. Kräutlein, and K. Krone, "Melt treatment of Copper and Aluminium–The complex step before casting," *Proceedings of The International Conference on Continous Casting of Non-Ferrous Metals, Wiley-Vch, DGM,* pp. 3-22, 2006.
[79] B. D. S. D. Shu, J. Wang, T.X. Li, Y. H. Zhou, "Study of Electromagnetic seperation of Nonmetallic Inclusions rom Aluminium Melt," 1999.
[80] D. Apelian and R. Mutharasan, "Filtration: A Melt Refining Method," *JOM,* vol. 32, pp. 14-19, 1980.
[81] M. W. Kennedy, S. Akhtar, J. A. Bakken, and R. E. Aune, "Analytical and Experimental Validation of Electromagnetic Simulations Using COMSOL®, re Inductance, Induction Heating and Magnetic Fields," presented at the COMSOL Users Conference, Stuttgart Germany, 2011.
[82] T. Natarajan and N. El-Kaddah, "A methodology for two-dimensional finite element analysis of electromagnetically driven flow in induction stirring systems," *IEEE Transactions on Magnetics,* vol. 35, pp. 1773-1776, 1999.
[83] K. Zhang, "Liquid Permeability of Ceramic Foam Filters," 2012.
[84] B. Dietrich, "Pressure drop correlation for ceramic and metal sponges," *Chemical Engineering Science,* vol. 74, pp. 192-199, 2012.
[85] B. Dietrich, W. Schabel, M. Kind, and H. Martin, "Pressure drop measurements of ceramic sponges—Determining the hydraulic diameter," *Chemical Engineering Science,* vol. 64, pp. 3633-3640, 2009.
[86] M. D. M. Innocentini, L. Lefebvre, R. Meloni, and E. Baril, "Influence of sample thickness and measurement set-up on the experimental evaluation of permeability of metallic foams," *Journal of Porous Materials,* vol. 17, pp. 491-499, 2010.

[87] M. W. Kennedy, K. Zhang, R. Fritzsch, S. Akhtar, J. A. Bakken, and R. E. Aune, "Characterization of Ceramic Foam Filters used for Liquid Metal Filtration," *To be submitted to Metallurgical Transactions B,* 2012.
[88] R. Fritzsch, M. W. Kennedy, J. A. Bakken, and R. E. Aune, "Electromagnetic Priming of Ceramic Foam Filters (CFF) for Liquid Aluminum Filtration," *Light Metals 2013,* pp. 973-979, 2013.
[89] N. J. Keegan and S. F. Ray, "An evaluation of Industrial Filtration Systems," ed: Alcastek, 2002.
[90] T. Engh, B. Rasch, E. Bathen, and R. Miller, "Deep Bed Filtration Theory Compared with Experiments," *Light Metals,* pp. 829-836, 1986.
[91] F. Acosta G and A. Castillejos E, "A mathematical model of aluminum depth filtration with ceramic foam filters: Part II. Application to long-term filtration," *Metallurgical and Materials Transactions B,* vol. 31, pp. 503-514, 2000.
[92] H. Duval, C. Rivière, É. Laé, P. Le Brun, and J. Guillot, "Pilot-Scale Investigation of Liquid Aluminum Filtration through Ceramic Foam Filters: Comparison between Coulter Counter Measurements and Metallographic Analysis of Spent Filters," *Metallurgical and Materials Transactions B,* vol. 40, pp. 233-246, 2009.
[93] B. Prillhofer and H. Antrekowitsch, "Abscheidung von nichtmetallischen Einschlüssen bei der Raffination von Aluminiumlegierungen," *BHM Berg-und Hüttenmännische Monatshefte,* vol. 152, pp. 53-61, 2007.
[94] I. Bankman, *Handbook of medical image processing and analysis*: academic press, 2008.
[95] F. Weinhaus. (2014, 04.05.). *Digital Image Filtering*. Available: http://www.fmwconcepts.com
[96] J. Gegner, "2D-3D conversion of object size distributions in quantitative metallography," in *Proceedings of the MMT-2006 conference*, 2006, p. 3.
[97] E. Gates, "Diamagnetic separation," ed: Google Patents, 1900.

References

9. Supplements

Part I: Design of Induction Coils

Supplement 1

Design of Square Induction Coils for the Electromagnetic Priming of Ceramic Foam Filters

Robert Fritzsch, Mark William Kennedy and Ragnhild E. Aune

Light Metals 2016, page 777-784

DOI: 10.1002/9781119274780.ch132,

Design of Square Induction Coils for the Electromagnetic Priming of Ceramic Foam Filters

Robert Fritzsch[1], Mark William Kennedy[1] and Ragnhild E. Aune[1]

[1]Department of Materials Science and Engineering, Norwegian University of Science and Technology, N-7491 Trondheim, Norway.

Keywords: Induction, Coil, Aluminum, Ceramic Foam Filters, Priming

Abstract

Ceramic Foam Filter (CFF) ElectroMagnetic (EM) priming systems with square-shaped solenoidal coils are in the process of full-scale industrialization. The demands on the EM fields used in such a system are substantially different from the requirements in the existing EM pumping systems used for liquid metals. The same fundamental physics are applied, *i.e.* Lorentz forces induced by time varying EM fields; however, in the present case the forces are used to overcome the metal surface energy and force metal into the cold air filled pores of the CFF instead of producing bulk metal movement.

The present study discusses the design methodology for square shaped solenoidal coils applied to EM priming using a combination of analytical models, experimental measurements and Finite Element Modeling (FEM) with COMSOL® Multiphysics. The EM force field at different induction coil designs (4 [10.16] and 9 [22.86] inches [cm]) is estimated using FEM and validated against experimental results.

Introduction

The impact of the EM field generated by different induction coils inducing electromotive forces in liquid aluminum has been investigated in earlier publications by the present authors [1, 2], and is also the topic of this study. A reduction of the required metal head to successfully prime commercial filters has been discovered, and is now the subject of an international patent application [3]. The observed effect on the required metal height is shown in

Figure .

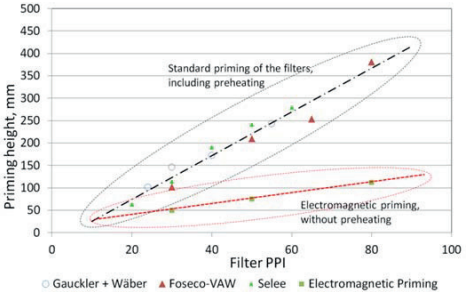

Figure **1**: Priming height versus filter pores per inch (ppi) for filters from different producers [4-6] compared to earlier electromagnetic priming trials using different 4" round filters and a flux density of 0.2 T [1, 7].

The focus of the present paper is on the induction coil itself, the priming of 3 stacked filters and how the shape of the magnetic field alters the priming of the most commonly applied physical filtration system, i.e. Ceramic Foam Filters (CFF) [8]. The applied frequency was 50 Hz and the variable field strength was obtained by the application of alternating currents of up to 1250 A RMS maximum. The main goal of the present study has been to compare the behavior of square and round double coils, validating the use of a 9'' (inch) square double coil for industrial trials.

Theory

To design an induction coil with a required magnetic flux density B_z, the inductance L can be applied as a useful parameter. The inductance L is defined as the flux linkages per unit current and is directly related to the magnetic flux density B_z, the area of the coil A and the applied current I, as shown in (Eq. 1):

$$L = \frac{N\Phi}{I} = \frac{B_z N A}{I} \quad (1)$$

where L is the inductance [H], Φ the total flux [Wb], I the current [A], N the number of turns [unitless], A the total area of the cross section of the induction coil [m^2] and B_z the magnetic flux density in the z-direction [T]. Only the z-component of the magnetic flux needs to be considered for symmetrical induction coils, as the sum of the r-components is zero after integration around the periphery. The computation of area A varies with geometry, *e.g.* round vs. square, which has a directly proportional effect on the inductance L. A good correlation between different coil shapes and the diameter can be obtained by using the equivalent diameter for the area A of the considered coil shape.

It is possible to calculate the exact inductance L for theoretical 'current sheet' cylindrical induction coils using the equation of Lorenz from 1879 [9]. This equation involves the solution of the double elliptical integrals *K(k)* and *E(k)* of the first and second kinds:

$$L_{Lorenz} = \mu_r \mu_0 \frac{8N^2 r^3}{3l_c^2}\left[\left(\frac{2k^2-1}{k^3}\right)E(k) + \left(\frac{1-k^2}{k^3}\right)K(k) - 1\right],$$

$$k = \sqrt{\frac{4r^2}{4r^2+l_c^2}} \quad (2)$$

Lorenz's equation was reformulated by Nagaoka in 1908 [10], as shown in Eq. (3), using a short coil correction factor K which he tabulated to 6 decimals. The short coil

correction factor K is dimensionless and varies between 1 and 0 with an increasing coil diameter to length ratio.

$$L_1 = K\frac{\mu_0\mu_r\pi N^2 r^2}{l_c} \quad (3)$$

where l_c is the length of the coil [m], $\mu_0 = 4\pi * 10^{-7}$ the permeability of free space [H/m], $\mu_r = 1$ the relative magnetic permeability for air [unitless], and K the short coil correction factor or Nagaoka coefficient [unitless], which considers accounting for the geometry of the coil.

In 1928 Wheeler presented an empirical formula for the inductance of a single layer short coil [11]. Wheeler's equation was subsequently reformulated by Knight [12] to estimate Nagaoka's short coil correction factor K to approximately 3 decimal precision for coils of 'typical' induction coil dimensions:

$$K = \frac{1}{1+0.4502\left(\frac{D_c+\delta_c}{l_c}\right)} \quad (4)$$

where D_c is the inner diameter of the coil conductors, and δ_c the electromagnetic penetration depth into the coil defined as:

$$\delta_c = \sqrt{\frac{2\rho}{\omega\mu_o\mu_r}} = \sqrt{\frac{\rho}{\pi f\mu_o\mu_r}} \quad (5)$$

where ρ is the resistivity of the copper conductor (1.7241 x 10^{-8} Ω·m for 100% IACS copper [13]), and f the frequency [Hz].

The magnetic field of a single layer induction coil can be found by equating Eq. (1) and Eq. (3) and substituting Eq. (4):

$$B_z = \frac{1}{1+0.4502\left(\frac{D_c+\delta_c}{l_c}\right)}\frac{\mu_0\mu_r NI}{l_c} \quad (6)$$

In 1982 Wheeler published a letter [14] where he presented new and more accurate empirical equations designed for use with both square and round single layer coils:

$$L_2 = \mu_0 N^2 r\left(\frac{4}{\pi}\right)\left(\ln\left(1+\frac{\pi r}{l_c}\right)+\frac{31.496}{3.64+2\frac{l_c}{r}+0.51\left(\frac{l_c}{r}\right)^2}\right) \quad (7)$$

where L_2 is the inductance of a single layer coil [μH], N the number of turns, r the radius measured on the wire centerline [m], and l_c the length measured top to bottom of the coil.

Eq. (2) through Eq. (6) can be used to estimate the average z-component of magnetic fields of single layer coils with good precision. The equations can, however, not be applied with precision to multi-layer coils. For multi-layer coils the magnetic flux density in the z-direction B_z can be found by first estimating or measuring the inductance L (where the coil already physically exists), and then applying Eq. (1). Another empirical equation of Wheeler [11] can be used to estimate the inductance L for a multi-layer coil, with good precision, prior to constructing the coil. The equation in question has been transformed from imperial to SI units with dimensions in [m] as follows:

$$L_3 = \frac{31.496\, r^2N^2}{6r+9l_c+10c} \quad (8)$$

where L_3 is the inductance of a multi-layer coil [μH], N the number of turns, r the average radius [m], l_c the length measured from the top to the bottom of the coil, and c the thickness of the coil [m] as shown in Figure 2.

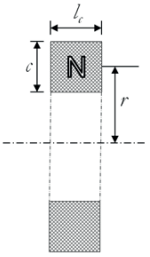

Figure 2: Model of a multi-layer induction coil with N turns, radius r, length $\mathbf{l_c}$, and thickness c. [11]

To prime a CFF with a conducting liquid metal, such as aluminum, a physical force in the form of the metallostatic pressure, has to be overcome. Earlier studies indicated that the Lorentz forces, induced by the electromagnetic flux density B_z, can help to prime non-preheated CFFs [2, 3, 7, 15]. In this case the Lorentz forces act as a driving force, as the axial variation of the magnetic field of real induction coils generates a curl [16], and thus produces electromagnetic or Magneto-Hydro-Dynamic (MHD) mixing. This mixing effect is well known and is discussed in several studies related to metal cleaning [17, 18].

The Lorentz forces F_L [N/m^3] are proportional to the square of the magnetic flux density B_z [19], and can be calculated as the cross product of the induced current density and the magnetic flux, e.g. from Eq. (6):

$$F_L = J \times B_z \quad (9)$$

where J is the induced current density [A/m^2].

The priming of the filters is induced by the EM flux and the curl in the Lorentz forces as shown Figure 3.

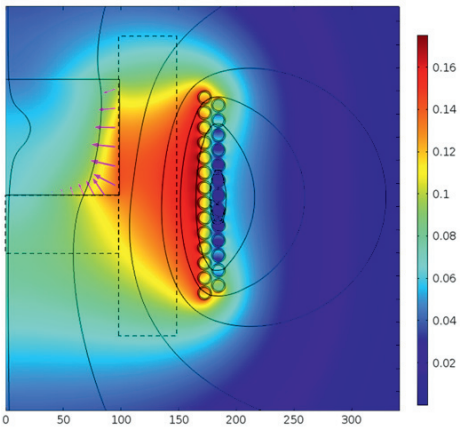

Figure 3: Real 9'' coil geometry, showing an axisymmetric COMSOL® 5.0 simulation of the magnetic flux density [T]. The

arrows represent the relative magnitude of the time averaged Lorentz forces inside the liquid metal above the filter prior to priming (shown as a black box). The dotted lines represent the Monalite® crucible and the filter element below the metal.

The design equations described in the present theory section are only applicable to an empty 'air-core' coil, *i.e.* a coil prior to priming. After priming, the space over, under and within the CFF's are filled with metal. This metal alters both the electrical resistance and the reactance of the system in a complicated way described elsewhere [20]. In practical terms the reduction of reactive impedance is greater than the increase in effective coil resistance, and for a fixed applied voltage the current and magnetic flux density increase as the CFFs become primed. Hence, the air-core case represents a minimum and therefore a reasonable design case.

Experimental

Experimental data were collected using two different round coils, *i.e.* a short single coil and a short double coil, shown in Figure 4 a) and b). In addition two square 9'' short coils were used, *i.e.* one single coil and one double coil, shown in Figure 5 a) and b) respectively.

The 4'' round coils, shown in Figure 4, have been designed to allow for approx. 1 kA at maximal cooling rates. The highest estimated magnetic flux densities vary from coil to coil and are in the center of coil a) ~0.13 and b) ~0.23. The multi-layer coils were connected by a jumper (the 'hoop' rising up in the picture), which allowed the current to flow between the two coils in series without disturbing the magnetic field inside the coil, as shown in Figure 4 b). Cooling water was provided in parallel, while current flowed in series.

The 9'' coil, as shown in Figure 5, was designed to allow for 2 kA, generating an estimated magnetic field of 0.2 T in the center of the coil. The inner coil prior to being insulated is shown in Figure 5 a) and after coupling both coils to create one double coil in Figure 5 b). The coils were connected by a jumper, visible in Figure 5 b). The square shape of the coil generated strong electromagnetic curls in the Lorentz forces at the corners of the coil, as well as strong 100 Hz electro-mechanical vibrations due to the 50 Hz alternating current (passing through zero twice each cycle). This required powerful restraints to maintain the physical stability of the coil, as indicated in the photograph shown in Figure 5 b).

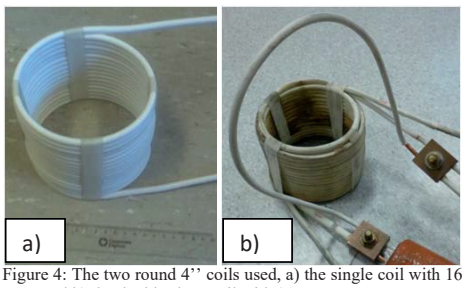

Figure 4: The two round 4'' coils used, a) the single coil with 16 turns and b) the double short coil with 31 turns.

The liquid metal priming (Al alloy 3003) trial casting temperature was aimed to be 700°C. No pre-heating was applied to the 3 stacked 50 ppi CFF, and they remained at room temperature until contact with the liquid metal. The coil was electrified with 1250 A generating an EM flux of 0.12 T (empty coil) as the metal was poured into the crucible. In total, a metal head of approx. 100 mm was poured into the crucible and a meniscus was formed instantaneously, as observed and discussed during earlier trials [2].

Two different experimental power supplies have been used, *i.e.* a step down transformer (45 kW, 230/30 V, 196/1500 A) for the small round coils, and two adjustable welding transformers (each 80 kW, 44/89 V, 500/1800 A), wired in parallel for the 9'' coils. The measurements for the magnetic fields were executed using a Hall Effect gauss meter model 6010 supplied by Pacific Scientific OECO, F.W. Bell®. The axial probe was standardized using an axial standard of 0.05 T ± 0.3 mT. The coil current was measured using a Fluke® inductive current probe i1000S with a resolution of 1 ampere and ±1% precision. The real (W) and reactive (VAR) power were measured using a Fluke® 43B Power Quality Analyzer with a resolution of 100 W. The experimentally derived coil inductances could then be calculated using the measured reactive power. The resulting experimental data were used to validate the FEM simulation results without 'fitting'.

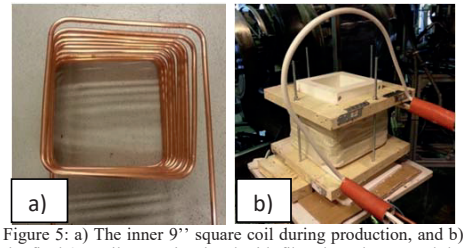

Figure 5: a) The inner 9'' square coil during production, and b) the final 9'' coil setup, insulated with fiberglass sleeves and the Monalite® crucible for liquid metal experiments. The coupling between the coils, by using a jumper, can be seen in b).

Results and Discussion

The validation of the present method to design simple induction coils of various shapes can be accomplished by comparison of the predicted analytical results of the modeled flux densities with the measured flux densities and by comparison of the calculated inductance and measured inductance. In the present study magnetic flux density of the designed coils was first estimated, then calculated by application of the software COMSOL® 5, and finally compared to experimental measurements of real coils. The data from the inductance measurements and the results of the priming trials are presented in Table I. Liquid metal priming of 3 stacked 50 ppi CFF filters, installed within the 9'' setup, was successfully conducted, as shown in Figure 6.

The round coils were built and tested by electromagnetic priming of liquid aluminum with CFFs, and the effect of the EM flux density (induced by the coils designed to generate the strongest EM flux) was shown in earlier investigations by the present authors for 4'' [7] and 9'' systems [2].

Table I: Summary of the experimental coil dimensions, measured and theoretical inductance and flux density values. All inductance estimates are for a frequency of 50 Hz.

			4'' (10.16 cm) coil		9'' (22.86 cm) coil	
			Single short	Double short	Single	Double
			Round		Square	
	Unit	Abr.	1	2	3	4
Inner Dia. Coil	[mm]	r	63	66	169,5	172,5
Total Height	[mm]	l_c	111	111	182	182
Coil Thickness	[mm]	c	6,5	14	13	26
Turns		N	16	31	14	27
Short coil cor.		K	0,660	0,650	0,543	0,538
Example			At 956 A	At 1 kA	at 1,250 kA	
Measured	[µH]	L	27,6	104	58	240
Lorenz (Eq.3)	[µH]	L_1	25,4	96,1	66,2	254
Single Coil (Eq.6)	[µH]	L_2	24,8	94,1	66,4	255
Multilayer (Eq.8)	[µH]	L_3	23,6	85,3	63,6	233
Calc. Flux D.	[T]	B_z	0,123	0,228	0,066	0,125
Meas. Flux D.	[T]		0,121	0,23	0,062	0,127

In the present experimental results the electromagnetic field, induced by a double square coil, was able to prime a stack of 3 cold 9'' 50 ppi CFF after a total of four minutes (see Table II). During the required 4 minutes, the EM field induced both MHD mixing within the liquid metal and heating. Solidification and freezing at the filter metal interface was avoided as the heat of the metal preheated the filter.

Table II: Summary of the events during the priming of the stacked filters.

Time	Comment
~60 seconds after pouring on the filter	Metal level dropped by approx. 50 mm; metal was refilled to a head of 100 mm.
~90 seconds after second filling	Metal level dropped another 50 mm; metal was refilled to a head of 100 mm.
~30 seconds after the 3third filling	The metal level dropped rapidly. Remaining metal was poured into the Monalite® crucible keeping the level above the filter.

The metal primed the stack of filters in three stages, *i.e.* each individual filter in sequence. The required times together with the observations are shown in Table II. A total of four minutes was required to prime three stacked cold 50 ppi CFFs, after which the coil was switched off.

After the filter reached the required temperature, the metal can penetrate into the filter, *i.e.* when the initial solidified aluminum 'skin' had been melted. The electrical conductivity of solid aluminum is approx. 2.5 times larger than for liquid aluminum at the same temperature. This focuses the induced current into any frozen metal inducing preferential heating. This induced heat, together with heat convected from the liquid metal due to MHD, rapidly melts any solidified material and avoids permanent blockage of the filter. The actual priming is accomplished by the velocity head created by the bulk MHD flow induced by the Lorentz forces, driving the metal into the filter. The curl of the magnetic field within the filter continues to generate MHD after the initial phase of priming, and assists in the removal of trapped gases. Mechanical vibrations generated by the alternating current are believed to produce the excellent wetting, which has been observed between the CFF and the metal. The change of the direction of the current produces a 'zero' point in the Lorentz forces twice in each cycle (*e.g.* 2x50 Hz), inducing mechanical vibrations in the liquid metal. The direction of the Lorentz force remains constant regardless of the current polarity, as both the magnetic field and the current reverse directions together. The final result of priming is shown in Figure 6 b) and c).

The 3D model designed with COMSOL® 5 gives an estimation of the resulting magnetic flux density of a square coil, but more computational resources and time is required to design a proper model. The advantages of such a 3D model are given by the possibility to visualize the corner effects, which can't be estimated by the axisymmetric models. However, one of the main disadvantages of 3D modeling is that the resolution of the mesh is typically reduced due to lack of computer memory. This is a particularly significant issue when applying high frequencies [21]. The total error obtained for the axisymmetric model is 2.65 % and for the 3D model showing minimal overall improvement 2.25 %. The presently obtained results are plotted together with an estimated flux density, shown as a black dotted line, in Figure 8. The calculations are based on the application of the empirical approach of Wheeler using the inductance L_3, from Eq. (8) and Eq. (6) to calculate B_z.

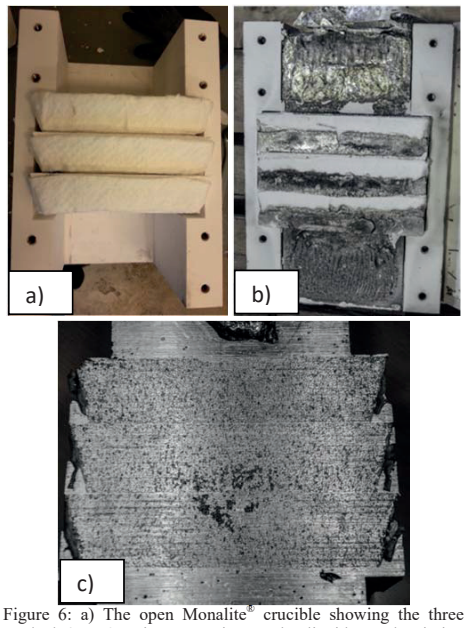

Figure 6: a) The open Monalite® crucible showing the three stacked 9'' 50 ppi CFFs prior to the liquid metal priming experiments. b) After the liquid metal priming experiment the completely filled filters with metal above and below are shown. The sealing, visible as the white foam around each filter, has worked properly and bypassing of metal has been prevented. c) A cut through the center of the sample reveals fully priming of the three stacked 50 ppi CFF. The total filter thickness was

150 mm. No ceramic filter surfaces are visible, affirming the total priming of the filter.

The coil geometry and the resulting magnetic flux density of the 9" (22.86 cm) square coil and the round coil is visualized in Figure 7 a) and b) respectively. The Figures 7 a) and b) were visualized by applying COMSOL® 5 using a 3D model of the square and round geometries.

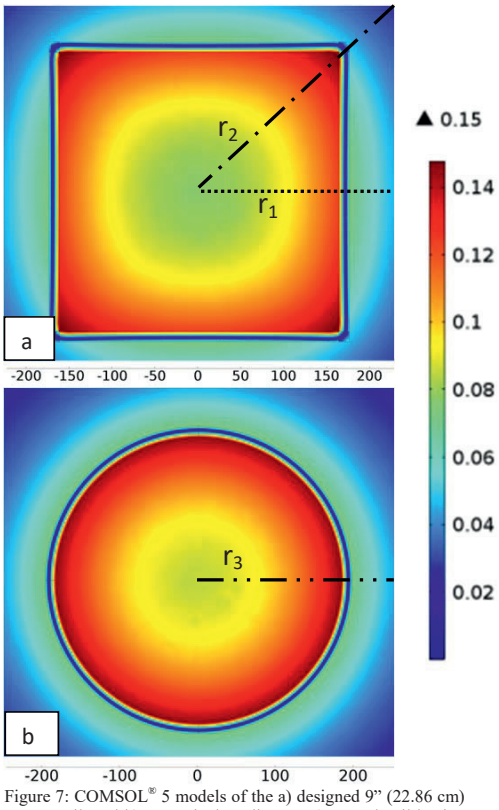

Figure 7: COMSOL® 5 models of the a) designed 9" (22.86 cm) square coil, and b) an equivalent diameter 9" round coil having the same total area. Both models have been meshed suitable for low frequency (spacing of less than δ_c). The applied current is equal to the measured current during the real experiments, *i.e.* 1250 A RMS. The maximal magnetic flux density is calculated to be 0.144 T in both models. The dashed lines show the different radiis r_1, r_2 and r_3 where measurements have been taken.

The COMSOL® 5 calculations and the measured data of the flux density are compared in Figure 8. As can be seen from the figure, the calculated values of the 9'' square 3D model at the centerline r_1, the diagonal r_2, and the 9'' round 3D model at r_3 are plotted together with the measured data from square coil no. 4 along the diagonal and along the centerline. The round coil 3D model with the equivalent diameter of the square coil gives the lowest flux density, whereas the square on the perpendicular 'centerline' gives the highest values. The real measurements fall in between these two sets of values.

The geometry has proven to have a strong effect on the resulting magnetic field. In the 3D model, the variation in the flux density, as a result of the coil shape, can be seen along the diagonal, whereas the 2D axisymmetric solution cannot provide this information. Hence, 3D modelling was necessary to understand the corner effects, and provide an accurate estimate of the flux density in this area. The comparisons of the measurements and the calculations from the 3D-model are also shown in Figure 8.

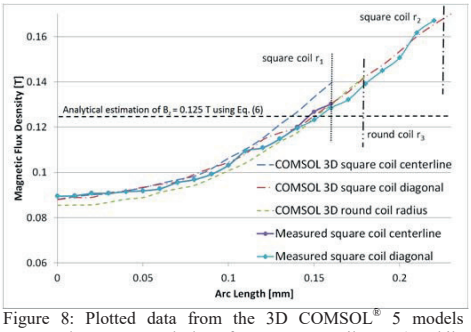

Figure 8: Plotted data from the 3D COMSOL® 5 models compared to measured data from square coil no. 4, while applying 1250 A. The measurements were taken every 10 mm from the center to the side, where the square coil has a short 'radius', shown as r_1 (measured perpendicular to the sidewall), and a long diagonal side, shown as r_2. The radius of the equivalent round coil is shown as r_3.

Conclusions

A simple method was shown capable of designing round, square, single and multi-layer solenoidal coils capable of generating a target magnetic flux density. The method allows the fitting of an induction coil to the limits of the available power transformer, and/or the specification of a new transformer, to achieve a target average flux density for a given coil dimension. Modern FEM software, such as Comsol® 5, allows the solution of simple, fast and accurate 2D axisymmetric models for round and symmetric coils. It also allows the design of 3D models, which can deliver a greater spatial resolution of the physics for any required coil geometry. The presently generated analytical solutions give the smallest error, whereas the FEM allows for the visualization of the resulting fields. These fields have been compared to high precision manual measurements of real coils.

The priming of a stack of three commercial 9'' 50 ppi CFF by liquid aluminum (3003 alloy), *i.e.* a 150 mm thick filter or 300% of the normally applied thickness of a 50 mm filter has been demonstrated by application of electromagnetic fields (0.12T) while only using 50% of the normal industrially applied metal head [4, 5].

Investigation of the metal samples after the experimental trial showed excellent results regarding priming and wetting of the filters at all levels. Metal was observed in all regions of the filter setup, and the alumina wool around each filter was not wetted by aluminum excluding bypassing. The EM field forces the metal towards the corners of each filter, ensuring the complete priming of the total filter area.

Future Work

The 9” square coils designed with the present theory will be up-scaled for the priming of 23” and 26’’ commercial CFF systems using induction coils. The future trials will also include fine filters, up to 80 ppi CFF, and from 50 to 150 mm thickness. These experiments are in the process of being executed in collaboration with an industrial partner.

Acknowledgement

The authors also wish to express their gratitude to Nigel Clear from Pyrotek® EMP™ Technologies and Dr. Neil Keegan from Pyrotek® Metallurgical Services Group, Kurt Sandaunet and Roar Jensen from SINTEF Materials and Chemistry, Shahid Akhtar from Hydro Aluminium in Karmøy and Trygve Schaunche from NTNU for their support, good discussions and help and to thank the Institute for Material Technology (IMT) at NTNU, Trondheim in Norway for using the casting laboratory equipment.

References

[1] R. Fritzsch, M. W. Kennedy, S. Akhtar, J. A. Bakken, and R. E. Aune, "Electromagnetically Modified Filtration of Liquid Aluminium with a Ceramic Foam Filter," Journal of Iron and Steel Research, International, pp. 72-76, 2012.

[2] R. Fritzsch, M. W. Kennedy, S. Akbarnejad, and R. E. Aune, "Effect of Electromagnetic Fields on the Priming of High Grade Ceramic Foam Filters (CFF) with Liquid Aluminum," Light Metals, pp. 929-935, 2015.

[3] M. W. Kennedy, R. Fritzsch, S. Akhtar, J. A. Bakken, and R. E. Aune, "Apparatus and Method for Priming a Molten Metal Filter," U.S. Patent, WO 2013160754 A1, 2012.

[4] J. E. Dore and C. Bickert, "A Practical Guide on How to Optimize Ceramic Foam Filter Performance," Light Metals, pp. 791-796, 1990.

[5] N. Keegan, W. Schneider, and H. Krug, "Evaluation of the Efficiency of Fine Pore Ceramic Foam Filters," Light Metals, pp. 1031-1041, 1999.

[6] M. W. Kennedy, K. Zhang, R. Fritzsch, S. Akhtar, J. A. Bakken, and R. E. Aune, "Characterization of Ceramic Foam Filters used for Liquid Metal Filtration," Metallurgical and Materials Transactions B, vol. 44, pp. 671-690, 2013.

[7] R. Fritzsch, M. W. Kennedy, J. A. Bakken, and R. E. Aune, "Electromagnetic Priming of Ceramic Foam Filters (CFF) for Liquid Aluminum Filtration," Light Metals 2013, pp. 973-979, 2013.

[8] K. Butcher and D. Rogers, "Update on the Filtration of Aluminum Alloys with Fine Pore Ceramic Foam," 1990, pp. 797-803.

[9] L. Lorenz, "Ueber die Fortpflanzung der Electricität," Annalen der Physik, vol. 243, pp. 161-193, 1879.

[10] H. Nagaoka, "The Inductance Coefficients of Solenoids," Journal of the College of Science, vol. 27, pp. 18-33, 1909.

[11] H. A. Wheeler, "Simple Inductance Formulas for Radio Coils," Proceedings of the IRE, vol. 16, pp. 1398-1400, 1928.

[12] D. Knight. (2013, 14th July). Solenoids: Part 1 http://www.g3ynh.info/zdocs/magnetics/part_1.html.

[13] V. Callcut, "Coppers for Electrical Purposes," IEE Proceedings A Physical Science, Measurement and Instrumentation, Management and Education, Reviews, vol. 133, pp. 174-201, 1986.

[14] H. A. Wheeler, "Inductance Formulas for Circular and Square Coils," Proceedings of the IEEE, vol. 70, pp. 1449-1450, 1982.

[15] M. W. Kennedy, "Removal of Inclusions from Liquid Aluminium using Electromagnetically Modified Filtration," PhD, Department of Materials Science and Engineering, NTNU, Trondheim, 2013.

[16] M. W. Kennedy, S. Akhtar, J. A. Bakken, and R. E. Aune, "Electromagnetically Enhanced Filtration of Aluminum Melts," Light Metals, pp. 763-768, 2011.

[17] N. El-Kaddah, A. Patel, and T. Natarajan, "The Electromagnetic Filtration of Molten Aluminum using an Induced-Current Separator," JOM, vol. 47, pp. 46-46, 1995.

[18] D. Shu, B. Sun, K. Li, J. Wang, and Y. Zhou, "Effects of Secondary Flow on the Electromagnetic Separation of Inclusions from Aluminum Melt in a Square Channel by a Solenoid," ISIJ international, vol. 42, pp. 1241-1250, 2002.

[19] M. W. Kennedy, "Magnetic Fields and Induced Power in the Induction Heating of Aluminium Billets," Licentiate, Materials Science and Engineering, KTH, Stockholm, Sweden, 2012.

[20] M. W. Kennedy, S. Akhtar, J. A. Bakken, and R. E. Aune, "Empirical Verification of a Short-Coil Correction Factor," Industrial Electronics, IEEE Transactions on, vol. 61, pp. 2573-2583, 2014.

[21] M. W. Kennedy, S. Akhtar, J. A. Bakken, and R. E. Aune, "Analytical and Experimental Validation of Electromagnetic Simulations Using COMSOL®, re Inductance, Induction Heating and Magnetic Fields," presented at the COMSOL Users Conference, Stuttgart Germany, www.comsol.com/paper/analytical-and-experimental-validation-of-electromagnetic-simulations-using-coms-10999, 2011.

Supplement 2

Design of circular, square, single and multi-layer Induction Coils for electromagnetic priming using inductance Estimates

Robert Fritzsch, Mark W. Kennedy and Ragnhild E. Aune

Submitted to IEEE

DESIGN OF CIRCULAR, SQUARE, SINGLE AND MULTI- LAYER INDUCTION COILS FOR ELECTROMAGNETIC PRIMING USING INDUCTANCE ESTIMATES

Robert Fritzsch, Mark W. Kennedy and Ragnhild E. Aune
Department of Materials Science and Engineering
Norwegian University of Science and Technology (NTNU)
N-7491 Trondheim, Norway
robert.fritzsch@ntnu.no

***Abstract*— Special induction coils used for ElectroMagnetic (EM) priming of Ceramic Foam Filters (CFFs) in liquid metal filtration have been designed using a combination of analytical and Finite Element Modelling (FEM). Relatively simple empirical equations published by Wheeler in 1928 and 1982 have been used during the design process. The equations were found to accurately predict the *z*-component of the magnetic flux densities of both single- and multi-layer coils as verified both experimentally and by using COMSOL® 5.1 Multiphysics simulations.**

The present study discusses the design methodology, showing a simple design path for single and multi-layer round and square solenoidal coils for application to EM priming.

Keywords: Induction, Coil, Single-Layer, Multi-Layer, Inductance, Design, FEM

Introduction

The most commonly applied metal filtration system uses Ceramic Foam Filters (CFFs) [1]. In order to use CFFs for filtration, they must be filled with metal, and the air they initially contain must be removed. This process is referred to as 'priming'. It is remarkably difficult to overcome the high surface energy of liquid metals such as aluminum and achieve an adequate degree of priming, specially without pre-heating of the filter. The concept of applying EM fields to more effectively achieve priming of commercial CFFs using a greatly reduced metal 'head' has been studied by the present authors in earlier publications [2, 3], and is the subject of an international patent application [4]. The gradient in the induced Lorentz forces generates strong Magneto-Hydro-Dynamic (MHD) mixing, which in turn produces a velocity field (velocity 'head') that assists the metal in overcoming the surface tension between the metal and the filter media. As a result, the metal can penetrate the filter (the initial stages of priming). In addition, the MHD can produce a meniscus above the filter, which can add to the natural gravity head and further assist the priming of the filters. The magnetic field and induced Lorentz forces produced by this concept are presented schematically in Figure 1 by the use of a 2D-axisymmetric COMSOL® model.

The demands on priming systems are substantially different from the requirements in the existing EM pumping systems used for liquid metals. Extremely powerful Lorentz forces are required, but only for short periods of time in order to overcome the metal surface energy and force the metal into the cold air filled pores of the filter.

The main focus of the present study has been on the design methodology for the induction coil itself, and how it can be practically designed to create the flux density and high Lorentz forces required to achieve the priming. The present research approach was driven by the need to produce large flux densities on a very intermittent basis, while at the same time provide space for the required physical and thermal protection required in an industrial filter box setup. This necessitated the use of small liquid cooled hollow conductors operating at unusually high current densities > 25 A/mm^2]. Traditional measures of the electrical efficiency of a coil were therefore not included in the present design process.

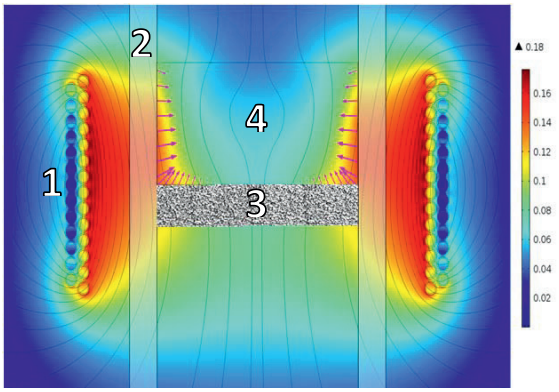

Figure 1: The concept of the EM priming technology showing (1) the double 9-inch induction coil, (2) the crucible, (3) the CFF, and (4) the metal above the filter in the initial stage of priming. The magnetic flux density is shown with its flux lines and with a color coded magnitude distribution [T]. The magenta colored arrows indicate the direction and the magnitude of the induced Lorentz forces at the initial stage before filling of the filter with liquid metal.

The practical design, validation and construction of square and round single and double coils can be made by the use of the well-known equations from Wheeler [5, 6], together with the analytical mathematics described by Baker [7] and Vaughan and Williamson [8].

The analytical equation for the estimation of the time averaged Lorentz forces produced by short coils has been

published by the present research group [9, 10], and has been derived beginning with the real part of $\vec{J} \times \vec{B}$, *i.e.*:

$$\left|\vec{F}_L\right| = Re\left\{\vec{J}^* \times \vec{B}\right\} \quad (1)$$

where $\vec{F}_L$ is the time averaged Lorentz force acting on the fluid [N/m^3], $\vec{J}^*$ the complex conjugate of the RMS value of the induced current density [A/m^2], and $\vec{B}$ the complex RMS value of the magnetic flux density [T]. This method requires the use of a short coil correction factor to be able to correctly estimate the magnetic field, as well as the magnetic flux density $\vec{B}$ of 'real', *i.e.* non-infinite coils, which also has been previously described by the present research group [11].

Theoretical Considerations

The inductance L can be used as the main parameter to design an induction coil with a defined magnetic flux density, B_z, along the coil axis. The inductance L is defined as the flux linkages per unit current and is directly related to the magnetic flux density, B_z, the area of the coil, A, the applied current, I, and the total reactive power, Q, as shown in the following equation:

$$L = \frac{N\Phi}{I_c} = \frac{B_z NA}{I_c} = \frac{Q}{I_c^2 2\pi f} \quad (2)$$

where L is the inductance [H], Φ the total flux [Wb], I_c the current [A] applied to the coil, N the number of turns [unitless], A the total area of the cross section of the induction coil occupied by flux, i.e. including magnetic penetration into the coil itself [m^2], B_z the magnetic flux density in the z-direction [T], f the frequency of the applied current [Hz], and Q the total reactive power [VAr]. Only the z-component of the magnetic flux needs to be considered for all symmetrical induction coils, as the sum of the r-components is zero after integration around the periphery for regular shaped coils. The computation of area A varies with geometry, *e.g.* round vs. square, or single vs. double coil, which has a directly proportional effect on the inductance.

It is possible to calculate the exact inductance for theoretical round 'current sheet' induction coils using the equation of Lorenz from 1879 [12], which involves the solution of the double elliptical integrals *K(k)* and *E(k)* of the first and second kinds:

$$L_{Lorenz} = \mu_r \mu_0 \frac{8N^2 r^3}{3l_c^2}\left[\left(\frac{2k^2-1}{k^3}\right)E(k) + \left(\frac{1-k^2}{k^3}\right)K(k) - 1\right],$$

$$where\ k = \sqrt{\frac{4r^2}{4r^2+l_c^2}} \quad (3)$$

Lorenz's equation was reformulated by Nagaoka in 1908 [13] using a short coil correction factor, K, which was tabulated to 6 decimals. K is dimensionless and varies between 1 and 0 with increasing coil diameter to length ratio.

$$L_1 = K\frac{\mu_0 \mu_r \pi N^2 r^2}{l_c} = K\frac{\mu_0 \mu_r A N^2}{l_c} \quad (4)$$

where l_c is the length of the coil [m], $\mu_0 = 4\pi * 10^{-7}$ the permeability of free space [H/m], $\mu_r = 1$ the relative magnetic permeability for air [unit less], and K the short coil correction factor or Nagaoka coefficient [unitless] which accounts for the shape factor of the coil. A is the frequency dependent effective area occupied by the coil and the 'air-gap' of a real, *i.e.* non-current sheet coil, as presented in Figure 7 and given by the following equation which is valid only for cases where $\delta_c < d_c$:

$$A = \frac{\pi(D_c+\delta_c)^2}{4} \quad (5)$$

In 1928 Wheeler presented an empirical formula for the inductance of a single layer short coil [5], which was subsequently reformulated by Knight [14] and can be used to estimate Nagaoka's short coil correction factor K to approximately 3 decimal precision for induction coils of 'typical' dimensions, i.e. $(D_c+\delta_c)/l_c$ of ~0.25:1 to 2:1 with great simplicity:

$$K = \frac{1}{1+0.4502\left(\frac{D_c+\delta_c}{l_c}\right)} \quad (6)$$

where D_c is the inner diameter of the coil conductors, and δ_c the electromagnetic penetration depth into the coil defined as:

$$\delta_c = \sqrt{\frac{2\rho}{\omega\mu_o\mu_r}} = \sqrt{\frac{\rho}{\pi f \mu_o \mu_r}} \quad (7)$$

where ρ is the resistivity of the copper conductor, defined as: 1.7241 x 10^{-8} Ω·m for 100% IACS copper [15].

The magnetic field of a single layer induction coil can be found by equating equations (2) and (4) and substituting with equation (6):

$$B_z = \frac{1}{1+0.4502\left(\frac{D_c+\delta_c}{l_c}\right)}\frac{\mu_0\mu_r N I_c}{l_c} \quad (8)$$

In 1982 Wheeler published a letter [6], where he presented new and more accurate empirical equations designed for the use with both round (L_{2r}) and square (L_{2s}) single layer coils, identified as:

$$L_{2r} = \mu_0 N^2 r\left(\ln\left(1+\frac{\pi r}{l_c}\right) + \frac{1}{2.3+1.6\frac{l_c}{r}+0.44\left(\frac{l_c}{r}\right)^2}\right) \quad (9)$$

$$L_{2s} = \mu_0 N^2 r\left(\frac{4}{\pi}\right)\left(\ln\left(1+\frac{\pi r}{l_c}\right) + \frac{1}{3.64+2\frac{l_c}{r}+0.51\left(\frac{l_c}{r}\right)^2}\right) \quad (10)$$

where L_{2r} is the inductance of a single layer round coil [µH], L_{2s} the inductance of a single layer square coil [µH], N the number of turns, r the radius [m], and l_c the length measured top to bottom of the coil [m]. The dimensions and ratios of square and round coils are also presented in Figure 7.

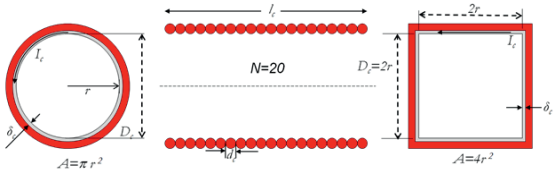

Figure 2: A sketch, similar to the sketch by Baker published in 1957 [7], of a 20 turn single layer induction coil with round and square cross sections. The pitch is shown at the minimum, *i.e.* equal to the diameter of the coil wires. D_c = inner coil diameter [m]; r = coil radius [m]; A = coil area [m^2]; N = number of turns [unitless]; l_c = axial coil length [m]; I_c = applied coil current [A]; δ_c = electromagnetic penetration depth in the coil [m], and d_c = width of the coil [m].

Equations (3) through (10) can be used to estimate the average z-component of magnetic fields of single layer coils with good precision. The equations cannot, however, be applied with precision to multi-layer coils. The empirical equation of Wheeler [5] for the inductance of a round multi-layer coil can be used to estimate L prior to constructing a coil, and has been transformed from imperial to SI units with dimensions in [m] as follows:

$$L_3 = \frac{31.496\, r^2 N^2}{6r+9l_c+10c} \qquad (11)$$

where L_3 is the inductance of a multi-layer coil [µH], N the number of turns, r the average radius [m], l_c the length measured top to bottom of the coil [m], and c the thickness of the coil [m], as presented in Figure 8.

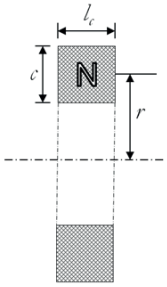

Figure 3: Simple model of a multi-layer induction coil with N turns, radius r, length l_c, and thickness c. [11]

Constructing the multi-layer coil and than measuring L is also an alternative approach. In that case B_z can be calculated by applying equation (2).

For any given coil, the strength of the magnetic field is directly proportional to the current as indicated by equation (2). The RMS current, I, required to achieve a targeted B_z can therefore be determined using equation (2) for either a single or multi-layer coil. The RMS voltage, V, required to produce the necessary current can be found via the coil impedance, Z:

$$V = IZ \qquad (12)$$

$$Z = \sqrt{R^2 + X^2} \qquad (13)$$

$$X_{total} = \omega L = 2\pi f L \qquad (14)$$

where Z is the coil impedance, [Ω], R the coil resistance [Ω], and X_{total} the total reactance, which is assumed to only have a inductive component [Ω].

Baker approximated the coil reactance as being equal to the empirically estimated resistance using a formula, which was only accurate at high frequency and for coils where the diameter is much greater than the penetration depth [7].

High frequency can be practically defined by a coil $d_c > \sim 2\delta_c$. At high frequency the resistance and reactance of the coil do not become equal, but approach a constant ratio. Baker's resistance formula, which he equated to the reactance, cannot be accurately applied at low frequency and will in those cases give a serious error for cases where $\delta_c > d_c$. The alternating current resistance R of the coil used in equation (13) can, however, be estimate for both low and high frequency [16]:

$$R = \pi \frac{N^2 \rho (D_C + \delta_C)}{(\delta_C l_c k_r)} \qquad (15)$$

where k_r is the coil space factor [unitless], *i.e.* the fraction of the coil length occupied by copper:

$$k_r = \frac{d_C N}{l_C} \qquad (16)$$

where d_C is the height of the copper conductors [m].

For cases where $\delta_c > d_c$ the equations (5), (6), (8) and (15) should be calculated based on the coil's equivalent current sheet diameter, *i.e.* the diameter taken on the conductor centerline in accordance with classical assumptions.

Conceptually the total flux, inductance and reactive power can be imagined as the sum of three 'parts', *i.e.* originating in the volume occupied by: (i) the air gap, (ii) the coil conductors and (iii) the workpiece (if there is one) [7, 8]. The total reactive power shown in equation (2) can then be calculated by the sum of the following three parts:

$$Q = Q_g + Q_c + Q_w = I_c^2 L 2\pi f = I_c^2 X_{total} \qquad (17)$$

where Q_g is the reactive power produced inside the air gap [VAR], Q_c the reactive power produced by the flux inside the coil [VAR], and Q_w the reactive power produced by the flux linking the workpiece with the coil if a work piece is present [VAR], which can be calculated using methods described elsewhere [11, 17]. As there is no work piece present in the present study, the reactive power of the work piece is zero, *i.e.* $Q_W = 0$.

At very high frequency, *e.g.* at frequencies > 5kHz for the system presented in Figure 4, $(Q_c + Q_W) < 1\%\ Q_g$, the EM penetration depths into the coil (and work piece if there had been one) diminish, and their contribution to the total reactive power asymptotically approach zero. Their contribution to the total reactive power can therefore be assumed to be zero with a negligible error, $i.e.\ Q_c + Q_W \ll Q_g$ [17].

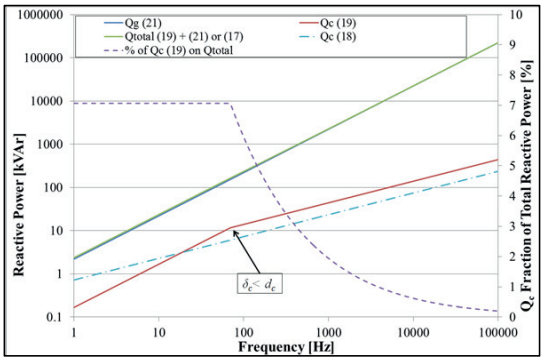

Figure 4: Reactive power calculations using: (I) equation (19) with equation (20) and equation (25) [red line] compared with equation (18) [aqua long dash dotted line] for Q_c, and (II) equation (21) with equation (24) [blue line] for Q_g, assuming no workpiece from 1 Hz to 1MHz. The magenta colored dotted line gives the fraction of the total reactive power contributed by the flux within the coil. The applied current for the calculations was 1250 A [18], and the calculation made for coil 4.

At intermediate frequency ranges the reactive power of the a single layer coil can be found using a modified version of an equation proposed by Baker [7] for high frequencies:

$$Q_c = \frac{\pi D_c \rho_C (KIN)^2}{l_c \delta_c} \qquad (18)$$

Equation (18) implicitly assumes that $\delta_c < d_c$, which may not be true at low frequency, and it also implicitly assumes that $\delta_c << D_c$. In the present study the low frequency and equation (19) and equation (20) were found to give reasonable estimates for both low and high frequency, *i.e.* these equations are preferred as they are more universally applicable:

$$Q_c = I_c N B_z A_c 2\pi f = I_c^2 L_{coil} 2\pi f = I_c^2 |X_c| \qquad (19)$$

where L_{coil} is the inductance of the coil due to the flux within the coil itself [H], and A_c the frequency dependent effective area of the round aircore coil [m^2] presented in equation (20):

$$A_c = \frac{\pi[(D_c+\delta_c)^2 - D_c^2]}{4} \qquad (20)$$

For the final step to determine the reactive power of the air gap the following equation can be used:

$$Q_g = I_c^2 L_g 2\pi f \qquad (21)$$

where L_g is the inductance of the air gap for an empty coil, and can be found by:

$$L_g = L - L_{coil} \qquad (22)$$

In order to specify a power supply it is necessary to also define both the required apparent [VA] and real power [W]:

$$P_{apparent} = IV \qquad (23)$$

$$P_{real} = IV\cos(\varphi) \qquad (24)$$

$$P_{reactive} = IV\sin(\varphi) \qquad (25)$$

where φ is the phase angle between the current and the voltage, and $\cos(\varphi)$ is traditionally referred to as the power factor, which can be calculated by:

$$\cos(\varphi) = \frac{R}{\sqrt{R^2+X^2}} \qquad (26)$$

In the present study the apparent, real and reactive powers, as well as the power factor, have been measured.

The quality or efficiency of an inductor is often designed by maximizing the Q factor, given in equation (27). Q is a dimensionless parameter representing the efficiency of the coil [19]. A high Q value indicates a low energy loss per cycle compared to the total magnetic energy stored, or if the coil is in resonance it represents a slowly decaying oscillation (or a low dampening factor). As the induction coil is a single inductor it can be expressed as the ratio of reactive power to real power of the empty coil, or as the reactance divided by resistance at the operating frequency:

$$Q(\omega) = \omega * \frac{Max.Energy\ Stored}{Power\ Loss} \cong \frac{X}{R} \qquad (27)$$

The Q factors for the coils used in the present study were between 4 and 16, whereas a normal value for inductors is stated to be between 100 and 1000 [19, 20]. Nevertheless, Q was not a significant operating issue as the coils were only to be operated for seconds during priming. Hence, the magnitudes of coil losses were relatively immaterial. Instead the coils were designed to allow for the presence of thermal insulation, carry maximum possible current without experiencing boiling of the cooling water, and to still fit within a filter box of reasonable dimensions. In other words, the use of a compact conductor with high resistance was a design requirement.

The design equations described in this theory section are only applicable to an empty 'air-core' coil, *i.e.* a coil prior to priming. After priming, the space above, below and within the CFF's are filled with metal. This metal alters both the resistance and reactance of the system in a complicated way, as introduced here and further described elsewhere [11, 17].

In practical terms the reduction of reactive impedance is greater than the increase in effective coil resistance, and for a fixed applied voltage the current and magnetic flux density increase as the CFF's become primed. Hence, the air-core case represents a minimum flux density and therefore a reasonable case for general coil design.

Experimental

In the present study the applied frequency was the mains frequency, 50 Hz, and variable field strength was obtained by the application of alternating currents of up to 1250 A RMS supplied by variable auto-transformers.

Experimental data were collected using 4 different coils including: 1) a short single round, 2) a short double round, 3) a single square, and 4) a double square coil. These coils are presented in Figure 5 and Figure 6. The data, showing the

results of the inductance measurements and the theoretical calculations are presented in Table I.

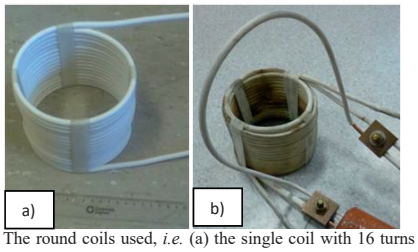

Figure 5: The round coils used, *i.e.* (a) the single coil with 16 turns and (b) the double short coil with 31 turns. The visible jumper (see (b)) is connecting the two coils in series.

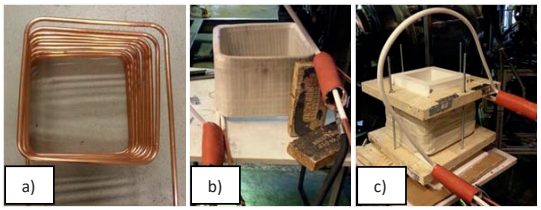

Figure 6: (a) the inner 9 inch square coil during production, (b) the finished square double coil after insulating with fiberglass sleeves, and (c) the final 9 inch coil setup. The jumper coupling of both coils in series can be seen in (b) and (c).

The 4 inch round coils, presented in Figure 5, have been designed to allow for the use of ~1 kA RMS at maximum cooling water flow (at 5-6 Bar pressure). The highest magnetic flux density varies from coil to coil and are for the coils 1) ~0.13 and 2) ~0.23 T along the axis, and measured at the peak of the centerline at the midpoint of the coil. The multi-layer coils were connected by a jumper, see as the 'hoop' rising up in Figure 5 (b), which allowed the current to flow between the two coils in series without substantially disturbing the magnetic field inside the coil. The cooling water was provided in parallel to achieve maximum flow; hence, current and magnetic field for the available water pressure.

The 9 inch coils, presented in Figure 6, have been designed to allow for 2 kA RMS at high cooling water flow (up to 10 Bar pressure). The maximum magnetic flux densities varies from the single to the double coil and are ~0.06 T for the single coil and ~0.12 T for the double coil, measured at the peak of the centerline at the midpoint of the coil. The inner coil, prior to being insulated, is seen in Figure 6 (a), and after coupling both coils to create one double coil in Figure 6 (b). The coils were connected by a jumper, visible in Figure 6 (b) and (c). Cooling water was provided in parallel, while the current flowed in series. Due to restrictions of the available power supply, a maximum RMS current of 1.25 kA was realized.

The square shape of the coil generates strong gradients in the Lorentz forces at the corners of the coil, and strong 100 Hz electro-mechanical vibrations as a result of the 50 Hz alternating current that is passes through zero twice each cycle. This required powerful physical restraints to maintain the stability of the coil, as indicated in Figure 6 (c).

SUMMARY OF THE EXPERIMENTAL COIL DIMENSIONS, AND THE MEASURED AND THEORETICAL ELECTRICAL VALUES. ALL REACTANCE ESTIMATES ARE FOR A MAINS FREQUENCY OF 50 HZ.

Induction Coil	**Unit**		**4'' (10.16 cm) coil**		**9'' (22.86 cm) coil**	
			Single Round	***Double Round***	***Single Square***	***Double Square***
			1	***2***	***3***	***4***
Coil / Eq. Dia.	mm	D_c	126	132	327	333
Total Height	mm	l_c	106	111	182	182
Coil Thickness	mm	c	6.5	14	13	26
Turns	[ ]	N	16	31	14	27
Coil space factor	[ ]	k_r	0.91	0.86	0.93	0.91
Cond. Height	mm	d_c	6	6	12	12
Inductance						
Lorenz (Eq.4)	µH	L_1	24.6	96.1	62.3	239.9
Single coil (Eq.9)	µH	L_{2r} / L_{2s}	24.1	94.1	62.7 / 74.6	240 / 286
Multilayer (Eq.11)	µH	L_3	22.9	85.3	60	221.1
Modeled	µH	L	25.1	98.5	60.8	241.0
Measured	µH	L	26.4	104	58	240
Estimate field strength			***0.956 kA***	***1kA***	***1.250 kA***	
Coil cor.		K	0.649	0.650	0.548	0.541
Impedance (Eq.13)	Ω	Z	0.0087	0.028	0.022	0.0756
Modeled	Ω	Z	0.010	0.020	0.021	0.075
Measured	Ω	Z	0.013	0.026	0.022	0.075
Reactance (Eq.14)	Ω	X	0.0072	0.027	0.0196	0.0754
Modeled	Ω	X	0.0078	0.031	0.0213	0.0747
Measured	Ω	X	0.0083	0.026	0.0199	0.0735
Resistance (Eq.15)	Ω	R_{AC}	0.0021	0.0081	0.0023	0.0089
Voltage (Eq.12)	V	V_0	8.5	27.99	27.5	94.5
Measured	V	V_0	13.17	26.56	27.10	94.64
Flux Density (Eq.8)	T	B_z	0.118	0.228	0.066	0.128
Modeled	T	B_z	0.122	0.243	0.0654	0.124
Measured	T	B_z	0.121	0.23	0.0623	0.127

The experimental power supplies have consisted of one step down transformer (45 kW, 230/30 V, 196/1500 A) for the small round coils, and two adjustable welding transformers (each 80 kW, 44/89 V, 500/1800 A) wired in parallel for the 9 inch coils. The measurements for the magnetic fields were taken using a Hall Effect gauss meter model 6010 supplied by Pacific Scientific OECO, F.W. Bell®. The axial probe was standardized using an axial standard of 0.05 T ± 0.3 mT. The coil current was measured using a Fluke® inductive current probe i1000S with a resolution of 1 ampere and an accuracy

of ±1%. The real (W) and reactive (VAR) power were measured using a Fluke® 43B Power Quality Analyzer with a resolution of 100 W. The real coil inductances could then be calculated using the measured reactive power, and the coil dimensions by applying equations (12) and equation (23). The resulting geometric and experimental data were used to calculate valid FEM simulation results without the use of any fitting parameters during the simulations.

Results and Discussion

The use of a frequency dependent equivalent coil diameter, defined by $D_c + \delta_c$ in equation (5), implies that the inductances of the coils are not independent of frequency. This was subsequently verified using the FEM and analytical modeling. The 50 Hz frequency applied during the present investigation was relatively 'low' in comparison with usual induction coil designs. The frequency alters the inductance by changing the penetration depth and thereby the effective area of the coil occupied by the flux. The inductance was measured at 50 Hz and is compared with analytical calculations using equations (4) and equation (5), and FEM as presented in Figure 7 and Figure 8. The 4 inch single coil, presented in Figure 5 (a), was used in the previous experimental trials performed by the present research group. [11, 16]

At low frequency, where full magnetic penetration into the coil was achieved, the inductance was constant, as the area did not change. As the penetration depth became smaller the thickness of the coil tubing material, and the inductance of the coil changed, *i.e.* was reduced with the frequency. This was in accordance with the reduced area within the coil conductor occupied by magnetic flux, which was estimated using
equation (5). When the frequency exceeds a certain limit where the $\delta_c << d_c$, the inductance will again become essentially independent of the frequency.

The validation of the proposed method for the design of simple induction coils of various shapes was accomplished by comparison of the analytical predictions with the measured and FEM flux densities. The calculated and measured inductances were also compared.

The RMS magnetic flux density [T] of the designed coils was first estimated, then calculated by the use of the COMSOL® 5.1 software, and finally compared to experimental measurements. The analytical and experimental results are summarized in Table I. The measurements of the electromagnetic field of the 9 inch square coil are plotted together with the theoretical model of the equivalent circular diameter coil, and the results from the COMSOL® 9 inch square coil model in Figure 10 and Figure 11. The visualization of the model and the locations of the measurements are presented in Figure 7.

As can be seen from Figure 10, the measured axial magnetic flux density B_z of the double square coil (coil 4) are compared, as a function of radial position through the middle of the coil, to the results from analytical and computational methods. A 2D-axisymmetric and a 3D COMSOL® model were created to estimate the magnetic flux density. Measurements were obtained as indicated in Figure 7 (a) and (c). The 2D-axisymmetric model uses the equivalent diameter, which gave the same total area as the square coil and hence the same total lines of flux in theory. The figure indicates that the method, though highly simplified, provides an accurate estimation of the resulting magnetic flux density for the actual square coil, as shown by the good agreement with the experimental measurements in Table I.

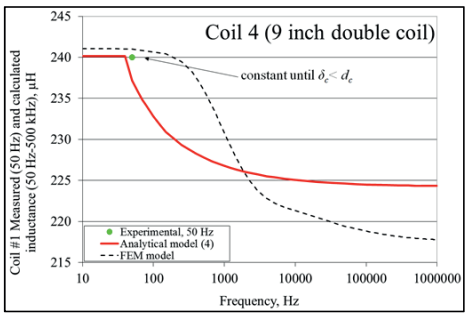

Figure 7: Inductance over frequency for the 9 inch double square coil (presented in Figure 6 (b) and (c)). The theoretical model based on equation (4) and FEM modeling by COMSOL® 5.1, shows the frequency dependency of the inductance L utilizing the short coil correction factor. The real coil was measured at 50 Hz (green marker), in Table I shown as coil 4.

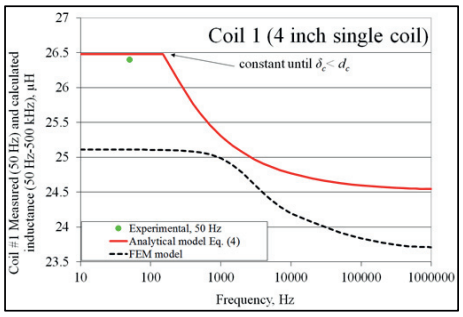

Figure 8: Inductance over frequency for the 4 inch single coil (presented in Figure 5 (a)). The theoretical model based on equation (4) and FEM modeling, shows the frequency dependency of the inductance L utilizing the short coil correction factor. The real coil was measured at 50 Hz during previous experiments and is marked in Table I as coil 1.

The 3D COMSOL® FEM model provided a more accurate spatial resolution of the resulting magnetic flux density of a square coil than the equivalent diameter model. The advantages are given by the possibility to visualize the corner effects, which cannot be estimated by the 2D-axisymmetric models. The disadvantage is the resolution of the mesh, when discussing high frequencies, which is a well-known problem [10]. If the mesh spacing at interfaces is larger than the electromagnetic penetration depth, then large errors may be obtained. As a result this necessitates the use of very fine meshing and significant computational requirements for accurate high frequency modelling. The 50 Hz 3D results are

plotted in Figure 10 for a section taken across the width of the coil at the midpoint along the length of the coils. The section is marked as a black line in Figure 9 (a).

The coil geometry and the resulting magnetic flux density of the 9 inch (22.86 cm) square coil, as well as the equivalent diameter 9 inch round coil, are visualized in Figure 7 (a) and (c) for a section taken at the midpoint along the length of the coils. A 3D image of the spherical electromagnetic domain surrounding the square coil is presented in Figure 7 (b), giving a perspective view of Figure 7 (a). It was necessary to restrict the size of the EM domain to avoid an excessive number of cells, as well as extended computational times. A larger 'space' would have been preferred to minimize the possible impact of external magnetic reluctance [10].

The geometry of the coil proved to have a strong effect on the resulting magnetic field. The 3D model results along the diagonal revealed the effect of the coil shape, whereas the 2D-axisymmetric solution could not provide any information in regards to the variation in the flux density in the corners. 3D modelling was necessary to understand the corner effects, and provide an accurate estimate of the flux density in this area. Measurements were also taken along the diagonal through the middle of the square coil, as presented in Figure 7 (a). The comparison of these measurements and the calculations from the 3D-model are presented in Figure 11, and appear to be in excellent agreement.

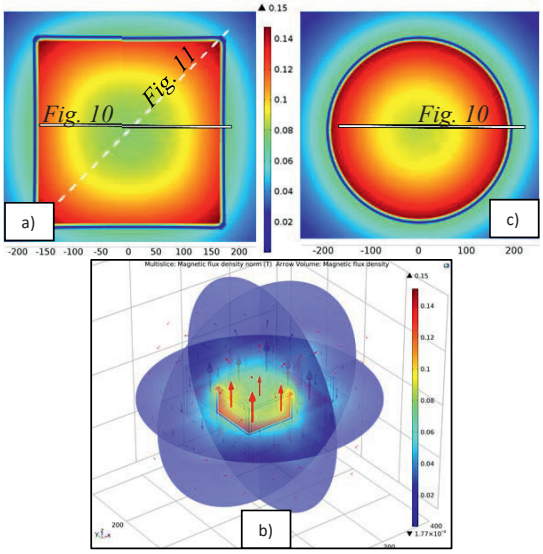

Figure 9: COMSOL® 5.1 models of the (a) and (b) designed 9 inch (22.86 cm) square and (c) a comparable equivalent diameter 9 inch round coil with the same total area as (a). Both models have meshing suitable for low frequency, *i.e.* spacing of less than δ_c. The applied current is equal to the measured current during the real experiments, *i.e.* 1250 A RMS. The data for the square coil was obtained at the white line with a black frame, which represents the centerline, and at the white dashed line. The equivalent radius is found between these two values.

The FEM integrated magnetic flux density was found to be 0.131 T for the 2D-axisymmetric model and 0.128 T across the middle cut of the 3D model. The results are presented as the solid line in Figure 9 (a) and (c), both at the coil midline. The analytically calculated field strength is effectively a double integral along the length and radius of the coil. In Table I a comparison is therefore made against a double integral value extracted from the FEM models, showing excellent agreement with the analytical result (<1% difference). The agreement between the 2D and 3D crosscuts, and the analytical model, indicate that the axial symmetric approach gives rapid and accurate overall field/inductance estimates even for square coils.

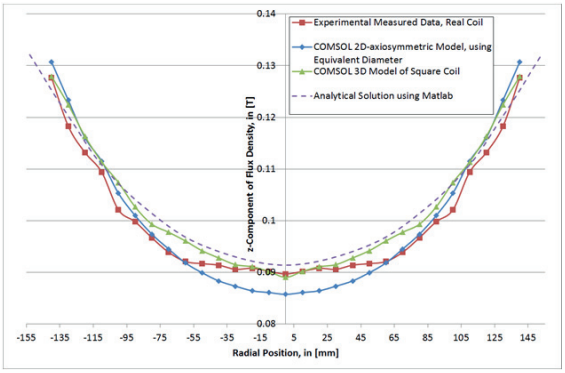

Figure 10: Radial measurements of the axial flux density B_z for coil 4, measured every 10 mm at the center of the coil, compared with 2D-axisymmetric models using the equivalent diameter and a 3D model solved by the use of COMSOL® 5.1. The analytical estimate of the average flux density was determined using the inductance formula of Wheeler, equation (11) L_3, and by an analytical solution using Matlab® modeling of the radial estimated axial flux density using the Biot Savart Law. The result is presented as a black dotted line. The magnetic field was generated by application of 1250 A RMS, and measured from r_c= 0 to 140 mm. The data is mirrored at the centerline, r_c= 0 mm.

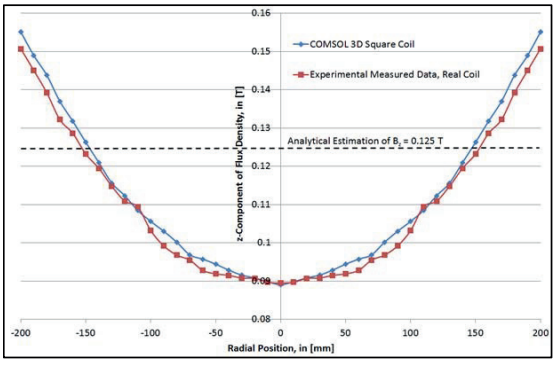

Figure 11: The data taken in the middle of coil 4, measured every 10 mm along the diagonal, compared with the full size 3D model using COMSOL® 5.1 (presented in Figure 7 (a)). The analytical estimate using the inductance formula of Wheeler, equation (11), L_3 is shown as the dotted black line and represents the double integral along length and radius. The magnetic field was generated by the application of 1250 A RMS, and measured from r_{dia}= 0 to 200 mm. The data is mirrored at the centreline r_{dia}= 0.

Considering the 'quality factor' from equation (30), the cost to prime an industrial filter system by the designed coils is very much dependent on the price of electricity, the size of the coil, and the coil 'quality'. Experiments have shown that larger coils require more time to fully prime the filters, while higher currents are required to generate similar magnetic flux densities. A cost to prime different sized filters was estimated assuming an electricity price of 6.84 US cents per kWh [21], as presented in Figure 12. Filter priming is required only once for each cast, which consists of many tons of liquid aluminium metal, i.e. typically ~ 3 times each day for each casting line.

The preheating of the filters with a gas driven burner would require 1 to 2 hours of preheating time using burners with a capacity of 100 to 150 kW. Base on this, the cost of gas is estimated to be ~$3.20 to $9.60 for each priming assuming the US market price from 2012 of $0.032/kWh [21]. Comparing the cost of EM priming, estimated to be $0.01-0.07/priming, to the gas fired cost confirms that the coil quality factor is not a significant design factor for the improved filter boxes. The coil was therefore correctly optimized with regards to the magnetic field, the protection from the liquid metal, adequate cooling, and industrial safety standards.

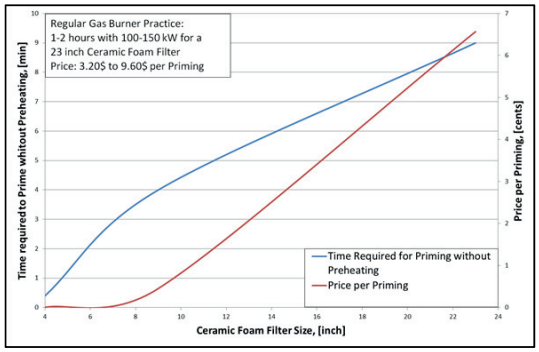

Figure 12: Estimated cost for priming assuming an electricity price of 6.84 US cents/kWh [21].

Conclusions

Theoretical design equations for induction coils of various shapes have been presented based on simple inductance and magnetic flux equations. A straight forward method was shown which is capable of designing round, square, single or multi-layer induction coils that are capable of generating a target magnetic flux density beginning with only the coil geometry. Wheelers equation (11) was found to be accurate in determining the inductance for 50 to 60 Hz cases, but will be less accurate at high frequency when $\delta_c < d_c$.

In regards to the magnetic flux densities, the application of an equivalent round diameter to the theoretical calculations of a square coil has been shown to be sufficiently accurate for design purposes, *e.g.* to match a coil to a power supply or vice versa.

To achieve a target average flux density for a given coil dimension, a method to design an induction coil to the limits of an available power transformer, or for the specification of a new transformer, has also been shown by relating the magnitude of B_z to the value of the inductance as indicated in equation (2).

The application of modern finite element software, such as COMSOL® 5.1, allows the solution of simple, fast and accurate 2D-axisymmetric models even as an approximate solution for square coils. 3D models give a spatial resolution of the results, but are much slower to execute. If applied at high frequency, the ability to mesh at a spacing of $< \delta_c$ becomes doubtful, and violation of this criteria has already been shown to lead to extreme numerical errors [10]. The analytical solutions were identified to give the smallest error, whereas the FEMs allow the visualization of the resulting fields. FEM is furthermore capable of combining the EM results with fluid dynamics and Joule heating simulations to design more advanced aspects of the systems.

Future Work

A similar work on the effect of frequency and shape on the coil impedance is planned.

FEMs allowing for the use of more complex 3D structures and induction coils of various shapes will be generated, and compared to observations/measurements.

Acknowledgement

The authors wish to express their gratitude to the Norwegian University of Science and Technology (NTNU), Department of Materials Science and Engineering (DMSE), and their industrial partners from Pyrotek® EMP™.

The financial support granted by the Faculty of Sciences and Technology at NTNU for the support of Dipl. Ing. Robert Fritzsch is greatly acknowledged.

References

[1] K. Butcher and D. Rogers, "Update on the Filtration of Aluminum Alloys with Fine Pore Ceramic Foam," pp. 797-803, 1990.

[2] R. Fritzsch, M. W. Kennedy, S. Akhtar, J. A. Bakken, and R. E. Aune, "Electromagnetically Modified Filtration of Liquid Aluminium with a Ceramic Foam Filter," *Journal of Iron and Steel Research, International,* pp. 72-76, 2012.

[3] R. Fritzsch, M. W. Kennedy, S. Akbarnejad, and R. E. Aune, "Effect of Electromagnetic Fields on the Priming of High Grade Ceramic Foam Filters (CFF) with Liquid Aluminum," *Light Metals,* pp. 929-935, 2015.

[4] M. W. Kennedy, R. Fritzsch, S. Akhtar, J. A. Bakken, and R. E. Aune, "Apparatus and Method for Priming a Molten Metal Filter," U.S. Patent, WO 2013160754 A1, 2012.

[5] H. A. Wheeler, "Simple Inductance Formulas for Radio Coils," *Proceedings of the IRE,* vol. 16, pp. 1398-1400, 1928.
[6] H. A. Wheeler, "Inductance Formulas for Circular and Square Coils," *Proceedings of the IEEE,* vol. 70, pp. 1449-1450, 1982.
[7] R. Baker, "Design and Calculation of Induction Heating Coils'," *AIEE Trans,* vol. 57, pp. 31-40, 1957.
[8] J. Vaughan and J. Williamson, "Design of Induction-Heating Coils for Cylindrical Nonmagnetic Loads," *American Institute of Electrical Engineers, Transactions of the,* vol. 64, pp. 587-592, 1945.
[9] M. Kennedy, S. Akhtar, J. Bakken, and R. Aune, "Electromagnetically Modified Filtration of Aluminum Melts—Part I: Electromagnetic Theory and 30 PPI Ceramic Foam Filter Experimental Results," *Metallurgical and Materials Transactions B,* vol. 44, pp. 691-705, 2013.
[10] M. W. Kennedy, S. Akhtar, J. A. Bakken, and R. E. Aune, "Analytical and Experimental Validation of Electromagnetic Simulations Using COMSOL®, re Inductance, Induction Heating and Magnetic Fields," presented at the COMSOL Users Conference, Stuttgart Germany, 2011.
[11] M. W. Kennedy, S. Akhtar, J. A. Bakken, and R. E. Aune, "Empirical Verification of a Short-Coil Correction Factor," *Industrial Electronics, IEEE Transactions on,* vol. 61, pp. 2573-2583, 2014.
[12] L. Lorenz, "Ueber die Fortpflanzung der Electricität," *Annalen der Physik,* vol. 243, pp. 161-193, 1879.
[13] H. Nagaoka, "The Inductance Coefficients of Solenoids," *Journal of the College of Science,* vol. 27, pp. 18-33, 1909.
[14] D. Knight. (2013, 14th July). *Solenoids: Part 1* http://www.g3ynh.info/zdocs/magnetics/part_1.html.
[15] V. Callcut, "Coppers for Electrical Purposes," *IEE Proceedings A Physical Science, Measurement and Instrumentation, Management and Education, Reviews,* vol. 133, pp. 174-201, 1986.
[16] M. W. Kennedy, S. Akhtar, J. A. Bakken, and R. E. Aune, "Review of Classical Design Methods as Applied to Aluminum Billet Heating with Induction Coils," *TMS 2011, EPD Congress,* pp. 707-722, 2011.
[17] M. W. Kennedy, "Magnetic Fields and Induced Power in the Induction Heating of Aluminium Billets," Licentiate, Materials Science and Engineering, KTH, Stockholm, Sweden, 2012.
[18] D. Cho, D. Armstrong, and R. Anderson, "Combined Vapor and Chemical Explosions of Metals and Water," *Nuclear Engineering and Design,* vol. 155, pp. 405-412, 1995.
[19] E. I. Green, "The story of Q," *American Scientist,* pp. 584-594, 1955.
[20] A. Rand, "Inductor Size vs. Q: A Dimensional Analysis," *IEEE Transactions on Component Parts,* vol. 10, pp. 31-35, 1963.
[21] U. S. E. I. Administration. (2015, 10.12.). *Energy and Natural Gas Prices*. Available: http://www.eia.gov/electricity/

Robert Fritzsch was born in Berlin, Germany, in 1985. He received a Dipl. Ing. (equivalent to M. Sc.) in Material Science and Engineering from the Technical University of Berlin, Germany in 2012. After receiving the Dipl. Ing. he started his Ph. D. at the Department for Material Science and Engineering at the Norwegian University of Science and Technology (NTNU) working on electromagnetic interactions on liquid metals.

Mark W. Kennedy (S'11–M'12) was born in Toronto, Ontario, Canada, in 1965. He received a B.Sc. degree in Chemical Engineering from the University of Waterloo, Waterloo, ON, in 1989, a M.Sc. degree in Metallurgical Engineering from McGill University, Montreal, QC, Canada, a Technical Licentiate degree in Materials Science from KTH – Royal Institute of Technology, Stockholm, Sweden, in 2013, on induction heating of aluminum billets, and a Ph.D. degree in Materials Science from the Norwegian University of Science and Technology (NTNU), Trondheim, Norway, in 2013, on electromagnetically modified filtration of liquid aluminum.

Ragnhild E. Aune (M'11) was born in Trondheim, Norway, in 1965. She received a M.Sc. degree in Metallurgical and Materials Technology, a Ph.D. degree in Theoretical Metallurgy, and a Docent degree in Theoretical Process Metallurgy with Emphasis on Functional Materials from KTH - Royal Institute of Technology, Stockholm, Sweden, in 1993, 1998, and 2005, respectively. Since 2009, she has been a Full Professor in Process Metallurgy at the Norwegian University of Science and Technology (NTNU), Trondheim, Norway.

Part II: *Priming and Upscaling*

Supplement 3

Electromagnetically Modified Filtration of Liquid Aluminium with a Ceramic Foam Filter

R. Fritzsch, M. W. Kennedy, S. Akhtar, J. A. Bakken, and R. E. Aune,

Journal of Iron and Steel Research International (1006-706X, 2012 Issue S1), page 72-76

Electromagnetically Modified Filtration of Liquid Aluminium with a Ceramic Foam Filter

R. Fritzsch[1], M.W. Kennedy[1], S. Akhtar[2], J.A. Bakken[1], R.E. Aune[1,3]

[1]Dept. of Materials Science and Engineering, Norwegian University of Science and Technology, 7491 Trondheim, NORWAY
[2] Hydro Aluminium Karmøy, 4265 Håvik, NORWAY
[3]Dept. of Materials Science and Engineering, Royal Institute of Technology, 100 44 Stockholm, SWEDEN

Abstract: Conventional Ceramic Foam Filter (CFF) technology has some difficulties in removing fine particulates (*e.g.* < 20 µm) from liquid aluminium. In the present work the filtration behaviour of 30, 50 and 80 ppi CFF filters have been studied in the presence of magnetic fields in the range of 0.06-0.2T, produced by induction coils operated at 50 Hz. A feed recipe containing 90 wt. % of the aluminium alloy A356 doped with 10 wt. % A356 composite, containing 15 wt. % SiC particles with a particle size ranging from 13 to 23 µm, was used. When the results obtained for the experiments conducted under the influence of a magnetic field where compared with similar reference gravity filtration experiments profound changes were observed in the distribution of particulates within, over and below the filter. Significant improvements in the wetting behaviour of the liquid metal to the CFF surface were also observed. It is believed that a successful change in filtration mechanisms is obtained as a result of the presence of the Lorentz forces and the metal recirculation produced by the magnetic field. The magnitude of the Lorentz forces, *i.e.* the magnetic pressure, are in the present work discussed in relation to the filtration results, and quantified based on experimental data and validated 2D axial symmetric Finite Element Modelling (FEM).
Keywords: electromagnetic, filtration, Ceramic Foam Filter, CFF

1. Introduction

Premium quality aluminium castings require a high level of metal cleanliness, and are crucial for critical structural components. The development of more efficient filtration methods for liquid aluminium is therefore essential in order to produce very clean aluminium, *i.e.* have conditions that allows for particulates down to 10 µm to be removed. As a result, the particulate removal efficiency of CFF's has become a subject of interest.
The generation of a magnetic field by an induction coil in combination with a CFF causes recirculation of the melt through the filter media, modifying the inclusion separation. Applying an alternating magnetic field produced by a solenoid has clearly several advantages, *i.e.* (i) avoidance of contamination by physical contact with the stirring device, (ii) no sub-cooling during filtration, (iii) better priming of the filter element with a lower metallic head, and (iv) subsequently higher casting rates for high pores per inch (ppi) filter grades [1].
In the present study the influence of the magnetic field on the priming and wetting ability that the aluminium alloy A356 has on the ceramic surface of the CFF will be studied, as well as the possible impact it may have on the filtration mechanisms inside the ceramic filters by analysing the distribution of the 13-23 µm SiC particles. 2-D axial symmetric COMSOL® (Version 4.2) models and analytical modelling will be performed to estimate the heat and Lorentz forces produced, as well as to study the flow pattern induced in the melt inside of the filter elements.

2. Materials and Experimental Methods

In the present experimental set-up the time varying magnetic field induces currents in the molten metal that is contained in the apparatus. The cross product of the induced current and the magnetic field generates in turn a magnetic pressure, and the gradient of the flux density along the axis of the coil creates a pressure gradient. The pressure gradient results in a curl which then induces a bulk flow in the metal. The curl of the Lorentz force is highly dependent on the conductivity of the metal and the effective conductivity of the metal within the CFF, which is reduced due to the tortuosity and porosity of the filter. The induced liquid metal velocity within the CFF can be determined by using the fluid permeability of the filter media. Due to the high induced velocity within the filter both the Darcian and Non-Darcian permeability terms are required to be solved for the resulting flow field using a Finite Element Model (FEM). A review of the pertinent theory [2], the experimental development [1], and the validation [3-4] of the COMSOL® induction heating/magnetic field model [5] have already been published earlier by members of the present research group. The details of the model computations are beyond the scope of the present paper and can be found elsewhere [3-5].

Bach filtration experiments were conducted using ~5000 g of molten charge, *i.e.* 90 wt. % of the aluminium alloy A356 doped with 10 wt. % A356 composites, containing 15 wt. % SiC particles with a particle size ranging from

13 to 23 µm. The melt was heated to ~750°C in a high frequency induction furnace, *i.e.* one separate melt for each batch filtration experiment. The experimental filtration set-up was energized at 50 Hz, and the molten metal was poured into the apparatus until a metallic head of ~100 mm above the filter was reached. For each filter grade, experiments were conducted at 3 and 10 minutes treatment times. Gravity reference experiments were also performed for each filter grade. Special trials to investigate the required gravity priming height of the different grade CFF's studied were also executed. For the metallographic evaluation of the obtained results 12 samples were extracted from each of the filter elements. Scanning Electron Microscopy (SEM) was used to analyse the samples using the Back Scattered Electron (BSE) mode. The magnetic field density was estimated using FEM by integrating from the bottom to the top of the innermost coil along the surface of the work piece, and the average Lorentz force along the surface of the filter integrated from the bottom to the top of the filter. The Lorentz force obtained under the filter was, however, integrated from the bottom of the liquid metal to the bottom of the filter.

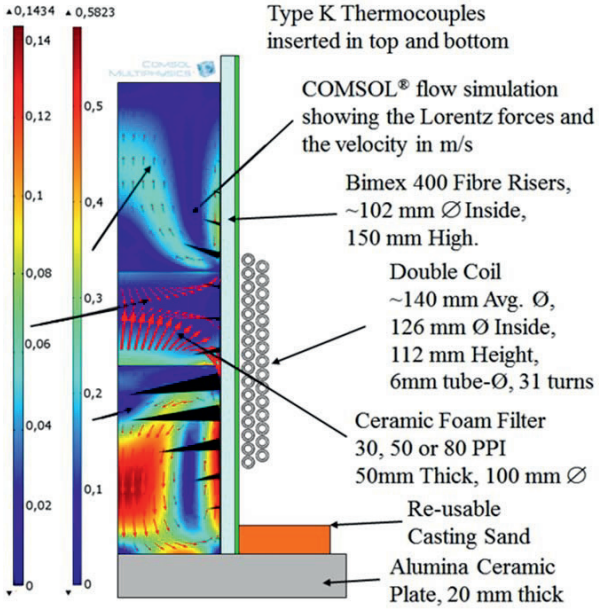

Figure 1: Presently adopted experimental setup with COMSOL® FEM simulation of the flow field (arrows and shading), as well as the Lorentz forces (cones), for a 50 ppi CFF. The applied conditions are summarised in Table 1. A detailed description of the coil design has been presented in earlier papers by members of the present research group [2-5].

In Figure the experimental apparatus used (i) for the 50 and 80 ppi experiments, (ii) for the FEM calculated flow field for a 50 ppi CFF, and (iii) for the FEM calculated induced Lorentz forces on the outer surface of the work piece is presented. It should be mentioned that due to the effect of the Lorentz forces, the flow velocity inside the filter is estimated to be one order of magnitude higher compared to normal industrial casting conditions (as indicated in Figure 1). Typical experimental data and FEM model results are summarised in Table 1.

Table 1: Summary of experimental and modelling data obtained using a magnetic field and various CFF grades. The apparent porosity has been calculated from the total filter density (*e.g.* 0.47 g/cm^3) and the density of the ceramic particles (*i.e.* 3.48 g/cm^3).

CFF (ppi)	Temp. (°C)	Apparent Porosity (%)	Metal Conductivity (MS/m)[5]	Amps (A)	FEM Magnetic Field (T)	FEM Calculated Power (kW)	Effective Resistivity of Filter (R_f/R_m)	Average Surface Lorentz Force Filter/Under-Filter (10^4 N/m^3)
30	727	89.3	3.22	715	0.166	1.70	1.5	10.8 / 10.9
50	765	86.3	3.16	719	0.156	1.54	2.5	5.48 / 11.0
80	705	86.5	3.26	718	0.157	1.44	3.7	2.51 / 11.4

3. Results and Discussion

3.1 Priming and wetting

CFF's are normally operated in a "filter bowl" and are primed using a gravity head of liquid metal with a recommended pre-heating procedure. In other words, the gravity head forces the metal into and through the CFF, displacing much of the entrapped air. The poor wetting characteristics of alumina by aluminium [7], and the need to remove the trapped air, can lead to difficulties at the start of the filtration process (particularly with high pore density filters). The typical heights of industrial priming heads are, for different grades of commercial filters, plotted in Figure 2. As can be seen from the figure, the presence of an electromagnetic field secures a significant reduction in the required metal head during priming.

In Figures 3 a) and b) metallographic pictures of the 50 and 80 ppi CFF's after a gravity priming experiment with 100 mm metal head above the filter element is presented. As can be seen from the figures the experiments failed and the molten metal solidified over the filter elements with nearly complete lack of penetration of metal into the filters. This was, however, expected based on the industrial priming data presented in Figure 2.

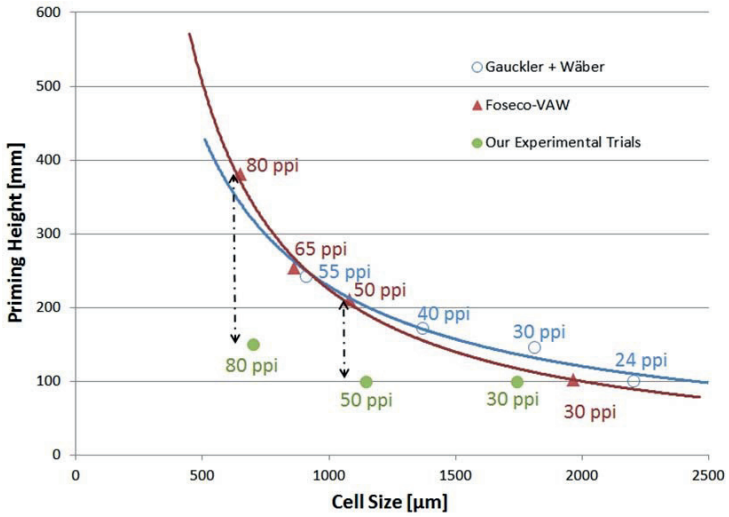

Figure 2: The presently measured priming height from the electromagnetic field experiments are plotted as a function of the filter cell size. The measured priming height from earlier publications has been included as a comparison [8].

When applying a magnetic field of ~0.16 T, the filters studied were nearly perfectly primed and wetted using the same 100 mm of metal head, see Figures 3 c) and d) representing the results obtained for 3 and 10 minutes treatment time. The SEM micrographs obtained shows a greatly improved wetting, as well as successful removal of gas with an increased electromagnetic stirring time. The electromagnetic priming phenomena are now the subject of an US patent application filed by the present authors [9].

3.2 Particle redistribution

For gravity filtration it is common to observe a dense filter cake above the CFF, as well as bridging and clogging in the upper part of the filter. Profound changes in the distribution of particles, both inside and below the filter

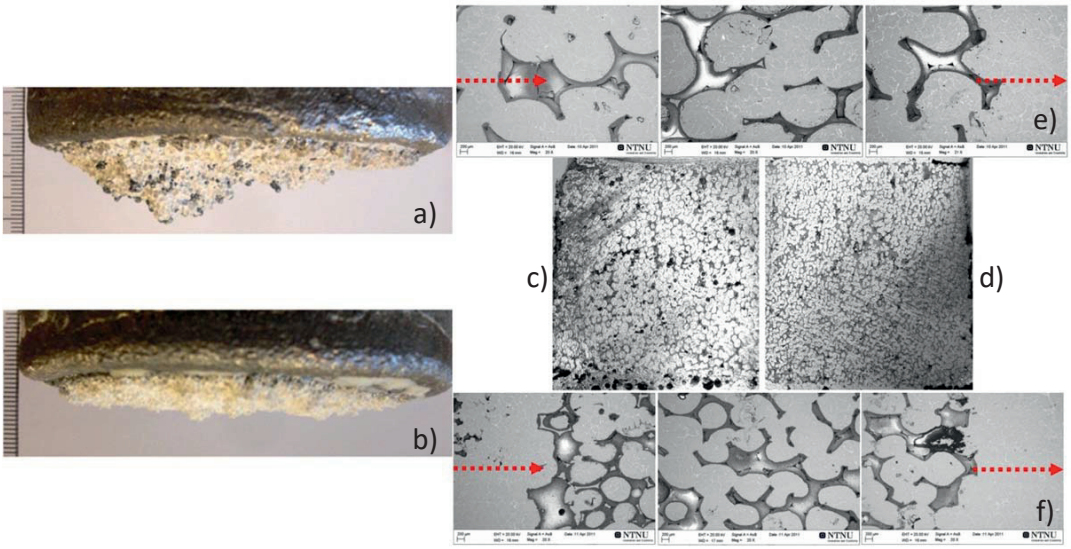

Figure 3: Unsuccessful gravity experiments with (a) 50 ppi CFF's and (b) 80 ppi CFF's. Fully primed and well wetted filters were obtained after 3 minutes of electromagnetic stirring, for (c) 50 ppi CFF's, and for (d) 80 ppi CFF's shown as half filter sections. Complete gas removal was obtained after 10 minutes of electromagnetic stirring for 80 ppi CFF's. The arrows represent the flow direction of the melt.

media have, however, been observed in the present work due to the influence of the electromagnetic field, see Figure 4. As can be seen from the figure, when using electromagnetic forces the highest particle density obtained was observed in Area 2. In addition, the backflow of the melt caused by the curl in the Lorentz forces has resulted in Area 3 also having a higher concentration of particles. Area 4, however, was nearly particle free due to that clean metal re-enters the filter from below.

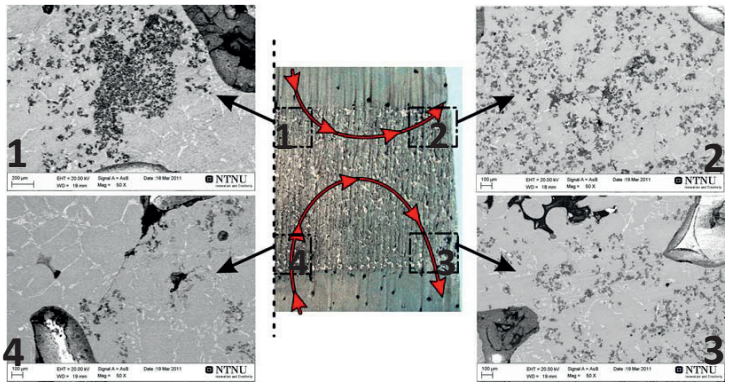

Figure 4: Observed distribution of particles in a 30 ppi half filter section and the FEM estimated flow field (arrow) inside the filter media. The numbers mark the areas clockwise starting at the centre on the top (Area 1) and ending in the centre below the filter (Area 4). In Area 2 the highest density of particles was observed, followed by Area 3 and Area 1 with a more or less equal distribution of particles. Nearly no particles were observed in Area 4. The original gravity feed of metal was from the top to the bottom.

4. Conclusion

The present study has proven that by applying an electromagnetic field a substantial improvement of the wetting between alumina and liquid aluminium in 30, 50 and 80 ppi CFF's can be obtained with a significant reduction of the required metal head. Nearly perfect priming of high pore density filters was demonstrated. A redistribution of particles inside the CFF was also observed. Based on this it is clear that the electromagnetically induced bulk flow secures that the filter media do not clog, and changes the filtration mode from cake-filtration to deep-bed and in-bed-cake-filtration for the high pore density filters.

5. Acknowledgements

The present study was carried out as part of the RIRA (Remelting and Inclusion Refining of Aluminium) project funded by the Norwegian Research Council (NRC) - BIP Project No. 179947/I40. The authors wish to express their gratitude to Egil Torsetnes (NTNU, Trondheim, Norway) for helping with design and construction of the experimental apparatus. Deepest gratitude is also due to Kurt Sandaunet (SINTEF, Trondheim, Norway) for the use of the SINTEF laboratory and his contribution in the execution of the experiments. Also, a special thanks to Liss Pedersen (Alcoa, Lista, Norway) for the supply of filter materials, and Kexu Zhang (M.Sc. student at NTNU, Trondheim, Norway) for providing the CFF permeability data.

6. References

[1] KENNEDY M W, AKHTAR S, BAKKEN J A, AUNE R E, Electromagnetically Enhanced Filtration of Aluminium Melts. Light Metals, 2011, 763-768.
[2] KENNEDY M W, AKHTAR S, BAKKEN J A, AUNE R E, Review of Classical Design Methods as Applied to Aluminium Billet Heating with Induction Coils. EPD Congress, 2011, 707-722.
[3] KENNEDY M W, AKHTAR S, BAKKEN J A, AUNE R E, Analytical and Experimental Validation of Electromagnetic Simulations Using COMSOL®, re Inductance, Induction Heating and Magnetic Fields presented at the COMSOL User Conference, Stuttgart, Germany, 2012, 1-9.
[4] KENNEDY M W, AKHTAR S, BAKKEN J A, AUNE R E, Analytical and FEM Modelling of Aluminium Billets Induction Heating with Experimental Verification. Light Metals, 2012, 269-275.
[5] KENNEDY M W, AKHTAR S, BAKKEN J A, AUNE R E, Improved Short Coil Correction Factor for Induction Heating of Billets. 3rd International Symposium on High-Temperature Metallurgical Processing, 2012, 373-382.
[6] BRANDT R, NEUER G, Electrical Resistivity and Thermal Conductivity of Pure Aluminium and Aluminium Alloys up to and above the Melting Temperature. International Journal of Thermophysics, 2007, 1429-1446.
[7] FREUND H, ZEISER T, SCHWEIGER W, INAYAT A, Determining the Specific Surface Area of Ceramic Foams: The Tetrakaidecahedra Model Revisited. Chemical Engineering Science, 2011, 1179-1188.
[8] KEEGAN N J, SCHNEIDER W, KRUG H P, Evaluation of the Efficiency of Fine Pore Ceramic Foam Filters. Light Metals, 1999, 1031-1041.
[9] KENNEDY M W, FRITZSCH R, AKTHAR S, BAKKEN J A, AUNE R E, U.S. Patent Application 61/639,196, Apparatus and Method for Priming a Molten Metal Filter, May, 2012.

Supplement 4

Electromagnetic Priming of Ceramic Foam Filters (CFF) for Liquid Aluminum Filtration

R. Fritzsch, M. W. Kennedy, J. A. Bakken, and R. E. Aune

Light Metals 2013, page 973-979

DOI: 10.1002/9781118663189.ch165

Electromagnetic Priming of Ceramic Foam Filters (CFF) for Liquid Aluminum Filtration

Robert Fritzsch[1], Mark William Kennedy[1,2], Jon A. Bakken[1], Ragnhild E. Aune[1,3]

[1]Department of Materials Science and Engineering, Norwegian University of Science and Technology, N-7491 Trondheim, NORWAY
[2]Proval Partners S.A., 70 Rue de Genève, 1004 Lausanne, SWITZERLAND
[3]Department of Materials Science and Engineering, Royal Institute of Technology, 100 44 Stockholm, SWEDEN
Communicating author: ragnhild.aune@ntnu.no

Keywords: Priming, Electromagnetism, CFF, Aluminum

Abstract

Commercial Ceramic Foam Filters (CFF) of 30, 50 and 80 Pores Per Inch (PPI) have been primed, using magnetic field strengths of 0.06-0.2T, for periods of 1-10 minutes. The influence of time and field strength on the gas removal from the CFF structure, and the resulting improvements in filter productivity, are discussed. The obtained results are related to Finite Element Modeling (FEM) of the metal flow fields induced by the electromagnetic Lorentz forces. Higher filtration rates were obtained for 50 PPI magnetically primed, than for 30 PPI gravity primed filters. This suggests that electromagnetic priming offers an opportunity to use 50 PPI filters, with a higher overall filtration efficiency than 30 PPI filters, in existing cast house applications where the low productivity/high priming head of these filters would otherwise rule them out. Estimated filtration efficiency of different filter types are presented as functions of velocity and thickness.

Introduction

Aluminum melts contains a large number of inclusion particulates of ≤ 50 µm in size. These inclusions may be particles, bifilms or clusters of: oxides (Al_2O_3, SiO_2), spinels ($MgO{\cdot}Al_2O_3$), carbides (SiC, Al_4C_3), nitrides (AlN), borides (TiB_2), sulfides, phosphides and intermetallics [1]. Large concentrations or inclusions over critical size limits can render metal un-fit for purpose and result in serious financial consequences for metal producers. Inclusions in the aluminum melt can have a negative impact on the machinability, mechanical properties, and can lead to increased gas porosity and shrinkage of the material during casting [1]. Higher utilization of post-consumed and process aluminum scrap will increase the potential for melt contamination by inclusions and result in greater challenges to achieve both metal yield and the required quality standards. These challenges can be expected to increase in the future.

The aluminum industry has developed a number of treatment processes to improve metal cleanliness. CFFs are the most commonly applied filtration process and have been used to filter >50% of the world production of aluminum since the 1990's [2].

Recently the impact of electromagnetic fields generated by solenoidal coils on the filtration of SiC inclusions with CFFs has been a subject of experimental study. Batch filtration experiments [3, 4] to investigate the impact of the electromagnetic (EM) field on metal flow inside the filter and flow filtration experiments to determine the quantitative filtration efficiency [5] have been conducted with 30, 50 and 80 PPI CFFs. The particle sizes in the recent experiments were small, the particles were well wet by the aluminum (unlike alumina or bifilms) and the concentration was extremely high; hence, the measured filtration efficiency is not directly comparable to industrial conditions. The focus of this paper is therefore on measured priming behavior and not experimental filtration efficiency. Filtration efficiency will be discussed on the basis of published filtration models for 'normal' particles in standard alloys, and for commercially significant casting velocities.

Theory

Electromagnetic priming was discovered during early development work and is the subject of a recent US patent application [6]. It has been found that in the presence of an AC magnetic field, CFFs of 30-80 PPI can be primed without preheating, while using only 100-150 mm of metal head. This simple and highly effective procedure will be described in further detail in this paper and the possible implications for the commercial filtration process discussed.

Helical induction coils have been combined with standard Ceramic Foam Filters (CFFs) in recent experiments in order to study the impact of electromagnetic Lorentz forces on the filtration of liquid aluminum, as shown in Figure 1 [5]. An alternating current (50 Hz) was applied to the coil in the phi-direction, which produced a time varying magnetic flux density, B_z [T] along the vertical z-axis of the apparatus. The time varying magnetic field induced currents, J_ϕ [A/m^2] in the liquid metal over, inside and under the CFFs, in a direction opposing the current applied to the coil (negative phi-direction). Electromagnetic Lorentz forces, F_r [N/m^3] were produced by the interaction

of the flux density and the induced current density, according to the cross product (in the negative r-direction):

$$F_r = J_\phi \times B_z \qquad [1]$$

A gradient exists in the flux density along the z-axis of real, i.e. 'short' coils [3], which in turn leads to a gradient in the induced current. These two gradients combine to make a significant gradient and curl in the induced Lorentz forces. The curl is further accentuated by the differences in the electrical conductivity in the filter region [4], causing powerful magneto-hydrodynamic mixing (MHD) effects to be created. The effective conductivity of the metal within the CFF, is reduced due to the tortuosity and porosity of the filter [7]. Lorentz forces and the resulting MHD flow fields will be presented based on the output from a COMSOL® 2D axial symmetric finite element model (FEM). The validation of the COMSOL® induction heating/magnetic field model has been published elsewhere [8-10].

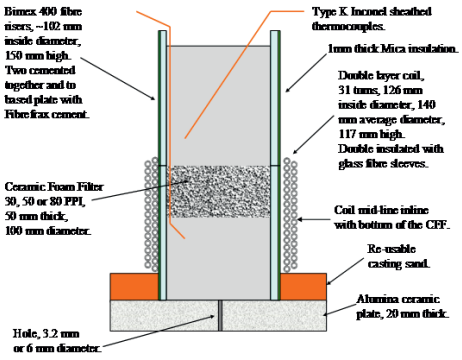

Figure 1. Schematic of the experimental apparatus used for filtration experiments. The mid-line of the coil and highest flux density is in line with the bottom of the CFF [5].

Experimental Methods and Materials

Experiments (12) were recently conducted using 150 kg batches of melt, for 4 experiments of up to 25 kg each. The charge was mixed and melted in a graphite agitated resistance furnace with a target temperature of 1023 K. The melt recipe was 90% A356 alloy, and 10% A356 composite master alloy, which reportedly containing 15 wt. % SiC particles, with a size range of 13-23 µm. The detailed experimental procedures have been described elsewhere [3, 5].

The filters were primed electromagnetically for 6 minutes at the start of each the EM experiments. A current of approximately 730 A was applied to the 31 turn induction coil (shown in Figure 1) and aluminum was added to the apparatus without preheating of the filter element. The electromagnetic field was active while pouring of the melt into the crucible. During the priming, the metallic head was kept relatively constant at ~150 mm. A maximum head of 150 mm was sufficient to prime 30, 50 and 80 PPI filters in all cases. After priming a discharge hole was opened in the bottom of the alumina plate for subsequent filtration efficiency measurements, as shown in Figure 2. Flow rate during filtration was determined by gain-in-weight on the receiving vessel and weightometer shown in Figure 2.

Electromagnetic priming has also been explored via batch experiments using:

- Different coil configurations (single and double layer),
- Various magnetic flux densities (0.06-0.2 T),
- Various test durations (1-10 minutes), and
- Filter types (30, 50 and 80 PPI).

Experiments using gravity priming for 30, 50 and 80 PPI have also been conducted.

Figure 2. Experimental apparatus for the flow filtration experiments, showing aluminum metal being added continuously via a ladle and discharging into a receiving vessel placed on a weightometer [5].

Priming and wetting

CFF's are normally operated in a "filter bowl" and are primed using a gravity head of liquid metal with a recommended pre-heating procedure [11]. The gravity head forces the metal into and through the CFF, displacing much of the interstitial air. The poor wetting characteristics of alumina by aluminum and the need to remove air can lead to difficulties at the start of the filtration process, particularly with high pore density filters. The typical magnitudes of industrial priming heads are plotted in Figure 3 for different grades of commercial filters [12, 13].

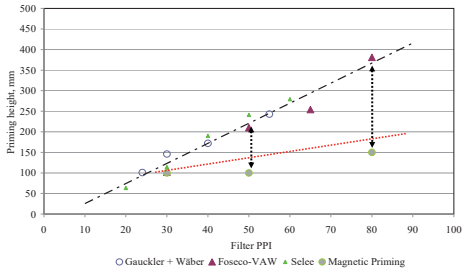

Figure 3. Priming height vs. filter PPI from different producers compared with electromagnetic priming at ~0.17 T [12, 13]. 30 PPI filters could have been primed with less than 100 mm of metal head, as indicated by the dotted red line.

Photographic images of the (a) 50 and (b) 80 PPI CFFs after a gravity priming experiments using 100 mm metal head, are shown in Figure 4. The filters failed to prime, as had been fully expected based on Figure 3. The molten metal solidified over the filter elements with nearly complete lack of penetration of metal into the filters. The filters have been removed, showing the 7-18 mm of penetration, i.e. the small amount of CFF remaining attached to the underside of the frozen metal.

Repeating the experiments in the presence of an electromagnetic field (~0.17 T), results in complete filter priming, with the same initial 100 mm of metal head as indicated for (a) 50 PPI and (b) 80 PPI CFF in Figure 5. 150 mm of head is recommended for 80 PPI CFFs as shown in Figure 3, based on experiences over many batch and flow experiments, to ensure rapid metal penetration without requiring excessive initial metal superheat.

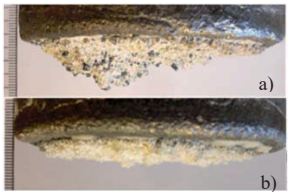

Figure 4. 'Unsuccessful' gravity experiments with 150 mm of head showing metal frozen over the filter with: (a) ~18 mm of metal penetration, using a 50 PPI CFF and (b) less than 7 mm of metal penetration, using a 80 PPI CFF.

The vertical filter sections Figures 5 (a) and (b), show improved filter wetting, as well as successful removal of most gas after only 3 minutes of electromagnetic priming. This can be better observed in the SEM micrographs (c) 50 PPI and (d) 80 PPI, after 10 minutes of electromagnetic priming.

Additional experiments have successfully primed stacks of (3) 30, 40, 50 and 80 PPI CFFs, with a metal head of 150 mm using an ~0.17 T electromagnetic field and the same coil pictured in Figures 1 and 2.

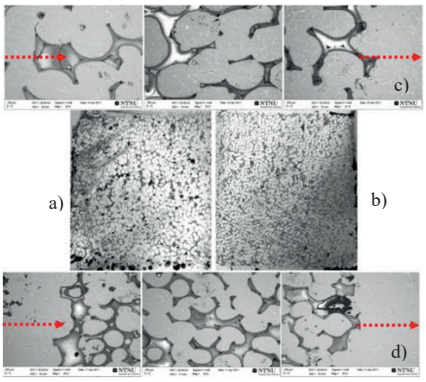

Figure 5. Fully primed and well wetted filters were obtained after 3 minutes of electromagnetic stirring, for (a) 50 PPI and for (b) 80 PPI CFFs, shown as half filter sections (50 mm thick and 50 mm radius). Complete gas removal was obtained after 10 minutes of electromagnetic stirring for c) 50 PPI and d) 80 PPI CFFs. The arrows represent the flow direction of the melt.

Filter productivity

It had been assumed that more efficient removal of gas would leave more of the interstitial volume of the CFFs available for flow, reducing the internal liquid velocity and pressure drop during filtration. Lower pressure drop would lead to increased productivity for any applied metal head during subsequent gravity filtration. The gravity filtration productivity, when using ~150 mm metal head has been plotted in Figure 6 for 30 PPI (gravity and EM primed) and 50 PPI filters (EM primed). Results indicate that both the EM primed 30 and 50 PPI filters had 25% more throughput than a gravity primed 30 PPI CFF. The high initial discharge rate for the 50 PPI filter was not maintained past 10 kg, due to the build up of 'cake' pressure drop. A very high loading of inclusions was used, such that each kg of metal filtered was equivalent to approximately 4 mt of typical industrial quality metal [5].

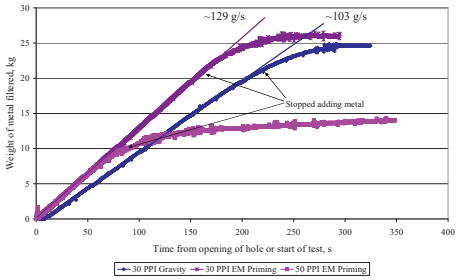

Figure 6. Impact of electromagnetic priming on filter productivity using ~150 mm of metal head for 30 PPI filters with and without EM priming, and a 50 PPI filter with EM priming. The EM primed 50 PPI filter had the same initial discharge rate as the 30 PPI EM primed and had a 25% greater discharge rate than the 30 PPI with gravity priming.

Efficiency of inclusion removal during gravity filtration after electromagnetic priming appeared to behave like conventional gravity filtration after gravity priming, once the increased superficial velocity was accounted for [5]. With electromagnetic priming, higher velocities were obtained as indicated in Figure 6 for a fixed metal head, and therefore slightly lower filtration efficiencies resulted.

Flow Field Modeling

In order to better understand the impact of the electromagnetic fields on priming, 2D axial symmetric FEM, using the commercial COMSOL® 4.2a code, were used to solve for steady state flow field solutions. Results are described in more detail elsewhere [5].

In Figure 7, the velocity field during the initial phase of the priming process is shown. The priming process begins with no metal and hence no Lorentz forces inside of the CFFs, greatly enhancing the curl, and creating substantial pressure gradients. The velocity magnitude is marked in Figure 7 with red arrows, and is estimated to be up to ~100 times higher than the typical industrial casting velocity as indicated in Table I [11].

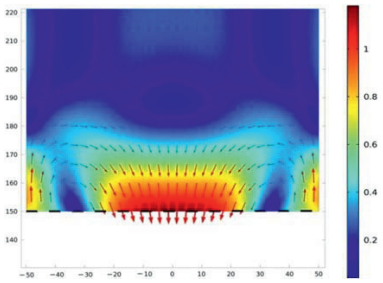

Figure 7. Initial induced flow field at during filter priming, showing the velocity field induced in the metal above the filter [m/s]. Metal is being continuously added to maintain the total metal head and is flowing 'out' at the bottom, i.e. filling the porous media of the ceramic filter [14].

Table I. Industrial Casting Velocity, Metal Flux and PPI Range for Different Casting Applications [11]

Type of Casting	Superficial Velocity mm/s	Metal Flux kg/s/m^2	Typical Pore Range
Billet	8-15	19-36	30-40
Slag	7-12	17-29	40-65
Continuous	2.5-8	6-19	20-50

After complete metal filling of the experimental apparatus shown in Figure 1 and 2, a very different flow pattern emerges. Current and hence Lorentz forces are now generated within the filter media and an upward metal flow is produced as indicated in Figure 8 for 30-80 PPI filters [5]. The upward flowing metal progressively removes gas trapped within the filter, as shown previously in Figure 5.

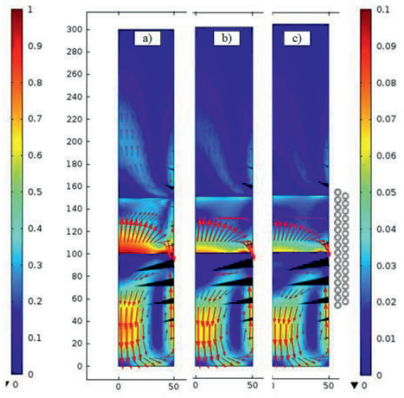

Figure 8. Flow fields calculated for (a) 30, (b) 50 and (c) 80 PPI filters, velocities scales indicated in m/s, left-hand scale is for metal regions, and the right-hand scale is for porous media regions. Position of induction coil is shown. Peak velocities in metal: 0.71, 0.64 and 0.64 m/s and in the filter: 0.19, 0.15 and 0.13 m/s, respectively. Conical arrows indicate relative Lorentz force strength (RMS). Regular arrows indicate direction and magnitude of fluid flow in metal and porous media regions, sizes are not comparable between regions [5].

Filtration Efficiency Modeling

The filtration efficiency is defined based on particle counts (either total or grouped into suitable size ranges):

$$E = \frac{N_i - N_0}{N_i} \qquad [2]$$

Where N_{in} is the count of particles entering into the filter per unit time, and N_{out} is the count of particles out of the filter per unit time.

Filtration efficiency can be empirically modeled using relatively simple models such as the one introduced by Iwasaki in 1937 [15]. Iwasaki defined the initial filtration efficiency E_0 (i.e. prior to the accumulation of significant particulates) using an initial filter coefficient λ_0 [mm^{-1}]:

$$E_0 = 1 - \exp^{-\lambda_0 L} \quad E_0 = 1\text{-}\exp^{-\lambda_0 L} \qquad [3]$$

Where L is the filter thickness [mm]. For most commercial CFFs, L has a magnitude of ~50 mm.

A slightly modified version of Iwasaki's equation was adopted by Apelian *et al.* [16] for the modeling of aluminum filtration, which accounts explicitly for superficial velocity.

$$E_0 = 1 - \exp^{-\frac{K_0 L}{u_s}} \quad \text{E}_0 = 1\text{-exp}^{\frac{\cdot K_0 L}{u_s}} \qquad [4]$$

Where E_0 is the initial filtration efficiency [unitless], u_s the velocity [mm/s] and K_0 was defined by Apelian as the initial 'kinetic' parameter [s^{-1}]. Apelian found that while K_0 increases with velocity, that the overall filtration efficiency decreases with higher velocity. The observation of reduced filtration efficiency at higher velocity has been verified in subsequent investigations using CFFs [11, 17, 18], as well as in the current study using SiC [5].

Examining Equation [4] it is clear that filtration efficiency should improve with thicker filters. Filters deeper than 50 mm are probably not currently applied due to the difficulty in priming such filters. With electromagnetic filtration filters as thick as 150 mm have already been primed using less than commercial priming heights as discussed previously.

K_0 in Equation [4] is an empirical value, which is particular to each type or grade of filter, and related to the physical characteristics of the particles being filtered (size, wetting, shape, etc.). K_0 values are expected to be higher for filters of higher PPI grade. Industrially determined K_0 values taken from LiMCA (Liquid Metal Cleanliness Analyzer) data for 30 and 50 PPI filters have been used to explore the sensitivity of filtration efficiency to velocity, thickness and filter type using Equation 4 [11]. The original K_0 values of Ray *et al.* have been adjusted to be in accordance with the use of superficial velocity in Equation [4] as shown in Table II.

Table II. K_0 Values for Pseudo-interstitial Velocity [11] and Superficial Velocity for 30 and 50 PPI CFFs

Size Group	30 PPI CFF	50 PPI CFF	30 PPI CFF	50 PPI CFF
	Pseudo-interstitial K_0 from literature [11]		Superficial corrected K_0	
15-20 µm	0.205	0.301	0.164	0.241
20-25 µm	0.250	0.360	0.200	0.288
25-30 µm	0.283	0.429	0.226	0.343
30-35 µm	0.323	0.478	0.258	0.382
35-40 µm	0.375	0.547	0.300	0.438
40-45 µm	0.409	0.627	0.327	0.502
45-50 µm	0.452	0.783	0.362	0.626
50-55 µm	0.509	0.940	0.407	0.752
55-60 µm	0.596	1.100	0.477	0.880
60+ µm	0.725	1.350	0.580	1.080

The impact of superficial velocity on filtration efficiency can be estimated using the adjusted K_0 values from Table II and Equation [4], as shown for both 30 and 50 PPI CFFs in Figure 9 for the industry standard 50 mm filter thickness as functions of particle size. The base case superficial velocity of 7.3 mm/s is equivalent to the 9.1 mm/s pseudo-interstitial velocity of Ray *et al.* [11]. Velocities covering a similar range to those shown in Table I have been selected. The estimated filtration efficiencies plotted in Figure 9 suggest that very high efficiency (>80%) can be obtained even for small 15-20 µm particles provided the filters are operated with a low enough velocity for 30 PPI filters. This would imply that filters of large area would be required to maintain productivity at such a low superficial velocity.

Figure 9 implies that a 50 PPI filter should be able to operate at significantly higher throughput (e.g. 7.3 vs. 5 mm/s) and achieve similar filtration efficiencies than a 30 PPI. At the same filtration velocity, about 10-20% higher filtration efficiency is achieved.

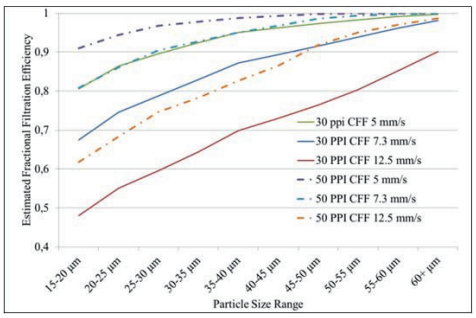

Figure 9. Estimated fractional filtration efficiency vs. particle size from 15 to >60 µm, for different superficial velocities using 50 mm thick 30 PPI CFFs (continuous lines) and 50 PPI CFFs (dotted lines).

An alternative to a very large filter area, is thicker filters to achieve similar high efficiencies. The impact of alternate thicknesses on filter performance is explored in Figure 10 for 30 PPI filters using the base case filtration velocity of 7.3 mm/s.

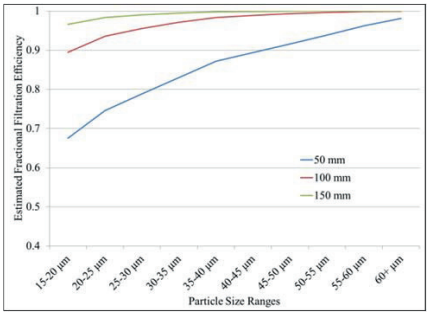

Figure 10. Estimated fractional filtration efficiency vs. particle size from 15 to >60 µm for three different filter thicknesses from 50-150 mm using 30 PPI CFFs.

Approximately 90% filtration efficiency can be obtained at the default 7.3 mm/s filtration velocity using 100 mm or thicker 30 PPI filters, representing an improvement of over 20%.

Filter Pressure Drop

If the option of thicker filters is to be applied, it is also necessary to calculate the metal head required to sustain the desired superficial velocity. The pressure gradient over the CFF can be estimated using the Forchheimer equation, as shown in Equation [5].

$$\frac{\Delta P}{L} = \frac{\mu}{k_1} u_s + \frac{\rho}{k_2} u_s^2 \qquad [5]$$

where ΔP is the pressure drop [Pa], L is the filter thickness [m], u_s is the fluid superficial velocity [m/s], μ is the fluid dynamic viscosity [Pa·s], ρ is the fluid density [kg/m^3], k_1 [m^2] and k_2 [m] are empirical constants called the Darcian and non-Darcian permeability coefficients. Recommended values for k_1 and k_2 are shown in Table III [7].

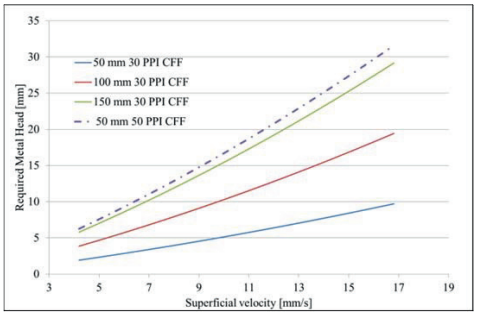

Figure 11. Metal head required to sustain flow as a function of superficial velocity, u_s shown in [mm/s] and filter thickness, L shown in [mm] from Equation [5], for 30 and 50 PPI filters.

A comparison of Figure 3 and Figure 11, indicates that much higher metal heads are required to prime than to sustain flow after priming, even assuming much thicker, e.g. 150 mm filters, than applied in industry today. An opportunity exists to apply electromagnetic priming to stacks of filters in existing filter box installations to prime 2 or 3 standard thicknesses of 50 mm filters and achieve higher filtration efficiencies, as indicated by the estimates shown previously in Figure 10.

Alternatively electromagnetic priming can be used to prime and enhance the productivity of higher grade, e.g. 50 PPI filters, which achieve improved filtration performances over 30 PPI as shown previously in Figure 9. Figure 11, indicates the required pressure drop to maintain flow for such a filter, verifying that priming head and not pressure drop during filtration is likely the factor determining usage.

Table III. Darcian K_1 and Non-Darcian K_2 Values for calculating the metal head regarding the superficial velocity for 30 and 50 PPI CFFs using the Forchheimer equation [7].

Filter Type (PPI)	Eq. 5 Forchheimer k_1 (m^2)	Eq. 5 Forchheimer k_2 (m)
30	5.08E-08	5.46E-04
40	3.10E-08	3.38E-04
50	1.57E-08	1.66E-04
80	6.52E-09	1.15E-04

Conclusions

Electromagnetic priming has been demonstrated to prime CFFs with less than the industry standard metal heads. The required metal head for electromagnetic priming of high PPI CFFs (50 and 80) was ~1/3rd of the standard height as published previously for industry. Furthermore, using electromagnetic priming, stacks of up to 3 filters have been primed using the same low metal heads.

The maximum allowable metal height in filter boxes currently dictates the type of filters and filtration rates that can be applied in industry. Based on the analysis of the filter permeability, it is the priming height and not the pressure drop during casting, which should typically limit the type of filter applied. Electromagnetic priming should allow higher PPI filters to be applied in existing filter bowls, than could otherwise be applied.

Furthermore the more efficient removal of gas from the CFFs should allow for lower metal height during filtration for a given throughput or a higher throughput for a given metal height. This may also make it practical to use for example 50 PPI filters with more consistent filtration performance to replace 30 PPI filters.

Improved melt quality can be achieved either by the use of higher PPI filters, lower velocities (and hence larger filtration areas) or thicker filters. With the use of electromagnetic priming both thicker filters and higher PPI filters become practicable for existing filter boxes.

Future Work

Experimental trials will be conducted to electromagnetically prime a stack of 3, 30 PPI grade CFFs. Lower grade CFFs may also be tested, e.g. 10 or 20 PPI. Gravity filtration experiments will be conducted to determine the filtration efficiency and verify the estimates given in Figures 9-10. Furthermore the application of an electromagnetic field to prime standard sized filters will be demonstrated in slightly modified industry standard filter boxes.

Acknowledgements

The present study was carried out as part of the RIRA (Remelting and Inclusion Refining of Aluminium) project funded by the Norwegian Research Council (NRC) - BIP Project No. 179947/I40. The industrial partners involved in the project are: Hydro Aluminium AS, SAPA Heat Transfer AB, Alcoa Norway ANS, Norwegian University of Science and Technology (NTNU) and SINTEF Materials and Chemistry. The funding granted by the industrial partners and the NRC is gratefully acknowledged.

The authors also wish to express their gratitude to Egil Torsetnes at NTNU for helping with the design and construction of the experimental apparatus. Sincere gratitude is also due to Kurt Sandaunet and Arne Nordmark of SINTEF for their support and help, as well as for the use of the SINTEF casting laboratory.

References

1. D. E. Groteke, "The Reduction of Inclusions in Aluminum by Filtration," Modern Casting, vol. 73, (1983), 25-27.
2. K. Butcher and D. Rogers, "Update on the Filtration of Aluminum Alloys with Fine Pore Ceramic Foam," Light Metals, (1990), 797-803.
3. M. W. Kennedy, S. Akhtar, J. A. Bakken and R. E. Aune, "Electromagnetically Enhanced Filtration of Aluminum Melts," Light Metals, (2011), 763-768.
4. R. Fritzsch, M. W. Kennedy, S. Akhtar, J. A. Bakken and R. E. Aune, "Electromagnetically Modified Filtration of Liquid Aluminium with a Ceramic Foam Filter," Accepted for Journal of Iron and Steel Research International, (2012), 1-4.
5. M. W. Kennedy, R. Fritzsch, S. Akhtar, J. A. Bakken and R. E. Aune, "Electromagnetically Modified Filtration of Aluminum Melts Part II: Filtration Theory and Experimental Filtration Efficiency with and without Electromagnetic Priming for 30, 50 and 80 PPI Ceramic Foam Filters," To be submitted to Metallurgical Transactions B, (2012), 1-69.
6. M. W. Kennedy, R. Fritzsch, S. Akhtar, J. A. Bakken and R. E. Aune, "Apparatus and Method for Priming a Molten Metal Filter," U.S. Patent Application, (2012), 1-26.
7. M. W. Kennedy, K. Zhang, R. Fritzsch, S. Akhtar, J. A. Bakken and R. E. Aune, "Characterization of Ceramic Foam Filters used for Liquid Metal Filtration," To be submitted to Metallurgical Transactions B, (2012), 1-46.
8. M. W. Kennedy, S. Akhtar, J. A. Bakken and R. E. Aune, "Analytical and Experimental Validation of Electromagnetic Simulations Using COMSOL®, re Inductance, Induction Heating and Magnetic Fields," COMSOL Conference 2011, Stuttgart, Germany, (2011), 1-9.
9. M. W. Kennedy, S. Akhtar, J. A. Bakken and R. E. Aune, "Analytical and FEM Modeling of Aluminum Billet Induction Heating with Experimental Verification," Light Metals, (2012), 269-275.
10. M. W. Kennedy, S. Akhtar, J. A. Bakken and R. E. Aune, "Improved Short Coil Correction Factor for Induction Heating of Billets," 3rd International Symposium on High-Temperature Metallurgical Processing, (2012), 373-382.
11. S. Ray, B. Milligan and N. Keegan, "Measurement of Filtration Performance, Filtration Theory and Practical Applications of Ceramic Foam Filters," Aluminium Cast House Technology, (2005), 1-12.
12. J. E. Dore and C. Bickert, "A Practical Guide on How to Optimize Ceramic Foam Filter Performance," Light Metals, (1990), 791-796.
13. N. Keegan, W. Schneider and H. P. Krug, "Evaluation of the Efficiency of Fine Pore Ceramic Foam Filters," Light Metals-Warrendale, (1999), 1-10.
14. R. Fritzsch, "Filtration of Aluminium Melts using Ceramic Foam Filters (CCF) and Electromagnetic Field," Trondheim: NTNU, Norway, (2011), 1-86.
15. T. Iwasaki, J. Slade and W. E. Stanley, "Some Notes on Sand Filtration [with Discussion]," Journal of American Water Works Association, vol. 29, (1937), 1591-1602.
16. D. Apelian and R. Mutharasan, "Filtration: A Melt Refining Method," Journal of Metals, vol. 9, (1980), 14-19.
17. C. Conti and P. Netter, "Deep Filtration of Liquid Metals: Application of a Simplified Model Based on the Limiting Trajectory Method," Separations Technology, vol. 2, (1992), 46-56.
18. H. Duval, C. Rivière, É. Laé, P. Le Brun and J. B. Guillot, "Pilot-Scale Investigation of Liquid Aluminum Filtration through Ceramic Foam Filters: Comparison between Coulter Counter Measurements and Metallographic Analysis of Spent Filters," Metallurgical and Materials Transactions B, vol. 40, (2009), 233-246.

Supplement 5

Effect of Electromagnetic Fields on the Priming of High Grade Ceramic Foam Filters (CFF) with Liquid Aluminum

R. Fritzsch, M. W. Kennedy, S. Akbarnejad, and R. E. Aune

Light Metals 2015, page 929-935

DOI: 10.1002/9781119093435.ch156

EFFECT OF ELECTROMAGNETIC FIELDS ON THE PRIMING OF HIGH GRADE CERAMIC FOAM FILTERS (CFF) WITH LIQUID ALUMINUM

Robert Fritzsch[1], Mark William Kennedy[1,2], Shahin Akbarnejad[3], Ragnhild E. Aune[1]
[1]Dept. of Materials Science and Engineering, Norwegian University of Science and Technology (NTNU), Trondheim, NORWAY
[2]Proval Partners S.A., 70 Rue de Genève, 1004 Lausanne, SWITZERLAND
[3]Department of Materials Science and Engineering, Royal Institute of Technology, 100 44 Stockholm, SWEDEN.

Communicating author: robert.fritzsch@ntnu.no

KEYWORDS: Electromagnetism, Priming, Aluminum, CFF, Liquid Metal, Filtration

Abstract

Electromagnetic fields can influence the behavior of liquid metals in commercial Ceramic Foam Filters (CFF's). In the present study 9 inch industrial CFF's of high grade with 50 and 80 pores per inch (ppi) have been investigated. The main objective was to prime the 9 inch industrial scale CFF's with a standard aluminum casting alloy (3XXX - alloy) by the use of various magnetic field strengths (max. 0.12 T) induced by a coil. The obtained results were compared with reference gravity experiments. The influence of the electromagnetic Lorentz forces on the obtained results was calculated with 2D Finite Element Modeling (FEM) using the COMSOL® software. The fluid flow characteristics inside the CFF were considered and are part of another publication within the group.

Introduction

Aluminum melts contains a large number of inclusion particulates of ≤ 50 µm in size. These inclusions may be particles, bifilms or clusters of: oxides (Al_2O_3, SiO_2), spinels ($MgO{\cdot}Al_2O_3$), carbides (SiC, Al_4C_3), nitrides (AlN), borides (TiB_2), sulfides, phosphides and intermetallics [1]. Large concentrations or inclusions over a critical size limit can render the metal un-fit for industrial applications and result in serious financial consequences for metal producers. Many types of inclusions in the aluminum melt can have a negative impact on the machinability, mechanical properties, and can lead to increased gas porosity and shrinkage of the metal during casting [1]. Use of more post-consumed and process aluminum scrap further increases the potential for melt contamination by inclusions. This results in greater challenges to achieve metal yield and the required quality standards. These challenges can be expected to increase in the future.

In recent years, the aluminum industry has developed a number of treatment processes to improve metal cleanliness. CFF's are the most commonly applied filtration technology for aluminum alloys and have been used to filter over 50% of the world production of aluminum since the 1990's [2].

Electromagnetically (EM) enhanced filtration of aluminum has been the topic of recent studies [3]. Batch experiments with filters and liquid metal have been conducted to understand the impact of the magnetic field on the metal flow and particle migration inside the filter [4]. Flow filtration experiments with an applied EM field using a small scale setup, have been executed to investigate the effect also on the filtration efficiency [5]. All experiments that have been conducted so far were using 30, 50 and 80 ppi CFF's and using A356 aluminum alloy.

In the course of the previous filtration work it was discovered that priming of the filters, defined as the filling of the pores with metal and the removal of entrained gas, could also be achieved using the EM Lorentz forces produced in liquid metal by the alternating current induction coil. It was found that the Lorentz forces could be used to prime CFF's of up to 80 ppi without preheating and using only a fraction of the metal head that was typically required in conventional industrial filter units. These studies applied 100 to 150 mm of metal head to prime CFF's with an 80 ppi grade [4, 5] instead of the typical industrial values of up to 350 mm, showing that it was primarily the EM forces and not gravity, which primed the filters. The discovery of electromagnetic priming is now the subject of a US patent application [6].

Recently, the effect of an electromagnetic field generated by a square helically wound induction coil on the priming of a 9 inch commercial CFF has been the subject of experimental study. The current study focuses on the design and verification of a pilot scale filter unit, including the induction coil and the filter box. The required metal head to sufficiently prime and wet a commercial 9 inch filter with liquid aluminum is the main topic of this article. Experimental and FEM results computed using the multi-physics software COMSOL® will be presented.

Theory

In a helically wound induction coil an applied alternating current flows primarily in the phi direction and generates a time varying magnetic flux density B_z $[T]$ in the z-direction of the coil (noting that strong radial components also exist in the flux at the ends of the coil). The z-component of the magnetic flux then induces a current J_ϕ $[A/m^2]$ that opposes the main current in accordance with Lenz's law and the conservation of energy, in this case in the negative phi direction.

It is known that 'short' induction coils have a gradient in the local flux density B_z along the z-axis. The gradient in the magnetic field results in a similar variation in the magnitude of the induced current in the liquid metal. The magnitudes of the induced current are furthermore influenced by the effective

electrical conductivity within the filter media. The current and the magnetic flux therefore have different magnitudes above, within and under the filter. For a given applied current, filter type and aluminum conductivity the position of the filter within the coil then determines the amount of current induced by the local magnitude of the EM field.

Lorentz forces $F_L\,[N/m^3]$ are the cross product of the induced current density and the magnetic flux, as shown by [Eq. 1]. These forces act axial symmetrically on the aluminum and ignoring the small radial component of the flux density, can be assumed to act exclusively in the r-direction.

$$F_L = J_\phi \times B_z \qquad \text{[Eq. 1]}$$

The coil was placed as shown in Figure in order to maximize both the magnitude of the EM field on the surface of the filter and the curl in the induced Lorentz forces. Prior to priming, there is no electrical conductivity in the CFF and therefore no induced Lorentz forces. Therefore there initially exists a very strong axial gradient of F_L in the z-direction, which results in forceful Magneto-Hydro-Dynamic (MHD) movement and hence, the initial priming of the filter.

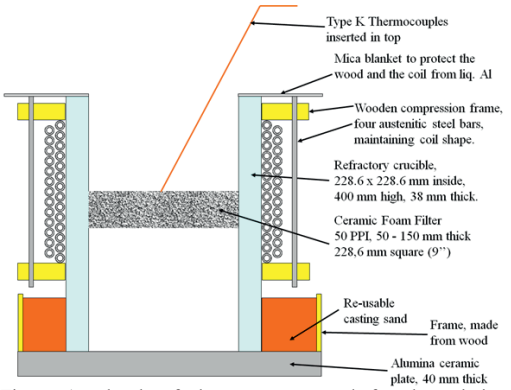

Figure 1: Sketch of the apparatus used for the priming experiments. The coil is placed with its center line at the top line of the CFF to generate the highest flux density at the entrance to the filter. During the experiments the coil was compressed by a wooden frame, covered in alumina sheets, to suppress vibrations and protect it from mechanical and thermal damage.

The difference in the effective conductivity of the filter area and the liquid metal region ensures a continuing curl in the Lorentz forces and continuing strong MHD mixing even after the initial priming [4]. This continuing MHD mixing also ensures that gas bubbles are removed and wetting is improved within the CFF after some time. The time varying value of the Lorentz forces induces metal vibrations, which combined with inductive heating, may contribute to improved gas release and wetting of the CFF by the liquid metal.

The effective conductivity of the filter region is determined by the porosity and tortuosity of the ceramic material. The effective conductivity was directly measured using reference metal of a known conductivity in a special coil set-up completely filled with liquid metal impregnated CFF's. The effective electrical conductivity could then be determined by the reduction in the induced power from the metal-only case. Estimates of tortuosity were then made from the effective electrical conductivity and the measured total porosity [7].

$$\frac{\sigma_m}{\sigma_f} = \frac{\tau}{\varepsilon} \qquad \text{[Eq.2]}$$

Where σ_f is the effective electrical conductivity of the filter media [S/m], σ_m is the conductivity of the metal [S/m], τ is the tortuosity [unit less] and ε as the total porosity [%].

The effective conductivity is essential to be able to generate 2D axial symmetric multi-physics models. The validation of the COMSOL® models for heating and for the magnetic field has been published elsewhere [8-10]. The method was successfully applied to round 100 mm filters in flow and batch experiments [11] and is now being applied on this next step to large industrial scale, i.e. the 9" or 229 mm scale.

Experimental Method and Materials

A square induction coil was built to generate an EM field, induce current and Lorentz forces in liquid aluminum within a standard commercial 9 inch filter. A schematic of the experimental setup used is shown in Figure . The experimental setup was designed to generate strong axial magnetic fields in the area of the CFF. Strong 100 Hz electro-mechanical vibrations were induced by the low frequency alternating current and this required powerful restraints to hold the coil as indicated in the photograph shown in Figure 2.

Batch filtration experiments were conducted using ~8 kg of molten aluminum with the composition given in Table 9. The melt for the experiments was prepared in a standard resistance furnace with a holding temperature of 800°C. After skimming of the dross the metal was manually poured on the CFF. No pre-heating was applied; the filter was at room temperature prior to pouring. The temperature of the metal before casting was measured to be ~760°C. To prove that the filters do not prime by gravity forces the metal rested for a time of 15s above the filter before the current was applied to the coil. Pure gravity reference experiments have been conducted earlier [4], which validated the negligible penetration of liquid metal into the filters without sufficient metal head (100 mm was used).

The EM experiment was initialized by energizing the double coil at 50 Hz with 1250 A ±1% and 1 A resolution (RMS), generating a magnetic field strength of ~0.12 T ±1% at the center line of the empty coil as measured using a Hall Effect gauss meter model 6010 engineered by Pacific Scientific OECO, F.W. Bell®. The axial probe was standardized using an axial standard of 0.05 T ± 0.3 mT. The magnitude of the magnetic field was then compared by measuring the applied AC current and the induced power using a Fluke® 43B Power Quality Analyzer with a resolution of 100 W. The current was measured by a inductive current probe i1000S with a resolution of 1 A and ±1%, engineered by Fluke®. The conductivity at room temperature of the used metal was determined by an AutoSigma 3000 electrical conductivity meter with an accuracy of ±0.5%

using a high frequency probe. The resulting numbers were used to calculate valid FEM simulation results, i.e. no fitting parameters of any kind were used during the simulations.

Initial priming occurred 6 to 10 seconds after the field was activated and it was turned off after the priming was finished, i.e. when the metal reservoir above the filter was fully drained. The metal remained in the crucible to cool down and solidify. After solidification, the filter has been sectioned to investigate the wetting behavior and the remaining gas inside the filter.

Table 9: The chemical composition in wt. [%] of the aluminum alloy.

Alloy	Si	Fe	Cu	Mn	Zn	Al
3xxx	0.06 – 0.12	0.17 – 0.22	0.1 – 0.15	0.95 – 1.05	0.15 – 0.2	remaining

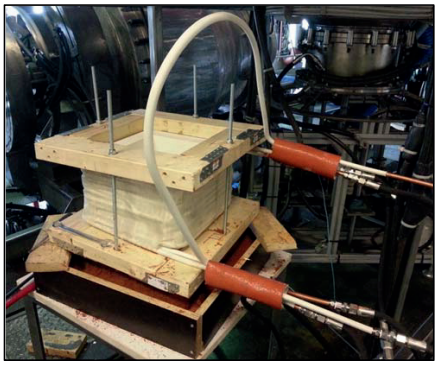

Figure 2: Experimental apparatus for the 9 inch filter experiment, showing the uncompressed double coil (and large loop 'jumper') made of 12 mm copper tubes, the wooden frame to suppress vibrations, the refractory crucible, embedded into red casting sand, and the high pressure hose system for cooling.

Priming and Wetting Results and Discussion

CFF's applied in industry are normally operated in a filter box, which uses a certain gravity head of liquid metal and a recommended pre-heating technique to achieve priming [12]. Gravity forces the metal into and through the filter, removing a sufficient fraction of the interstitial air and partially wetting the filter media. In Figure 3 typical magnitudes of industrial priming heights are shown [11, 13, 14].

The impact of EM enhanced priming was very significant in earlier experiments and further increased in the current investigation. The experimental trial to investigate lower metallostatic pressure involved priming a 50 ppi CFF with a target of 50 mm metal head (56 mm was actually applied). The head proved to be sufficient to prime the filter without freezing or blocking of the CFF as indicated in Figure 3.

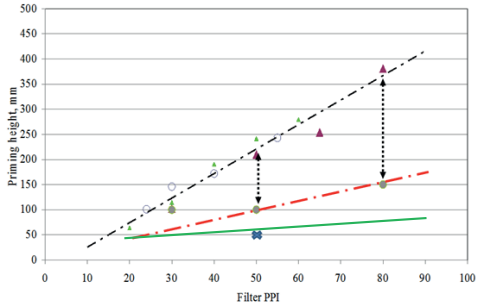

Figure 3: Priming height vs. filter ppi from different producers [13, 14] compared to the earlier conducted electromagnetic priming at 0.17 T using 100mm round CFF (red dotted line) [11] and the new results using 0.12 T on a 9'' filter (full line and cross).

In Figure 4 a) to d), the results of the successful low metal head experiment are shown. 56 mm metal head generated by ~8 kg of liquid aluminum were poured on an un-preheated 50 ppi CFF and were allowed to rest for 15 seconds on the filter without any field or stirring, as shown in Figure 4 a). In Figure 4 b) the coil was electrified with 1250 A (RMS) generating a magnetic field that formed a stable meniscus as shown in Figure 6 c). The filter started to prime after 6 seconds finished after 10 seconds as shown in Figure 4 d).

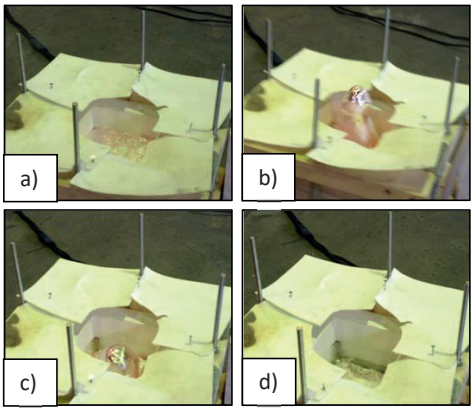

Figure 4: Trial of a low metal head priming experiment, using 56 mm of height above the 9'' 50 ppi CFF. Image a) shows the metal resting above the filter for 15 seconds without any effect (casting temperature ~760°C). Image b) shows the effect of the electromagnetic field when activated with full strength of 0.12 T. Image c) shows that the metal then formed a stable meniscus and it took in total 6 seconds to begin to prime the metal through the CFF, as show image d).

Due to the low metal head and the position of the filter within the coil, a strong and stable meniscus with the height of approximately 160 mm was formed by the interaction of the EM

Lorentz forces, surface tension and gravity. The creation of a meniscus would logically appear to be highly beneficial to improving the priming of a filter by using the EM forces to artificially increase the effective gravity forces. Therefore the effective metal head in the center of the meniscus was approx. 160 mm, which is still not sufficient to prime the 50 ppi CFF by gravity force alone as indicated by the industrial data for pre-heated filters shown in Figure 3. Figure 5 shows a 'steady state' FEM solution of the flow field of the metal inside the meniscus. It shows a strong push into the filter in the center of the meniscus in addition to the 'enhanced' gravity force. This may be the reason that priming was effective with such a low initial metal height of 56 mm. The interaction of gravity and Lorentz forces generate strong flow patterns, which further aid the priming. This was discovered and investigated by the research group earlier [15].

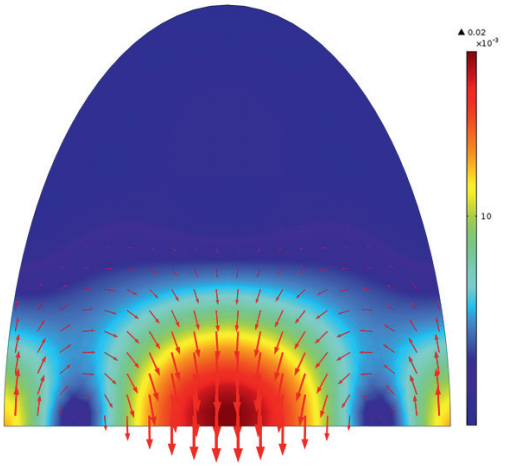

Figure 5: Steady state FEM model generated with COMSOL® 4.4 shows the induced flow field during the priming stage inside the meniscus. The bottom line represents the filter surface and is modeled as an open border boundary condition. The driving force of gravity and of the flow field into the filter is highest at the center.

Higher grade CFFs, such as: 50, 60 or even 80 ppi; have a higher tortuosity and less web-like structure than low grade: 30 and 20 ppi which are more commonly applied. The longer path length and more labyrinth-like structure favors the trapping of air inside the filter, the creation of dead zones and the freezing of metal during the priming stage. Freezing would result in a blockage of the filter prior to priming. The good mixing and inductive heating, together with the strong electromagnetic 'push' into the filter reduces the chance of freezing filters prior to priming.

An experimentally validated FE-model for a meniscus can be seen in Figure 6 [16]. This model shows a meniscus with a solid plate at the bottom. The induced current generates strong MHD-mixing and the flow field results in a stable meniscus. The metal homogenizes inside the meniscus, generates a flow field in a shape of a loop as seen in Figure 6 and eventually melts any frozen metal at the surface of the filter, such that the metal gets pushed into the filter as indicated in Figure 5.

The total area available for particle attachment of each CFF varies by the differences of wetted surface, dead volume and entrapped air. In the literature the total filtration efficiency varies in some cases up to 70% [12]. It is expected that a fully wetted filter has a larger surface area for filtration and lower pressure drop during the filtration. Some of the variation of filtration efficiency might be correlated with insufficient filter priming, a large variation of the internal area available for flow and resulting changes in the so called 'interstitial' velocity due to partial blockage by air.

The less volume that is available for fluid flow, the higher the resulting interstitial velocity inside the filter channels and therefore, the lower the resulting filtration efficiency of the filter in accordance with the models of Apelian [17], shown with [Eq.3]. Increasing the amount of fully wetted filter surface could therefore increase the overall filtration efficiency as proposed earlier [11]. Reducing the pressure drop of the filter and allowing thicker filters to be applied will make it easier to adjust the filter throughput to the required metal cleanliness. The correlation is shown:

$$E_0 = 1 - exp^{-\frac{K_0 L}{u_s}} \qquad \text{[Eq.3]}$$

Where E_0 is the filtration efficiency, K_0 is the kinetic parameter [1/s], defined by Apelian, L as the physical thickness of the filter [m] and the superficial velocity u_s in [m/s].

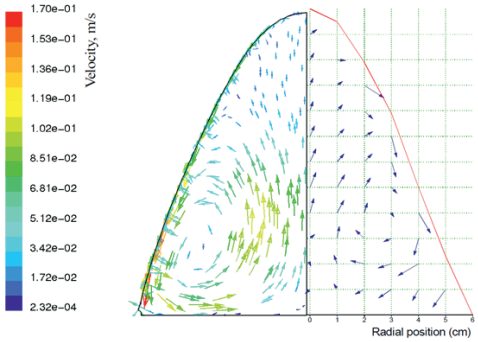

Figure 6: Visualization of a k-ε turbulence model showing a sodium meniscus. Left is the model and right is the measured velocity **[16].**

Metallostatic Pressure and required Metal Head

The required pressure to prime is traditionally created by the metal head above the filter. After the priming the metal head also creates the pressure to sustain the desired superficial velocity. To estimate the required metal head for either of the steps, the knowledge of the tortuosity and porosity of each filter type is essential. The tortuosity is necessary to calculate the interstitial velocity, which represents the real velocity inside the filter media and can be calculated as shown in [Eq.4]. Due to the reduced area inside the filter for the flow and the

incompressible liquid the interstitial velocity will be greater than the superficial velocity. The interstitial velocity has a major effect on the filtration efficiency; making filtration modes such as sedimentation by gravity inside the filter less favored in higher ppi CFF's. Theoretical calculations on the filtration modes related to the interstitial velocity have been presented elsewhere [5].

$$v_i = \frac{v_s \tau}{\varepsilon(1-f_d)} \quad \text{[Eq.4]}$$

Where v_i is the interstitial velocity [m/s], τ is the tortuosity [unitless], ε is the total porosity [unitless] and f_d is the fraction dead volume [unitless] of the total filter volume.

The dead volume is estimated to be of the order of 30%, as results in the literature vary between 16 to 40% [5, 18, 19]. Using this dead volume and the porosities and tortuosities as shown in Table 2, results in an increase of the effective velocity inside the filter (v_i/v_s) by a factor of 2.1 for a 30 ppi, 3.6 for a 50 ppi and 5.3 for an 80 ppi CFF.

The resulting interstitial velocity has a critical impact on the probability of particle collection. Filtration mechanisms have been discussed in earlier publications [3, 5], showing settling and bridging (cake filtration) as the main filtration modes. Both mechanisms suffer at higher interstitial velocities, resulting in the need for larger or thicker filters. Higher interstitial velocity would increase the effect of inertia, direct interception and effects of turbulence [20]. Filtration mechanisms and efficiencies have not been a topic in this investigation and are part of the plans for future work.

Flow through a porous media as defined by the superficial velocity creates a pressure gradient, which can be calculated using the Forchheimer equation [Eq.5].

$$\Delta P = L\left(\frac{\mu}{k_1} v_s + \frac{\rho}{k_2} v_s^2\right) \quad \text{[Eq.5]}$$

Where ΔP is the pressure drop [Pa], L is the thickness of the filter [m], μ is the dynamic viscosity [Pa*s], v_s is the superficial velocity [m/s], ρ is the fluid density [kg/m^3], k_1 [m^2] and k_2 [m] are empirical permeability constants. The recommended values for the Darcian and non-Darcian terms k_1 and k_2 are topic of another publication [21] and have been compared with earlier publications [5, 11].

The pressure drop is not dependent on the size or shape of the filter, but on the thickness and the resistance of the filter to flow. Therefore pressure drop is strongly influenced by the filter grade or ppi, as represented by the permeability constants which define the resistance of the filter to flow. The required metal head for the priming and to maintain a given superficial velocity during filtration is therefore highly dependent on the thickness and type of the filters. The dead volume, tortuosity, and porosity of the filter relate strongly to the permeability constants and hence the total pressure drop for a given metal flow rate per unit filter area.

CFF's are typically 50 mm thick plates which are relatively difficult to efficiently prime. Problems in priming have been a barrier to the use of increased thickness to achieve higher filtration efficiencies. The technology to sufficiently prime various thicknesses of high ppi CFF has been recently patented [6] and further steps are initiated.

The graph in Figure 7 shows the required metal head after priming to maintain a superficial velocity (i.e. casting rate) using 50 and 150 mm filter thicknesses, for 30 (solid line) and 80 (dashed line) ppi CFF. A thicker filter will have a substantially increased filtration efficiency as indicated by equation 3 by Apelian [17]. The analytical solution reveals that the required metal head for a fully primed 150 mm thick 80 ppi CFF will be 100 mm to maintain 9 mm/s superficial velocity through the filter, which is a standard casting velocity for billet casing in industry as shown in Table 2. An inefficiently primed filter will have blocked areas (retained gas) and areas of higher and lower interstitial velocity. Overall the filter will have both higher pressure drop and lower filtration efficiency.

Table 10: Data used for simulation and calculations regarding the used CFF. [3]

Grade [ppi]	Porosity [%]	Tortuosity, τ	Darcy Constant k_1 [m^2]	Forchheimer 2nd Order k_2 [m]
30	0.892	1.3	5.08E-08	5.46E-04
50	0.863	2.2	1.57E-08	1.66E-04
80	0.865	3.2	6.52E-09	1.15E-04

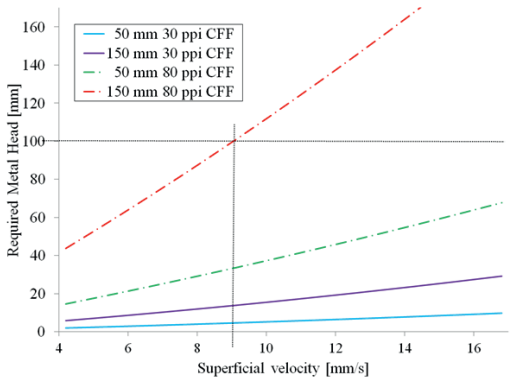

Figure 7: Calculated metal head to maintain a given filtration superficial velocity in mm/s through the filter. As an example, the dark lines indicate that at 100 mm of head for EM priming, a gravity flow of 9 mm/s, which is typical of an industrial billet casting velocity, can be maintained for a 150 mm thick high grade 80 ppi CFF.

Multi-Physics Modelling

To develop a better understanding of the influence of the EM field on the behavior of the liquid metal entering and flowing through the filter, 2D axial symmetric FE modeling using COMSOL® 4.4 was used to solve for the steady state Lorentz force and flow fields. The EM field for the priming case is shown in Figure 8.

It has been shown in previous research that sufficient head over the coil can suppress the formation of a meniscus. The following CFD models therefore assume no meniscus in contrast

to the experiment modelled in Figure 5. The simulation starts with no metal inside the filter and therefore no Lorentz forces are induced inside or below the CFF. The metal above the filter will experience powerful induced Lorentz forces, as shown in Figures 8 and 9 for a 228 mm filter. Combined with the lack of Lorentz forces in the un-primed filter region it results in a strong MHD flow pushing the metal into the filter as shown in Figure 9. The velocity field shown in Figure 9 is at the exact moment priming is initiated.

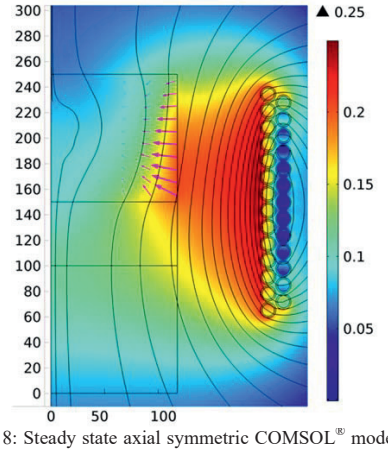

Figure 8: Steady state axial symmetric COMSOL® model of the experimental setup during priming (no metal in or under the CFF). The axis of symmetry is located at r = 0, the coil to the right, the highest square represents the metal above the filter before priming. The stream lines and the surface show the magnetic flux density (normalized in [T]) and the magenta colored arrows show the time averaged Lorentz force contribution (F_L) inside the liquid metal.

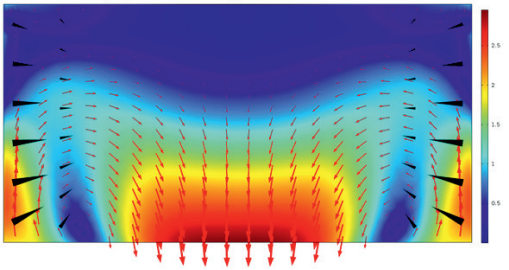

Figure 9: Steady state CFD simulation of the metal above the 9'' CFF showing the initial induced flow field during the start of priming. The colors imply that the application of 1250 A(RMS) current induce a superficial velocity of 2.5 m/s in the center of the filter. The resistance of the filter to priming can generate a meniscus above the filter as shown in Figure 4 b) and c) and Figure 5 until the resistance/blockage of the filter is broken (re-melting the metal that blocks the cold filter) and the metal penetrates into the filter. Sufficient height of metal over the coil can suppress meniscus formation.

After the filter and the volume below are filled with metal, the velocity field changes direction and generates a strong back mixing effect, discussed in earlier publications [4, 5, 15]. The magneto hydrodynamic (MHD) mixing for the filled crucible, coil position and RMS-magnitude of Lorentz forces (black cones) is shown in Figure 10. The simulation uses the properties of a 50 ppi CFF, as presented in Table 10.

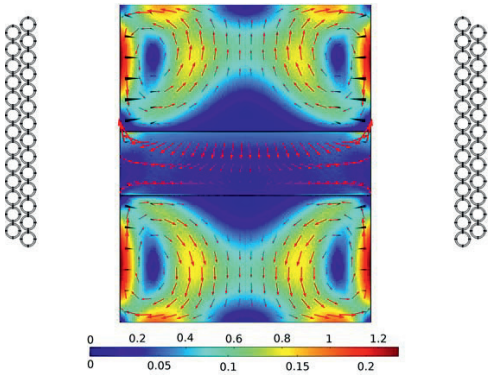

Figure 10: Flow field simulation showing the MHD for a 9" 50 ppi CFF using a 27 turn double coil with an applied alternating current of 1250 A (RMS). The coil position is centered at the upper line of the filter to guarantee a maximal force during the priming stage. Peak velocities are calculated to be 1.28 m/s in the metal and 0.22 m/s in the filter. The top legend is scaled for the metal region, and at bottom for the filter region, both in m/s. The red arrows indicate the direction and magnitude of fluid flow and the black cones the Lorentz forces in metal and porous media regions; sizes are not comparable between regions.

The air gap results in a significant reduction in magnetic field and induced Lorentz forces in the liquid metal. Application of 1250 A (RMS) generates a sufficiently strong EM field to prime the filters and inducing a velocity of up to 0.22 m/s inside the filter and more than 1 m/s in the metal phase after priming.

Conclusions

The effect of an electromagnetic field on the priming of a small 9" commercial Ceramic Foam Filter (CFF) has been demonstrated with less metal head than anticipated based on previous experiments [11] and much less than standard industrial priming heads [13, 14]. Priming of a 50 ppi CFF succeeded with only 56 mm metal head, which is less than 25% of the standard metal head used by industry today. Electromagnetically enhanced priming will enable higher grade (higher ppi) or thicker CFFs to be used with standard priming heights.

Increasing the available area for filtration by greater removal of gas from the inside of the filters, as well as improved filter wetting will allow higher throughput and casting velocities while not altering the filtration efficiency of the applied filter grade. This might allow an optimized (similar) metal head for both priming and casting, implying the use of thicker filters.

An improved the melt quality can be achieved by removing more solid inclusions using a higher grade filter, a thicker filter or slower filtration. With EM priming a higher grade and/or

thicker filter can both be primed efficiently with low metal head achieving higher filtration efficiencies for a given filter box installation.

Future Work

Priming trials will be executed using the 9'' industrial size filter box with 30 to 80 ppi CFFs. A stack of up to three 50 mm thick commercial filters will be used. Flow experiments with artificial inclusions will be used to investigate filtration efficiency and the behavior of stacked filters in order to verify the casting rate estimates shown in Figure 7.

Metallographic investigations will be carried out on particle distribution, and to study the filtration mechanisms and interfacial wetting between alumina and aluminum.

Acknowledgements

The industrial partners involved in the project are: Hydro Aluminium AS supporting with casting alloys, Norwegian University of Science and Technology (NTNU) and SINTEF Materials and Chemistry.

The authors also wish to express their gratitude to Kurt Sandaunet and Roar Jensen from SINTEF and Trygve Schaunche from NTNU for their support and help, as well as for the use of the casting laboratory of the Institute for Material Technology (IMT) at NTNU, Trondheim in Norway.

Reference

1. D. E. Groteke, "The Reduction of Inclusions in Aluminum by Filtration," Modern Casting, vol. 73, 1983, pp. 25-27.
2. K. Butcher and D. Rogers, "Update on the filtration of aluminum alloys with fine pore ceramic foam," 1990, pp. 797-803.
3. M. W. Kennedy, "Removal of Inclusions from liquid Aluminium using Electromagnetically Modified Filtration," PhD, Department ofMaterials Science and Engineering, NTNU, Trondheim, 2013.
4. R. Fritzsch, M. W. Kennedy, S. Akhtar, J. A. Bakken, and R. E. Aune, "Electromagnetically Modified Filtration of Liquid Aluminium with a Ceramic Foam Filter," Electromagnetic Processing of Materials (EPM2012), Beijing, China, 2012.
5. M. Kennedy, R. Fritzsch, S. Akhtar, J. Bakken, and R. Aune, "Electromagnetically Modified Filtration of Aluminum Melts Part II: Filtration Theory and Experimental Filtration Efficiency with and without Electromagnetic Priming for 30, 50 and 80 PPI Ceramic Foam Filters," To be submitted to Metallurgical Transactions B, 2012, pp. 1-69.
6. M. W. Kennedy, R. Fritzsch, S. Akhtar, J. A. Bakken, and R. E. Aune, "Apparatus and Method for Priming a Molten Metal Filter," U.S. Patent, 2012.
7. M. W. Kennedy, K. Zhang, R. Fritzsch, S. Akhtar, J. A. Bakken, and R. E. Aune, "Characterization of ceramic foam filters used for liquid metal filtration," Metallurgical and Materials Transactions B, vol. 44, 2013, pp. 671-690.
8. M. W. Kennedy, S. Akhtar, J. A. Bakken, and R. E. Aune, "Analytical and Experimental Validation of Electromagnetic Simulations Using COMSOL®, re Inductance, Induction Heating and Magnetic Fields," COMSOL Users Conference, Stuttgart Germany, 2011.
9. M. W. Kennedy, S. Akhtar, J. A. Bakken, and R. E. Aune, "Analytical and FEM Modeling of Aluminum Billet Induction Heating with Experimental Verification," TMS Light Metals, Orlando Florida, 2012.
10. M. W. Kennedy, S. Akhtar, J. A. Bakken, and R. E. Aune, "Improved Short Coil Correction Factor for Induction Heating of Billets," EPD Congress, Orlando Florida, 2012.
11. R. Fritzsch, M. W. Kennedy, J. A. Bakken, and R. E. Aune, "Electromagnetic Priming of Ceramic Foam Filters (CFF) for Liquid Aluminum Filtration," TMS Light Metals, 2013, pp. 973-979.
12. S. Ray, B. Milligan, and N. Keegan, "Measurement of Filtration Performance, Filtration Theory and Practical Applications of Ceramic Foam Filters," 2005, pp. 1-12.
13. J. E. Dore and C. Bickert, "A Practical Guide on How to Optimize Ceramic Foam Filter Performance," Light Metals, 1990, pp. 791-796.
14. N. Keegan, W. Schneider, and H. P. Krug, "Evaluation of the efficiency of fine pore ceramic foam filters," Light Metals-Warrendale, 1999, pp. 1-1.
15. M. W. Kennedy, S. Akhtar, J. A. Bakken, and R. E. Aune, "Electromagnetically Enhanced Filtration of Aluminum Melts," TMS Light Metals, 2011 pp. 763-768.
16. E. Baake, A. Umbrashko, B. Nacke, A. Jakovics, and A. Bojarevics, "Experimental investigations and LES modelling of the turbulent melt flow and temperature distribution in the cold crucible induction furnace," 2003, pp. 214–219.
17. D. Apelian and R. Mutharasan, "Filtration: A melt refining method," Journal of Metals, vol. 9, 1980, pp. 14-19.
18. B. Hübschen, J. Krüger, J. Keegan, and W. Schneider, "A new approach for the investigation of the fluid flow in ceramic foam filters," TMS Light Metals, 2000, pp. 809–815.
19. E. Moreira, M. Innocentini, and J. Coury, "Permeability of ceramic foams to compressible and incompressible flow," Journal of the European Ceramic Society, vol. 24, 2004, pp. 3209-3218.
20. F. Frisvold, "Filtration of aluminium: theory, mechanisms, and experiments," Norwegian University of Science and Technology, 1990.
21. S. Akbarnejad, R. Fritzsch, M. W. Kennedy, and R. E. Aune, "An Investigation on Permeability of Ceramic Foam Filters (CFF)," Accepted to 2015 TMS Annual Meeting & Exhibition, 2015.

Part III: Quantification of Filtration

Supplement 6

Automated Quantification of SiC-Particles in Solidified A356 Aluminium using ImagePro® Plus 7.0

R. Fritzsch, B. Mirzaei, M. W. Kennedy, and R. E. Aune

Characterization of Minerals, Metals, and Materials 2013 (TMS 2013), page 67-77,

DOI: 10.1002/9781118659045.ch8

AUTOMATED QUANTIFICATION OF SIC-PARTICLES IN SOLIDIFIED A356 ALUMINIUM USING IMAGEPRO® PLUS 7.0

Robert Fritzsch[1], Behzad Mirzaei[1] , Mark William Kennedy[1,2], Ragnhild E. Aune[1,3]

[1]Department of Materials Science and Engineering, Norwegian University of Science and Technology, N-7491 Trondheim, NORWAY.
[2]Proval Partners S.A., 70 Rue de Genève, 1004 Lausanne, SWITZERLAND.
[3]Department of Materials Science and Engineering, Royal Institute of Technology, 100 44 Stockholm, SWEDEN.

Communicating author: ragnhild.aune@ntnu.no

Keywords: Image processing, automation, particle counting, Melt quality, ImagePro® Plus 7.0

Abstract

The quantitative particle concentration can give important information about the cleanliness of melts for quality control in primary and secondary production of aluminum. Manual quantification of the particle concentration is normally a time consuming process and human control can bias the acquired images and particle count.

The present paper explains the automated image-processing steps for the quantification of SiC-particles, with equivalent diameters from 2 to 25 µm, in solidified A356. A total of 700 micrographs, acquired with a standard white light microscope with 10 x magnification, were analyzed. The applied software (Image Pro-Plus 7.0 from MediaCybernetics®) allows for programming of macros which in turn provides the user with a higher degree of control. The automated results are compared with the results obtained by manually counting the particles in the same micrographs. The impact of the automated results on the estimated filtration efficiency was established to be only ~3%.

Introduction

Inclusions are both indigenous and exogenous particulates that are present in commercial metals such as aluminum. If large individual or large numbers of inclusions are present, they can have a significant negative impact on the appearance, mechanical and chemical behavior of products produced from the metal. Aluminum is known to contain large numbers of inclusions ≤ 50 µm in size, e.g. typically <1 ppm by volume or <100,000 inclusions of >20 µm per kg of metal as detectable using a Liquid Metal Cleanliness Analyzer, LiMCA [1]. Depending on the final application of the aluminum, inclusions can render the metal 'not fit for purpose', and result in serious economic consequences to metal producers.

It is not surprising that the aluminum industry has developed a number of treatment processes to improve metal cleanliness, given the large number of high value products whose quality can be adversely affected by inclusions. CFFs are the most commonly applied filtration process and have been used to filter >50% of the world production of aluminum since the 1990's [2].

Inclusions in aluminum may be particles, bifilms [3] or clusters of: oxides (Al_2O_3, SiO_2), spinels ($MgO \cdot Al_2O_3$), carbides (SiC, Al_4C_3), nitrides (AlN), borides (TiB_2), sulfides, phosphides and intermetallics [4].

Due to the demand for a higher degree of inclusion removal, inclusions as small as 10 μm are now considered problematic. It is therefore desirable to develop an analytical method capable of counting such particles, which is faster, more practical, accurate and precise, and also less susceptible to human bias, than manual counting. Current industrial state-of-the-art analytical techniques such as the Liquid Metal Cleanliness Analyzer (LiMCA) [5] have difficulty to accurately detect particles of less than 20 μm. LiMCA can not distinguish individual particles within clusters and results are affected by the particle shape (e.g. rod or ellipsoid), which can not be determined by this method. The objective of the current work was to quantitatively determine the efficiency of removal for particles >10 μm, therefore, LiMCA could not be applied, and a new analytical technique had to be developed.

Recently an automated macro based particle counting method has been developed using ImagePro® Plus 7.0 (IPP) from MediaCybernetics®. The IPP method has been benchmarked against a meticulous manually controlled particle count and the accuracy determined. The comparison between these two analytical methods is the major topic of this paper.

The IPP method is based on the application of point operations for black and white, using thresholding, gamma curves and histogram equalization. The computer automated method gives a reproducible and reliable tool applicable for metallographic samples. The method can determine the area and counts of particles over 2 μm using 10 x magnification on an optical microscope.

The use of automation in counting can lead to results which are: more rapid, with higher accuracy, less bias, and requiring less manpower. This report describes the development of a macro automated counting method using IPP and the application to the counting of SiC particles of 2 to 25 μm.

Method

The main steps for the quantitative analysis technique comprised: (i) the acquiring of images and (ii) automated image analysis with IPP. The automatically counted (IPP) method was benchmarked by comparing the results obtained with a manually assisted ImageAccess easy Lab6®, (IAeL) particle count for a common set of images. 700 digital photographic images taken at 10 x magnification with a white light microscope from 32 individual samples, with a total measured area of 28.2 mm^2 per sample. The analysis time required was six months for manual and one hour for automated counting using IPP. This time saving resulted in a bias of ~3 % in the estimated filtration efficiency.

Rapidly solidified spectrographic disc samples were machined flat, sanded (SiC-based paper with P120 to P4000 grit), polished to a mirror like finish (diamond paste 6 and 1 μm on fleece) and optically analyzed using an LEICA MEF4M white light microscope, equipped with a Jenoptic® ProgRes-C10 Plus, 10 MP digital camera. The imaging software used was ProgRes Image Capture Software from Jenoptic®.

The samples were first analyzed using the IAeL software. This less automated software required about 15% of the particles to be manually identified and an additional 5-10% required ‘paint shop’ alteration to ‘complete’ the particles (where one side was merged into the matrix), in order to achieve a nearly perfect count for particles exceeding 2 μm. The result was a manually controlled process with nearly

100% particle identification using 700 images. This represented less than 10% of the images that required analysis as part of the total project. As six man months where used performing the analysis, this clearly indicates the impracticality of the manual method. The IPP results required about five minutes for each set of samples and about one hour to re-produce the work of six man months.

Image Processing

The image processing consists of five main steps using Image-Pro: 1) Adjusting the image intensity, 2) Correction of the contrast, 3) Using a sharpen filter function, 4) Flattening the image, and 5) Counting the separated particles, as shown in Figure 1.

The images acquired by the image capture software had a resolution of 2080x1542 pixels (3.2MP), a resolution of 150 dpi and a bit depth of 8. The images have been converted after acquiring using the 'convert to greyscale' function of the ProgRes® Image Capture Software from Jenoptic®.

The first step in the application of the software is to define the magnification and image resolution. This establishes for the software the real length of a pixel. This is selected using the command in the submenu of "Measure," "set calibration" and then "set system." 10 x magnification at a resolution of 2080x1542 is equivalent to 0.515 µm per pixel.

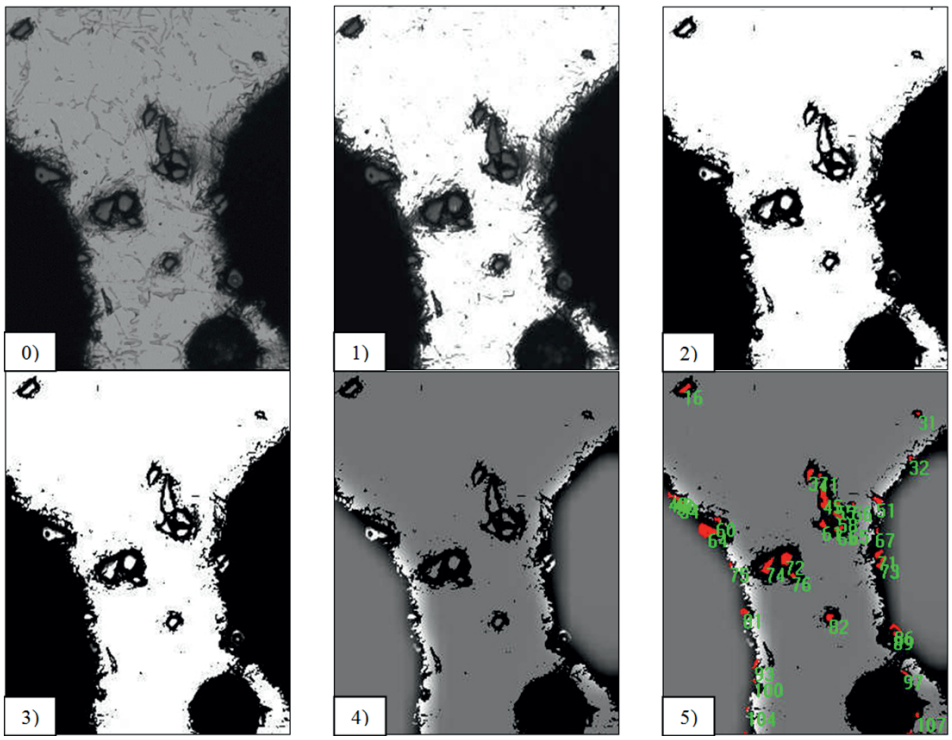

Figure 1. 0) acquired raw image, 1) adjusting of the intensity level, 2) correction of gamma, contrast and brightness, 3) application of a sharpen function, 4) flattening of the image background and 5) counting the objects.

The six images in Figure 1 illustrate the five main image processing steps applied to each micrograph. The example in Figure 1-0 is an enlarged micrograph (200%) of a highly contaminated sample with many pores. This type of image is too difficult for an accurate manually controlled particle count.

Applying the "Contrast Enhancement" function to Figure 1-0 removes the eutectic AlSi-phase and background noise, as shown in Figure 1-1. This was achieved by adjusting the image intensity. The value was changed by manipulating the intensity with a 1/8 tone curve. Different sets of images have slightly different luminosity, requiring a set-wise adjustment for brightness, contrast and gamma. Nominal values for the "Contrast Enhancement" attributes were: brightness 72%, contrast 88%, and gamma of 0.88. The results are shown in Figure 1-2.

Using only the "Contrast Enhancer" function can cause problems for particles with a diameter below 10 pixels or 5.15 µm. Particles in a size range from 2 to 10 µm have a tendency to agglomerate resulting in very small inter-particle distances, e.g. 0.5 µm to 3 µm. The minimum distance of 0.5 µm represents only one pixel as shown in Figure 2 a). A sharpen function must be applied to avoid counting these agglomerates as a single object, as shown in Figure 2 b). In IPP a filter module is available that applies a "unsharp mask" Gaussian sharpening function. The first 'Gauss filter' blurs sharp edges and expands inter-particle distances and edges of particles. The second 'Hi-Gauss-filter' enhances high frequency information and reduces noise. The second filter redefines the blur edges and enhances the image sharpness.

The filter has been applied using a 5x5 pixel matrix (kernel) to every point of the image; a weighting value of 10 equals to 100% application of the filter over the image. The results from the application of the filter can be seen in Figure 1-3 and more clearly seen on a higher resolution image Figure 2 b).

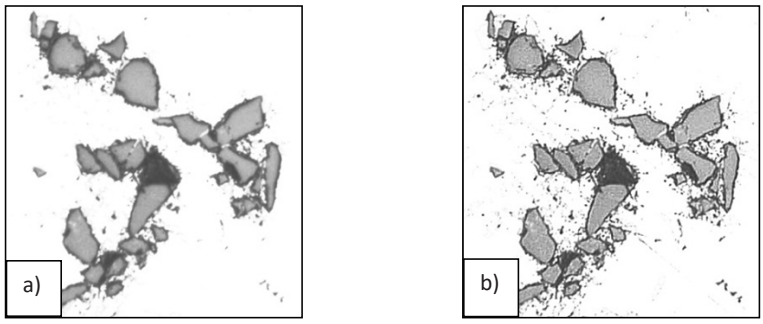

Figure 2. a) 200% digital zoom on a 20 x magnification image with a resolution of 2080x1542. The tendency for particle agglomeration and small inter-particle distance is clearly visible. The effect of the sharpen function is shown with the image b).

To avoid counting pores as giant particles in step 5, it is necessary to apply step 4, flatten image. This function flattens the background and whitens large dark areas. All pores can be excluded using this function. The selected parameters were a bright background and a maximal feature size of 50 pixels. The result of the flatten image is shown in Figure 1-4.

Counting was the final step, i.e. step 5. The option “fill holes” was chosen to count particles as solid objects in order to acquire the correct total area. The “clean border” function was applied to all sides of the images to prevent counting of partial particles. The intensity range was set to a range of 90 to 255. The measured output parameters were particle area and count. The result of the counting step is shown in Figure 1-5.

The above steps were automated using a macro. The “recording macro” option in IPP allows the program to record steps made by the user directly in a computer language similar to Basic. The automated script required minor editing and adjustment to achieve the desired accuracy.

The data acquired for each sample (40 images from each) were exported to a Microsoft Office® Excel2010 spreadsheet using the data collector of IPP. The equivalent circular diameter was estimated from the measured area by applying Eq. [1].

$$D_{eq} = \sqrt{\frac{4A_{Obj}}{\pi}} \qquad [1]$$

Where D_{eq} is the equivalent circular diameter [m], and A_{Obj} is the object area [m^2].

All equivalent diameters have been modified using a stereoscopic correction factor of √1.5 [6]. The resulting object sizes from each sample have been collected into individual data sets. The sum of all object areas was calculated and the particle counts have been grouped into 6 discrete size ranges of D_{eq}: 2-5 µm, 5-10 µm, 10-15 µm, 15-20 µm, 20-25 µm and >25 µm, and used to produce histograms.

Method Comparison

IAeL and IPP results are compared in Figure 3. The experimental program associated with this investigation had the objective to determine the overall efficiency for the removal of particles from liquid metal.

$$E = \frac{N_i - N_o}{N_i} \quad \mathrm{E} = \frac{\mathrm{N_i\text{-}N_0}}{\mathrm{N_i}} \qquad [2]$$

Where E is the filtration efficiency [%], N_i is the count of particles entering into the filter per mm^2, and N_0 is the count of particles leaving the filter per mm^2. N_i and N_0 can be determined from a normalized count (particles per unit area) on the initial and final filtration samples.

Eq. [2] has been used to determine the filtration efficiency of Ceramic Foam Filters (CFF) and is discussed elsewhere [7].

The mean of the absolute percentage difference between IAeL and IPP counts, for all particle size groups combined was ~10% and can be seen in Figure 3. Initial ‘*highly contaminated*’ samples as shown in Figure 4 a), analyzed by IPP were biased by -13.5% on average, while the ‘*less contaminated*’ samples, as shown in Figure 4 b) were biased by -6.3% on average. The different biases resulted in an underestimation of filtration efficiency by ~3%.

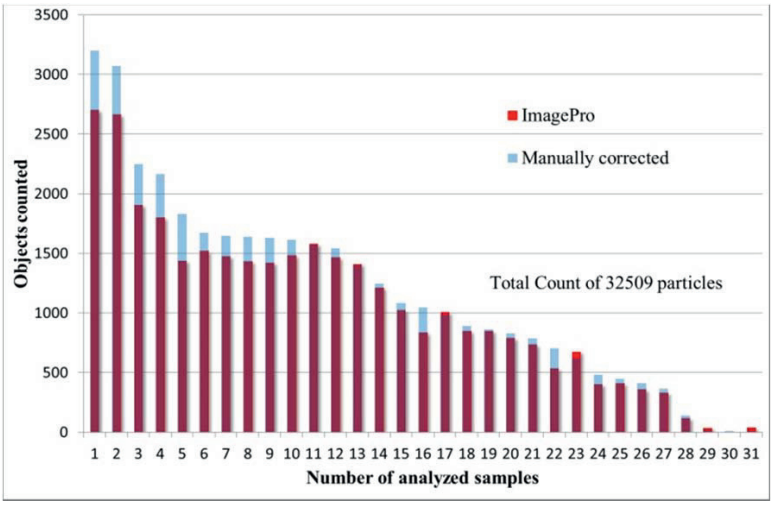

Figure 3. Histogram showing the comparison of the IPP and the IAeL methods, with a total IAeL particle count of 32509 from 700 images of 32 samples. IPP indicated by black bars and IAeL indicated by grey bars.

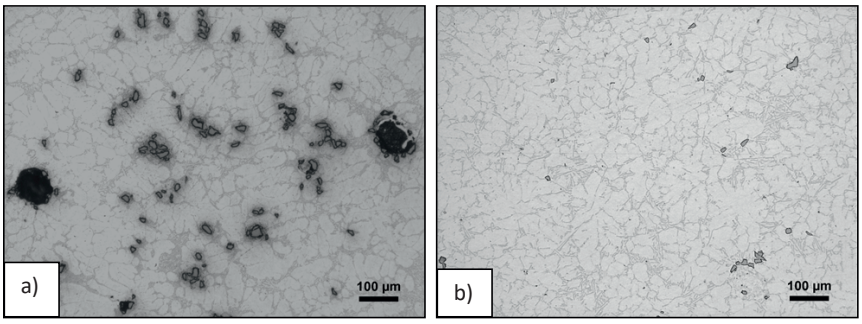

Figure 4. Comparison between a) 'highly contaminated' samples and b) 'less contaminated' samples, both acquired with a 10 x magnification.

LiMCA data are traditionally sorted into 5 µm ranges, in a similar manner to that shown in the histogram, Figure 5. In Figure 6 the estimated filtration efficiency using Eq. [2] is plotted versus the number of particles for each filtered sample. Results calculated using both the IPP and IAeL data are presented. The differences are highlighted by the arrows on the graph. Figure 6 clearly indicates that the bias is higher for the 'highly contaminated' samples.

The initial SiC content of the melt in these experiments was orders of magnitude higher than industrial quality aluminum. Filtration efficiency using artificially introduced SiC particles is also lower than the industrial norm; hence, the filtered samples are more heavily contaminated than the norm and indicate a larger bias than would be typical for 'real' samples. For normal particle loadings and normal industrial

filtration efficiencies of 50 to 90% [8] the melt will be less contaminated and the bias will therefore be much less significant.

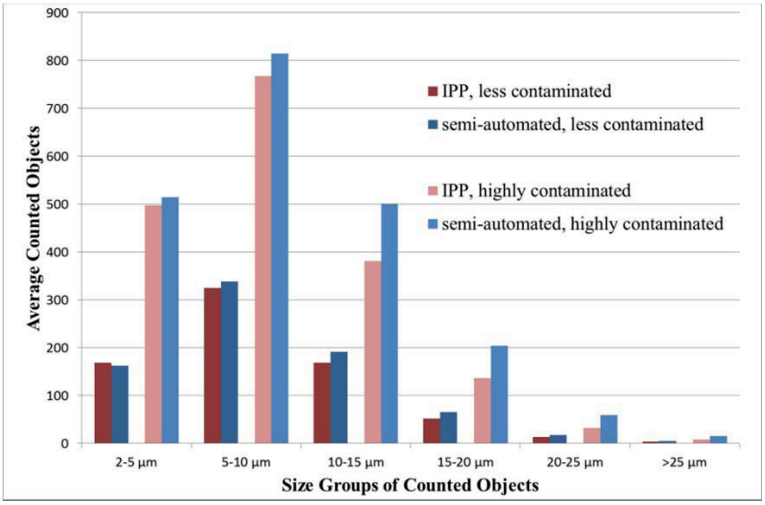

Figure 5. Histogram showing the comparison of IPP and IAeL methods, for both '*highly*' and '*less*' contaminated samples, grouped into 5 µm size ranges.

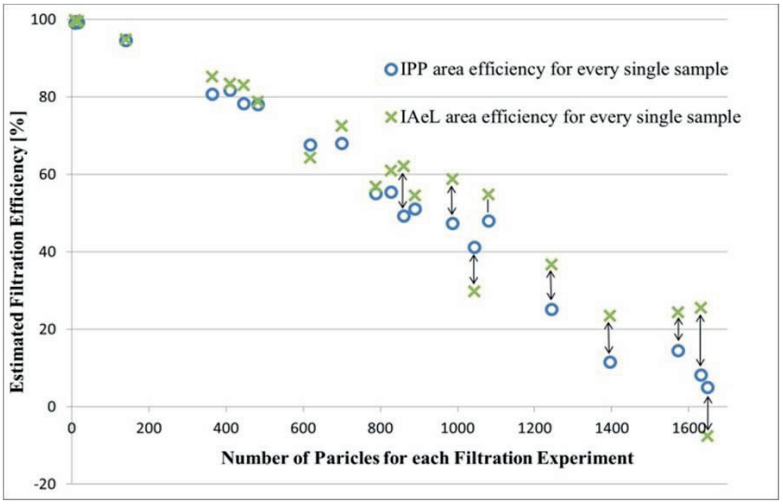

Figure 6. Estimated filtration efficiency using Eq. [2] plotted versus the number of particles for each filtered sample. IPP results are represented by blue circles and IAeL results with green crosses. The differences are highlighted by arrows.

Results and Discussion

The newly developed method is a powerful tool to analyze highly contaminated samples using minimal time and effort. The impact on 'normal' filtration efficiency estimates will be less than the 3% as described previously. The significant time savings are worth the small sacrifice in accuracy, due to the fact that the method becomes practical for application in industry and research. The current results can be reproduced in less than one hour of analysis compared with six man months by the manual method.

Furthermore, the current method can be adjusted and used for other investigations to determine particle, phase, intermetallic or pore content, for application to any number of micrographs and samples. In the recent experiments the numbers of samples were purposely reduced due to the expected time required to analyze the samples. Improved statistical results will therefore be obtained in future experimental work by the use of greatly increased number of samples, which can now be analyzed using the IPP methodology.

The most significant advantage of the new method is the ability to count particles as small as 2 μm with acceptable precision. Currently in the literature there are highly limited efficiency results available for particles less than 15 μm due to the inability of LiMCA to analyze below this size limit. Therefore this new method enables new research to be performed, which could not be executed previously, i.e. filtration efficiency for particles between 2 and 20 μm.

One advantage of the current method is that the samples are not destroyed by analysis and therefore additional analysis can be undertaken to verify any unusual result. Additional data, like sphericity, is obtained by this optical method, allowing for a more detailed level of investigation, e.g. impact of particle shape on the obtained filtration efficiency.

Potentially customer problems, which can not currently be correlated to melt quality, can now be analyzed with this new methodology.

Future work

Future investigations on samples with normal particle loading from industrial processes will be conducted. Increasing the magnification will allow particles smaller than 2 μm to be resolved with accuracy. This will require a greatly increased number of images, which will be impractical to acquire manually. A motorized sample holder can be combined with a suitable computer algorithm to acquire unbiased representative images over the entire area of the sample for any resolution, which can then be analyzed in a reasonable time frame.

Acknowledgment

The present study was carried out as part of the RIRA (Remelting and Inclusion Refining of Aluminum) project funded by the Norwegian Research Council (NRC) - BIP Project No. 179947/I40. The authors wish to express their gratitude to the metallographic lab of DMT, NTNU for the intensive usage of the microscopes and the lab. Also special thanks to Rita Skare Peaker (Scan Imaging AS, Bergen, Norway) for technical support with ImagePro® Plus 7.

References

1. C. Dupuis, G. Béland and J. Martin, "Filtration Efficiency of Ceramic Foam Filters for Production of High Quality Molten Aluminum Alloys," in Proceedings of the 32nd Annual Conference of Metallurgists, Quebec, Canada, 29 August – 2 September, (1993), 349-358.
2. K. Butcher and D. Rogers, "Update on the Filtration of Aluminum Alloys with Fine Pore Ceramic Foam," Light Metals, (1990), 797-803.
3. J. Campbell, "Entrainment Defects," Materials Science and Technology, vol. 22, (2006), 127-145.
4. D. E. Groteke, "The Reduction of Inclusions in Aluminum by Filtration," Modern Casting, vol. 73, (1983), 25-27.
5. R. Guthrie and M. Li, "In Situ Detection of Inclusions in Liquid Metals: Part II. Metallurgical Applications of LiMCA Systems," Metallurgical and Materials Transactions B, vol. 32, (2001), 1081-1093.
6. A. Çiftja, "Solar Silicon Refining; Inclusions, Settling, Filtration, Wetting," Trondheim: NTNU, Norway, (2009), 170.
7. M. W. Kennedy, R. Fritzsch, S. Akhtar, J. A. Bakken and R. E. Aune, "Electromagnetically Modified Filtration of Aluminum Melts Part II: Filtration Theory and Experimental Filtration Efficiency with and without Electromagnetic Priming for 30, 50 and 80 PPI Ceramic Foam Filters," To be submited, Metallurgical and Materials Transactions B, (2012), 1-69.
8. S. Ray, B. Milligan and N. Keegan, "Measurement of Filtration Performance, Filtration Theory and Practical Applications of Ceramic Foam Filters," Aluminium Cast House Technology 2005, 9th Australasian Conference and Exhibition, Melbourne, Australia, 12-15 September, (2005) 1-12.

Supplement 7

A novel Method for Automated Quantification of Particles in Solidified Aluminium

R. Fritzsch, S. Akbarnejad, and R. E. Aune

TMS 2014 Supplemental Proceedings, pages 535-543

DOI: 10.1002/9781118889879.ch65

A novel Method for Automated Quantification of Particles in Solidified Aluminium

Robert Fritzsch[1], *Shahin Akbarnejad*[1,2] , *and Ragnhild E. Aune*[1,2]

[1]*Dept. of Materials Science and Engineering, Norwegian University of Science and Technology (NTNU), Trondheim, NORWAY*
[2]*Dept. of Materials Science and Engineering, Royal Institute of Technology (KTH), Stockholm, SWEDEN*

Communicating author: robert.fritzsch@ntnu.no

Keywords: Image processing, automation, particle counting, melt quality, ImagePro® Plus 7.0

Abstract

Particle concentration and size distribution in the melt can give important information regarding the filtration efficiency and the quality of the aluminium. LiMCA (Liquid Metal Cleanliness Analyser) system, used in primary and secondary production of aluminium, provides in-situ data for granulometric and total density information on the inclusion content, but has problems quantifying particles < 20 µm in size.
To be able to determine the required cleanliness with particle counts down to 10 µm for modern alloys a novel method for automated quantitative results has been developed. Results are obtained using a user friendly technique based on the ImagePro® Plus 7.0 software. The different image processing steps adopted for automated quantification of the particle count in a size range from 2 to 50 µm is described and discussed together with the obtained results. The automated technique has been benchmarked elsewhere with a manual particle count reviling an error of ~3% on the overall filtration efficiency.

Introduction

The knowledge of the quality and it's cleanliness of a melt is crucial for the industry and the production of all sorts of products. The cleanliness is defined by the amount of inclusions, as indigenous/endogen and exogenous particulates that are present in commercial metals such as aluminium [1]. Depending on the size, single large individual inclusions or high numbers of small inclusions can negatively affect the appearance same as major influencing the mechanical and chemical behaviour of end products. It is known, that aluminium contains large numbers of inclusions in the size class ≤ 50 µm, were as inclusions > 10 µm can lead to holes in foils and already can lead to spoiled products [2]. Applications for aluminium is packaging, were aluminium foil, defined to be thinner as < 200 µm, takes a main position. Another example is a can body sheet were the thickness is < 300 µm. Inclusions can be various sized and shaped particles, bifilms [3] or clusters. They can be separated into groups of oxides, spinels, nitrides, carbides, borides, phosphides, sulphides and intermetallics [4].
To maintain the cleanliness of the metal, the industry has developed a variety of different treatment processes. The most common applied method for inclusion removal, which has

been applied to more than 50% of the world production of aluminium since the 1990's, is the ceramic foam filter (CFF) [5].

Different techniques have been developed to evaluate the size and the distribution of the inclusions present in the metal. State of the Art technology is represented by the Liquid Metal Analyser [6], LiMCA, that counts particles in-situ during the casting process down to the size of 20 µm spherical diameter. Hence the nature of the LiMCA principle, it can not distinguish between gaseous, liquid and solid inclusions. Additionally, LiMCA lacks the ability to distinguish between agglomerates, clusters or folded bifilms. This alters the particle count and can lead to errors in cleanliness characterization. As mentioned earlier, inclusions < 10 µm spherical diameter are now considered to be problematic. Therefor it is required that an analytical method will be developed, which is capable of counting smaller particles, is faster, more practical, accurate, precise, and also less susceptible to human bias, than manual counting. The objective of the current work is to develop a method to auto acquire micrographs of high magnification representing large surfaces and process them with an easy to apply automated macro to count inclusions, phase content and porosity of all images. The macro has been developed using ImagePro® Plus 7.0 and ImagePro® Premier 9.1 (IPP) from MediaCybernetics®. The method has been benchmark and validated elsewhere [7].

The advantages and disadvantages, critical steps and what can increase the accuracy of the method are discussed in this paper. Same as the time required to measure filtration efficiency, the reproducibility of data and gives possible applications of the new developed method. The image processing is based on application of point operations for black and white, using various filters, thresholding, gamma curves, histogram equalization and shape factors. It can determine the area, shape factors and counts of particles larger than 2 µm using a 50x magnification with a 1.0 aperture on an optical white light microscope "Reichert MeF3 A" from Leica using a Sony DXC 950P 1.2 MP camera, as shown in Figure .

Figure 1: Automated stage microscope "Reichert MeF3 A". The computer controlled automated stage control unit, the manual control levers, the light source and it is regulations and the microscope itself is shown in the image.

Experimental background

Rapid solidified spectrographic disc (RSSD) samples have been taken from seven industrial scale trials, testing various filter materials and pore size distribution for CFFs. In total, 68 RSSD samples have been manually taken every ten minutes before and after the filter box. In total twelve to fourteen samples per experimental trial.

The spectrographic discs have been machined flat to half the sample thickness, mounted in epoxy, sanded (SiC-paper with P120 to P4000 grid), polished to a mirror like finish (diamond

paste 6 and 1 µm on fleece) following a slightly modified Struers® technique for aluminium alloys. The samples have been optically analysed using a automated moving desk mounted on a Reichert MeF3 A, shown in Figure 1. The light source of the microscope was a normal white light source, with l=400 to 700 nm. The objective of the microscope used had a magnification of 50 times and the numerical aperture was one. The image field was 191 x 143 µm and the digital image size was 764 x 580 pixels. The dimension of one pixel was equal to 0.25 x 0.25 µm. The colour depth was 8-bit with inverted LUT. The resolution of the microscope is given by:

$$\delta = \frac{\lambda}{2 * \text{num.aperture}} \qquad \text{(Eq. 1)}$$

Following (Eq. 1) the resolution for the microscope with the used objective and applied aperture is in the range of 0.2 to 0.35 µm. The digital and the microscope resolution are in the same order of magnitude and the distance between two pixels is 0.25 µm. For each sample a total area of 19.91 mm^2 was automatically recorded. This represents a grid of 27 x 27 images of 27313 μm^2 with a distance of tree not acquired images between each image resulting in a sample area of 3.186 cm^2. This represents the inside square of the RSSD samples. In Figure 2 the sketch of the area and the sequence of image acquiring is shown.

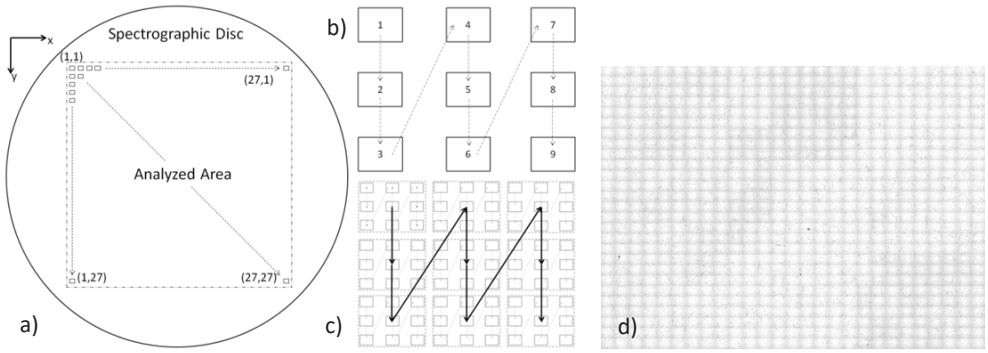

Figure 2: a) Sketch of the distributions of the micrographs taken on every single spectrographic disc. 27 times 27 images with the dimensions of 191 x 143 µm and a distance of each micrograph to the next was defined as 573 µm in x- and 429 µm in y-direction from each other.
b) The first sequence of the automated method to acquire one unit, representing 9 images, acquired by the automated moving desk with automated focus and recalibration every 9 images.
c) The second sequence of the automated method to avoid inaccuracy while acquiring the images moves is this pattern over the sample. After acquiring 9 of the units shown in b) the method is following the same scheme on the larger units.
d) Merged overview image of all 729 images of the 3th RSSD sample of the second experimental trial taken after the filter after acquiring all images.

To identify critical artefacts, focus errors or surface preparation problems, the software merges all images, in this case 729, to a low resolution collage shown in Figure 2. In this image detailed image and sequence information is embedded, to reconstruct and check the programmed and applied acquiring pattern of the moving desk.

Method

The method to identify the particle content in each image can be separated into 6 main steps. The set of images are separated by the individual experiments. First, the pixel size of the

camera will be related to the real size of the acquired area for the microscope and the used objective/ aperture. Then various filters have been used. The luminosity, contrast and gamma functions get adjusted to count the particles. Figure 3 shows image number 329 from the second experimental trial and shows the unmodified image quality after the automated image acquiring. This sample was chosen in order to show the powers of the applied image processing steps combined in the macro and its limits regarding the low resolution of the used camera.

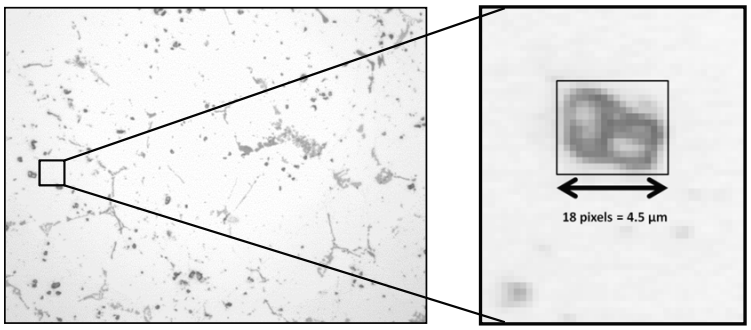

Figure 3: Image from experimental trial 2, after the CFF. The surface was acquired with a 50 x optical magnification and an aperture of 1. The metal phase (white), the eutectic (brighter grey) and the particles (brighter gray to dark grey) can be seen on this image. To the right side is an enlarged part of the image, showing the resolution of the original image. The section shows the size of a cluster of 2 to 3 particles, which have been agglomerated. The size of the particles was defined by defining the length of one pixel to be 0.25 µm x 0.25 µm.

In Figure 4, the six main image processing steps are shown. The enlarged cluster can be seen for each step in the original image resolution. The first step for the automated image processing is to flatten the image. It is shown in Figure 4 a) and it is hardly any difference visible. This function homogenizes the image contrast and brightness / luminosity, introduced by the inhomogeneity and spherical shape of the spot of light sources and lenses present in all magnification objectives. Without a correction, the corners of the images would react differently to the mathematical filters than the centre of the image.
The second step, Figure 4 b), is done to enhance the contrast and sharpness of pixels that are surrounded by other darker pixels. A filter function resembling the a high pass Gaussian probability in the area of a small kernel (3x3x1) is used to increase the difference of the grey scale levels for metal, eutectic and inclusions [8]. This function is called HiGauss filter in IPP and can only be applied as a small kernel filter using the 3-D filter and defining the kernel matrix as a 2-D plane.
The next step, as shown in Figure 4 c) consists of a sharpen function, using the unsharp masking technique with another small kernel of 3x3 pixels.

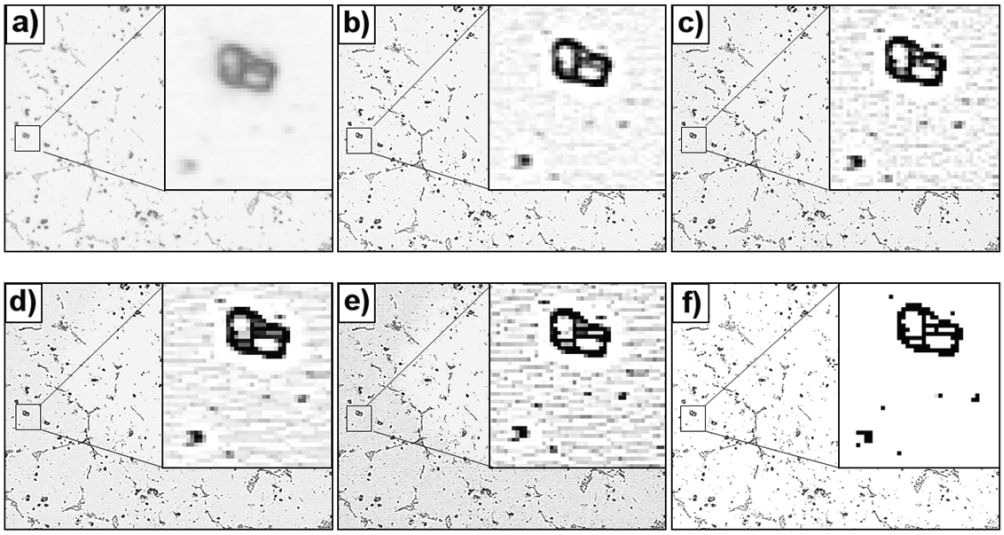

Figure 4: The modified image shown in Figure 3 after: a) running a flatten function processing the images evenness, b) application of a modified high pass Gaussian filter, c) use of a sharpen function, d) processing the image with a morphological function of IPP called "Close", applied in a 3x1 matrix, e) another sharpen function with same intensity and f) adjusting the intensity level, with changes of gamma, contrast and brightness volumes

After this step, most of the inclusions are separated from the metal, but it is the same with the eutectic. To be able to distinguish between eutectic and inclusions we need to apply another filter function. The function is called "Close", a morphological filter that fills gaps and enlarges protrusions of certain sizes to connect objects that are close together. The kernel size was chosen to be 3x1 as a row in x-direction. Using this filter, the eutectic phase gets reduced to single loose lines and can therefore be removed. This can be seen in Figure 4 d), the contour of the particles get slightly more blurry and the white areas inside more homogeneous, whereas the 3x1 kernel modifications can be identified by the trend of all grey scale lines going from left to right. The particles are due to their consistent shape and more homogeneous grey levels not altered. The eutectic is represented as long and thin lines after the application of the filters in step b) and c).

The final step before the contrast enhancement is another sharpen-filter function to reduce the introduced blur from the inclusions, shown in Figure 4 e). In the last step, the contrast, brightness and gamma values get corrected. First by manipulating a 1/8 tone curve, removing all bright and light grey levels from the image (all values from 165 are set to be 255). Then the parameters are directly manipulated and adjusted, only black and white remains. The obtained result is presented in Figure 4 f) and Figure 5, where in Figure 5 the counting has been done. The counting method was coupled by some sorting functions. Two parameters where chosen to reduce the count of inclusions. The area was set as a parameter and its value was set to count everything above 20 pixels (1.25 µm2) and below 1000 pixels (62.5 µm2). The second parameter was the roundness. It is defined by IPP as the perimeter squared over the product of the area times π times four, as shown in Eq.2. It was set to be between 0.5 and 1.2. This removes the rest of the earlier counted eutectic, due to the shape of the eutectic.

$$\text{Roundness} = \frac{(\text{perimeter})^2}{4\pi * \text{area}} \qquad \text{(Eq.2)}$$

The particles observed in this study are all in the range of rounded and well-rounded [9], with a roundness factor between 0.6 to 1.
The data acquired for each sample, i.e. 729 micrographs from each sample, were automatically exported to a Microsoft Office® Excel 2010 spread sheet using the internal data collector of IPP. The equivalent circular diameter of the object was estimated from the measured area by applying the following relationship:

$$D_{eq} = \sqrt{\frac{4 \cdot A_{Obj}}{\pi}} \qquad \text{(Eq.3)}$$

where D_{eq} is the equivalent circular diameter [m] and A_{Obj} the object area [m^2].

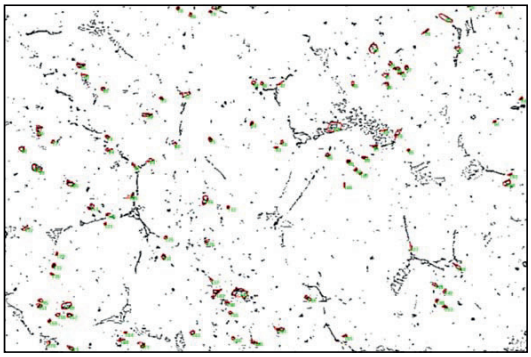

Figure 5: The same image as shown in Figure 3 after applying all the image processing steps discussed and shown in Figure 4 a) to f) and after the final count (red circles around the particles larger than 1.5 µm^2) of the macro used in IPP.

The automated script required minor editing and adjustment to achieve the desired accuracy for each set of images. As shown in Figure 5, the macro still counts some eutectic as small particles due to the similar shape and grey scale level.
The calculated equivalent diameters were modified using a stereoscopic correction factor of √1.5. [10] The resulting object sizes from each sample were collected into individual data sets. The sum of all object areas was calculated and the particle counts grouped into 23 size ranges, one for each µm starting from $2 < x_{3\mu m} < 3$ µm until 24 µm $< x_{25\mu m} < 25$ µm.
It is assumed that the distribution of the inclusions is mostly uniformly across the cutting plane all over the samples. It is also assumed that the acquired area of each sample gives a representative statistical trend of the inclusion density. The filtration efficiencies can give a way of understanding the filters, the settling over time during casting and other processes during the cast process regarding the cleanliness of the metal.
To calculate the density of inclusions per sample, a common metallographic method first mentioned by S. A. Saltykov [11] and improved by J. Gegner [12] is used.

Filtration Efficiency

The following relationship was used to determine the filtration efficiency of the different CFF when filtering liquid aluminium.

$$E = \frac{N_i - N_0}{N_i} \qquad \text{(Eq. 3)}$$

where E is the filtration efficiency [%], N_i the count of particles entering into the filter per mm^2, and N_0 is the count of particles leaving the filter per mm^2. N_i and N_0 can be determined from a normalized count (particles per unit area) on the initial and final filtration samples. The step-by-step derivation of this equation has been discussed in detail in earlier publications [13].

The contamination of the melt in this experiment was a realistic casting trial with no artificial inclusions or particles added.

Results

The filtration efficiency for the experimental trials of a 50 PPI (Figure 6 a)) and for a 60 PPI CFF (Figure 6 b)) are compared. From the average counts it can be seen, that the higher grade filters remove a higher average number of small particles. The used 60 PPI CFF shown in Figure 6 b) showed remarkable good removal efficiency for particles in the size range above 11 µm for that no particle could be identified and a moderate and detectable removal efficiency of 37.8 % of all particles in the size range 6 to 11 µm. It has to be mentioned the filtered metal was a clean primary cast alloy. Most of the identified particles are Ti_2B grain refiner and some other small particles. For experiment 2, 7 RSSD samples before and 5 after with a total amount of 8748 images have been analysed. The identified particles after filtration have been smaller than 11 µm. For experiment 0, 4 RSSD samples with a total amount of 2916 images have been analysed. The larges identified particles after the filtration have been 23 µm in size. The samples were taken every 10 minutes.

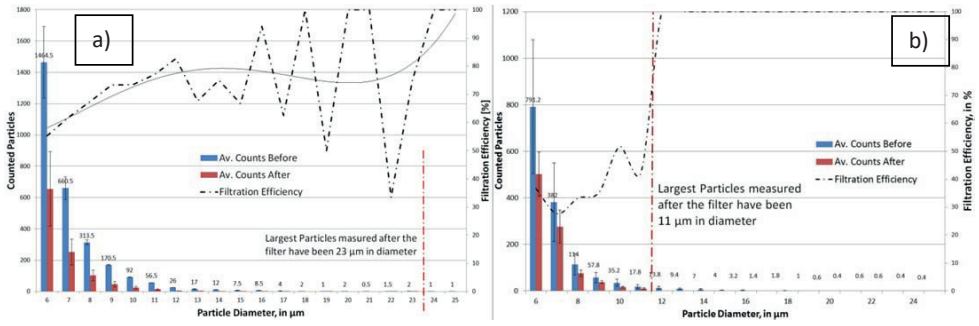

Figure 6: Histograms showing the results for the total particle count of Experiment 0 in graph a) and experiment 2 in graph b). For a 50 ppi alumina and for b) a 60 PPI alumina CFF were used. In Figure a) the filtration efficiency for the particles in the size range above 16 µm is jumping due to a low number of total counts after the filtration.

To prove the error of the applied macro, a manual particle count of 10 % of one set of images of the second experimental trial was conducted. As shown in Figure 5 some of the spherical shaped eutectic is still counted as particles. For all particle size groups, the error was approx. 14 %, were the "small" inclusions with a size below 6 µm corrected spherical diameter are biased by 22.5 % on average. Above 6 µm the bias is reduced to only ~3 %. This result in slightly reduced filtration efficiency of approx. 6 % bias in filtration efficiency, but the trend is similar before and after the filtration. Initial clean metal samples, Figure 7 a), gave

statistically a higher count for particles below 6 µm and more "fail" eutectic counts. A normal contaminated melt sample from before the cast is shown in Figure 7 b).

The method has its primary weaknesses in analysing particles within the size range < 6 µm corrected spherical diameter.

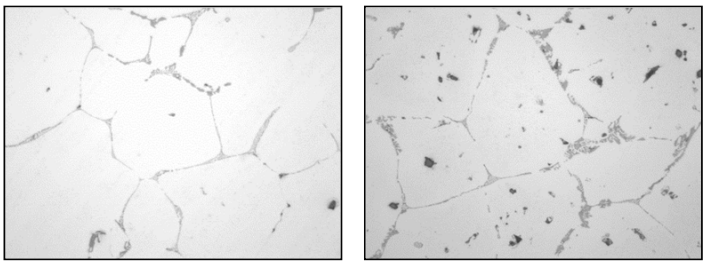

Figure 7: a) Clean metal sample. b) Contaminated sample from before and after filtration of experimental trial 0. Both micrographs were acquired with a 50 x magnification on the automated stage.

Discussion

The further developed method gives a more powerful tool to analyse normal cast and wrought aluminium alloys using a minimal amount of time. The automated stage on the standard light microscope gives the possibility to acquire large areas of prepared metal samples, compared to manually acquired images. The further adjustments of the macro, from the last publication [7], removed the problems of counting bubbles, scratches or agglomerates/clusters. Bubbles and scratches are completely removed from the count, while agglomerates are counted as the set of single particles that build the cluster. The method gives reproducible and accurate information of the metal cleanliness, regarding the concentration of smallest inclusions (<25 µm). The impact on normal filtration efficiencies for particles in the size range above 6 µm will be in the range of a statistical bias of up to 6 %. The significant potential of saving time are worth the small sacrifice in accuracy. It has a high potential to become practical for application in industry and research, due to the flexibility to be adapted to new conditions and its stability counting the particles or phase. The flexibility of the macro gives the possibility to change some parameters and analyse the phase, intermetallic, pores or particle content of any amount of samples. Being able to analyse large amount of area in a cheap way with high magnification gives new possibilities for quality control and monitoring.

The imaging system with the 1.2 MP camera used in this experimental trial was identified to be the weak point of the method. Due to the low resolution of the camera, the most significant advantage of the automated method counting particles down to 2 µm was partly fulfilled. The precision with the lower resolution of the used images is acceptable to a spherical diameter of 6 µm. Particles were identified down to 1.5 µm spherical diameter. In the literature there are limited filtration efficiency results available for particles less than 15 µm in aluminium due to the inability of LiMCA to analyse below this limit.

The method is a non-destructive analytical process. It gives the advantage of being able to reanalyse any amount or numbers of samples to verify any unusual results.

Future requirements for metal cleanliness regarding smaller inclusions and other potential customer problems, which can not currently be correlated to melt quality, could now be analysed with this methodology.

Acknowledgment

The present study was founded by the Norwegian Research Council (NRC). The authors wish to express their gratitude to the Department of Materials Science and Engineering and Department for Chemistry at NTNU for the intensive usage of the microscope lab.

The financial support granted by the Faculty of Sciences and Technology at NTNU for the support of Dipl. Ing. Robert Fritzsch is greatly acknowledged.

References

[1] B. Prillhofer and H. Antrekowitsch, "Abscheidung von nichtmetallischen Einschlüssen bei der Raffination von Aluminiumlegierungen," *BHM Berg-und Hüttenmännische Monatshefte,* vol. 152, pp. 53-61, 2007.

[2] B. Friedrich, C. Kräutlein, and K. Krone, "Melt Treatment of Copper and Aluminium–The Complex Step Before Casting," in *Proceedings of The International Conference on Continous Casting of Non-Ferrous Metals, Wiley-Vch, DGM*, 2006, pp. 3-22.

[3] J. Campbell, *Complete Casting Handbook: Metal Casting Processes, Metallurgy, Techniques and Design*: Elsevier, 2011.

[4] D. E. Groteke, "The Reduction of Inclusions in Aluminium by Filtration," *Modern Casting,* vol. 73, pp. 25-27, 1983.

[5] K. Butcher and D. Rogers, "Update on the filtration of aluminium alloys with fine pore ceramic foam," 1990, pp. 797-803.

[6] R. Guthrie and M. Li, "In Situ detection of inclusions in liquid metals: Part II. Metallurgical applications of LiMCA systems," *Metallurgical and Materials Transactions B,* vol. 32, pp. 1081-1093, 2001.

[7] R. Fritzsch, B. Mirzaei, M. W. Kennedy, and R. E. Aune, "Automated Quantification of SiC-Particles in Solidified A356 Aluminium Using Imagepro® Plus 7.0," *Characterization of Minerals, Metals, and Materials 2013,* pp. 67-77, 2013.

[8] P. J. Burt, "Fast filter transform for image processing," *Computer graphics and image processing,* vol. 16, pp. 20-51, 1981.

[9] M. C. Powers, "A new roundness scale for sedimentary particles," *Journal of Sedimentary Research,* vol. 23, pp. 117-119, 1953.

[10] A. Çiftja, "Solar silicon refining; Inclusions, settling, filtration, wetting," PhD, Department of Materials Science and Engineering, NTNU, Trondheim, 2009.

[11] S. Saltykov, "Stereometric Metallography (2nd edn.) Metallurgizdat," *New York,* 1958.

[12] J. Gegner, "2D-3D conversion of object size distributions in quantitative metallography," in *Proceedings of the MMT-2006 conference*, 2006, p. 3.

[13] M. Kennedy, R. Fritzsch, S. Akhtar, J. Bakken, and R. Aune, "Electromagnetically Modified Filtration of Aluminium Melts Part II: Filtration Theory and Experimental Filtration Efficiency with and without Electromagnetic Priming for 30, 50 and 80 PPI Ceramic Foam Filters," *To be submitted to Metallurgical Transactions B,* pp. 1-69, 2012.

Supplement 8

Solidified Metal Cleanliness Analysis Using Automated Image Acquisition and Macro Based Digital Image Processing

R. Fritzsch, S. Akbarnejad, K. Marthinsen, and R. E. Aune

submitted to *IEEE Image Processing*

Solidified Metal Cleanliness Analysis Using Automated Image Acquisition and Macro Based Digital Image Processing

Robert Fritzsch, Shahin Akbarnejad, Knut Marthinsen, and Ragnhild E. Aune

Dept. of Materials Science and Engineering, Norwegian University of Science and Technology (NTNU), Trondheim, NORWAY

Communicating author: robert.fritzsch@ntnu.no

Abstract

In the present work a novel method for automated quantitative stereology has been developed, which is able to determine the cleanliness of aluminium melts. The method is capable of identifying particles and inclusions down to 6 µm, and it can distinguish between phases, pores and particles. Based on the use of a normal light microscope, stage automation and basic programming tools (Image Pro® Plus 7.0 software by Media Cybernetics®), the present analytical method is easy to use, cheap to apply and it is capable of delivering a reproducible and statistically reliable particle load analysis. The method has been tested for automated quantification of a particle load in the size range of 6-35 µm in spherical diameter, and it has been benchmarked with a manual particle count giving a total error of ~7.4 % on the overall filtration efficiency.

Keywords: Digital image processing, automated image processing, particle counting, metal cleanliness, melt quality, ImagePro®, quantitative stereology

1. Introduction

Knowledge of the cleanliness of an aluminium melt is crucial for the industry as it can affect *e.g.* the mechanical and chemical properties of the end product, as well as the overall quality. In this regards both single/large inclusions, as well as a high number of small inclusions, are of importance.

Aluminium and its alloys do often contain a high amount of inclusions in the size range ≤ 50 µm, and all inclusions > 10 µm can lead to defects and loss of performance of the end product [1]. The inclusions present in the melt, either as agglomerates, spherical particles, folded bifilms [2] and/or clusters, can be separated into different groups, *i.e.* oxides, spinels, nitrides, carbides, borides, phosphides, sulphides and intermetallics [3]. All the mentioned inclusion types have different effects on the physical and chemical abilities of the end product. The term “cleanliness” of aluminium is therefor defined by the amount of inclusions present in the melt, *i.e.* the amount of indigenous/endogen and exogenous particulates [4].

To secure the cleanliness of the aluminium melt a variety of different treatment processes have over the years been developed. The most commonly applied method, which has been used for production of more than 50% of the world's aluminium production since the 1990's, is filtration by the use of Ceramic Foam Filters (CFF's) [5]. In the case of analysis of both the particle size and the size distribution of the inclusions present in the filtered metal, different refining methods have been developed.

The Liquid Metal Cleanliness Analyser (LiMCA) [6], which is mounted in-line during the casting process, is today considered to be the state-of-the-art in regards to particle counting during casting of aluminium. This technology enables the count of particles down to 20-25 μm in spherical diameter, but it cannot distinguish between gaseous, liquid and solid inclusions. Moreover, it lacks the ability to distinguish between spherical particles, agglomerates, folded bifilms and/or clusters. This affects the accuracy of the results, *i.e.* it affects the particle count in view of particle size and size distribution during cleanliness characterization. As a result, there is clearly a necessity for the development of an analytical method, which is capable of accurate counting particles less than 20 μm in spherical diameter. The method should also be more time efficient than presently known methods, as well as less susceptible to human bias than manual counting.

Various attempts to apply image processing to improve the efficiency and accuracy of different processes have been found in both the industrial and scientific area, as well as in our daily life. Topics related to the medical and biotechnology sectors have a clear focus on in- and ex-situ image processing. The development of automated methods for quantification of the concentration of particles/inclusions with automated image acquisition is therefore not new. However, the knowledge and calculation power of computerized and automated systems has experienced tremendous developments in the last decades, enabling the method to be used in less traditional areas. Modern literatures address specific topics of image processing, usually by application of mathematical models to modify the acquired images, or to rectorate and digitalize existing film material.

The main objective of the present work has been to develop a user friendly, computer based method for counting the number of particles/inclusions and phases present in solid aluminium samples. The method should be capable of auto acquiring micrographs at high magnification of solidified metal surfaces, and to process the micrographs by the use of an easy to apply computerized macro programmed with the use of the Image Pro Plus 7.0 (IPP) software. Based on the obtained results, the particle size and distribution, as well as the degree of porosity in solid aluminium samples will be evaluated. The advantages and disadvantages of the image processing steps, as well as the strength and weaknesses of the method, will be described and discussed. The reproducibility and accuracy of the obtained data will also be given attention.

2. Experimental

Rapid Solidified Spectrographic Disc (RSSD) samples have been collected during seven industrial scale filtration trails using CFF's of two different pore size distributions, *i.e.* 50 and

60 Pores Per Inch (PPI). In total 68 RSSD samples were manually collected during the trails, *i.e.* one sample every ten minutes before and one after the filter box (12-14 samples from each trail). The dimension of each RSSD sample was 50 mm in diameter and 15 mm in height.

The spectroscopic disc samples were machined flat to approximately half of the original sample thickness before being mounted in EpoFix® epoxy, grained and polished. The sample preparation technique consisted of the following two steps: (i) grinding from P120 to P4000 by the use of SiC sandpaper, and (ii) polishing to a mirror like surface-finish using diamond paste 6 and a 1 µm particle size rotating disc. The sample preparation technique used was based on a procedure recommended by Struers® for preparation of aluminium alloys, with some minor modifications. All samples were digitalized and optically analysed using a computer automated stage control unit (a moving desk) mounted on a "Reichert MeF3 A" microscope from Leica using a sideway mounted Sony DXC 950P 1.2 MP digital camera. In Figure 1 the imaging system used is presented.

Figure 1: The imaging system used consists of an automated stage microscope (Reichert MeF3 A), a computer controlled automated stage control unit, manual control levers and a light source. The sideway-mounted Sony DXC 950P digital CCD camera is not visible in the picture.

All micrographs were automatically processed and analysed by a self-developed macro. The macro was programmed using the ImagePro® Plus 7.0 (IPP) software system developed by MediaCybernetics®. The method has been benchmarked and validated elsewhere [7], and the macro verified by a manual count of the same micrographs. It should, however, be mentioned that the present study did not aim to develop a new mathematical model, but to apply existing models/functions to enhance the collected micrographs in such a way that it was possible to distinguish between phases, pores and particles.

The fundamentals of the method presently adopted are partly covered by an issue recognised in literature as a denoising problem [8, 9]. The use of a Gaussian filter [10, 11], a morphological filter [12] and a sharpening function, using the un-sharpening masking

technique, was therefor chosen as the main approach for processing the collected micrographs and thereby suppressing the problem. To quantify the inclusions, a simple threshold function using the theory of quantitative stereology [13] was applied. In this regard it should be mentioned that a contour model [14] known as snakes [15] could have been used to enhance the accuracy of the adopted method, but due to the required simplicity the contour model was excluded. Instead it was decided to base the processing of the micrographs on an application of point operations for the colours black and white allowing for the determination of the area of interest, the shape factor, and the count of the particles present in each image.

It is a well-known fact that the resolution of a microscope is given by the wavelength of the light source over the double numerical aperture:

$$\delta = \frac{\lambda}{2\alpha} \qquad \text{(Eq. 1)}$$

where δ is the smallest distance between the particles that can be resolved [m], λ the wavelength [m], and α the numerical aperture, *i.e.* the ability that the objective of the microscope has to gather light in its cone. Based on Eq.1, the resolution of the presently used microscope, equipped with a standard light source and a normal dry lens with a numerical aperture of 1, *i.e.* $\alpha = 1$, was calculated to be in the range of 0.2 to 0.35 μm. The digital resolution of the camera, as well as the resolution of the microscope, where established to be in the same order of magnitude. In regards to the specifications of the imaging system, the following is valid:

1. a normal white light source with λ = 400 - 700 nm,
2. a lens with a magnification x = 50
3. an eyepiece with a magnification of 10x,
4. a numerical aperture equal to 1,
5. an image field of 191 x 143 μm, and
6. a digital image size of 764 x 580 pixels where the dimension of 1 pixel is equal to 0.25 x 0.25 μm.

For each RSSD sample a total area of 0.1991 cm^2 was automatically recorded using a magnification of 500x. This resulted in a grid of 27 x 27 images for each sample with an area of 27 313 μm^2. This in turn resulted in a total measurable surface area of 3.186 cm^2. In other words, 6.25% of the total sample area was digitalized, and hence made available for digital image processing. In Figure 2 the sequences of the applied image acquiring process is

schematically presented.

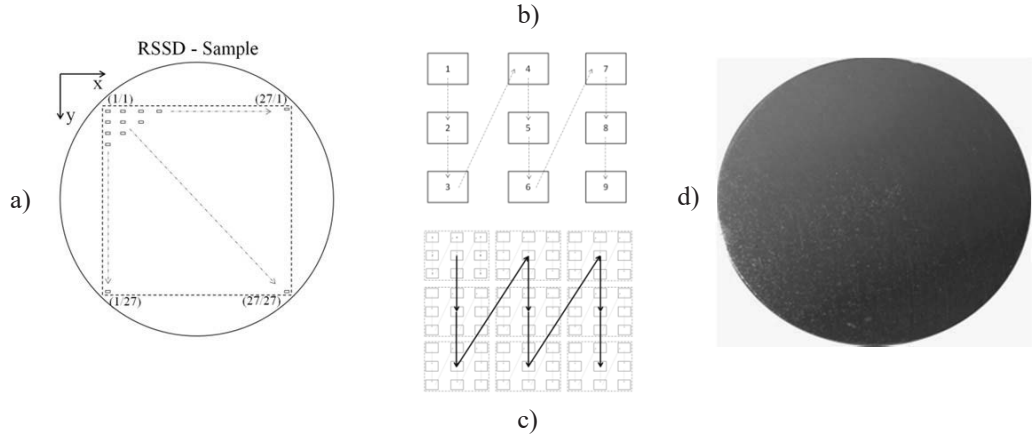

Figure 2: (a) A sketch of the pattern of images that were acquired by the automated stage for each of the samples investigated. The factor between each image is 3, *i.e.* in both *x*- and *y*-direction, for the periodic sampling. (b) and (c) shows the programmed path for the automated stage in regards to acquiring the images, and (d) the surface of a polished metal sample.

To be able to identify artefacts, such as huge pores, focus errors and/or surface preparation problems, the software was programed to merge all images (in the present case 729 images) to a low-resolution collage, as seen in Figure 3. This precaution secured easy access to examine all images manually in one single step, and to evaluate the reliability of the automated results. Additionally, the collage provided detailed image and sequence information, which was embedded in the storage file. Hence, a reconstruction and evaluation of the applied pattern of the automated stage control unit would be possible if needed.

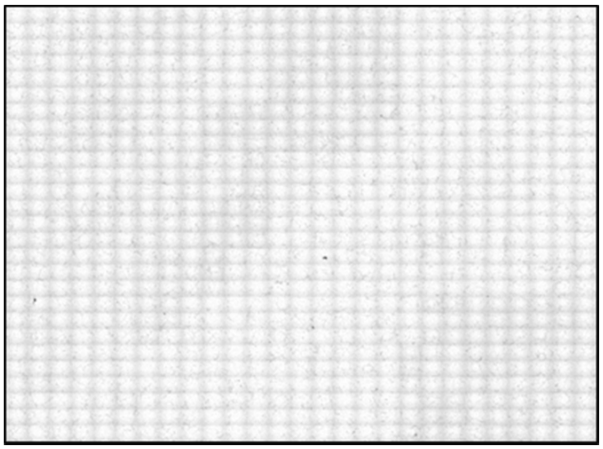

Figure 3: Low-resolution collage of 729 merged images showing 6.25% or ~0.2 cm^2 of the total surface of the sample digitalized at 500x magnification.

3. Method

To evaluate the results, every single image of each set of measurements must be analysed by a static macro applied through the IPP software. It is important to point out that the macro

analyses all images separately and not the collage. This is due to the method used for creating the collage, which results in the resolution decreasing and the edges/corners of each single image being merged. The factor for periodic sampling allows, however, the moving stage to statistically cover a larger area analysing only every fourth image in both *x*- and *y*-direction. Based on the periodic sampling, the collage is generated. It should be noted that particles/inclusions/pores that are present at the edge of a single image would bias the total count. This bias can, however, be removed when analysing single images by excluding every count that has contact with the edge of the image.

The core aspect of image processing is the quality of the digital images recorded. The image data from the camera is therefore recorded as a tagged image file format (*.tif) to avoid compression and/or loss of information such as the pixel size. During the first step of the image-processing procedure the macro reads the dimension of a pixel, and sets a spatial (three-dimensional) calibration for the following steps.

To be able to identify a single element, *e.g.* particles, a general difference in contrast between neighbouring pixels are required. The size of one single pixel captured by the camera defines the minimal size of details of the real image that can be resolved. The camera used in the present study was able to identify and resolve a difference in contrast for every 0.25 µm, thereby defining a pixel as 0.25 x 0.25 µm, or 0.0625 μm^2. The critical size for identifying differences in the image details is defined by the size of a pixel.

As previously mentioned, one pixel represents the smallest component of a digital image which can be resolved by the optical system, and thus detected by the camera. For binary images every pixel has a range between 0 (black, no white) and 1 (white), whereas the images have a colour depth of 8 bits, which allows for 256 different intensities. A single particle can be resolved in *x*- and *y*-direction with a minimum of 8 pixels or 2 µm. This criterion defines a single edge, or a boundary layer to be 3 pixels or 0.75 µm. The identification of the particles is based on the gradients of the grey scale and the shape functions generated by these gradients.

The particles present in the samples to be evaluated have a less reflective surface, and appear therefore as darker objects. They have a diameter of 1 to 8 µm on average, and the observed bifilms a minimum diameter down to 0.1 µm [4]. All particles above 0.2 µm are in the range of the resolution of visible light, and could thereby be identified. However, due to the noise of the imaging system, as well as the resolution of the camera, the identification of particles in the size range < 2 µm proved to be impossible.

The limit of the resolution is directly connected to the detector of the camera, resolving the grey level gradients distinguishable for each individual particle. In Figure 4 (a) and (b) two digitally enlarged ~3 µm particles, recorded by the use of two different cameras with different resolutions, are presented. The particle with the blurred edge, shown in Figure 4 (b), will give a ‘wrong’ area count, and thus bias the total particle/inclusion count. The particle shown in Figure 4 (a) will allow for a ‘more’ accurate count. To remove the blur and sharpen

the contour of the particles, different mathematical filters and methods can be applied [16, 17].

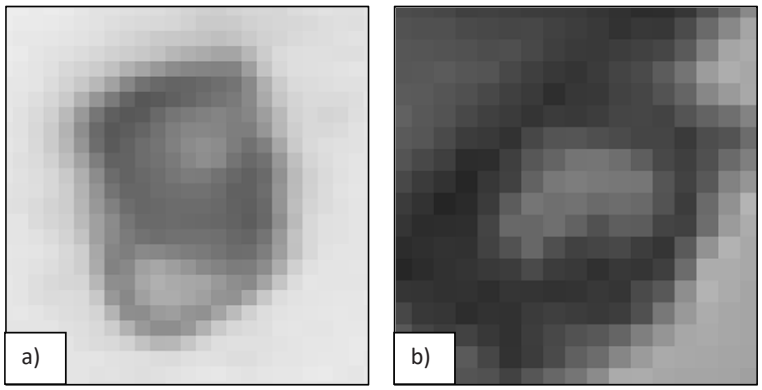

Figure 4: Two images of a digitally enlarged ~3 µm particle taken at different resolutions: (a) 0.0625 μm^2/pixel and (b) 0.2656 μm^2/pixel.

3.1 Image-processing steps

The different steps of the image-processing method proposed in the present study are compiled in a macro assessed through the IPP software. The steps are:

1. applying a filter to flatten the image,
2. subtracting the background noise image,
3. applying a high pass Gauss filter,
4. using a sharpen function,
5. processing the image with a morphological filter function,
6. additional sharpen function, and
7. adjustment of the values of gamma, contrast and brightness.

The final step of the macro is to count all objects of a certain size and spherical shape.

The effect of the different steps of the digital image processing method is illustrated in Figure 6 (a) to (d). It should be noted that all images are displayed without a scale or a scale bar.

3.2 Testing of the method

Contrast and luminosity are critical variables to be adjusted during image acquisition. The light source used during the present study had a constant intensity over time with small fluctuations in the power. These fluctuations resulted in small variations in both contrast and illumination during acquisition of the images. Additionally, the brightness was inhomogeneous, resulting in a bright spot in the centre of each image and darker corners. The collage of images presented in Figure 3 illustrates this issue. This was, however, resolved by

applying a general flattening filter (step 1) on every single image (not on the collage). Furthermore, a background noise origination from the microscope and the camera was subtracted (step 2). In Figure 5 (a) and (b) the improvements obtained to the image, as a result of applying the flatten function and background correction, are presented. As can be seen from Figure 5, the flattening function homogenizes the luminosity to a constant value, *i.e.* it has the same effect as the contrast and gamma has on a set of images. The subtraction of a slightly out of focus background image removes a major part of the background noise and the lens effects, *i.e.* it has the same effect as the spherical shape of the light source.

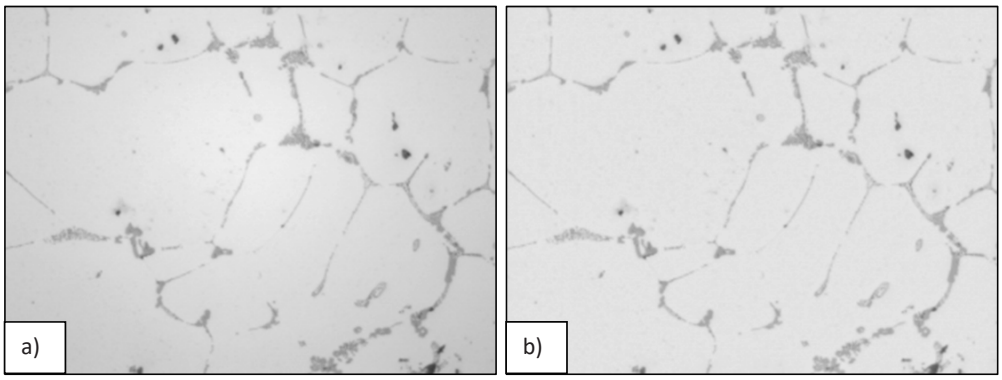

Figure 5: Micrographs of an aluminium silicon alloy after filtration. (a) The aluminium matrix is displayed as the brightest phase, the eutectic AlSi-phase as the darker greyish fishbone like phase, and the round particles/inclusions by a dark grey-blackish colour. The inhomogeneity of the luminosity is clearly visible. (b) The same image after applying "background correction" and "flattening" to improve the noise and luminosity.

As a result of applying a flattening function together with the background subtraction a static macro that corrects the corners of the images, which otherwise would react differently on the mathematical filters than the centre of the image, is obtained. The images are now homogenized and can be further processed.

To identify the elements of interest present in each image the contrast must be enhanced. This was achieved by using the difference in greyscale of the boundary layer of the particles. An adjusted high pass Gaussian filter (step 3) with a medium sized kernel matrix of 5x5 was applied. The Gaussian filter separates step edges analytically and results in larger gradients on the edge of all particles, as well as on intermetallics. A sharpen filter function (step 4) was then applied with a smaller kernel than the Gaussian filter, *i.e.* a 3x3 kernel matrix. This reduced the blur that was introduced into the image by the earlier filter, and enhanced the grey level gradient of the edge of the particles further. The result is shown in Figure 6 (b). For comparison a "dirty", or a ¨worst case scenario¨ image, is presented in Figure 6 (a).

To separate and identify particles and inclusions that were not closed loops, or that were not completely surrounded by an equal grey level of pixels, a set of morphological filters (step 5) were applied to the images. The function used is called "close" function, and works as a morphological filter with an unsymmetrical kernel matrix. The filter fills gaps and enlarges protrusions of certain sizes to connect objects that are close together. The kernel matrix size was chosen to be 3x1, as a row in *x*-direction and another to be 1x3 as a row in *y*-direction.

The result is presented in Figure 6 (c). The particles and inclusions are not altered and remain equal in size and shape even after being manipulated by the filters.

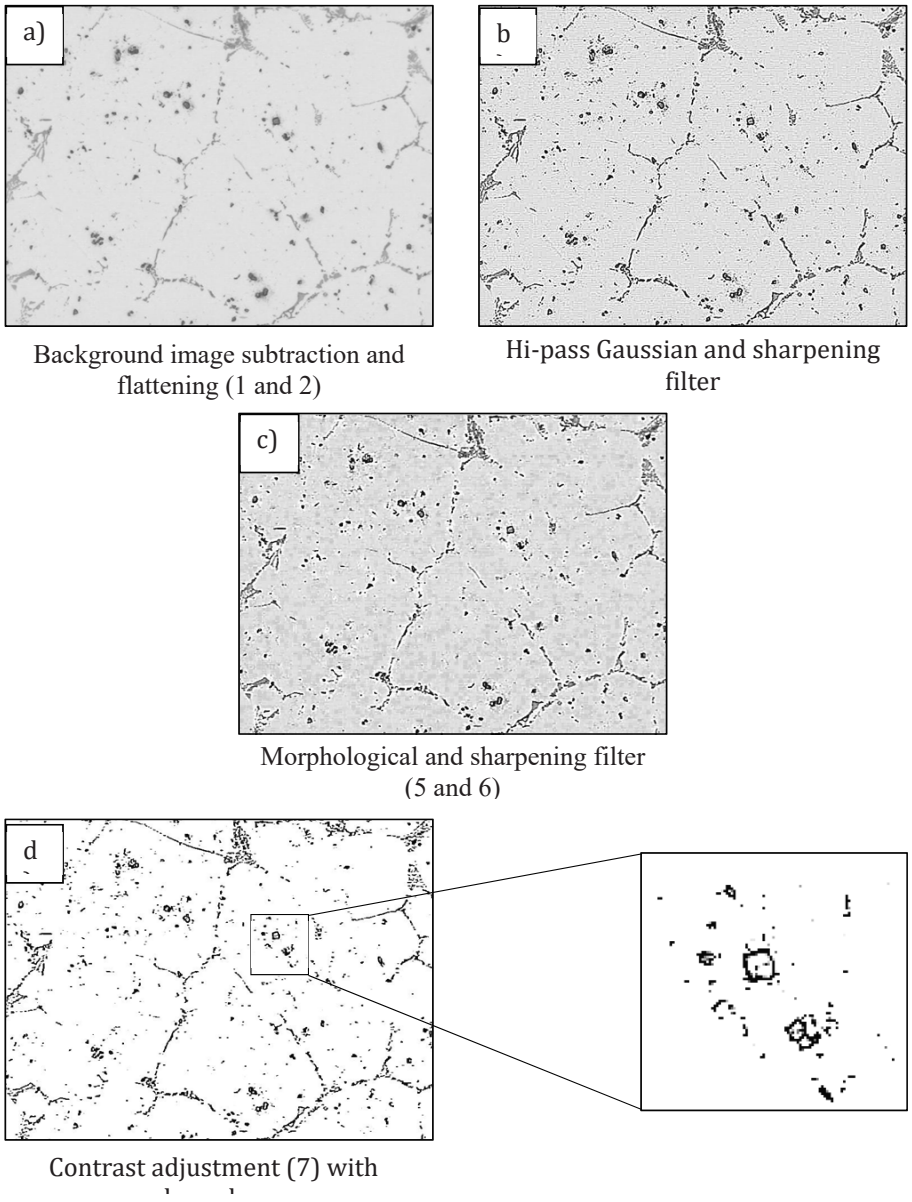

Figure 6: Micrograph of an aluminium sample before filtration. (a) The metal before the filter box and degasser. A person skilled in the art can identify the dark particles as a large amount of small inclusions. The average size of the inclusions is in the range of 1-2 µm with a few particles in the range of 5-8 µm. (b) Application of a high pass Gaussian filter (5x5 kernel matrix) and a sharpening filter (3x3 kernel matrix). (c) Application of morphological filters (3x1 and 1x3 kernel matrix). (d) Application of the contrast adjustment function. The enlarged area demonstrate the thickness of the boundary layers.

By application of another small kernel sharpen filter the introduced blur was removed (step 6) before the next step was executed which intention was the contrast and gamma correction

(step 7). The remaining information was enough to identify and close a line around the areas of interest, separating the particles/inclusions from the rest of the image, as presented in Figure 6 (d). This was achieved by manipulating the tone curve to set all values above 159 to 255. After that the values of gamma, brightness and contrast were adjusted to fulfil the counting requirements. At this point the image contained only the remaining filtered edge information, and the final measurement could be performed. As the software will identify and count all kind of closed loops, *i.e.* pores, particles and eutectics, the images were further improved by applying additional adjustable parameters and filters.

The "counting measurement" menu of the IPP software presents a variety of options and parameters to distinguish between particles and/or inclusions. The parameters chosen from the IPP menu for the present study was the "*area*", "*roundness*", "*radius (max)*" and "*count*" parameters. The parameters can be describes as follows:

- *Area*: Area of object without counting holes (a maximum was set to 25000 μm^2 (~158 x 158 pixels), while the small particles below 9 μm^2 (12 x 12 pixels) was excluded).
- *Roundness*: Described in Eq.3 below and set to 0.7 and 1.7.
- *Radius (max)*: The distance between the objects centroid and the outer line (the distance was set to be 15 µm).
- *Count*: Adjusted counts of all counted particles.

In Figure 7 a comparison is made between two micrographs before the use of the macro (step 1 to 7), see Figure 7 (a), and after, see Figure 7 (b). In Figure 7 (b) the accurate count of particles are also presented.

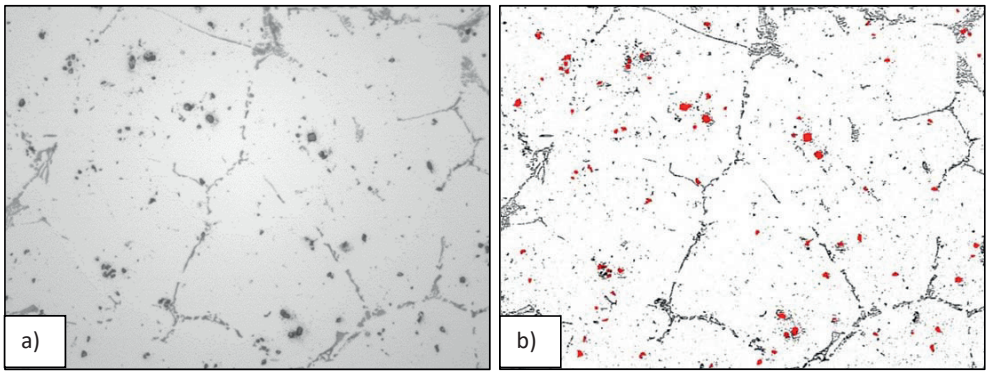

Figure 7: Micrographs of the same image as the one presented in Figure 6. (a) Before application of the macro. (b) After application of all filters, parameters and counting options (the identified particles in red).

4. Results and Discussion

The macro required a minor manual modification before it could analyse the 729 images recorded in the present study. After modification the macro identified the particles present in all images automatically, stored them in an internal data collector, and automatically exported the data to a Microsoft Office® Excel spread sheet. The data output, given in square millimetres, was recalculated to an equivalent circular diameter, as estimated by the following relationship:

$$D_{sph.,eq} = \sqrt{\frac{4*A_{Obj}}{\pi}} \qquad \text{(Eq. 2)}$$

where A_{obj} is the object area [m^2], and $D_{sph.,eq}$ the resulting equivalent circular diameter [m]. For the use of Eq. 2, all particles and inclusions were assumed to be round and/or spherical shaped.

The counting parameter "roundness" was applied to remove all particles that did not given an answer between 0.7 and 1.7 for the following relationship:

$$"Roundness" = perimeter^2/(4\pi * area) \qquad \text{(Eq.3)}$$

where all information is given by the applied pixel definition.

The calculated equivalent diameters were modified using the well know stereoscopic correction factor of $\sqrt{1.5}$ to adjust the count to a real estimate [13, 18]. The resulting object sizes from each sample were collected into individual data sets. The sum of all object areas was calculated and the particle counts were grouped into 23 size groups, *i.e.* one group for each µm starting from 2 µm ≤ x < 3 µm until 24 µm < x < 25 µm. Only the groups above 6 µm were used in the present study.

It was assumed that the inclusion distribution was uniform across the cutting plane. Moreover it was assumed that the acquired area of each sample gave a representative statistical trend of the inclusion density.

To validate the accuracy of the digital image processing, the filtration efficiency was determined by the automated macro presented, and the results compared to a manual count performed on the same images. To determine the filtration efficiency of the different Ceramic Foam Filters (CFFs) used for filtration of liquid aluminium, the following relationship was used:

$$E = \frac{N_i - N_0}{N_i} \qquad \text{(Eq. 4)}$$

where E is the filtration efficiency [%], N_i the count of particles entering into the filter per mm^2, and N_0 the count of particles leaving the filter per mm^2. N_i and N_0 can be determined from a normalized count (particles per unit area) on the initial and final filtration samples.

All samples evaluated in the present study were manually taken at 10-minute intervals during the casting of billets. Two casting trials was analysed, and the variation in filtration efficiency will be discussed.

For the first trial a 50 PPI filter was used, 4 RSSD samples retrieved, and 2916 images analysed. The results are shown in Figure 8. As can be seen from the figure, the largest identified particles after filtration were 23 µm in size. For the second trial a 60 PPI filter was used, 12 RSSD samples retrieved, *i.e.* 7 samples before the filter and 5 samples after, and 8748 images analysed. The results are shown in Figure 9. As can be seen from the figure, all particles after the filter were < 11 µm is size. The filtration efficiency in both cases was compared with the results from manual counts. From the average counts it was observed that the higher-grade filter removed a higher average number of particles.

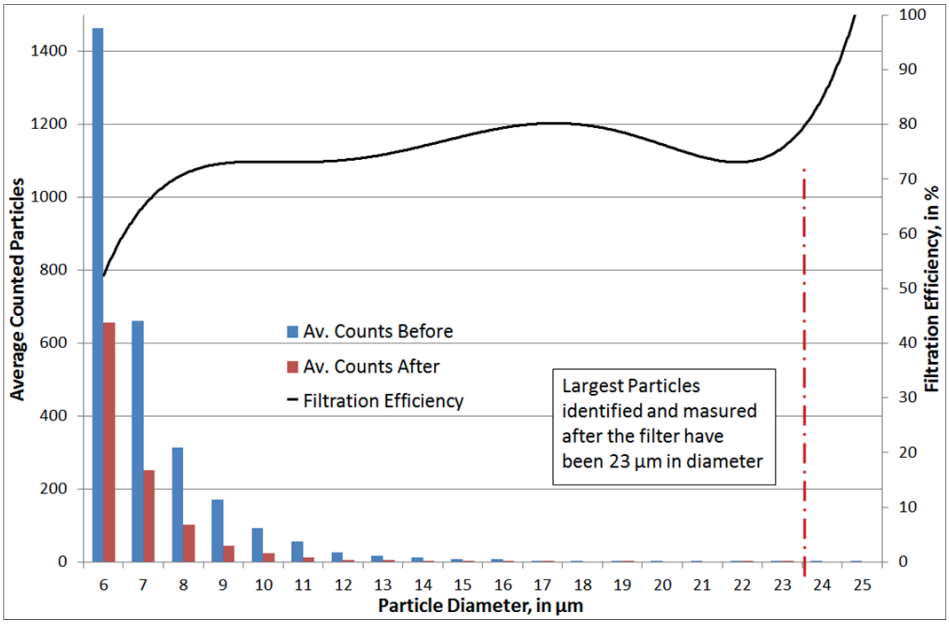

Figure 8: Histogram of the total particle count from the filtration trail using a 50 PPI CFF.

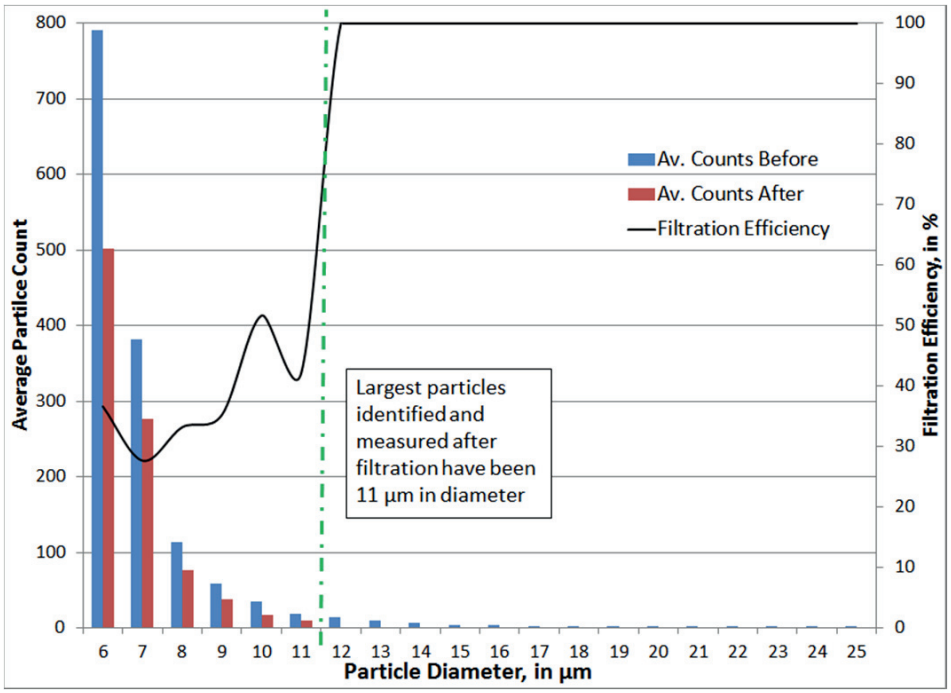

Figure 9: Histogram of the particle count from the filtration trial using a 60 PPI CFF. The total filtration efficiency, and the filtration efficiency of particles above 11 µm, has been included.

From Figure 9 it can be seen that remarkable good removal efficiency was obtained for particles in the size range above 11 µm for the 60 PPI filter, *i.e.* no particle could be identified by the automated method or manually in the size range above 11 µm. Only a moderate removal efficiency of 37.8 % of all particles in the size range of 6 to 11 µm was, however, found. A very high quantity of 2 µm large particles were also identified, but not considered to be inclusions. It is believed that these particles are titaniumdiborite (Ti_2B) particles originating from the grain refiner added directly prior to casting. Small inclusions in general tend to form larger agglomerates.

To benchmark the error of the applied macro a manual corrected particle count based on 10 % of one set of images from the first experimental trial with the 50 PPI CFF, *i.e.* of 289 images, was performed. The results are shown in Figure 10 and Figure 11.

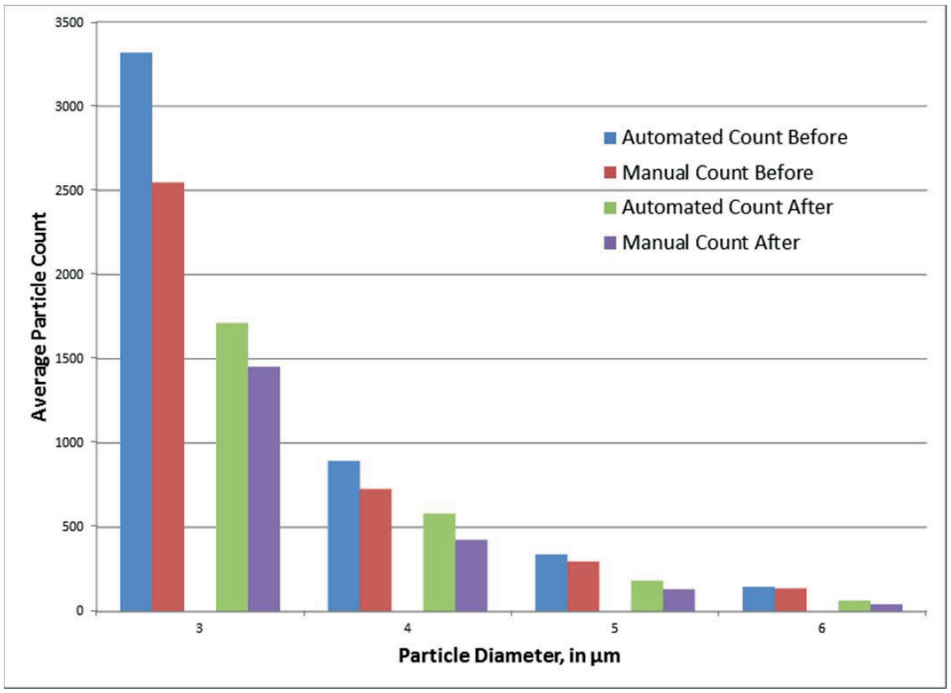

Figure 10: Total amount of particles present in a sample obtained from the filtration trial using a 50 PPI CFF. In total 289 images where evaluated based on both the manual and automated count of particles in the 3-6 µm size range.

The inclusions with a size ≤ 6 µm corrected spherical diameter proved to be biased by 20.7 % on average between automated to manual count. The reason for this high number is due to difficulties to resolve the particles properly, as earlier mentioned. For the particles with a size > 6 µm the bias was reduced to ~ 6 %. This result in a lower total filtration efficiency of 7.4 % in the size range from 3 to 23 µm for the automated particle count compared to the manual count. The trend is similar before and after the filter. Comparing the number of the automated count with the manual count, it is concluded that the automated method clearly identifies more particles. Nevertheless; the error is most significant for particles in the size range from 3 to 6 µm, and grouped as the critical size range for the used resolution. As a result the counts of particles in the size range from 3 to 6 µm were excluded.

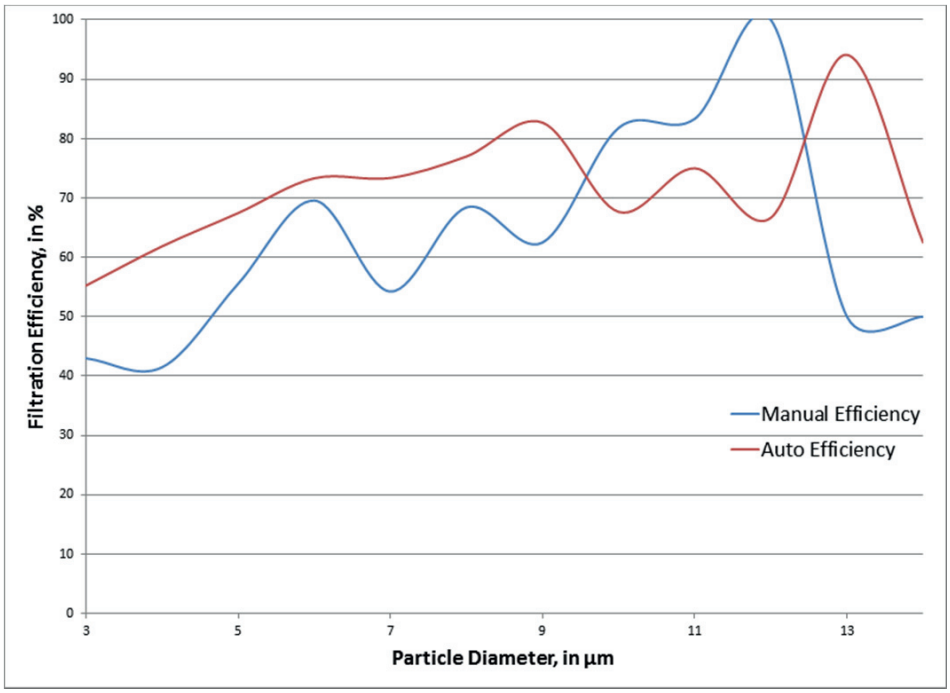

Figure 11: Resulting filtration efficiencies evaluated based on the manual and automated count of particles in the 3-14 µm size range.

Initial clean metal samples, see Figure 12(a), gave statistically a higher count for particles below 6 µm spherical diameter, and several wrong counts in the eutectic regions. It is concluded that the trend of wrong counts was higher on clean metal samples than on contaminated samples. A highly contaminated melt sample from before the cast is shown in Figure 12 (b). Samples similar to this proved to have a much higher contamination, but a lower variation of error of identified particles and inclusions.

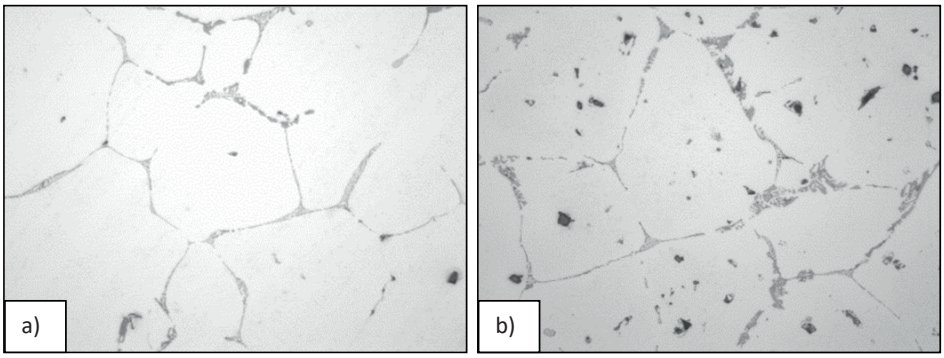

Figure 12: Comparison of (a) a clean aluminium sample after filtration, and (b) a highly contaminated sample before filtration.

5. Summary

The automated image acquisition method proposed and applied in the present study uses a statistical approach to identify particles by investigating the 2D surface plane of each sample. Rapidly solidified aluminium samples were used as the starting material to avoid particle migration. It is in this regard important to remember that a 2D study does not represent the real 3D structure of the particle network inside the sample. Further, the chance of cutting the particles at the centre line is statistically not highly favoured. Additionally, the presence of only symmetrical particles was considered. The spherical correction factor was applied to estimate the real size of the identified inclusions. To achieve realistic and statistical representative data, large areas with high resolution were studied. The results were found to be reproducible, as shown in earlier publications by the same research group [7].

The 1.2 MP camera used in the experimental trials were identified to be the weak point of the proposed method due to the resolution of the camera. The resolution is, as previously mentioned, the key element of importance and defines the ability the setup has to resolve image information during recording. Due to the low resolution, accurate identification of particles/inclusions down to 2 μm was not possible.

In the present setup one single pixel proved to resolve an area of 0.0625 μm^2, and four pixels were established to be enough to resolve an edge of an obstacle. To be on the safe side, twelve pixels in one direction were therefore set as the logical limit to be able to identify the beginning and the end of a particle. This resulted in that 3 μm corrected spherical diameter was the smallest obstacle that could be identified, and up to 6 μm in regards to corrected spherical diameter. To avoid high uncertainties and inaccurate results, the small particles were excluded from the study. Nevertheless, particles/inclusions/obstacles/pores/phases with a corrected spherical diameter down to 1.5 μm were identified.

In regards to work on aluminium and its alloys, the present authors have not found filtration efficiency data reported in literature for particles less than 15 μm in diameter. This is believed to be due to LiMCAs inability to analyse inclusions below the limit of 20 μm in size. Furthermore, LiMCA cannot distinguish between different types of inclusion, agglomerates, gas bubbles, bi-films or 3D resolution of inclusion shapes. When comparing the trends of the particle load in aluminium samples to the particle count in steel samples, similarities can be found [19].

It has been reported in literature [20] that algorithms exists that are capable of increasing the resolution by using multiple low-resolution images of the same area, reasonable assumptions, and an observation model that maps the high-resolution image to the low-resolution image. In other words, the method allows for the generation of a so called “Super Resolution” (SR).

Application of a SR method to enhance the resolution of the camera used in the present study would generate large amount of data to be handled, and it would also introduce additional possibilities of errors by adding or removing areas of the images. Modifications on the pixels itself by breaking each pixel into a matrix of pixels will always introduce an uncertainty.

6. Conclusions

The automation of image acquisition method is a powerful tool that quickly can quantify the melt quality obtained during *e.g.* casting processes. The results obtained can be used to estimate the particle concentration, as well as the particle size and size distribution. Detailed knowledge of the total number of small particles cannot only provide valuable information in regards to metal cleanliness, but also in regards to the filtration efficiency during cast house operations. Moreover, the method can give a new and/or complementary way to study filters (materials, flow patterns, PPI, geometries etc.), the settling behaviour of particles/inclusions over time, as well as other issues of importance during filtration of molten metal. Additionally, the effect of human bias can be removed.

The knowledge of digital image processing in the area of edge detection and particle separation has been known for many years, but it has rarely been applied to material science. The reason for this is believed to be partly due to the small grey level variations that exist between the eutectic, metal matrix and particles/inclusions found in metallographic images of metal samples. In the present study, however, image processing and a method to separate and identify inclusions/particles/pores was successfully tested and applied on standard industrial aluminium cast house samples. Based on the results obtained it is concluded that the method is efficient, easy to use, and gives reproducible results. As the method does not destroy the samples during analyses, *i.e.* non-destructive in regards to the samples analysed, it also allows for reanalyses of any sample if necessary. Not to forget is that the method is quick and requiring very limited investment. In other words, it has a good chance of being implemented as a fully automated method resulting in a major time saving in comparison with the analytical techniques used for cleanliness analyses by the aluminium industry today, *i.e.* spark analysis.

Further developments in regards to improving the overall error of the method are, however, needed, especially in regards to small particles (> 6 μm). This requires further developments on the equipment side with enhancing the automated image acquisition and image quality, on the programming side with further developing robust and precise method, and on the metallographic side with developing and implementing known skills for perfect surface preparation.

7. Acknowledgement

The authors wish to express their gratitude to the Department of Materials Science and Engineering (DMSE), as well as the Department of Chemistry, at the Norwegian University of Science and Technology (NTNU) for the intensive usage of the optical equipment in the microscopic laboratory. The financial support granted by the Faculty of Sciences and Technology at NTNU for the financial support of Dipl. Ing. Robert Fritzsch is greatly acknowledged.

8. References

[1] B. Friedrich, C. Kräutlein, and K. Krone, "Melt Treatment of Copper and Aluminium–The Complex Step Before Casting," in *Proceedings of The International Conference on Continous Casting of Non-Ferrous Metals, Wiley-Vch, DGM*, 2006, pp. 3-22.

[2] J. Campbell, *Complete Casting Handbook: Metal Casting Processes, Metallurgy, Techniques and Design*: Elsevier, 2011.

[3] D. E. Groteke, "The Reduction of Inclusions in Aluminum by Filtration," *Modern Casting,* vol. 73, pp. 25-27, 1983.

[4] B. Prillhofer and H. Antrekowitsch, "Abscheidung von nichtmetallischen Einschlüssen bei der Raffination von Aluminiumlegierungen," *BHM Berg-und Hüttenmännische Monatshefte,* vol. 152, pp. 53-61, 2007.

[5] K. Butcher and D. Rogers, "Update on the Filtration of Aluminum Alloys with Fine Pore Ceramic Foam," 1990, pp. 797-803.

[6] R. Guthrie and M. Li, "In Situ Detection of Inclusions in Liquid Metals: Part II. Metallurgical Applications of LiMCA Systems," *Metallurgical and Materials Transactions B,* vol. 32, pp. 1081-1093, 2001.

[7] R. Fritzsch, B. Mirzaei, M. W. Kennedy, and R. E. Aune, "Automated Quantification of SiC-Particles in Solidified A356 Aluminum Using Imagepro® Plus 7.0," *Characterization of Minerals, Metals, and Materials 2013,* pp. 67-77, 2013.

[8] M. Elad and M. Aharon, "Image Denoising via Sparse and Redundant Representations over Learned Dictionaries," *Image Processing, IEEE Transactions on,* vol. 15, pp. 3736-3745, 2006.

[9] R. Eslami and H. Radha, "Translation-invariant Contourlet transform and its Application to Image Denoising," *Image Processing, IEEE Transactions on,* vol. 15, pp. 3362-3374, 2006.

[10] R. Haddad and A. N. Akansu, "A Class of Fast Gaussian Binomial Filters for Speech and Image Processing," *Signal Processing, IEEE Transactions on,* vol. 39, pp. 723-727, 1991.

[11] A. Jain and R. Gupta, "Gaussian Filter Threshold Modulation for Filtering Flat and Texture Area of an Image," in *Computer Engineering and Applications (ICACEA), 2015 International Conference on Advances in*, 2015, pp. 760-763.

[12] M. S. Hamid, N. R. Harvey, and S. Marshall, "Genetic Algorithm Optimization of Multidimensional Grayscale Soft Morphological Filters with Applications in Film Archive Restoration," *Circuits and Systems for Video Technology, IEEE Transactions on,* vol. 13, pp. 406-416, 2003.

[13] E. E. Underwood, *Quantitative stereology*: Addison-Wesley Pub. Co., 1970.

[14] T. F. Chan and L. Vese, "Active Contours Eithout Edges," *Image processing, IEEE transactions on,* vol. 10, pp. 266-277, 2001.

[15] M. Kass, A. Witkin, and D. Terzopoulos, "Snakes: Active Contour Models," *International journal of computer vision,* vol. 1, pp. 321-331, 1988.

[16] I. Bankman, *Handbook of Medical Image Processing and Analysis*: academic press, 2008.

[17] F. Weinhaus. (2014, 04.05.). *Digital Image Filtering*. Available: http://www.fmwconcepts.com

[18] A. Çiftja, "Solar Silicon Refining; Inclusions, Settling, Filtration, Wetting," PhD, Department of Materials Science and Engineering, NTNU, Trondheim, 2009.

[19] J. Gegner, "2D-3D Conversion of Object Size Distributions in Quantitative Metallography," in *Proceedings of the MMT-2006 conference*, 2006, p. 3.

[20] J. Yang, J. Wright, T. S. Huang, and Y. Ma, "Image Super-resolution via Sparse Representation," *Image Processing, IEEE Transactions on,* vol. 19, pp. 2861-2873, 2010.